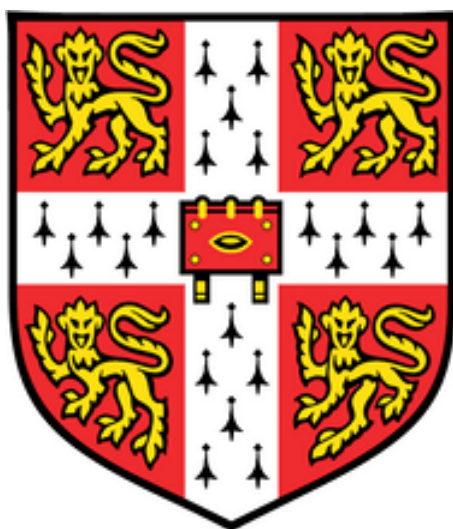


Nuclear Magnetic Resonance Studies of Lithium Metal Anodes



Anna Bergljót Gunnarsdóttir

Department of Chemistry

University of Cambridge

This dissertation is submitted for the degree of

Doctor of Philosophy

Pembroke College

September 2020

This work is dedicated to my parents Olga and Gunnar

Declaration

I hereby declare that except where specific reference is made to the work of others, the contents of this dissertation are original and have not been submitted in whole or in part for consideration for any other degree or qualification in this, or any other University. This dissertation is the result of my own work and includes nothing which is the outcome of work done in collaboration, except where specifically indicated in the text. This dissertation contains less than 60,000 words excluding the table of contents, figure captions, bibliography, acknowledgments and appendices.

Anna Bergljót Gunnarsdóttir

September 2020

Abstract

Nuclear Magnetic Resonance Studies of Lithium Metal Anodes

Anna Bergljót Gunnarsdóttir

Lithium metal has received a renewed interest as a promising anode material for next-generation, high-energy batteries owing to its high specific capacity (3860 mAh g^{-1}) and low reduction potential (-3.04 V vs. the standard hydrogen electrode). However, lithium metal batteries suffer from low capacity retention, short cycle life and safety problems associated with microstructural and dendritic growth of lithium. In this work, nuclear magnetic resonance (NMR) spectroscopy is used to understand the effect of the solid electrolyte interphase (SEI) on lithium metal deposition.

In situ NMR is used to quantify the lithium microstructures formed during plating and allows the current efficiency and porosity of the structures to be estimated. The effect of the fluoroethylene carbonate (FEC) additive is explored along with a range of plating conditions. NMR measurements show that the isotope exchange between a ^6Li -enriched lithium metal and a natural abundance electrolyte depends significantly on the electrolyte and the corresponding SEI. A numerical model is developed to describe the processes during isotope exchange and is discussed in the context of the standard model of electrochemical kinetics. The model is used to extract both an exchange current at the open circuit voltage and the SEI formation current as a function of time.

In situ NMR methods are then developed to study ‘anode-free’ lithium metal batteries where the lithium is plated directly onto a bare copper current collector from a LiFePO_4 cathode. The low cycling stability of lithium metal batteries becomes clear when there is no excess of lithium in the cell. The ‘dead lithium’ and SEI formation can be quantified by NMR and their relative rates of formation are here compared in carbonate and ether-electrolytes. Importantly, the NMR experiments reveal that the dissolution of lithium metal during the periods when the battery is not in use, i.e., when no current is flowing, demonstrating that dissolution of lithium remains a critical issue for lithium metal batteries. Strategies to mitigate lithium corrosion are explored; the work demonstrating that both polymer coatings and the modification of the copper surface chemistry stabilising lithium metal. Overall, this work demonstrates that the NMR approach offers unique insight into the dynamic processes occurring on lithium metal both during electrochemical measurements and at the open circuit voltage.

Acknowledgements

First and foremost, I would like to thank my supervisor, Professor Clare Grey, for her endless support, guidance and encouragement throughout my time here. I feel incredibly privileged to have had the opportunity to learn from such a brilliant and inspiring scientist and group leader.

I would like to thank the entire Grey group for the kind help and support over the last four years. I feel so lucky to have worked in such a friendly and collaborative environment for which we have Clare to thank who brings us together with science, hiking, music and friendship.

Many thanks to those who have guided me through my PhD. I would like to thank Lauren Marbella for supervising me for the first two years of my PhD, for her insight and ideas and for teaching me how to do NMR. I would like to thank Svetlana Menkin for all her teaching, the endless discussions and her contagious enthusiasm for science and electrochemistry. I would like to thank Adam Best for giving me the opportunity to visit him and work for three months in CSIRO–Australia, for all the motivating discussions and useful ideas as well as for being an extremely nice host and a good friend. My collaborators, in particular Sundeep Vema for always be willing to discuss, Chibueze Amanchukwu, Michael Hope, Bernardine Rinkel, Pieter Magusin and Tamsin Newlove for their help and contributions. Katharina Märker, Chris O’Keefe, Evelyn Wang and Erlendur Jónsson are gratefully acknowledged for proofreading this thesis. My office mates over the past four years, Phil Reeves, Yuning Zhou, Steffen Emge, Michael Jones, Francesca Firth, Zachary Ruff and Chao Xu. As well, I would like to thank David Halat, Kent Griffith and Gunwoo Kim for teaching me much about NMR.

My greatest gratitude goes to my mother and father for their endless love and generosity, without them, none of this would have been possible. To my siblings Gunnhildur, Snorri and Þorleifur, and everyone at Lindarbraut and Vesturbrún, especially Bryndís for the summer we had in Cambridge. To my friends in the U.K., particularly Lewis, Luise and Joana for encouraging me to take breaks and enjoy Cambridge. To Prof. Brian Thrush for being such a lovely neighbour and telling me about the Chemistry department back in the old days. To my friends back home, Sunna, Tóta, Sæmi, Steinunn, Líska and Urturnar for never letting me grow apart. Finally, I would like to thank Jóhann for his love and support that has helped me through hard times, for our four years in the U.K. and the four months of lockdown this spring, that strangely I have started to feel nostalgic towards, and for raising my spirit every single day.

List of Publications

Chapter 4 and Chapter 5 contain material from the publication:

Gunnarsdóttir, A. B.; Vema, S.; Menkin, S.; Marbella, L. E.; Grey, C. P. Investigating the Effect of a Fluoroethylene Carbonate Additive on Lithium Deposition and the Solid Electrolyte Interphase in Lithium Metal Batteries Using in Situ NMR Spectroscopy. *J. Mater. Chem. A* **2020**, *8* (30), 14975–14992.

Publications not included in this thesis:

Hope, M. A.; Rinkel, B. L. D.; Gunnarsdóttir, A. B.; Märker, K.; Menkin, S.; Paul, S.; Sergeyev, I. V.; Grey, C. P. Selective NMR Observation of the SEI–Metal Interface by Dynamic Nuclear Polarisation from Lithium Metal. *Nat. Commun.* **2020**, *11* (1), 2224.

Menkin, S.; O’Keefe, C.; Gunnarsdóttir, A. B.; Dey, S.; Pesci, F.; Shen, Z.; Agudero, A.; Grey, C. P. Preprint: Towards an Understanding of the SEI Formation and Lithium Preferential Plating on Copper. *ChemRxiv* **2020**.

Contents

Contents	xv
List of Figures	xviii
List of Tables	xxix
List of Abbreviations	30
Chapter 1 Introduction.....	32
1.1 Thesis Overview	33
Chapter 2 Energy Storage and Electrochemistry.....	36
2.1 Li-ion Batteries and Beyond	36
2.2 Lithium Metal Batteries	37
2.2.1 Cell configurations.....	40
2.2.2 The solid electrolyte interphase	41
2.2.3 Characterisation techniques	43
2.3 Electrochemistry	45
2.3.1 Electrode kinetics.....	45
2.3.2 Electrochemical corrosion	48
2.3.3 Electrochemical methods	50
Chapter 3 Nuclear Magnetic Resonance Spectroscopy.....	59
3.1 Basic Principles of NMR	59
3.2 NMR of Metals	62
3.2.1 Knight shift	62
3.2.2 Bulk magnetic susceptibility.....	65
3.2.3 Skin depth of metals.....	69
3.2.4 Quantification of metals.....	71
3.3 <i>In situ</i> NMR	72
3.3.1 <i>In situ</i> NMR studies of Li metal	72

3.3.2	Experimental considerations	73
Chapter 4	<i>In situ</i> NMR Studies of Lithium Metal Plating.....	75
4.1	Introduction.....	75
4.2	Experimental Details.....	77
4.2.1	Materials	77
4.2.2	Cell fabrication.....	77
4.2.3	Electrochemical measurements.....	78
4.2.4	<i>In situ</i> NMR spectroscopy	78
4.2.5	Pulsed-field gradient NMR spectroscopy	79
4.2.6	Scanning electron microscopy	80
4.3	Results.....	80
4.3.1	Constant plating with and without an additive	80
4.3.2	Voltage traces in coin cells as an indirect way to study surface kinetics	86
4.3.3	Pulse plating.....	88
4.4	Discussion.....	97
4.5	Conclusions.....	98
Chapter 5	Lithium Isotope Exchange	101
5.1	Introduction.....	101
5.2	Experimental Details.....	104
5.2.1	Materials	104
5.2.2	NMR spectroscopy.....	104
5.2.3	Electrochemical impedance spectroscopy	105
5.3	Numerical Modelling	105
5.4	Results.....	111
5.4.1	Isotope exchange measurements in different electrolytes	111
5.4.2	Impedance spectroscopy	119
5.4.3	Temperature dependence on isotope exchange.....	121

5.5	Discussion	125
5.6	Conclusions and Outlook	128
Chapter 6	<i>In situ</i> NMR Studies of Full-Cell Lithium Metal Batteries	131
6.1	Introduction.....	131
6.2	Experimental Details.....	134
6.2.1	Materials and cell fabrication.....	134
6.2.2	Electrochemistry	135
6.2.3	<i>In situ</i> NMR spectroscopy	135
6.2.4	Susceptibility calculations	136
6.3	Results.....	137
6.3.1	Detection of dead Li by <i>in situ</i> NMR.....	137
6.3.2	Capacity losses during plating and stripping	140
6.3.3	Bulk magnetic susceptibility effects of Li metal	148
6.3.4	Dissolution of Li metal	158
6.3.5	⁷ Li shift of the diamagnetic peak	164
6.4	Discussion	167
6.5	Conclusions and Outlook.....	170
Chapter 7	Conclusions and Future Work	173
References	176

List of Figures

Figure 2.1 The main challenges of Li metal anodes. **a)** Before cycling, the SEI forms spontaneously on the Li metal electrode. The thickness of the SEI depends on the soaking time in the electrolyte.¹⁸ **b)** The nonuniform plating of Li results in microstructural growth that can eventually lead to **c)** fractal dendritic growth and short-circuiting of the cell. **d)** The spontaneous SEI formation that occurs both chemically and electrochemically during cycling. **e)** The dissolution of Li during stripping can result in the detachment of the microstructures from the electrode, which leads to the formation of inactive or ‘dead Li’. **f)** After continuous plating and stripping there is an increased impedance of the cell, a combined effect of the thick dead Li layer and depletion of the electrolyte due to continuous SEI formation.^{2,19}38

Figure 2.2 Li metal cell configurations: ‘Symmetrical Li-Li cells’ contain two Li metal electrodes (with an SEI layer) separated by a separator soaked in an electrolyte. In ‘Li-Cu cells’, the Li deposition is studied on a Cu current collector. ‘Anode-free’ cells contain no Li metal, but a lithium-containing cathode and a Cu current collector. The electrolyte-interphase on the cathode-side is commonly referred to as the cathode electrolyte interphase (CEI). ‘Li metal cells’ contain a cathode and a Li metal electrode.40

Figure 2.3 Schematic of the electrochemical and chemical SEI formation on Li metal. The electrochemical SEI formation occurs concurrently with Li deposition whereas the chemical SEI formation occurs with no net current passed in the circuit and involves Li oxidation coupled to SEI reduction reaction.43

Figure 2.4 The Nernst diffusion-layer thickness, δ , obtained by extrapolating the linear portion of the concentration gradient to the bulk concentration value. The figure is reproduced from reference [⁸⁹]51

Figure 2.5 Schematic of the **a)** applied current j_p in a galvanostatic pulse plating experiment, with the pulse length T_{ON} and rest period T_{OFF} and **b)** the corresponding Faradaic current j_F used for the metal deposition in orange. **c)** For significant effects of the capacitive charging,

the current profile starts to resemble constant current conditions. The figure is reproduced from reference ¹⁰⁷53

Figure 2.6 The voltage profile and the corresponding applied current in symmetric Li-Li *in situ* cells for a single current pulse at 1 mA/cm² and T_{ON} = 1s, 50 ms and 5 ms. Charging of the double-layer is observed for both 50 ms and 5 ms pulse. For all pulse lengths the overpotential reaches a maximum indicating that charging of the double-layer capacitance is completed during the current pulse. The potential drop at the end of the pulse is due to the way the data was acquired, data points were only acquired for when ±10 mV differences were detected in the overpotential.....54

Figure 2.7 **a)** The equivalent circuit and the simulated Nyquist plot of the Randles circuit, with R_{bulk} = 10 Ω, R_{CT} = 100 Ω and C_{dl} = 10 μF. **b)** The simulated Nyquist plot for the corresponding equivalent circuit, with R₁ = 10 Ω, R₂ = 80 Ω, C₂ = 10 μF, R₃ = 50 Ω and C₃ = 0.5 μF. **c)** The simulated Nyquist plot for the corresponding equivalent circuit with a constant phase element, which shows a depressed semicircle with R₁ = 10 Ω, R₂ = 100 Ω and Q₂ = 10 μF with n = 0.8. The spectra were simulated using the open-source R-package, ‘impedanceR’.¹¹⁴ **d)** Experimental Nyquist spectrum of a symmetrical Li-Li cell with 1M LiPF₆ in EC:DMC.56

Figure 3.1 A schematic showing the effect of the 90° rf-pulse in the rotating frame using the vector model representation.¹¹⁹ **a)** The bulk magnetization **M**, aligned along the z-axis parallel to the external field. **b)** On applying a **B**₁-field along the x-axis, the magnetization **M** rotates about x. **c)** Free precession of the magnetization vector within the xy-plane. The figure is reproduced from reference ¹²⁰60

Figure 3.2 The spin bands of the conduction electrons plotted against energy. **a)** When there is no applied magnetic field, the population of electrons is equal in the up and down spin bands. **b)** In an applied magnetic field, the population of electrons will adjust to make the energies equal at the Fermi level, E_F. This results in a net magnetization, M. The schematic is reproduced from reference [⁸⁷].....63

Figure 3.3 A typical ⁷Li NMR spectrum of a symmetrical Li-Li *in situ* cell, showing the diamagnetic electrolyte/SEI peak around 0 ppm and the Li metal peak at around 245 ppm. .64

Figure 3.4 Experimental NMR spectra showing the bulk magnetic susceptibility effects on the ⁷Li metal shift. Due to the bulk magnetic susceptibility of Li metal, an orientation dependence is seen when placing a Li metal foil in the magnetic field, with a shift at 272 ppm (blue) when

the electrode is placed parallel to the B_0 magnetic field, and a shift at 243 ppm (orange) when placed perpendicular to B_0 .	67
Figure 3.5 A typical <i>in situ</i> ^7Li NMR spectra of a symmetrical Li-Li cell showing the pristine Li metal peak at around 245 ppm (in orange) and the Li metal peak after plating (in blue) with the additional peak at around 260 ppm corresponding to Li microstructures.	67
Figure 3.6 Simulated NMR spectrum of electrodeposits on Li metal from the susceptibility calculations of a pristine Li metal (in blue) and Li electrodeposits (in orange), the sum of the two shown in black. a) The simulated NMR spectrum with 20% coverage of Li microstructures (each microstructure is represented in a single voxel as illustrated in the inset) and b) of Li dendrites with 2.5% coverage (each dendrite is represented in $1 \times 1 \times 8$ voxels as illustrated in the inset), which reproduces the results found in reference [75] with the shift of mossy microstructures at around 260 ppm and around 270 ppm for dendrites.	68
Figure 3.7 The experimental ^7Li nutation curve of the electrolyte and Li metal in an NMR <i>in situ</i> cell containing 75 μL 1 M LiPF_6 in EC:DMC, glass fibre separator and two pieces of Li metal foil.	70
Figure 3.8 Photos of the <i>in situ</i> PEEK capsule cell used throughout this work. Cu current collector (or Al current collector) is threaded into the cell and sealed with o-rings. Inside the cell, an electrode-separator/electrolyte-electrode stack is made in between the current collectors and the system kept intact by the cylindrical capsule. See further details on cell assembly in the following reference. ¹²³	74
Figure 4.1 a) <i>In situ</i> NMR spectra obtained under a constant current of 0.5 mA/cm^2 in LP30 and LP30 + FEC. b) The total integrated intensity detected by NMR converted into mass change (mg) for a constant current of 0.5 mA/cm^2 in LP30 (green) and LP30 + FEC (orange). c) SEM images of the microstructures formed during 0.5 mA/cm^2 constant current in LP30 (left) and LP30 + FEC (right).	81
Figure 4.2 The integrated intensity detected by NMR converted into mass change (mg) for the a) the total intensity b) the metal intensity and c) the microstructural. The dashed line indicates m_{chem} , the mass deposited calculated based on the electrochemistry. d) An example of how the spectra for the LP30 electrolyte were deconvoluted into two overlapping metal peaks and one microstructural peak.	83
Figure 4.3 The ^7Li shift of the fitted peaks in the two electrolyte systems LP30 (left) and LP30 + FEC (right) during constant plating at 0.5 mA/cm^2 .	84

Figure 4.4 The quantified intensities of the fitted ${}^7\text{Li}$ metal peaks for the constant current experiments of a-c) 1 mA/cm ² and d-f) 2 mA/cm ² in the two electrolytes LP30 (green) and LP30 + FEC (orange). The dashed line indicates m_{echem} , the calculated mass deposited according to the current passed by the electrochemistry.	85
Figure 4.5 SEM images of the microstructures formed during 2 mA/cm ² constant plating in a) LP30 and b) LP30 + FEC.....	86
Figure 4.6 Galvanostatic cycling of symmetric Li-Li coin cells during a) the first 10 cycles at 0.5 mA/cm ² for both stripping and plating. In the first cycle, shown in the enlargement in b) 0.5 mA/cm ² was used for plating and 1.0 mA/cm ² for stripping. First cycle using c) 1.0 and d) 2.0 mA/cm ² plating and 1.0 mA/cm ² for stripping in LP30 (green) and LP30 + FEC (orange).	87
Figure 4.7 Representative pulsed current plot for symmetric Li <i>in situ</i> cell at 1 mA/cm ² with $T_{\text{ON}}, T_{\text{OFF}} = 1$ s in the LP30 + FEC electrolyte.	88
Figure 4.8 Pulse plating in LP30 a) The deconvoluted intensities of the <i>in situ</i> spectra for LP30 during constant plating (CP) at 0.5 mA/cm ² (green, also shown in Figure 4.2) and pulse plating (PP) at 1 mA/cm ² with $T_{\text{ON}}, T_{\text{OFF}} = 1$ s (purple) and $T_{\text{ON}}, T_{\text{OFF}} = 5$ ms (yellow). The dashed line indicates m_{echem} . SEM images of the Li metal morphology using 1 mA/cm ² and $T_{\text{ON}}, T_{\text{OFF}}$ b) 1s c) 5 ms.....	89
Figure 4.9 The deconvoluted intensities of the <i>in situ</i> NMR spectra during constant plating and pulse plating (PP) in the LP30 electrolyte with current density 1 mA/cm ² and various pulse lengths of $T_{\text{ON}}:T_{\text{OFF}}$	90
Figure 4.10 SEM images of the microstructures formed during a) constant plating with 0.5 mA/cm ² and pulse plating at 1 mA/cm ² and b) $T_{\text{ON}}, T_{\text{OFF}} = 1$ s c) $T_{\text{ON}}, T_{\text{OFF}} = 500$ ms d) $T_{\text{ON}}, T_{\text{OFF}} = 50$ ms and e) $T_{\text{ON}}, T_{\text{OFF}} = 5$ ms.	91
Figure 4.11 Pulse plating in LP30 a) The deconvoluted intensities of the <i>in situ</i> spectra during pulse plating with $T_{\text{ON}}:T_{\text{OFF}} = 5$ ms:15 ms using current density 1 mA/cm ² (pink) and 2 mA/cm ² (blue). SEM images of the Li metal morphology using $T_{\text{ON}}:T_{\text{OFF}} = 5$ ms:15 ms and b) 1 mA/cm ² c) 2 mA/cm ²	92
Figure 4.12 <i>Ex situ</i> ${}^7\text{Li}$ NMR spectra of pitting on the stripping electrode showing a) the <i>in situ</i> cell before and b) after cycling. c) The <i>ex situ</i> NMR of the disassembled cell on the plated electrode (working electrode, WE), d) and of the stripping electrode (counter electrode, CE)	

with the corresponding SEM images showing the pits. **e)** And the sum of spectra c and d, of the WE and CE. The metal peak of the stripping electrode after cycling, shown in green, has shifted to higher frequency (247.5 ppm compared to 245 ppm before cycling) and indicates roughening of the electrode surface.¹⁶⁴ Shown for LP30, 2 mA/cm² and T_{ON} = 5 ms, T_{OFF} = 15 ms.93

Figure 4.13 Pulse plating in LP30 + FEC **a)** The deconvoluted intensities of the *in situ* NMR in LP30 + FEC during constant plating (CP) at 0.5 mA/cm² (orange, also plotted in Figure 4.2) and pulse plating (PP) at 1 mA/cm² with T_{ON}, T_{OFF} = 1 s (purple) and T_{ON}, T_{OFF} = 5 ms (yellow). SEM images of the Li metal morphology using 1 mA/cm² and T_{ON}, T_{OFF} **b)** 1s and **c)** 5 ms. **d)** The deconvoluted intensities of the *in situ* NMR with T_{ON}:T_{OFF} = 5 ms:15 ms using current density 1 mA/cm² (pink) and 2 mA/cm² (blue) and the SEM images for **e)** 1 mA/cm² **f)** 2 mA/cm².95

Figure 4.14 The SEM images and the corresponding voltage profile for **a)** constant plating at 5 mA/cm², **b)** constant plating at 10 mA/cm² and **c)** pulse plating using 10 mA/cm² with T_{ON}:T_{OFF} = 5 ms:15 ms in LP30. **d)** Constant plating at 10 mA/cm² and **e)** pulse plating using 10 mA/cm² with T_{ON}:T_{OFF} = 5 ms:15 ms in LP30 + FEC.96

Figure 5.1 A schematic representing the 5mm J-Young NMR tube, the yellow cap seals the NMR tube making it airtight. The dominant processes occurring at the metal-electrolyte interface are shown, which will influence the exchange rate.103

Figure 5.2 A schematic of the numerical model showing **a)** the geometry of the Li metal electrode. **b)** Model I, which describes the isotope exchange with one fitting parameter, the exchange flux J_{ex} [mol m⁻² s⁻¹] describing the rate of exchange and **c)** Model II, which describes both isotope exchange and SEI formation, with the time-dependent exchange flux $J_{ex}(t)$ [mol m⁻² s⁻¹], which depends on the SEI permeability constant β_{ex}108

Figure 5.3 ⁷Li NMR spectra of the electrolyte (around 0 ppm) and metal (around 275 ppm) during the ~75-hour time period that that the ⁶Li-enriched strip of metal was soaked in natural abundance LP30 + FEC electrolyte.112

Figure 5.4 The intensity changes of the ⁷Li NMR spectra recorded over 75 hours for **a)** the lithium metal signal and **b)** the diamagnetic lithium signal in the two electrolytes LP30 (green and purple) and LP30 + FEC (orange and light-green). The curve in pink shows the “control experiment” using a natural abundance Li metal strip where the effect of isotope exchange is removed.113

Figure 5.5 The intensity changes of the ^7Li NMR spectra (points) and the model fit results for Model I (dashed lines) and Model II (black lines) for a) the lithium metal and b) the lithium ions in the electrolyte, in the two electrolytes LP30 (green) and LP30 + FEC (orange).....	114
Figure 5.6 Sensitivity analysis using fixed values of $J_{ex,0}$ obtained from Model I.	116
Figure 5.7 a) The exchange current density j_{ex} ($\mu\text{A cm}^{-2}$) and b) the SEI formation current density j_{SEI} ($\mu\text{A cm}^{-2}$) in LP30 (green), LP30 + FEC (orange) and 4M LiFSI in DME (purple). The plot for the SEI formation current density is shown by zooming in on a subset of the data, to aid for comparison. The whole range is shown to the left.	117
Figure 5.8 The Nyquist plot for symmetric Li-Li coin cells at OCV in a) LP30 electrolyte, b) LP30 + FEC and c) 4M-LiFSI.	119
Figure 5.9 The fit to the EIS data in LP30, at time = 12 hours and the equivalent circuit used to fit the spectra, where R_1 and Q_1 (C_1 , capacitance and a_1 , parameter which describes how close it is to an ideal capacitor) are the resistance and the constant phase element (CPE) for the SEI compact layer respectively, R_2 and Q_2 (C_2 and a_2) for the porous part of the SEI layer respectively, R_3 and Q_3 (C_3 and a_3) for the charge transfer between SEI film and electrolyte, and R_4 is the bulk electrolyte resistance. Fitting of impedance spectra to the equivalent circuit was carried out in MATLAB using a code written by Sundeep Vema.	120
Figure 5.10 The resistance of the SEI on Li metal, $R_{SEI} = (R_1 + R_2 + R_3)/2$, determined from the fitting of the impedance spectra in LP30 (green), LP30 + FEC (orange) and 4M-LiFSI (purple).	121
Figure 5.11 The intensity changes of the ^7Li NMR spectra (points) for a) the Li metal and b) the diamagnetic Li^+ in the LP30 electrolyte and at three temperatures; 298 K (green, also displayed and analysed in section 5.4.1), 313 K (yellow) and 323 K (blue). In red is the measurement at 313 K, which has been soaked initially at 298 K for 25 hrs. The electrolyte was replaced at 25 hours with a fresh LP30 electrolyte and the temperature raised to 313 K. The corresponding fit to the curves, using Model II explained in 5.3, is shown in black.	122
Figure 5.12 a) The exchange current density and b) the SEI formation current density calculated from the fit in LP30 electrolyte at 298 K (green), 313 K (yellow) and 323 K (blue). In red is the measurement at 313 K, that has prior been soaked at 298 K for 25 hrs.	124
Figure 5.13 The temperature dependence of the exchange rate constant extracted from the simulation over the initial two hours of measurements. The rate constant is seen to decrease in	

magnitude, most noticeable at 323 K. The activation energy is calculated from the slope of the Arrhenius plot, only taking into account the first hour of measurements.....125

Figure 6.1. Schematic of the ^7Li *in situ* NMR technique used to study dead Li formation and the resulting ^7Li NMR spectra. **a)** The Cu-LiFePO₄ (LFP) cell before cycling and the corresponding ^7Li NMR spectrum showing the resonance of the diamagnetic Li (the SEI and Li⁺ ions) and the absence of the lithium metal peak. **b)** Charging the cell results in lithium metal electrodeposition, as shown in the ^7Li NMR spectrum of the Li metal region. **c)** At the end of discharge the Li metal signal can still be observed, which is attributed to dead Li. **d)** Further cycling of the Cu-LFP cell results in an accumulation of dead Li over the next cycles (cycle 2-5), the intensity of the Li metal signal increasing at the end of stripping in each cycle.138

Figure 6.2 Experimental nutation curves of **a)** the Li deposits on Cu (1 mAh/cm²) nutate sinusoidally as expected for samples that do not experience skin depth issues. **b)** The pristine Li metal foil nutates according to equation (3.13) due to skin depth effects.140

Figure 6.3. *In situ* ^7Li NMR measurement of a Cu-LFP cell cycled in LP30 electrolyte with 0.5 mA/cm² current density and 1 mAh/cm² capacity for each plating step. **a)** The ^7Li NMR spectra acquired during the plating and stripping of Li metal. The resonance of Li metal appears at around 270 ppm. **b)** The corresponding integrated intensity of the Li metal peak normalised to the intensity at the end of plating in the first charge and **c)** voltage profile for the galvanostatic cycling.141

Figure 6.4 The average value of the a) normalised total Li_{NMR} intensity at the end of plating, b) normalised dead Li_{NMR} intensity at the end of stripping and c) electrochemically obtained CE for the first five cycles in the three electrolytes, LP30 (green), LP30 + FEC (orange) and DOL/DME (purple). The error bars represent the standard deviation of the average values obtained in three different experiments. d) The dead Li_{NMR} measured in the first cycle plotted against the CE. e) The difference in dead Li_{NMR} between subsequent cycles plotted against the capacity loss (mAh/cm²) calculated from the CE. f) The SEI capacity (mAh/cm²) calculated in each cycle against the corresponding capacity loss (mAh/cm²).143

Figure 6.5 The average SEI formation capacity (top) and dead Li (bottom) per cycle, in LP30, LP30 + FEC and DOL/DME. The dashed lines show the values used to calculate the mean and the standard deviation, for the three different sets of *in situ* NMR experiments.146

Figure 6.6 The Li metal intensity for the ^7Li *in situ* NMR measurements when cycling Cu-LFP cells in LP30 with polymer-coated Cu. **a)** The normalised total Li_{NMR} intensity at the end of

plating, **b)** the normalised dead Li_{NMR} intensity at the end of stripping and **c)** the CE for PEO- (blue), PMMA- (yellow) and PVDF-coated (red) Cu electrodes. The measurements for bare Cu (in green) are shown here to aid comparison.147

Figure 6.7 Capacity losses in the first cycle, the SEI capacity C_{SEI} (circles) and the dead Li capacity $C_{\text{dead Li}}$ (triangles) plotted against the corresponding capacity loss, CL . **a)** In the three electrolytes, LP30, LP30 + FEC and DOL/DME on bare Cu current collector. The different data points corresponds to different sets of *in situ* experiments. **b)** In LP30 on bare Cu (green) and on polymer-coated Cu (PEO, PMMA and PVDF). More significant SEI formation is observed for the polymer-coated Cu cell.148

Figure 6.8 BMS effects on the pristine Li metal resonance: ^7Li NMR spectra of pristine Li metal oriented perpendicular to the magnetic field in three different configurations; Li-Cu cell, Li-LFP cell and Li-Li cell. The ^7Li shift of Li metal when assembled against the paramagnetic LFP cathode shifts from 245 ppm to 260 ppm due to BMS effects. The main plane of the rectangular electrode is facing perpendicular with respect to the applied magnetic field B_0 , that is at 90°149

Figure 6.9 BMS effects for the Li metal peak in the LP30 electrolyte. **a)** Stack plot of the Li metal spectra during charge (plating) in the first cycle (where the same metal spectra are shown vs. time in Figure 6.3a). **b)** The Li metal spectra during charge (plating) in the fourth cycle. **c)** The frequency of the Li metal shift, measured at the maximum intensity of the Li metal resonance, during cycling. **d)** The deconvoluted intensities of the Li metal spectra during cycling. **e)** An example of the fitted spectra at the end of charge in first and fourth cycle. ..151

Figure 6.10 BMS effects for the Li metal peak in the LP30 + FEC electrolyte. **a)** Stack plot of the Li metal spectra during charge (plating) in the first cycle. **b)** The Li metal spectra during charge (plating) in the fourth cycle. **c)** The frequency of the Li metal shift, measured at the maximum intensity of the Li metal resonance, during cycling. **d)** The deconvoluted intensities of the Li metal spectra during cycling. **e)** An example of the fitted spectra at the end of charge in first and fifth cycle.153

Figure 6.11 BMS effects for the Li metal peak in the DOL/DME electrolyte. **a)** Stack plot of the Li metal spectra during charge (plating) in the first cycle. **b)** The Li metal spectra during charge (plating) in the fourth cycle. **c)** The frequency of the Li metal shift, measured at the maximum intensity of the Li metal resonance, during cycling. **d)** The deconvoluted intensities

of the Li metal spectra during cycling. **e)** An example of the fitted spectra at the end of charge in first and fourth cycle.154

Figure 6.12 Simulated NMR spectrum of electrodeposits on Li metal from the susceptibility calculations of a pristine Li metal (in blue) and Li electrodeposits (in orange), the sum of the two shown in black. **a)** The simulated NMR spectrum with 20% coverage of Li microstructures and **b)** of Li dendrites with 2.5% coverage, reproducing the results found in reference [75] with the shift of mossy microstructures at around 260 ppm and around 270 ppm for dendrites. **c)** The simulated NMR spectrum with a microstructure coverage of 50%. The shift is at 256 ppm for the microstructure peak (in orange).155

Figure 6.13 The Li metal shift as a function of surface coverage of Li microstructures. **a)** The simulated NMR spectra of the microstructure deposits on Cu, varying the surface coverage from 2.5-95%. **b)** The ⁷Li metal shift at the peak maxima of the Li microstructure peak on a Cu (red) or Li metal (blue) electrode. The calculated shift at 2.5% surface coverage is 260 ppm on Cu and 263 ppm on Li.156

Figure 6.14 The normalised intensity of the deconvoluted peaks at **a)** the end of charge (plating, after depositing 1 mAh/cm² of Li metal) and **b)** at the end of discharge (stripping) in the three electrolytes. Peak 1, at the lowest ⁷Li metal shift, increases in intensity between cycles for all electrolytes during plating and is most apparent in the DOL/DME electrolyte. The dead Li peak measured in DOL/DME and LP30 is fully captured by Peak 3, at the highest ⁷Li metal shift.157

Figure 6.15 The normalised intensity of the deconvoluted peaks of Li metal spectra during cycling on **a)** PVDF-coated, **b)** PEO-coated and **c)** PMMA-coated Cu current collector.158

Figure 6.16. *In situ* NMR experiments of Li metal dissolution during the OCV period. **a)** A schematic representation of the processes that lead to Li metal corrosion: the chemical formation of the SEI on Li results in the spontaneous reduction of the electrolyte and oxidation of the Li metal. Galvanic corrosion results in the dissolution of Li metal (Li oxidation) and a cathodic reaction on the Cu electrode. **b)** Integrated intensity of the Li metal signal during the NMR experiment. The intensity increases during deposition (corresponding to 1 mAh/cm²) of charge and decreases constantly during the rest period at OCV for the three electrolytes, LP30, LP30 + FEC and DOL/DME. Plating and resting experiments for **c)** different polymer coatings: PEO-, PMMA- and PVDF-coated Cu current collector and **d)** different Cu treatments in LP30 electrolyte: Cu treated with HCl acid (green), Cu treated with glacial acetic acid (AcH, black).

The grey curve shows the effect of a slow SEI formation step before deposition on HCl-treated Cu at 0.02 mA/cm² followed by a 12 hours voltage hold at 3.2 V before deposition at 0.5 mA/cm² (grey). The green curve in b, c and d) is for the same experiment, performed on bare Cu treated in HCl-acid and in LP30 electrolyte. Each experiment was performed twice, and the rate of dissolution was found to be highly reproducible.....159

Figure 6.17. The linear fit to the corrosion curve of Li metal on bare Cu in LP30. The dashed lines show the linear fit obtained when accounting for only the first two hours compared to for the entire measurement. The corrosion current, i_{corr} for the first two hours is 49 $\mu\text{A cm}^{-2}$. Averaging over the whole measurement results in 28 $\mu\text{A cm}^{-2}$161

Figure 6.18 A bar chart showing the slope of the dissolution curve from a linear fit to the different sets of *in situ* NMR measurements in different electrolytes and with different polymer coatings.162

Figure 6.19 The long-term corrosion behaviour was probed by *ex situ* NMR measurements. In black is the corrosion of Li metal at the top of charge for the 6th deposition, normalised to the first cycle intensity, for the cell shown in Figure 6.3b. The dashed line represents the linear fit through the data points to guide the eye.163

Figure 6.20 *In situ* NMR measurements of the corrosion followed by stripping The normalised integrated intensity of the Li metal intensity during the first 2 hours of deposition using 0.5 mA/cm² (corresponding to 1 mAh/cm²) and the corresponding decrease during the OCV period of roughly 18 hours followed by stripping at 0.5 mA/cm² in DOL/DME (purple) and LP30 with the initial SEI formation on Cu using 0.02 mA/cm² (compared to 0.5 mA/cm² used in all experiments where it is not stated specifically, grey). The formation period on Cu using 0.02 mA/cm² before plating is not shown as there is no Li metal signal to integrate. Thus, time = 0 equals to the time at the start of Li plating.....164

Figure 6.21 The ⁷Li NMR spectra of the diamagnetic peak in Cu-LFP *in situ* cells before any current has been passed. **a)** A Cu-LFP cell that was rotated in the NMR rf-coil so that the electrodes were oriented at approximately 0°(parallel), 22°, 45°and 90° (perpendicular, same as all the *in situ* experiments unless otherwise stated) with respect to the magnetic field. **b)** Three different Cu-LFP cells (oriented perpendicular with respect to the magnetic field) using LP30 electrolyte, demonstrating how sensitive it is to cell assembly.....165

Figure 6.22 The ⁷Li NMR spectra of the diamagnetic region in a Cu-LFP cell during plating and stripping at 0.5 mA/cm² current density and with 1 mAh/cm² capacity. **a)** A heatmap of

the NMR spectra, showing how Peak A stays constant during cycling whereas Peak B cycles with the electrochemistry. **b)** The shift (ppm) and ‘shift change’ (Δ ppm) for Peak B. The shift is going towards lower shifts in each cycle due to capacity losses in the cell pushing the LFP to a higher state of charge in each cycle (and the plating capacity kept constant at 1 mAh/cm²).
.....166

Figure 6.23 **a)** The ⁷Li NMR diamagnetic region for a Cu-LFP cell, which was fully charged (delithiated) at 0.5 mA/cm² current density, reaching 2.3 mAh/cm² capacity. **b)** The ⁷Li shift (ppm) and shift change (Δ ppm) for Peak B.167

List of Tables

Table 5.1. List of all the model input parameters and methods used to measure or estimate their values.	109
Table 5.2 List of the fitted model parameters (J_{ex} , β_{ex} , $\alpha_{SEI,0}$ and β_{SEI}) obtained from the numerical simulation and the derived parameters for the isotopic exchange in the electrolytes, LP30 and LP30 + FEC from Model II. The upper and lower values for the 95% confidence bounds are given in brackets. The ratio between the values for (LP30 + FEC)/(LP30) is displayed.	115
Table 5.3 The rate constants calculated from the simulation of the isotopic exchange in the electrolytes, LP30, LP30 + FEC and 4M LiFSI in DME (4M-LiFSI).....	118
Table 5.4 The model parameters (J_{ex} , β_{ex} , $\alpha_{SEI,0}$ and β_{SEI}) obtained from the fits of the isotope exchange curves in LP30 electrolyte and at three different temperatures, shown in Figure 5.11. The 95% confidence intervals are given. The initial rate of the SEI formation is calculated as: $\alpha_{SEI,0} \times J_{ex}$	123
Table 6.1 The average CE, SEI formation capacity and dead Li capacity in the first cycle calculated using the dead Li_{NMR} intensity determined by <i>in situ</i> NMR and the CE determined from electrochemistry. The standard deviation is that derived from the three separate <i>in situ</i> NMR experiments.	145
Table 6.2. The mean of the slope (for two sets of experiments) obtained from a linear fit to the decreasing intensity of the ^7Li NMR metal signal during the OCV period (Figure 6.16). For experiments using the polymer-coated Cu, LP30 electrolyte was used in all cases.	162

List of Abbreviations

AFM – Atomic force microscopy

BMS – Bulk Magnetic Susceptibility

CE – Coulombic efficiency

CEI – Cathode electrolyte interphase

CV - Cyclic Voltammetry

CPE – Constant phase element

cryo-EM – Cryogenic electron microscopy

DNP – Dynamic nuclear polarization

DOL/DME – 1M LiTFSI in 1,3-dioxolane and 1,2-dimethoxyethane

EC – Ethylene carbonate

EIS – Electrochemical Impedance Spectroscopy

DMC – Dimethyl carbonate

FEC – Fluoroethylene carbonate

FFT – Fast Fourier transform

FSI – Bis(fluorosulfonyl)imide anion

FTIR – Fourier transform infrared spectroscopy

FWHM – Full Width at Half Maximum

LCO – LiCoO_2

LIBs – Lithium ion batteries

LMBs – Lithium metal batteries

LP30 – 1M LiPF_6 in ethylene carbonate/dimethyl carbonate solvent

MAS – Magic angle spinning

MD – Molecular dynamics

NMR – Nuclear magnetic resonance

OCV – Open circuit voltage

PEO – Poly(ethylene oxide)

PFG-NMR – Pulsed field gradient NMR

PMMA – Poly(methyl methacrylate)

PVDF – Poly(vinylidene fluoride)

RC – Resistance-capacitance

rf – radio frequency

SEI – Solid Electrolyte Interphase

SEM – Scanning Electron Microscopy

TEM – Transmission Electron Microscopy

TFSI – Bis-(trifluoromethanesulphonyl)imide anion

TIP – Temperature Independent Paramagnetism

TOF-SIMS – Time-of-flight secondary-ion mass spectrometry

VT – Variable temperature

XPS – X-ray Photoelectron Spectroscopy

B_0 – External magnetic field

B_1 – Applied rf-field

ω_0 – Larmor frequency

T_1 – Longitudinal (spin lattice) relaxation time constant

Chapter 1 Introduction

Electrochemical energy storage devices are a key technology for the integration of intermittent renewable energy technologies into the electric grid. Batteries convert electrical energy into chemical energy through charge transfer reactions. The Gibbs free energy of the redox reactions that occur on the anode and the cathode is:

$$\Delta G^\circ = \Delta G^\circ_{cathode} - \Delta G^\circ_{anode} = -nFV^\circ \quad (1.1)$$

where n is the number of electrons transferred and F is the Faraday's constant (C/mol) and V° is the open circuit voltage of the cell (in V).¹ The standard Gibbs energy ΔG° is the energy that would be released if the anode and the cathode were to react under standard conditions. The specific energy of a battery cell, E_{cell} (in Wh/kg) can be calculated as:

$$E_{cell} = \frac{V_{cell} \times C_{cell}}{W_{cell}} \quad (1.2)$$

where V_{cell} is often defined as the mid-point voltage during the discharge process, C_{cell} is the cell capacity (in Ah) and W_{cell} is the total cell weight (in kg).² Lithium is light-weight and has low standard reduction potential ($V^\circ = -3.04$ V of Li^+/Li vs. the standard hydrogen electrode, SHE), making it highly suitable for high energy density batteries.

The development of the rechargeable Li-ion battery (LIB) has enabled the portable electronic revolution. LIBs are transforming the transportation sector; through the electrification of bikes, buses and cars and are also a potential energy storage technology for the large-scale grid-storage needed in the nearby future for intermittent, renewable energy sources such as solar and wind.³

There is a constant push toward further improvements and the shift towards electrified future demands high-performance batteries with increased energy density and power performance, long lifetime, as well as being safe, cheap and environmentally friendly.⁴ The typical LIB comprises of a lithium-containing cathode and a graphite anode that acts as a host (intercalates Li^+). One pathway to increase the energy density is to replace the graphite anode with Li metal.

However, safety issues associated with dendrite growth of electrodeposited Li as well as the low capacity retention and short cycle life have hindered the commercialisation of the lithium metal battery (LMB). Nevertheless, LMBs are generally considered a promising future battery technology due to the predicted high energy density.⁵

There is currently an intense research effort underway to study microstructural and dendritic growth, and the capacity losses in LMBs. The formation of a stable solid electrolyte interphase (SEI) on the Li metal anode is generally regarded as the most effective strategy to suppress Li dendrite growth and ensure stable cycling. To optimise the SEI on Li metal and pave the way for practical LMBs, it is necessary to understand what properties of the SEI lead to more level Li deposition and high Coulombic efficiencies.

It is challenging to study the dynamic SEI layer and most techniques involve the disassembly of batteries for *ex situ* characterisation of its morphology, chemical composition and formation mechanism. NMR spectroscopy can be used to study LMBs *in situ* as it is both a non-invasive and a quantitative technique. The aim of this thesis is to develop and apply *in situ* NMR methods to study Li metal and to gain a better understanding of how the SEI affects the cyclability of LMBs.

1.1 Thesis Overview

Chapter 2 presents an overview of the recent literature in the field of lithium metal batteries and the essential theory on electrochemistry and electrode kinetics.

Chapter 3 presents the essential theory used in this work regarding NMR spectroscopy, which is the main technique of this thesis.

In Chapter 4, *in situ* NMR is used to study electrodeposition of Li metal with and without an electrolyte additive and the amount of Li microstructures is quantified under different electrodeposition conditions.

In Chapter 5, the methodology to study the SEI formation and the exchange between Li metal and the electrolyte at electrochemical equilibrium is developed using isotope labelling and NMR and the results related to the standard model of electrochemical kinetics.

Chapter 6 demonstrates a new *in situ* NMR metrology to study full-cell lithium metal batteries, and the different processes that leads to capacity losses are quantified.

Chapter 7 presents the main conclusions of this work and possible future research directions are suggested.

Chapter 2 Energy Storage and Electrochemistry

2.1 Li-ion Batteries and Beyond

Here a brief introduction is given to the development of the rechargeable Li-ion battery; many more extensive reviews are available on the subject.^{3,6,7} We will then look beyond the Li-ion battery and review recent research efforts in the development of the lithium metal battery.

The 2019 Nobel Prize in chemistry was awarded to Stanley Whittingham, John Goodenough, and Akira Yoshino for their contributions to the development of the lithium-ion battery. During the oil-crisis in the 1970s, Whittingham worked at Exxon Corporation and demonstrated the first rechargeable Li battery using layered TiS_2 as the cathode against a Li metal anode.⁸ Inspired by this work, Goodenough's research group began to explore intercalation materials with higher cell voltage, which led to the discovery of metal oxide cathodes. The layered LiCoO_2 (lithium cobalt oxide, LCO) became the cathode of choice, with operating voltage of ~ 4 V, good structural stability and high electrical and lithium-ion conductivity.⁹ However, the commercialisation was hindered due to the Li metal anode and the safety problems associated with Li dendrite growth upon cycling. The Li-ion battery was first commercialized in the early 1990's by Sony, when Yoshino and his team paired the LCO cathode with a lithium-free carbon anode.¹⁰ This battery is very close to the modern LIBs used today for most electronic consumer products, with LCO cathode paired against a graphite anode.⁷ However, major limitations are in the high cost, low abundance and toxicity of cobalt. Thus, there is a drive towards chemistries that both minimise cobalt and operate at high voltages. Cathode materials that include nickel, manganese and cobalt (termed NMC cathodes) are cheaper and have higher capacity than LCO, the NMC has thus become the dominant cathode-chemistry used in electric vehicles.¹¹

Currently, Li-ion battery technologies are reaching their limit in theoretical energy density and there is a critical need to find high-energy alternatives.^{5,12} The graphite has much lower theoretical gravimetric capacity (372 mAh/g) compared to Li metal (3860 mAh/g).¹³ The graphite anode, however, exhibits high reversibility and efficiency with the theoretical capacity roughly obtained in practice as well as improved safety to compared to Li metal.¹³

Nevertheless, there is a revived interest in Li metal anodes, which has been termed the “Holy Grail” of battery anode materials.¹⁴ Replacing the graphite electrode with lithium metal in a typical LIB can increase the specific energy by ~35% and the energy density by ~50%.¹² In addition, lithium-air and lithium-sulphur, considered promising high-energy battery technologies, use lithium metal as the anode.^{15,16} Long-term cyclability has not yet been obtained in LMBs and fundamental research is needed to understand the plating and stripping, and the electrode/electrolyte interface in detail.

2.2 Lithium Metal Batteries

Lithium is the lightest metal and has a low negative potential (-3.04 V vs. SHE), which enables large operating voltages when assembled with a lithium-containing cathode.¹⁴ Cycling of LMBs entails deposition of Li metal, $\text{Li}^+ + \text{e}^- \rightarrow \text{Li}^0$, during charge (plating) and the dissolution (stripping) of Li metal during discharge, $\text{Li}^0 \rightarrow \text{Li}^+ + \text{e}^-$. The greatest obstacles to the commercialisation of LMBs are (i) safety issues associated with dendrite growth of electrodeposited Li as well as (ii) poor capacity retention and short cycle life.¹⁷ The key issues in implementing Li metal anodes are summarised in Figure 2.1.

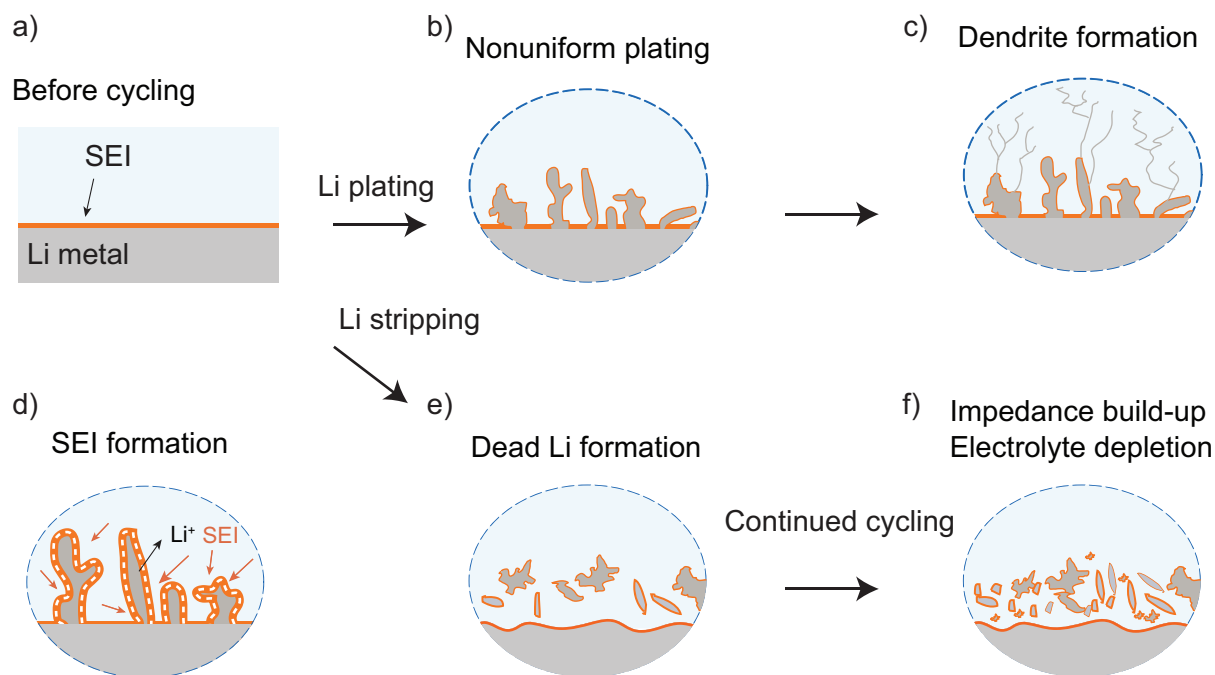


Figure 2.1 The main challenges of Li metal anodes. **a)** Before cycling, the SEI forms spontaneously on the Li metal electrode. The thickness of the SEI depends on the soaking time in the electrolyte.¹⁸ **b)** The nonuniform plating of Li results in microstructural growth that can eventually lead to **c)** fractal dendritic growth and short-circuiting of the cell. **d)** The spontaneous SEI formation that occurs both chemically and electrochemically during cycling. **e)** The dissolution of Li during stripping can result in the detachment of the microstructures from the electrode, which leads to the formation of inactive or ‘dead Li’. **f)** After continuous plating and stripping there is an increased impedance of the cell, a combined effect of the thick dead Li layer and depletion of the electrolyte due to continuous SEI formation.^{2,19}

Typically, microstructural growth of Li occurs during plating (Figure 2.1b) due to inhomogeneous current density on the electrode surface.²⁰ These Li microstructures can exhibit a range of different morphologies from needle and whisker-like to nodular and mossy structures. With continuous plating, this can develop into fractal dendritic growth (Figure 2.1c), which can short-circuit the battery cell and is a serious safety concern for LMBs.²¹ In general, the morphology of metal electrodeposits is influenced by the current distribution over the electrode surface, which is affected by factors such as the geometry of the cell, the nature of the electrode’s surface, the specific resistivity of the electrolyte solution, the activation overpotential and the concentration overpotential.²² Of these parameters, the surface of the Li metal electrode is particularly complex because of the SEI that forms instantaneously when Li metal is immersed in an electrolyte due to the low electrochemical potential of Li. The high reactivity of Li metal results in an irreversible decomposition of the electrolyte and

precipitation of the reduction products on the electrode surface, which forms the heterogeneous layer known as the SEI (Figure 2.1a). Furthermore, a ‘pristine’ Li metal foil is generally covered by a passivation layer, the “native SEI”, which is composed mostly of lithium oxides, hydroxides and carbonates and forms even under “inert atmospheres” (e.g. in a glovebox or a dry room), from trace amounts of oxygen, nitrogen, water and a variety of organic solvents.²³ This complicates studies of Li metal deposition, compared to electrodeposition of metals such as copper and silver, as it is difficult to have full control of the surface chemistry.

The morphology of Li metal deposits and the cycling performance is highly dependent on the choice of electrolyte system where improved cycling efficiencies are generally attributed to a uniform and stable SEI and will be described in more detail below.^{20,21,24–29} The SEI needs to be homogenous in chemical composition and morphology, electronically insulating but ionically conductive, mechanically stable and insoluble in the electrolyte.^{14,30} Full and homogeneous coverage of the SEI that effectively passivates Li metal is equally important to mitigate the continuous consumption of the electrolyte (Figure 2.1d) and promote homogeneous Li deposition.^{31,32} The irregular microstructural growth has been associated with local inhomogeneities on the Li metal surface and in the SEI that results in preferential deposition sites (so-called “hot spots”) with high local current density.^{20,24,33–35} These preferential deposition sites can originate from inhomogeneous transport properties in the SEI or cracks in the SEI where Li grows through the protrusions caused by internal stresses beneath the SEI.^{36–39} Thus, the main approach in the development of LMBs has been on mitigating dendrite formation through electrolyte and interfacial engineering, with the goal of manipulating the SEI.²¹

Fang et al. argued in a recent publication that dendrite formation is not the main concern for LMBs, but rather it is the low Coulombic efficiency (CE) that poses a greater problem, decreasing the battery cycle life.¹⁷ The low CE leads to a loss of active Li in the cell and can originate from two factors, the SEI formation as described above and with the formation of inactive Li metal, typically known as ‘dead Li’ in the literature (Figure 2.1e).^{40,41} Dead Li corresponds to Li that no longer has electronic contact with the current collector and forms due to inhomogeneous stripping of Li microstructures.^{19,41–43} This is attributed to faster Li metal dissolution at sites with relatively low impedance, e.g. on fresh Li deposits with relatively thin SEI or where the SEI has ruptured.^{37,44} The accumulation of dead Li at the electrode/electrolyte

interface after multiple plating and stripping (Figure 2.1f) results in a highly tortuous layer on the negative electrode, which leads to mass transport limitations during cycling and continuous consumption of the electrolyte forming the SEI.^{19,42}

2.2.1 Cell configurations

In order to make LMBs a viable technology, reversible Li plating and stripping must occur upon cycling the battery. However, the Coulombic efficiency (CE) of Li metal cycling in the commercial carbonate electrolytes is usually around 80-90%.^{29,45} Here, CE is defined as:

$$\text{CE} = \frac{\text{Stripping capacity}}{\text{Depositing capacity}} \quad (2.1)$$

Advanced electrolytes have achieved CEs of over 99%.⁴⁶⁻⁴⁸ A CE of 99.9% is required to achieve a cycle life of 200 and 99.98% is required to reach 1,000 cycles, while retaining 80% of the initial capacity.^{12,14} However, Xiao et al. argue that the CE is not an effective descriptor to estimate the lifespan of a LMB.⁴⁹ The cycling performance depends on the cell configuration, the amount of Li metal in the cell, the amount of electrolyte and cathode loading.^{2,49}

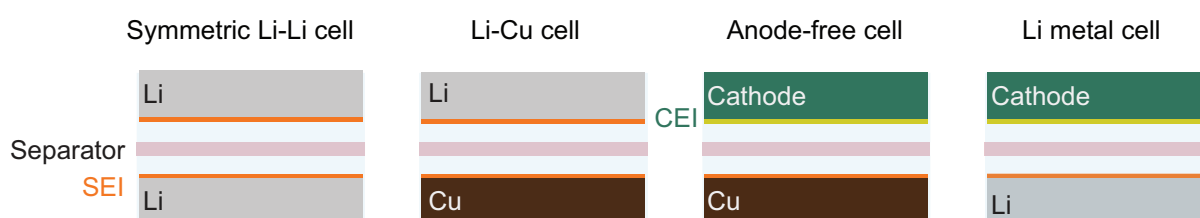


Figure 2.2 Li metal cell configurations: ‘Symmetrical Li-Li cells’ contain two Li metal electrodes (with an SEI layer) separated by a separator soaked in an electrolyte. In ‘Li-Cu cells’, the Li deposition is studied on a Cu current collector. ‘Anode-free’ cells contain no Li metal, but a lithium-containing cathode and a Cu current collector. The electrolyte-interphase on the cathode-side is commonly referred to as the cathode electrolyte interphase (CEI). ‘Li metal cells’ contain a cathode and a Li metal electrode.

Figure 2.2 shows the various cell configurations generally used when studying Li metal deposition. Most studies use symmetric Li-Li cells, which are useful to directly probe the behaviour on Li metal and to study the morphology of Li in different electrolytes. But the native SEI on Li metal is difficult to control and may change if Li metal is being stored for long time (even in an inert glovebox environment), complicating systematic studies.²⁰

Furthermore, the excess amount of Li metal can extend the cycle lifetime of the battery cell.² The low capacity retention of LMBs tends to be overlooked because an excess amount of Li metal is typically used in research-scale cells that leads to an artificially enhanced cycling efficiency.^{2,48,49} Limiting the amount of excess Li will better mimic practical LMB designs.^{2,12,48} In order to make use of the high specific capacity of Li metal anodes, commercial LMBs will need to have the so-called negative-to-positive (N:P) ratio as close to 1:1 as possible, that is by matching the capacity of the Li metal anode as close to the capacity of the cathode material.^{2,14}

Realistic LMB designs thus either limit the amount of excess Li, e.g., by using thin Li foils² or they operate in an ‘anode-free’ battery design that replaces the Li metal anode with a bare Cu current collector (Figure 2.2).^{48,50} The latter design has the obvious practical advantage that it is easier to assemble as it does not require handling Li metal. Both these battery designs tend to have a fast capacity fade, which is directly associated with the irreversible loss of active Li due to SEI formation and dead Li formation.^{40,41} Li-Cu cells are often used to directly study Li deposition on Cu, avoiding issues that may be associated with high-voltage cathodes.

2.2.2 The solid electrolyte interphase

The low potential of Li metal results in the spontaneous breakdown of the electrolyte at the Li surface. Much work is being carried out to correlate the electrochemical behaviour of Li metal to the properties of the SEI. Recent detailed reviews on the SEI on Li metal can be found in the following references, 55,60 and 61.

The interphase layer between the electrolyte and the Li metal electrode was first introduced by Peled in 1979.¹⁸ The SEI was presented as an ion conducting layer (one that transports Li⁺ ions) with high electronic resistivity.^{18,30} The thickness of the SEI was proposed to be limited by the electron tunnelling range, resulting in an SEI thickness on the order of ~10 nm.³⁰ The SEI structure depends on the electrolyte and is often visualized in terms of the mosaic model introduced by Peled,⁵⁴ where the SEI as a multi-component film with inorganic components (such as Li₂CO₃, LiOH, Li₂O and LiF) forming close to the Li metal and a higher content of organic (polymeric) species on the outer part of the SEI close to the electrolyte.³⁰

The SEI needs to be both chemically and mechanically robust, and fully passivating to ensure stable cycling of Li metal.^{31,32} Electrolyte engineering, where different salts and solvents are combined to tailor the SEI and optimise cycling performance, has driven the development of a suitable electrolyte system for LMBs.

Carbonate-based electrolyte are most commonly used in commercial Li-ion batteries due to their high oxidation stability (>4.3 V) with solvents such as ethylene carbonate (EC), dimethyl carbonate (DMC) and ethyl methyl carbonate (EMC).⁵⁵ However, the Li morphology in carbonate electrolytes is generally whisker-like, that leads to high surface area deposits and low cycling efficiency.⁵⁶⁻⁵⁸ It is common to use existing electrolytes with additives that improve the Li metal cycling, such as fluoroethylene carbonate (FEC), lithium bis(oxalato)borate (LiBOB), vinylene carbonate (VC) and lithium nitrate (LiNO₃).^{28,29,59} The additives are often sacrificial and break down to form the SEI.⁵¹

Ether-based electrolytes show much better cycling in LMBs, which is attributed to the formation of oligomers that have good flexibility and strong binding affinity to the Li surface.⁶⁰ However, ether based electrolytes suffer from low oxidation stability (<4 V vs Li⁺/Li) and high flammability rendering them unsafe for commercial batteries.⁵¹ High-concentration ether-based electrolytes (4 M) have gained significant attention with improved thermal and electrochemical stability⁶¹ and stable cycling of Li metal.^{62,63}

Of note, in this work a distinction is made between the chemical SEI formation, which forms spontaneously on Li when no net current is flowing in the circuit (studied in Chapter 4, Chapter 5 and Chapter 6) and the electrochemical SEI formation that forms as a side reaction during Li plating, consuming charge (studied in Chapter 4 and Chapter 6). The chemical SEI formation on Li metal is highly dynamic and occurs continuously after immersing Li metal into an electrolyte resulting in a growing SEI resistance with immersion time as probed by impedance spectroscopy.^{64,65} Allowing the chemical SEI formation to occur by immersing Li metal in the electrolyte for periods extending over days has been shown to result in enhanced cycling stability.^{66,67} The SEI reduction reaction is coupled to Li oxidation (Li metal dissolution) as shown in the schematic, Figure 2.3. In contrast, electrochemical SEI formation is a competing reaction to Li deposition and kinetics will determine which proportion of the current is used for SEI formation.⁶⁸ The magnitude of the current density will also influence the chemical composition of the SEI.⁶⁹ Similarly the chemical SEI formation may results in a different

chemical composition; Wang et al. studied the SEI formation on Li metal in an oxygen gas environment and reported different amounts of LiOH and other oxygen containing species formed electrochemically compared to the chemical SEI.⁷⁰

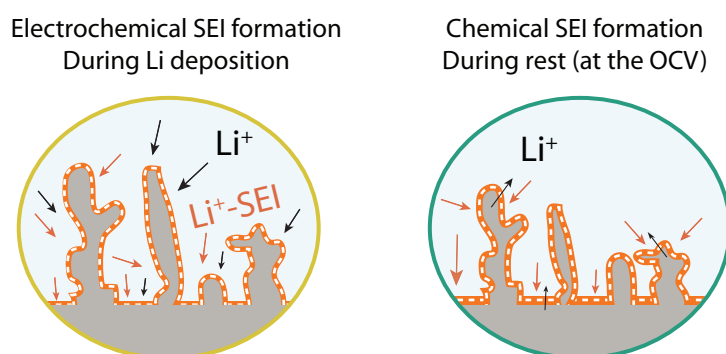


Figure 2.3 Schematic of the electrochemical and chemical SEI formation on Li metal. The electrochemical SEI formation occurs concurrently with Li deposition whereas the chemical SEI formation occurs with no net current passed in the circuit and involves Li oxidation coupled to SEI reduction reaction.

2.2.3 Characterisation techniques

The morphology and plating behaviour of Li metal is commonly studied with techniques such as scanning electron microscopy (SEM)⁷¹, *operando* optical microscopy^{41,44,72} and transmission electron microscopy (TEM).³⁷ Recently, a new analytic method was developed to quantify *ex situ* the amount of inactive Li formed on a copper current collector by reacting the Li metal with water.⁵⁶ Electron paramagnetic resonance (EPR) has been demonstrated as a semi-quantitative and non-invasive technique to observe *operando* Li microstructural growth in a flooded cell.⁷³

Of these techniques, *in situ* nuclear magnetic resonance (NMR) and magnetic resonance imaging (MRI) are unique as non-invasive techniques that provide quantitative and temporal information on Li metal deposition. *Operando* NMR has been used to study Li and Na plating and stripping by continuously acquiring NMR spectra during an electrochemical measurement.^{33,74-80} Bhattacharyya et al. developed a method to quantify and distinguish between different types of microstructures that form during Li deposition based on the skin depth effect of conductors and the bulk magnetic susceptibility (BMS) of Li metal in a magnetic field.⁷⁴ *In situ* NMR of Li metal deposition is the main technique used in this thesis. The NMR

of Li metal will be described in detail in Chapter 3. Note that *operando* and *in situ* are often used interchangeably, the former referring to measurements made while the device is operating while the latter is more general and refers to measurements made of the intact device.

Many studies are on the characterisation of the SEI composition, transport properties, mechanical properties, nanostructure and dynamic evolution, which are key to understand Li deposition. Due to the thin and highly reactive nature of the SEI, common surface chemistry techniques such as X-ray photoelectron spectroscopy (XPS)⁸¹ and electron microscopy⁸² may damage the organic polymer components of the SEI, which makes characterisation difficult. Cryogenic electron microscopy (cryo-EM) has become an increasingly useful tool to study the SEI on Li metal, as cooling down the sample to cryogenic temperatures reduces the electron beam damage.¹⁷ Cryo-EM studies have revealed that the nanostructure of the SEI on Li metal deposits differs significantly between electrolytes, allowing for correlation between structural composition and cycling performance.^{31,83}

Significant efforts have been made to study the SEI on silicon and graphite electrodes with NMR spectroscopy,^{84–86} however NMR can suffer from issues of sensitivity and selectivity to the SEI (as it probes the whole sample volume). It has even more challenging to study the SEI on Li metal using NMR, the main reason being that magic-angle spinning (MAS) of metallic samples in a magnetic field is not trivial and the samples need diluting to spin properly. This causes a decrease in signal-to-noise in these measurements. In a recent study, we used dynamic nuclear polarization (DNP) to enhance the signal intensity of the SEI on Li metal.⁸⁷ However, further method development is needed to perform quantitative characterisation of the chemical composition using DNP-NMR.

In conclusion, a fundamental question to address is how the nature of the SEI on Li metal affects the plating and stripping of Li, in order to systematically tackle microstructural growth and low capacity retention in LMBs. What determines a good SEI on Li metal? The SEI must be fully passivating and homogeneous in composition and morphology to ensure uniform Li ion transport through the SEI and stable Li deposition. A flexible SEI might be desirable that can accommodate infinite volume changes on plating and stripping Li metal. Although significant characterisation of SEI has been carried out, the nature and distribution of chemical components in the SEI, the ion transport within them and their relationship to microstructural growth and dead Li formation, is ill-defined.

In situ NMR studies will be used in Chapter 4 to study the effect the FEC additive has on Li plating under a range of plating conditions. In Chapter 5 the isotope exchange between Li metal and the electrolyte is measured using NMR, and the transport through the SEI as well as the time-evolution of the SEI estimated by simulations. In Chapter 6, the methodology to study ‘anode-free’ batteries *via in situ* NMR is developed to study the dead Li formation and other capacity losses in LMBs.

2.3 Electrochemistry

The transfer of charge across an interface accounts for a significant part of natural processes. The theory on charge transfer kinetics describes the functioning of biological systems, electrochemical synthesis, the stability of metals, and energy storage devices. By controlling the direction and rate of a charge transfer reaction, one can control the chemical reactions occurring in a given system. Here, a short introduction on the theoretical framework that is generally used when discussing electrochemical systems will be given and connections drawn to the processes relevant to electrodeposition of Li metal. The discussion is based on the work of Newman and Thomas-Alyea,⁸⁸ Bockris and Reddy,⁸⁹ and Bard and Faulkner.⁹⁰

2.3.1 Electrode kinetics

In order to understand how fast the charge-transfer reaction will occur at an electrode, the kinetics need to be considered to establish a relationship between current and overpotential. The rate ν , of an electrode reaction is related to the current density, j , by Faraday’s law:

$$\nu = \frac{j}{nF} \quad (2.2)$$

where n is the number of electrons transferred in the reaction and F is the Faraday constant. The rate depends on the electrolyte concentration at the electrode surface, the nature of the electrode surface and the electrode potential.⁸⁸ For a simple one-step, n -electron process:



the net rate of the reaction is the difference between the rate of the forward and backward reactions, associated with the cathodic k_c , and anodic rate constant k_a .⁸⁸ The rate constants are expected to have an Arrhenius temperature dependence that can be described in the form:

$$k_c = A_c \exp\left(-\frac{\Delta G_{0,c}^\ddagger}{RT}\right) \quad (2.4)$$

where $\Delta G_{0,c}^\ddagger$ is the activation energy of the transition state for the cathodic reaction and A_c is generally known as the frequency factor.⁹⁰

The rate of the forward and backward reaction depends on the applied potential E (the potential difference between the electrode and the electrolyte solution) and electrolyte composition at the electrode. The net reaction rate is equal to the difference between the rates and can be written in the form:⁸⁸

$$v = \frac{j}{nF} = k_a c_R \exp\left(\frac{(1-\beta)nF}{RT} E\right) - k_c c_O \exp\left(\frac{-\beta nF}{RT} E\right) \quad (2.5)$$

where c_R and c_O are the concentrations of the anodic and cathodic reactants. The β is a symmetry factor that represents the fraction of the applied potential that promotes the cathodic reaction. Similarly, $(1-\beta)$ is the fraction that promotes the anodic reaction. Often, β is assumed to be equal to 0.5.⁸⁸

At a potential E_0 , defined as the equilibrium potential, a “stalemate is reached between the electronation and de-electronation reactions”.⁸⁹ That is at potential E_0 the rate of the forward reaction is equal to the rate of the backward reaction and the net rate of the reaction becomes zero. Equation (2.5) can then be rearranged to:

$$k_a c_R \exp\left(\frac{(1-\beta)nF}{RT} E_0\right) = k_c c_O \exp\left(\frac{-\beta nF}{RT} E_0\right) \quad (2.6)$$

With further rearrangement, equation (2.6) yields a form of the Nernst equation:⁸⁸

$$E_0 = \frac{RT}{nF} \ln \frac{k_c c_O}{k_a c_R} \quad (2.7)$$

By defining the surface overpotential as $\eta_s = E - E_0$, and substituting equation (2.7) in to equation (2.5) we get:⁸⁸

$$\begin{aligned} \frac{j}{nF} = & k_a c_R \exp\left(\frac{(1-\beta)nF}{RT} \eta_s + (1-\beta) \ln \frac{k_c c_O}{k_a c_R}\right) \\ & - k_c c_O \exp\left(\frac{-\beta nF}{RT} \eta_s - \beta \ln \frac{k_c c_O}{k_a c_R}\right) \end{aligned} \quad (2.8)$$

By defining the exchange current density as:⁸⁸

$$j_0 = nF k_a^\beta k_c^{1-\beta} c_R^\beta c_O^{1-\beta} \quad (2.9)$$

equation (2.8) may be written as:

$$j = j_0 \left[\exp\left(\frac{(1-\beta)nF\eta_s}{RT}\right) - \exp\left(-\frac{\beta nF\eta_s}{RT}\right) \right] \quad (2.10)$$

Equation (2.10) is known as the Butler-Volmer equation of electrode kinetics. It concerns both the equilibrium current and the effect of an overpotential, thus describing both the chemical and electrical aspect of charge transfer.⁸⁹ For the special case when the rate constants are equal $k_a = k_c = k^0$ the exchange current density becomes:

$$j_0 = nF k^0 c_R^\beta c_O^{1-\beta} \quad (2.11)$$

k^0 is known as the standard rate constant and reflects the kinetic properties of the interfacial system and can vary by many orders of magnitude between different reactions; systems with large k^0 will achieve equilibrium quickly (according to Nernst equation) upon change in the potential,⁹¹ whereas small values of k^0 describe a more sluggish systems.^{89,90} The Butler-Volmer equation for Li deposition may now be written as:^{44,92}

$$j = Fk^0 [c_{Li} \exp\left(\frac{(1-\beta)F}{RT} \eta_s\right) - c_{Li+} \exp\left(-\frac{\beta}{RT} \eta_s\right)] \quad (2.12)$$

where c_{Li} is the surface concentration of Li metal and c_{Li+} is the concentration of Li ions at the surface.

The heterogeneous SEI layer on Li metal results in a distribution of rate constants on the Li metal surface.⁴⁴ Wood et al. found that spatial variations of rate constants for Li deposition must be minimized to improve the cycling performance of Li metal anodes.⁴⁴ By stabilising the Li metal surface a more homogeneous current distribution is expected. This may be achieved by an SEI that fully covers the Li deposits, with a flexible SEI that does not rupture or with protective coatings that provide homogeneous Li ion transport. This will be explored further in Chapter 5 using isotope exchange measurements.

2.3.2 Electrochemical corrosion

IUPAC defines corrosion as the general term for an irreversible interfacial reaction that often, but not always, leads to a degradation of the materials properties.⁹³ Electrochemical corrosion involves electrode reactions such as the dissolution of metals where there are at least two or more reactions occurring simultaneously, the anodic and the cathodic reactions.⁹³ Under these conditions, the open-circuit potential is at a mixed potential (the corrosion potential).⁸⁸

The corrosion potential is not an equilibrium potential corresponding to any of the occurring reactions but represents the steady state of the corrosion system. The corrosion potential will settle where the rates of the anodic and cathodic reactions are equal, resulting in a net zero current. For example, for a system where the anodic reaction is metal dissolution, the currents must be equal:

$$I_{corr} = I_M = -I_c \quad (2.13)$$

where I_{corr} is the corrosion current, I_M the metal dissolution current and I_c the cathodic current.^{88,89} The corrosion potential will be determined by the kinetics of the reactions, where the rates of the two reactions balance.

As an example, we look at the corrosion process of iron. The anodic process is the metal dissolution: $Fe \rightarrow Fe^{2+} + 2e^-$ and the cathodic process is usually the oxygen reduction or hydrogen evolution reaction. In the case of the oxygen reduction reaction, i.e. $O_2 + 4H^+ + 4e^- \rightarrow 2H_2O$, the rate of corrosion is determined by the mass transfer of oxygen to the corroding surface.⁸⁸

Corrosion processes do not always take place on a single electrode surface. Galvanic corrosion or contact corrosion is the enhancement of a corrosion reaction due to the contact of materials of different electrochemical potentials, effectively creating the conditions of a short-circuited galvanic cell. Thus, during the dissolution of iron, the cathodic process of oxygen reduction may take place on other metals such as tin or copper, which act as the cathode.⁸⁸

When both redox reactions follow Butler-Volmer kinetics with a symmetry coefficient $\beta = \frac{1}{2}$, the corrosion current has been shown to follow approximately:⁸⁹

$$I_{corr} = (I_{0,M} I_{0,c})^{1/2} \exp\left(\frac{F(E_c - E_M)}{4RT}\right) \quad (2.14)$$

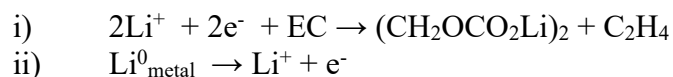
where $I_{0,M}$ is the exchange current for the metal dissolution, defined as the exchange current density multiplied by the available area: $I_{0,M} = j_{0,M} A_M$. E_c and E_M are the equilibrium potentials for the redox reactions. According to equation (2.14), there are two fundamental ways of minimising the metal dissolution. Either by reducing the first term in the equation:⁸⁹

$$I_{0,M} I_{0,c} = (A_M j_{0,M}) (A_{red} j_{0,c}) \quad (2.15)$$

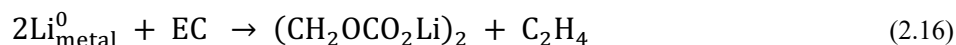
which is done either by decreasing the exchange current density by methods such as using surface inhibitors that adsorb to the metal surface⁹⁴ or by cutting down the areas in contact with the electrolyte by the formation of a passivating layer on the metal. Coatings may be used to slow down or prevent the corrosion, but if it becomes damaged this can lead to an increased corrosion rate on the exposed parts.⁹⁵ Cathodic protection then involves connecting the metal that needs protecting to a ‘sacrificial anode’, for example by connecting a steel structure to a magnesium anode, the magnesium then corrodes and needs to be changed regularly.⁹⁵

Li corrosion will be discussed in Chapter 6, defined as both the chemical formation of the SEI on Li metal accompanied by Li oxidation and the galvanic corrosion of Li on Cu, by the coupled Li-oxidation, reduction of copper oxides and/or reduction of the electrolyte on the Cu. Li metal deposition on Cu is analogous to the formation of a sacrificial protection, where the Li metal serves to inhibit Cu corrosion and potentially results in enhanced rates of corrosion for the Li.⁹⁶

One typical SEI reduction reaction is here taken as an example of chemical SEI formation. The examples involves the ring-opening of the EC solvent molecule,⁹⁷ described as follows:



When taken together, the overall reaction corresponds to:



The chemical SEI formation thus leads to a loss of Li metal in a battery cell and is effectively a corrosion process. A stable SEI should limit the continuous breakdown of the electrolyte and is analogous to a passivating coating as described above.²³

2.3.3 Electrochemical methods

2.3.3.1 Galvanostatic cycling

Li metal anodes are commonly studied by performing galvanostatic plating and stripping, where a constant current is applied and the voltage response is measured as a function of time.^{19,44,64} The current density and the plating capacity have been shown to influence the efficiency, cycle life and morphology of the Li deposits with high current densities generally associated with Li dendrite growth.^{37,42,98}

Under constant current conditions the salt concentration near the surface decreases. A concentration gradient develops, which drives the diffusional flux J_D towards the electrode surface. Using Fick's law of diffusion, the reaction rate can be described in terms of the flux:⁸⁹

$$\frac{j}{nF} = J_D = -D \left(\frac{dc}{dx} \right)_{x=0} \quad (2.17)$$

where D is the diffusion coefficient of the ions in the electrolyte and $x = 0$ is at the electrode surface. Over small distances, near the electrode, the concentration profile can be approximated as linear and when extrapolated towards the bulk electrolyte, the Nernst diffusion-layer δ is defined as where the curve intersects the bulk value (Figure 2.4). Equation (2.10) can be approximated as:

$$J_D = -D \frac{(c^0 - c_{x=0})}{\delta} \quad (2.18)$$

where c^0 is the bulk concentration.⁸⁹ The thickness of the Nernst diffusion-layer time increases initially with the square root of time and can be approximated for a constant current experiment as:⁸⁹

$$\delta = \frac{2}{\sqrt{\pi}} \sqrt{Dt} \quad (2.19)$$

This analysis is an approximation and natural convection will take over diffusion when the diffusion layer extends far into the solution.

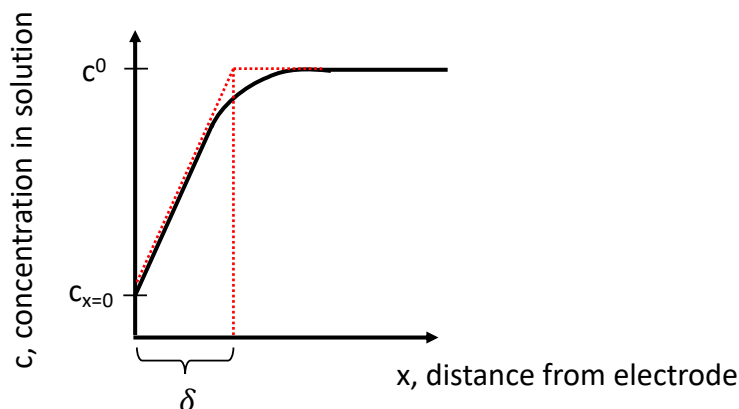


Figure 2.4 The Nernst diffusion-layer thickness, δ , obtained by extrapolating the linear portion of the concentration gradient to the bulk concentration value. The figure is reproduced from reference [⁸⁹]

Electrochemical models of mass transport in electrolytes have been developed to describe electrodeposition during a constant current experiment, relating the concentration gradients that develop in the electrolyte to dendritic growth.^{72,99–101} Two current regimes distinguish between the continuous development of the concentration gradient at the electrode surface and whether a steady-state is achieved. The limiting current density that separates between the two regimes is defined as:

$$j_{lim} = \frac{2Fz c^0 D_{amb}}{t_a L} \quad (2.20)$$

where F is the Faraday constant, z is the charge number of the cation ($z_{Li^+} = 1$), c^0 is the initial bulk concentration, D_{amb} is the ambipolar diffusion coefficient for the ions in the electrolyte, t_a the transport number of the anions in the electrolyte and L is the distance between

the two electrodes.^{72,100} Below j_{lim} , according to the theory, the concentration gradient in the electrolyte will reach a steady-state with a non-zero concentration of ions at the electrode and dendrite growth *via* this mechanism is not expected.⁷² In the high-current regime, for current densities $j > j_{lim}$, diffusion limitation leads to fractal dendritic growth at a characteristic time known as the Sand's time (the time at which the concentration of anions drops to zero in the diffusion layer at the electrode surface creating a large electric field).^{72,100,101} The Sand's time is given by the formula:^{72,101}

$$\tau_s = \pi D \left(\frac{c^0 z F}{2 j t_a} \right)^2 \quad (2.21)$$

There are two main conclusions that can be drawn from equation (2.21). For large current densities the transition to Sand's time is shorter and higher electrolyte concentrations increase the Sand's time. The onset of fractal Li dendrite growth has been shown experimentally to correlate well with this theory.^{33,102} But inhomogeneous microstructural growth is usually observed for Li metal deposition performed below j_{lim} , associated with non-uniformities in the SEI on Li metal.^{33,60,103}

2.3.3.2 Pulse plating experiments

Pulse electrolysis has been widely used in electrodeposition of a range of metals, including gold,¹⁰⁴ silver¹⁰⁵ and nickel¹⁰⁶, the reason being improved control over grain sizes (more fine-grained deposits can be obtained), morphology and porosity. There are multiple ways of performing pulse electrolysis. Here we focus on the galvanostatic square pulses that are separated by a rest period with zero current in the external circuit. Instead of one parameter, as is the case in constant current experiments, there are three variables when pulse plating; the applied current density j_p the duration of the pulse, T_{ON} and the duration of the rest period T_{OFF} (Figure 2.5a).

If the duration of the pulse is short, the concentration gradient near the electrode does not extend far enough into the solution for convection to be significant and the ion depletion layer near the electrode is replenished by diffusion.¹⁰⁷ Pulse plating thus leads to an improved mass transfer, which means higher instantaneous current densities may be used without the severe concentration depletion as described in the previous section.

Higher current densities generally induce higher overpotentials, as expected from Butler-Volmer kinetics. The kinetics of nucleation and growth of metal deposit depend significantly on the electrochemical overpotential.¹⁰⁸ For Li deposition, high overpotential has been shown to result in smaller Li nuclei size and higher surface coverages.¹⁰⁹ Thus, pulse plating may potentially be used to obtain more uniform Li deposition. However, the SEI will also influence the pulse plating as both diffusion and chemical SEI formation take place during the rest period. This is explored in Chapter 4 where pulse plating is performed in two electrolytes with similar transport properties but different SEI properties.

Previous Monte Carlo simulations have suggested shorter pulses are beneficial in mitigating Li dendrite growth.¹¹⁰ However, the rate of pulsing is limited by the rate of charging and discharging the electrical double layer at the electrode-electrolyte interface.^{107,111} For current pulse j_p , the total current consists of a double-layer capacitive current, j_{dl} and a Faradaic current j_F (in this case the current used for metal deposition):

$$j_p = j_{dl} + j_F \quad (2.22)$$

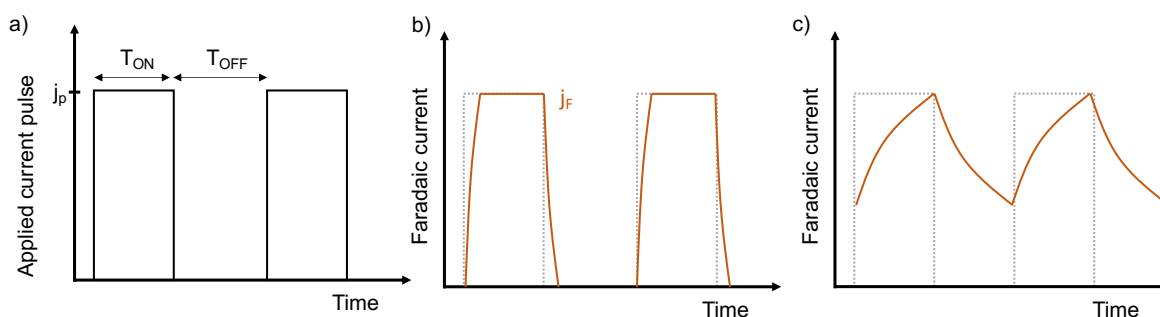


Figure 2.5 Schematic of the **a)** applied current j_p in a galvanostatic pulse plating experiment, with the pulse length T_{ON} and rest period T_{OFF} and **b)** the corresponding Faradaic current j_F used for the metal deposition in orange. **c)** For significant effects of the capacitive charging, the current profile starts to resemble constant current conditions. The figure is reproduced from reference ¹⁰⁷.

After charging the capacitor, $j_{dl} = 0$, and j_F equals the applied current. Figure 2.5b represents a pulse plating experiment where small damping is observed in the Faradaic current at the beginning and end of the current pulse. For significant capacitive effects (that may occur when using small values of T_{ON} and T_{OFF}), strong damping is observed for the Faradaic current (Figure 2.5c) and the properties of the plated metal start to resemble that obtained using

constant current.¹⁰⁷ Thus, there is a limit to how short a current pulse can be for pulse plating to be effective.

To estimate the charging time of the double layer capacitor, the electrode-electrolyte interface may be represented as an equivalent circuit of a capacitor, C_{dl} , and a resistor, R (representing the charge-transfer resistance at the electrode interface). The charging time can be estimated by computing the time needed for the potential to reach 98.2% of the potential associated with the Faradaic current, given by:¹¹¹

$$\tau = 4 \times RC_{dl} \quad (2.23)$$

A typical capacitance value of the electrode-electrolyte interface is 10^{-7} - 10^{-5} F.¹¹² The charge transfer resistance is on the order of 10-100 Ω .^{70,113} The estimated charging time is thus in the range of $\tau \sim 0.04 - 4$ ms for charge transfer resistance of 100 Ω . To observe whether any damping occurs, the capacitive effect can be further explored by plotting the voltage profile for a single current pulse. This was done in symmetrical Li-Li cells, shown in Figure 2.6. The capacitive effect is negligible for 1 s current pulse whereby a damping is seen for both 50 ms and 5 ms current pulse. For 5 ms the capacitive effect is significant as observed by the skewed voltage profile (Figure 2.6c).

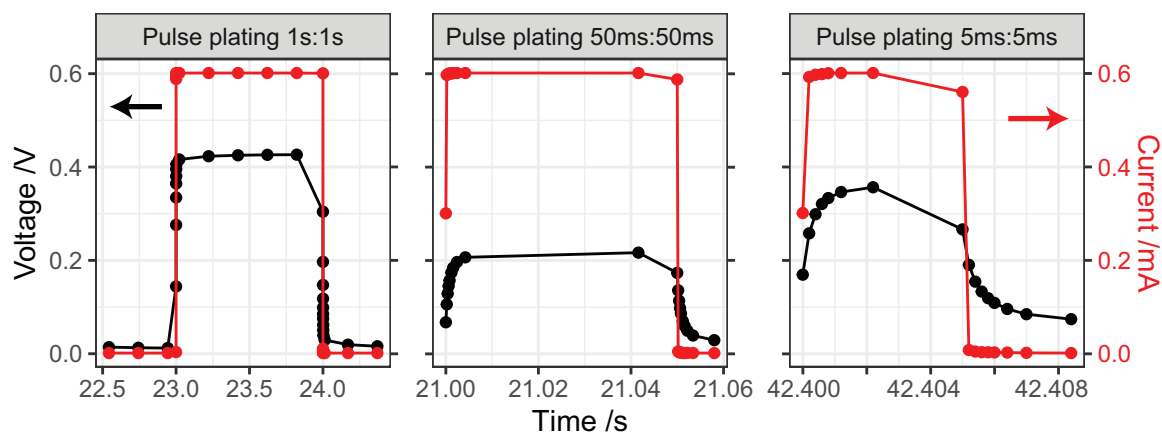


Figure 2.6 The voltage profile and the corresponding applied current in symmetric Li-Li *in situ* cells for a single current pulse at 1 mA/cm² and $T_{ON} = 1$ s, 50 ms and 5 ms. Charging of the double-layer is observed for both 50 ms and 5 ms pulse. For all pulse lengths the overpotential reaches a maximum indicating that charging of the double-layer capacitance is completed during the current pulse. The potential drop at the end of the pulse is due to the way the data was acquired, data points were only acquired when ± 10 mV differences were detected in the potential.

2.3.3.3 Electrochemical Impedance Spectroscopy

Impedance spectroscopy involves recording the response of a system to an electrical stimulus. An alternating voltage (or current) of amplitude V and angular frequency ω is applied to a system:

$$v(t) = V \sin(\omega t) \quad (2.24)$$

and the current (or voltage) response is measured:

$$i(t) = I \sin(\omega t + \phi) \quad (2.25)$$

where I is the amplitude of the current and ϕ is the phase angle. If the system cannot be represented by a pure resistor, there is a phase shift between the current and the voltage due to the capacitive reactance, X_c . The measured voltage is linked to the current through the vector, \mathbf{Z} , called the impedance:

$$\mathbf{Z}(\omega) = R - iX_c \quad (2.26)$$

where R is the resistance of the system and i the imaginary number. The voltage-current relationship may now be described as:

$$V = I \mathbf{Z} \quad (2.27)$$

which is a generalized version of Ohm's law. The impedance can be represented as:

$$\mathbf{Z}(\omega) = \text{Re}(\mathbf{Z}) - j\text{Im}(\mathbf{Z}) \quad (2.28)$$

where $\text{Re}(\mathbf{Z})$ and $\text{Im}(\mathbf{Z})$ are the real and imaginary parts of the impedance. The frequency-dependent impedance is often represented in a Nyquist plot that displays the $-\text{Im}(\mathbf{Z})$ vs. $\text{Re}(\mathbf{Z})$ for different values of ω , (Figure 2.7).

Equivalent circuits are a useful tool to analyse and interpret the resulting, often complex, electric response. Typically, an electrochemical cell has associated with it a bulk resistance (R_{bulk}) in series with frequency-dependent responses due to capacitive effects. The Randles equivalent circuit (Figure 2.7a) is frequently used when describing electrochemical systems, which consists of a bulk resistance (representing the electrolyte resistance) in series with an R-

C circuit element. The R-C circuit element consists of a resistor in parallel with a capacitor, representing the charge-transfer resistance (R_{CT}) and the double-layer capacitance (C_{dl}), and has associated with it a time constant $\tau = RC$.

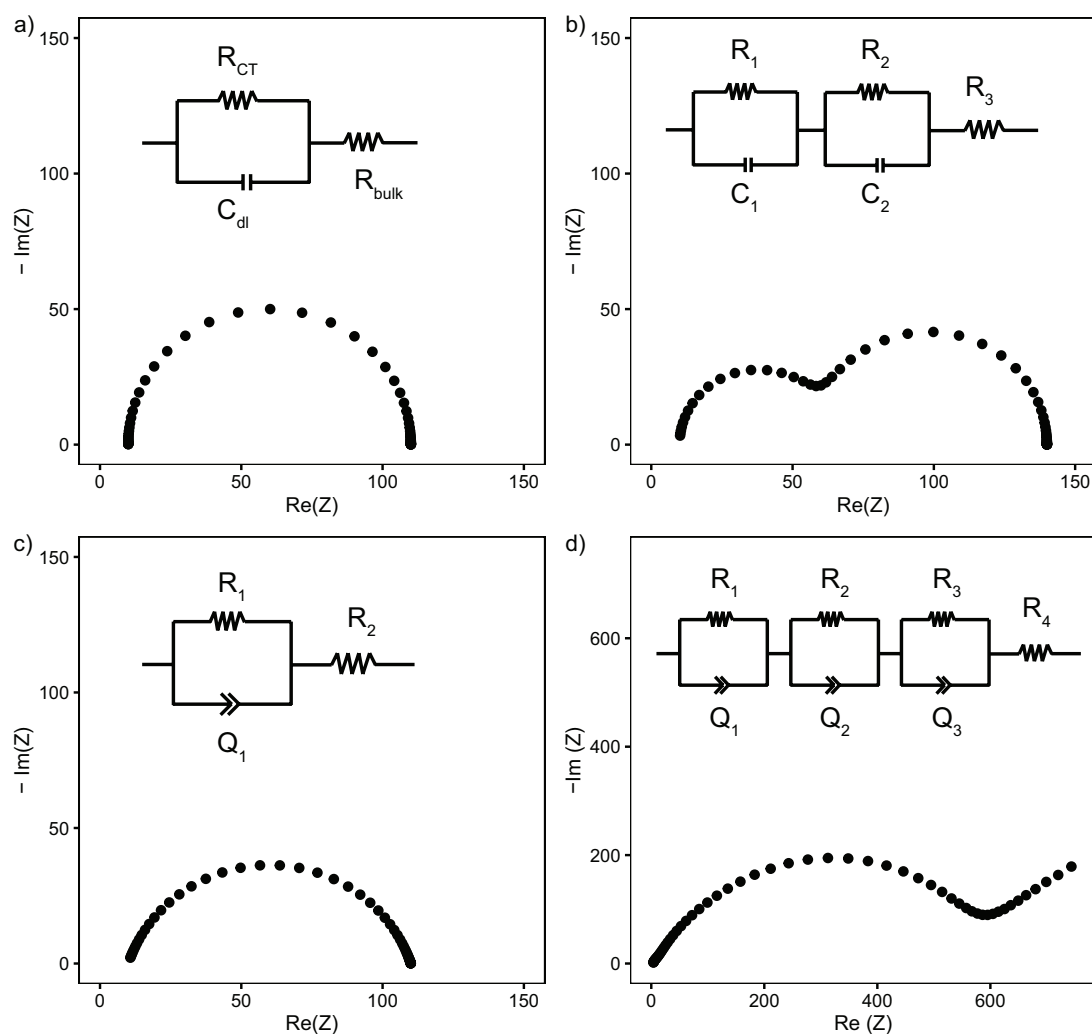


Figure 2.7 **a)** The equivalent circuit and the simulated Nyquist plot of the Randles circuit, with $R_{bulk} = 10 \Omega$, $R_{CT} = 100 \Omega$ and $C_{dl} = 10 \mu F$. **b)** The simulated Nyquist plot for the corresponding equivalent circuit, with $R_1 = 10 \Omega$, $R_2 = 80 \Omega$, $C_2 = 10 \mu F$, $R_3 = 50 \Omega$ and $C_3 = 0.5 \mu F$. **c)** The simulated Nyquist plot for the corresponding equivalent circuit with a constant phase element, which shows a depressed semicircle with $R_1 = 10 \Omega$, $R_2 = 100 \Omega$ and $Q_2 = 10 \mu F$ with $n = 0.8$. The spectra were simulated using the open-source R-package, 'impedanceR'.¹¹⁴ **d)** Experimental Nyquist spectrum of a symmetrical Li-Li cell with 1M LiPF₆ in EC:DMC.

The impedance of a pure capacitor is $Z_C = \frac{1}{j\omega C}$. The impedance of the Randles circuit is:

$$Z(\omega) = \frac{R}{1 + j\omega C} \quad (2.29)$$

and the Nyquist plot for a typical Randles circuit is a semicircle (Figure 2.7a). Having two R-C circuits in series results in two semicircles (Figure 2.7b) given the time constants are different enough. A depressed semicircle is seen when there is a close distribution of time constants. Generally this is the case in a lithium metal cell, where several time-constants are required to represent the Li ion transport in both the compact and porous phases of the SEI layer.^{115,116} This may be represented with a constant phase element (CPE), a circuit element that accounts for inhomogeneities in a sample. The impedance of the CPE element is defined as:¹¹⁷

$$Z_Q = \frac{1}{Q(j\omega)^n} \quad (2.30)$$

where Q is independent of frequency and n is the constant phase, $0 < n \leq 1$, typically between 0.75-1. The Nyquist plot for a simulated ‘R-CPE’ circuit element in series with the bulk resistance is shown in Figure 2.7c, with a typical depressed semicircle. The equivalent circuit used here to represent a symmetrical Li-Li cell, and will be discussed in more detail in Chapter 5, contains three R-CPE circuit elements in series and the bulk resistance (R_4).^{115,116,118}

Chapter 3

Nuclear Magnetic Resonance Spectroscopy

Nuclear magnetic resonance (NMR) spectroscopy is performed in a strong magnetic field where radio frequency (rf) irradiation is used in the form of short pulses to excite nuclear spins in a sample. NMR spectroscopy is the main technique used in this thesis and this chapter presents a brief introduction to the principles of NMR and the theory on NMR of metals.

3.1 Basic Principles of NMR

Most nuclei possess an intrinsic spin that gives rise to a non-zero magnetic moment, defined by the spin quantum number $I = \frac{n}{2}$:

$$\mu_I = \hbar \gamma_I I \quad (3.1)$$

where n is a non-negative integer value, \hbar is the reduced Planck constant and γ_I is the gyromagnetic ratio (an intrinsic property of the nuclei). A nucleus with spin quantum number I has $2I + 1$ spin states, specified by the quantum number $m_I (= -I, -I + 1, \dots, I - 1, I)$. In an applied external magnetic field, B_0 , these spin states become non-degenerate due to the Zeeman interaction between the magnetic field and the nuclear magnetic dipole moment. For $I = \frac{1}{2}$, this gives rise to an energy separation ΔE between consecutive spin states:

$$\Delta E = \hbar \omega_0 = -\hbar \gamma_I B_0 \quad (3.2)$$

where $\omega_0 = -\gamma_I B_0$ is known as the Larmor frequency and B_0 is the applied magnetic field. For magnetic fields typically used in NMR research laboratories (ranging from 4 – 23 T), the Larmor frequency is in the region of radiofrequency in the electromagnetic spectrum.

The population of the energy levels is given by the Boltzmann distribution and when a sample is placed in a magnetic field, a thermal equilibrium is achieved generating a net magnetization, \mathbf{M} , parallel to the magnetic field (represented in Figure 3.1a by the vector model formalism).

Applying a second magnetic field (B_1 -field) with the use of a rf coil perturbs the thermal equilibrium of the spin system. The spin states can thus be excited and manipulated by a so-called rf-pulse. The rf-pulse induces a B_1 -field, at or near the Larmor frequency and perpendicular to the B_0 field that results in a “nutation” of the magnetization. The effect of the pulse is easily depicted in the so-called “rotating-frame” of reference (i.e. a frame rotating about the z-axis at the Larmor frequency) where the B_1 -field induced by the pulse appears to be static (along x). Effectively this results in the bulk magnetization M being rotated from the laboratory z-axis into the transverse plane (Figure 3.1b), and at the termination of the pulse, M precesses about the B_0 – axis with frequency ω_0 (Figure 3.1c).

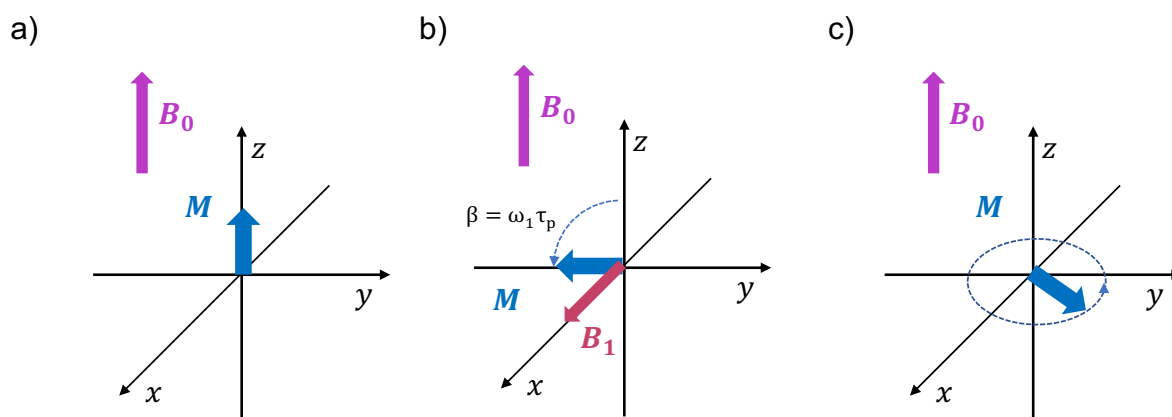


Figure 3.1 A schematic showing the effect of the 90° rf-pulse in the rotating frame using the vector model representation.¹¹⁹ **a)** The bulk magnetization M , aligned along the z-axis parallel to the external B_0 field. **b)** On applying a B_1 -field along the x-axis, the magnetization M rotates about x. **c)** Free precession of the magnetization vector within the xy-plane. The figure is reproduced from reference¹²⁰.

For an on-resonance pulse, the flip angle β (in radians, depicted in Figure 3.1b) depends on the duration of the pulse, τ_p , and the field strength of the applied rf-pulse:

$$\beta = \gamma_1 B_1 \tau_p = \omega_1 \tau_p \quad (3.3)$$

and the induced magnetization M_{xy} depends on the flip angle:

$$M_{xy} \propto M_0 \sin(\beta) \quad (3.4)$$

where M_0 is the equilibrium magnetization.¹²¹ The simplest NMR experiment is the so called one-pulse (or Bloch-decay) experiment, where an applied “ $\pi/2$ pulse” (a 90° pulse) rotates M

into the transverse xy -plane (Figure 3.1b). The precession of the magnetization in the transverse plane (Figure 3.1c) is detected as an induction current in the NMR coil. Only the magnetization in the xy -plane is detected and thus the maximum signal intensity is obtained for a flip angle of $\beta = \pi/2$. A nutation experiment typically results in a sinusoidal curve, where the flip angle is calibrated before acquiring a spectrum by measuring the signal intensity as a function of the pulse duration and by that the 90° pulse is determined.¹²²

The signal is detected in the rf coil as an induction current produced by magnetization that rotates around the z -axis. The excited spin system gradually relaxes to equilibrium and is thus observed as a decaying rf response over time, referred to as the free induction decay (FID). A Fourier transform (FT) of the FID translates the voltage-time signal into an intensity-frequency signal and gives the NMR spectrum. The return to the thermal equilibrium proceeds through a process known as the longitudinal or spin-lattice relaxation, described by a time constant T_1 .¹²² The spin-lattice relaxation determines how fast one can repeat the NMR measurement (to improve the signal-to-noise ratio by signal averaging) and for the measurements to be quantitative, a recycle delay of $> 5 \times T_1$ is recommended.¹¹⁹

The detected resonance frequency of the nucleus is not only affected by Zeeman interaction (equation (3.2)), but also by the surrounding electrons and nuclei. Variations in the local magnetic field surrounding the nuclei of interest is the source of the sensitivity of NMR to local structure and dynamics. Furthermore, the signal intensity is directly proportional to the number of NMR active nuclei and allows different materials and environments to be quantified. The shift of the NMR resonance and the line shape are influenced by the ‘internal spin interactions’: the shift interactions (nuclear-electron interactions, the chemical shift, Fermi shift and Knight shift), the dipolar coupling (nuclear-nuclear spin, through space), the indirect spin-spin coupling (J -coupling, the interaction of nuclear spins with the involvement of electrons through bonds) and the quadrupolar interaction (coupling of the nuclear quadrupole moment with surrounding electric field gradients).¹²³

The nucleus of interest in this thesis is ${}^7\text{Li}$, which is a spin $I = \frac{3}{2}$ nuclide. The shift range for diamagnetic lithium compounds is relatively small and it is not always possible to distinguish between resonances of different compounds, e.g. in the SEI on battery electrodes.⁸⁶ However, the ${}^7\text{Li}$ NMR spectra of most battery materials are strongly affected by larger shift interactions

that include the hyperfine interaction for paramagnetic materials and the Knight shift for metals.¹²⁴

The unpaired electron spins in paramagnetic materials, such as in many lithium-containing cathodes, couple to the nuclear spins through the hyperfine interaction that can lead to large NMR shifts (Fermi contact shift).¹²⁵ The Knight shift is an interaction of the nuclear spins with the conduction electrons in metals (and other conductive materials) and will be described in more detail below. Quadrupolar nuclides (i.e., those with $I > \frac{1}{2}$) possess a nuclear quadrupolar moment, Q , that interacts with the electric field gradient (EFG) at the nucleus to give the quadrupolar coupling. The nuclear quadrupolar moment for the lithium isotopes it is relatively small, -0.0808 fm^2 for ${}^6\text{Li}$ and -4.01 fm^2 for ${}^7\text{Li}$.¹¹⁹ The smaller quadrupolar moment of ${}^6\text{Li}$ generally results in higher chemical resolution compared to ${}^7\text{Li}$. However, ${}^7\text{Li}$ has much higher natural abundance (92.5%) and higher gyromagnetic moment that result in higher sensitivity and thus is often the nuclide of choice when studying lithium batteries by NMR.¹²⁴

3.2 NMR of Metals

A paramagnetic system is defined as a molecule or a material that contains one or more ‘paramagnetic centres’, which are atoms or ions that have at least one unpaired electron.¹²⁵ The hyperfine interaction between the unpaired electrons and the observed nucleus can result in large shifts and additional broadening due to bulk magnetic susceptibility effects and rapid nuclear relaxation.¹²⁵ For metals, the conduction electrons couple to the nuclear spins resulting in the so-called Knight shift. Here will be given a brief overview of the theory relevant to the work presented in this thesis, with focus on the application of *in situ* NMR to Li metal.

3.2.1 Knight shift

Delocalized conduction electrons couple to the nuclear spins, causing a shift known as the Knight or the metallic shift which is useful for the study of the electronic structures of metals and other conductive materials.^{126,127} Here, the Knight shift of “simple metals” (with s- or p-conduction bands) will be described.¹²⁵

The Pauli paramagnetism or susceptibility of the delocalised conduction electrons is the source of the Knight shift in metals. The conduction electrons do not have discrete spin states, but rather occupy a band of spin states that are partially filled with spin up and spin down electrons, following the Pauli exclusion principle up to the Fermi level.^{128,129} When no magnetic field is applied (i.e., $B_0 = 0$) the populations of the spin-down and spin-up are equal and there is no effective magnetic moment from these electrons (Figure 3.2).

The magnetic moment is induced in a magnetic field, when $B_0 \neq 0$. The up and down spin states shift in energy, and the number of electrons in the up and down bands adjust so they share a common Fermi level (Figure 3.2). The populations of the spin bands have changed, which results in a net magnetic moment that augments the magnetic field known as Pauli paramagnetism. The net magnetization has a linear response to the magnetic field and is independent of temperature.¹²⁸ The temperature independence is a characteristic of Pauli paramagnetism, which is often referred to as temperature independent paramagnetism (TIP).

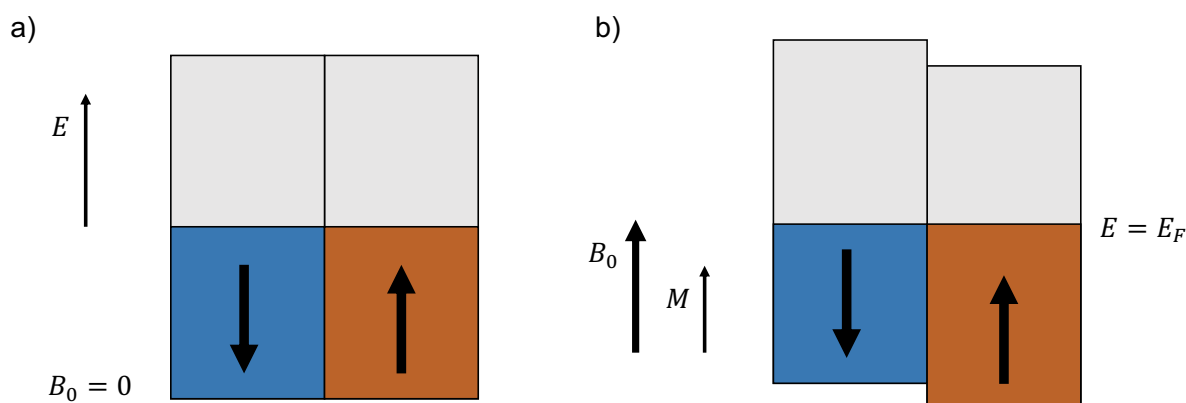


Figure 3.2 The spin bands of the conduction electrons plotted against energy. **a)** When there is no applied magnetic field, the population of electrons is equal in the up and down spin bands. **b)** In an applied magnetic field, the population of electrons will adjust to make the energies equal at the Fermi level, E_F . This results in a net magnetization, M . The schematic is reproduced from reference [87].

The Knight shift is defined as:^{125,130}

$$K = -\frac{\Delta B}{B_0} = \frac{2}{3} \langle |\phi(\mathbf{0})|^2 \rangle_{E_F} \chi_p V \quad (3.5)$$

with $\langle |\phi(\mathbf{0})|^2 \rangle$ being the average one-electron spin density over all the electronic states at E_F , the Fermi level. χ_p is the Pauli susceptibility of the conduction electrons per unit volume and

V is the atomic volume. K describes the fractional change in the gyromagnetic ratio that contributes to a constant offset to the resonance frequency, $B_{0,\text{eff}} = B_0(1 + K)$.¹³⁰

The Pauli susceptibility refers to the susceptibility of the electrons at the Fermi level and is proportional to μ_B the Bohr magneton and $N(E_F)$, the density of states at E_F .^{125,131}

$$\chi_p \propto \mu_B^2 N(E_F) \quad (3.6)$$

The Knight shift of materials is thus a valuable tool for studying the local behaviour of conduction electrons at the Fermi level at different atomic sites.^{128,131} The experimental Knight shift at room temperature for ${}^7\text{Li}$ metal is $K_{\text{Li}} = 0.026$ compared to $K_{\text{Na}} = 0.11$ for ${}^{23}\text{Na}$.^{128,131}

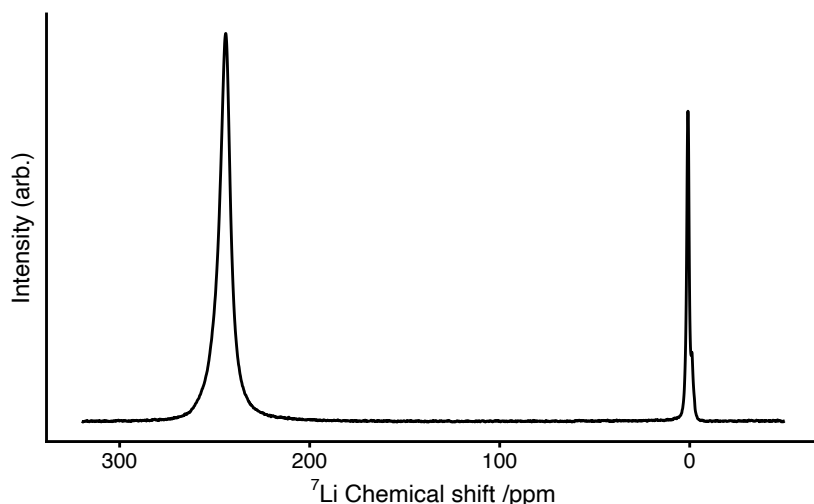


Figure 3.3 A typical ${}^7\text{Li}$ NMR spectrum of a symmetrical Li-Li *in situ* cell, showing the diamagnetic electrolyte/SEI peak around 0 ppm and the Li metal peak at around 245 ppm.

Due to the Knight shift, the resonance of Li metal is easily resolved from other lithium-containing components in the cell due to the metallic shift, the Knight shift, of lithium metal. Figure 3.3 shows a typical ${}^7\text{Li}$ NMR spectrum for an *in situ* cell, containing Li metal and Li^+ electrolyte. The Li metal is shifted to approximately 245 ppm due to the Knight shift and the resonances from the diamagnetic environments (Li^+ ions in the electrolyte and in the SEI) appear around ± 10 ppm. The electrolyte signal is usually sharp due to the rapid molecular motions which serves to average the anisotropic NMR interactions.¹²⁷

Furthermore, NMR studies of structural changes in battery anodes have been facilitated by the Knight shift. As lithium is intercalated into graphitic carbon, a distinct shift of the intercalated

Li signal is seen for the different stages during charge (and increased Li content) due to the metallic nature of LiC_x .¹³² The charge storage mechanism for sodium insertion into hard carbon was similarly studied by NMR, where a shift to higher frequencies is observed at low voltages indicative of the increasing metallic character of the material due to the formation of sodium clusters.¹³³ In a recent study, a greater metallic character of the quasi-metallic peak of sodiated hard carbon was correlated with the increasing pore size of hard carbon that allows for the growth of larger metallic sodium clusters within the pores.¹³⁴

3.2.2 Bulk magnetic susceptibility

In addition to local interactions, the macroscopic magnetic properties of a system, the bulk magnetic susceptibility (BMS), can affect the shift of resonances and lead to additional broadening of peaks in the NMR spectrum.¹³⁵ When a sample of a finite size is placed in a magnetic field, the interaction between the field and the magnetic moment of the sample induces a magnetic field, referred to as the demagnetizing field.¹³⁶

The magnetization M_d is defined as the magnetic moment per unit volume and depends on the magnetic susceptibility of the sample, χ , its' macroscopic shape and orientation with respect to the applied magnetic field.^{128,137} The magnetic susceptibility χ is a dimensionless quantity and expresses how readily the material develops a magnetic moment when placed in a magnetic field. For diamagnetic materials, $\chi < 0$, the demagnetizing field opposes the static external field. For paramagnetic materials, $\chi > 0$, the induced field adds to the external field. The susceptibility is often defined in terms of a mole of the substance (χ_M) or the volume of the substance (χ_V).

When the magnetic properties of the medium are linear, isotropic and homogeneous, the magnetization is directly proportional and parallel to the applied magnetic field:¹³⁶

$$M_d = \frac{\chi B_0}{\mu_0} \quad (3.7)$$

where μ_0 is the permeability of vacuum, $4\pi \times 10^{-7}$ H/m. The relationship described in equation (3.7) is not always valid. For anisotropic materials, such as solids and liquid crystals, the induced magnetic moment is not necessarily parallel to the external field and the magnetic susceptibility is represented by a susceptibility tensor.¹²⁷ The effect is known as the anisotropic

bulk magnetic susceptibility (ABMS).^{125,135} A shift in the NMR resonance arises when the magnetic susceptibility is anisotropic.^{135,138}

Bulk magnetic susceptibility calculations are performed by representing the spatial susceptibility distribution of the system in a three-dimensional matrix where equation (3.7) becomes:¹³⁹

$$M_d = \frac{\chi(r) B(r)}{\mu_0} \quad (3.8)$$

The susceptibility effects on a local magnetic field include the magnetization term and the indirect susceptibility effects, that includes the influence of the magnetization at all points in the sample.¹⁴⁰ By using a three-dimensional Fourier transformation of the distribution, the local magnetic field can be calculated at each position by the approach of Salomir et al.^{139–141}

In situ NMR measurements of batteries are performed under static conditions and significant BMS effects are typically observed due to the different metallic and paramagnetic components.^{135,137} Distortions to the field can result in inhomogeneous broadening of the NMR spectrum, which decreases resolution. The shift and the width of the resonances depend on a complex and additive effect from all of the different battery components, container shape, density, and orientation in the magnetic field.^{137,142} Zhou et al. showed how the BMS shift can be removed by orienting the electrochemical cell so that the normal of the cell is at the ‘magic angle’ (54.7°) to the magnetic field.¹³⁷

Previous work has demonstrated the orientation-dependent shift of Li metal electrode caused by BMS effects, which is of great advantage when studying Li deposition.^{74,135} The resonance of a pristine Li metal electrode when oriented perpendicular to the magnetic field has a shift of 244 ppm and a shift of 272 ppm when parallel to the magnetic field (Figure 3.4).¹³⁵

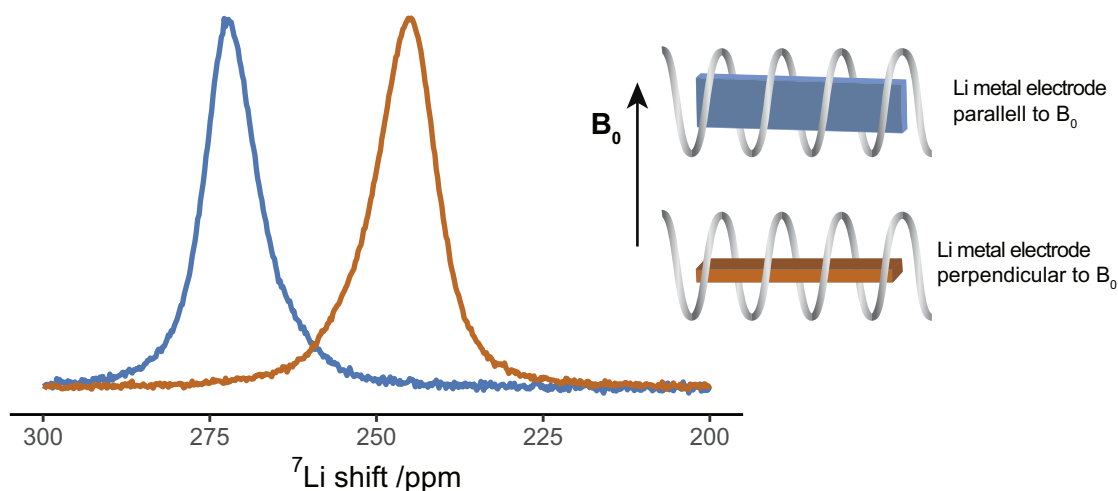


Figure 3.4 Experimental NMR spectra showing the bulk magnetic susceptibility effects on the ^7Li metal shift. Due to the bulk magnetic susceptibility of Li metal, an orientation dependence is seen when placing a Li metal foil in the magnetic field, with a shift at 272 ppm (blue) when the electrode is placed parallel to the B_0 magnetic field, and a shift at 243 ppm (orange) when placed perpendicular to B_0 .

Bhattacharyya et al. showed how the ^7Li shift of plated Li microstructures is shifted by approximately 15 ppm from the bulk Li metal, to 260 ppm (Figure 3.5) due to the same BMS effect.⁷⁴ Thus, the NMR spectrum of electrodeposited Li can be deconvoluted into ‘bulk metal’ and ‘microstructure’ peaks (Figure 3.5), which allows for quantification of Li microstructures during plating described in detail in section 3.2.4.^{74,76}

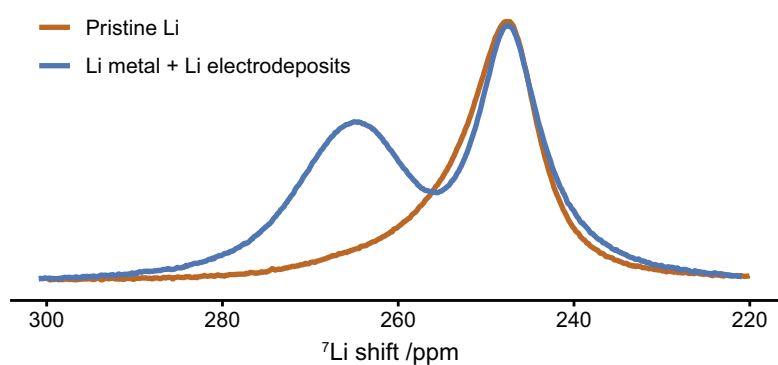


Figure 3.5 A typical *in situ* ^7Li NMR spectra of a symmetrical Li-Li cell showing the pristine Li metal peak at around 245 ppm (in orange) and the Li metal peak after plating (in blue) with the additional peak at around 260 ppm corresponding to Li microstructures.

Later, Chandrashekar et al. showed with MRI how the ^7Li shift can be used to distinguish between microstructures growing close to the Li metal (at around 260 ppm) and dendritic structure extending further away from the surface (at around 270 ppm).⁷⁶ The microstructures showed a wide shift range, ascribed to the disorder in orientation of these mossy structures with respect to the B_0 field. This was later confirmed by susceptibility calculations performed by Illott et al.⁷⁵ The results from reference 75 are reproduced here (Figure 3.6) for Li deposits on a Li metal electrode using the code written and provided by Dr. Andrew Illott (Bristol-Myers Squibb, previously at New York University).¹⁴¹

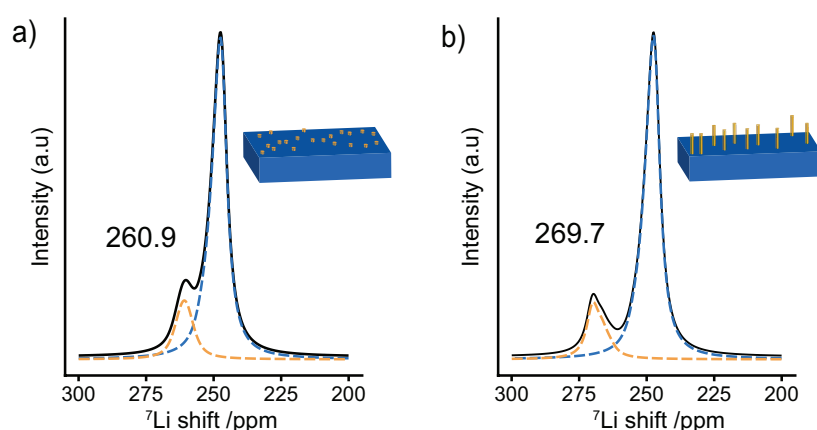


Figure 3.6 Simulated NMR spectrum of electrodeposits on Li metal from the susceptibility calculations of a pristine Li metal (in blue) and Li electrodeposits (in orange), the sum of the two shown in black. **a)** The simulated NMR spectrum with 20% coverage of Li microstructures (each microstructure is represented in a single voxel as illustrated in the inset) and **b)** of Li dendrites with 2.5% coverage (each dendrite is represented in $1 \times 1 \times 8$ voxels as illustrated in the inset), which reproduces the results found in reference [75] with the shift of mossy microstructures at around 260 ppm and around 270 ppm for dendrites.

Following previous study, the Li microstructures are represented by a single voxel randomly placed on the electrode surface with the surface coverage set to 20%, which results in a shift of 261 ppm (Figure 3.6a).⁷⁵ Li dendrites were simulated by creating $1 \times 1 \times 8$ voxels randomly placed perpendicular to the electrode's surface (as shown in the inset, Figure 6.12b) and the surface coverage set to 2.5% (for them to occupy the same volume as in the simulation of microstructures).⁷⁵ The shift of the dendrites is 270 ppm (Figure 3.6b) as a result of the BMS effects and agrees well with the experimental observations by Chandrashekar et al.^{33,75,76} The calculations are described in more detail in section 6.2.4 and 6.3.3.

3.2.3 Skin depth of metals

The reciprocity principle for NMR, described by Hoult, explains how the received field detected in the rf coil is proportional to the transmitted magnetization of the sample.^{121,143} The detected signal strength is thus proportional to magnetization of the sample in the transverse plane:

$$S \propto \mathbf{B}_1 \cdot \mathbf{M}_{xy} \quad (3.9)$$

However, the rf-field used to excite the nuclear spins penetrates good conductors only up to a certain depth due to skin effects and the induced current will vary at different points in the sample.¹²¹ For an rf-field of strength ω_1 , the field inside the metal at depth x from the surface decays exponentially according to:

$$\omega_1(x) = \omega_1(0)e^{-\frac{x}{d}} \quad (3.10)$$

where d is the skin depth. The skin depth for a field at frequency ν is:¹²⁸

$$d = \sqrt{\frac{\rho}{\pi\mu_0\mu_r\nu}} \quad (3.11)$$

where ρ is the resistivity of the metal (94.7 n Ω for Li metal at 298 K), μ_0 is the permeability of the vacuum ($4\pi \cdot 10^{-7}$ m kg s⁻² A⁻²), μ_r is the relative permeability of the medium ($\mu_r = 1.4$ for Li metal) and ν is the frequency of the applied rf-field.¹⁴⁴

Due to the depth-dependant strength of the rf-field in equation (3.10) the flip angle experienced by the Li spins in the surface layers of the bulk Li metal is not constant (as described in equation (3.3)).^{121,141,145} Due to this, the signal intensity does not follow a simple sinusoidal function when performing a ‘nutaton experiment’ as observed for samples that do not experience skin depth effects (see section 3.1).^{146,147}

The signal intensity from a metallic sample as a function of the rf excitation pulse can be calculated by making use of the reciprocity principle and computing the volume integral over the contributions from different points in the sample following the approach of Chandrashekar

et al.^{76,141,143} The signal intensity S obtained for a surface area A of a metal sample depends on the rf-field strength according to (3.10) and the pulse duration τ_p :

$$S = \frac{A s_0}{\omega_1(0)} \int_0^\infty dx [\omega_1(x) \sin(\omega_1(x)\tau_p)] \quad (3.12)$$

where s_0 is the signal intensity per unit volume of metal.^{76,141} Inserting equation (3.12) into equation (3.10) and computing the integral results in:

$$S = \frac{A s_0 d}{\omega_1(0)\tau_p} (1 - \cos(\omega_1\tau_p)) \quad (3.13)$$

According to (3.13), the maximum signal obtained for a pristine Li metal electrode corresponds to a flip angle of $\omega_1(0)\tau_p \approx 2.32$ rad or roughly 133° (instead of the typical 90° pulse for non-metallic sample).

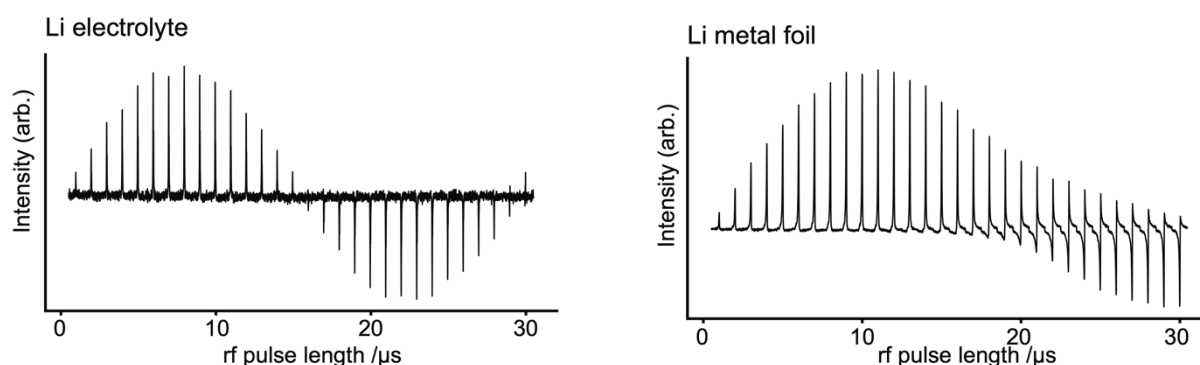


Figure 3.7 The experimental ^7Li nutation curve of the electrolyte and Li metal in an NMR *in situ* cell containing $75 \mu\text{L}$ 1 M LiPF_6 in EC:DMC, glass fibre separator and two pieces of Li metal foil.

The ^7Li NMR signal measured by a nutation experiment as a function of flip angle is shown in Figure 3.7, by acquiring a series of spectra with varying pulse duration τ_p . The nutation curve of the electrolyte signal in an NMR *in situ* cell (1 M LiPF_6 electrolyte in EC:DMC) shows the expected sinusoidal curve, where the 90° pulse gives the maximum signal intensity for $\tau_p = 7.4 \mu\text{s}$ (Figure 3.7a). However, for a rectangular piece of a pristine lithium metal the nutation

curve was obtained and has a maximum in signal intensity around 10.6 μs as expected (Figure 3.7b).

3.2.4 Quantification of metals

Due to skin depth effects, NMR is sensitive to the total surface area of a Li electrode.^{74,135} The increase in signal intensity of ^7Li metal upon cycling can thus be attributed to the formation of high surface area deposits where the signal intensity is directly proportional to the volume of Li metal excited by the radio-frequency (rf) field.^{74,76}

The theory used to quantify the amount of Li deposits is based on previous work by Bhattacharyya et al. and Chandrashekar et al.^{74,76} During Li deposition, total Li metal intensity $S(t)$ measured by NMR increases due to the formation of microstructures:

$$S(t) = S_{metal}(t) + S_{micro}(t) \quad (3.14)$$

Where the S_{metal} is here defined as the signal from the bulk Li metal (described by equation (3.13)) with a known surface area A and described by equation (3.13). The volume of Li microstructures (assuming the thickness of the microstructures to be less than the skin depth) can be fully excited by the rf-field and the signal intensity is thus described by:⁷⁶

$$S_{micro}(t) = V_{\mu}(t)s_0 \sin(\omega_1(0)\tau_p) \quad (3.15)$$

where $V_{\mu}(t)$ is the volume of the microstructures, changing with time during the electrochemical deposition. Before plating, $S_{metal}(t) = S_{metal,0}$ the peak of the pristine Li metal prior to electrodeposition is used to determine the signal intensity per unit volume of metal, s_0 , according to equation (3.13). Equation (3.14) becomes:

$$S(t) = S_{metal,0} + V_{\mu}(t)s_0 \sin(\omega_1(0)\tau_p) \quad (3.16)$$

And the volume of deposited microstructures is described by:

$$V_{\mu}(t) = \frac{S(t) - S_{metal,0}}{s_0 \sin(\omega_1(0)\tau_p)} \quad (3.17)$$

Integration of the Li metal peak measured by NMR during plating and stripping, that is $S(t)$, can now be used to quantify the volume of microstructures formed and readily converted to the amount of microstructure deposited. The density of lithium at room temperature is $\rho = 0.53 \text{ g/cm}^3$ and the total mass of microstructures:

$$m(t) = V_{\mu}(t) \times \rho \quad (3.18)$$

3.3 *In situ* NMR

3.3.1 *In situ* NMR studies of Li metal

Both *in situ* NMR spectroscopy and magnetic resonance imaging (MRI) have been widely used to study lithium-ion and lithium metal batteries.^{33,74–76,79,132,148} The initial NMR study on Li metal deposition by Bhattacharyya et al. developed the methodology to quantify the Li microstructures.^{74,76} Chandrashekar et al. used ^7Li MRI and showed that the shift of Li metal can be used to distinguish between electrodeposits growing close to the Li metal (at around 260 ppm) and dendritic structure extending further away from the surface (at around 270 ppm).⁷⁶ This was later confirmed in a detailed study by Chang et al., where different resonances in the *in situ* NMR spectra were correlated with SEM images of Li microstructure morphology formed under different stack pressures and using different separators.⁷⁵ Overall, the study by Chang et al. demonstrated how *in situ* NMR can track the Li metal morphology in real time.⁷⁵ MRI was used by Chang et al. to observe the build-up of concentration gradients in a Li^+ electrolyte during a constant current experiment. The authors were able to directly correlate the onset time of Li dendritic growth with changes in the electrolyte concentration gradient. The onset of dendrite growth for Li metal was shown to correlate with ‘the Sand’s time’, the time when the concentration at the electrode surface reaches zero.

In this thesis the methodology previously developed to quantify Li microstructures will be used with the focus on understanding the effect of the SEI on Li deposition using relatively low current densities and under different electrochemical conditions (Chapter 4). In Chapter 6, the methodology to study dead Li formation in an anode-free cell, where there is no Li metal

present in the cell, is developed. Furthermore, the BMS effects become important to consider when the paramagnetic LiFePO_4 (LFP) cathode is present. Both the BMS effects of the Li metal deposits on Cu as well as the effects LFP has on the diamagnetic electrolyte peak will be studied.

3.3.2 Experimental considerations

As mentioned in section 3.2.2, BMS effects can be largely ignored under MAS conditions. For static *in situ* NMR however, BMS effects can greatly influence the resolution and shifts of the resonances in the spectrum. Furthermore, eddy currents can be induced in the conducting components such as the current collectors and metals of interest on the application of the rf-pulses, which can modulate the strength of the rf-field and result in quantification errors. Those are apparent in MRI due to the application of strong magnetic field gradients.¹⁴⁹ The eddy currents depend on the sample shape and the orientation with respect to the rf-field. Aligning the metal electrodes in the rf-coil so they are parallel to the rf field direction, minimizes these distortions.^{141,150}

Other artefacts that can influence both the *in situ* NMR spectrum and the electrochemistry are interferences between the electrochemical circuit and the rf-circuit. The rf-circuit in the NMR probes used throughout this thesis are designed so they are shielded and do not interfere with the environment outside the rf coil. Having an electrochemical cell inside the rf coil can introduce significant noise into the NMR spectrum as the electrochemical circuit acts as an antenna which can intercept undesired radio signals from the environment.¹⁵¹ To overcome these issues, low pass filters are connected at the ports on the probe-head for the electrochemistry. The low pass filters allow the direct current from the potentiostat to pass but removes any unwanted alternating-current noise.^{123,151}

Changing sample conditions can further influence the rf-circuit, and recalibration of the circuit is often necessary. The Automatic Tuning Matching Cyclor (ATMC) NMR probe-head (designed by Oliver Pecher, Clare Grey and NMR Service GmbH) enables the re-tuning of the rf-circuit in between NMR experiments during the electrochemistry and allows for a more careful quantification of NMR signals.¹⁵¹ A PEEK capsule cell is used for all *in situ* battery testing in this work, shown in Figure 3.8.



Figure 3.8 Photos of the *in situ* PEEK capsule cell used throughout this work. Cu current collector (or Al current collector) is threaded into the cell and sealed with o-rings. Inside the cell, an electrode-separator/electrolyte-electrode stack is made in between the current collectors and the system kept intact by the cylindrical capsule. See further details on cell assembly in the following reference.¹²³

Chapter 4 *In situ* NMR Studies of Lithium Metal Plating

4.1 Introduction

The search for higher energy density rechargeable lithium batteries has created a renewed interest in Li metal anodes. Li metal has the highest volumetric and gravimetric energy density of all negative electrodes, however, it suffers from both capacity fading and safety issues.^{152,153} The uneven electrodeposition of Li on the metal anode results in high surface area microstructures that can ultimately lead to potentially hazardous situations such as cell short-circuiting and thermal runaway. The microstructures formed under Li deposition can exhibit a wide range of morphologies including needle, whisker, bush-like, mossy and fractal dendrites.^{20,21} A detailed understanding of the parameters that dictate the different growth modes of microstructural Li is necessary to develop effective strategies to mitigate microstructural growth and to enable the use of Li metal anodes in batteries.

Dendrite growth is described by the theory of mass transport (see section 2.3.3.1) and predicted to occur at a characteristic time referred to as Sand's time (equation (2.21)). The onset of dendrite growth on Li metal has been shown experimentally to correlate with Sand's time.^{33,102} According to that theory however, dendrite growth is not expected at current densities below the limiting current density j_{lim} (equation (2.20)).^{15,16} However, irregular microstructural growth occurs in most cases and has been associated with local inhomogeneities on the Li metal surface or in the SEI where preferential deposition sites result in so-called "hot spots" with high local current density.^{20,24,33-35} These preferential deposition sites can originate from inhomogeneous transport properties in the SEI or cracks in the SEI giving rise to mossy and/or whisker-like structures.³⁶⁻³⁹

The morphology of Li deposits and the cycling performance is highly dependent on the choice of electrolyte system where improved cycling efficiencies are generally attributed to a uniform and highly ionic conductive SEI.^{24–29} Thus, the main approach to tackle inhomogeneous Li deposition has been the development of a suitable liquid electrolyte system, by controlling the type of solvents, salts, and additives, and by varying the salt concentrations, with the goal of manipulating the corresponding chemical composition of the SEI. A fundamental question to address is how the nature of the SEI on Li metal affects the plating and stripping on Li metal anodes, in order to systematically tackle microstructural growth. Here we study the effect of the common fluorinated additive FEC, which has been shown to improve the CE of Li deposition in the standard carbonate electrolyte.^{29,45,154–156} Many studies have highlighted the differences in the chemical composition of this SEI: X-ray photoelectron spectroscopy (XPS) studies have reported increased fluorine content in the SEI formed with FEC,⁸² and a LiF-rich SEI.⁴⁵ Others have reported that Li plating with and without FEC results in a similar morphology, but a more ordered SEI is formed with FEC that results in homogeneous Li stripping.^{83,157} The challenge now is to identify why these differences alter the deposition and stripping performance, motivating further fundamental studies.

In this chapter, *in situ* NMR is used to study the differences in plating behaviour in two electrolyte systems; the standard carbonate electrolyte 1 M LiPF₆ in ethylene carbonate and dimethyl carbonate (EC:DMC 1:1 v/v, referred to as LP30) and the same electrolyte with the FEC additive (LP30 + FEC). Symmetrical Li-Li cells were operated below j_{lim} where fractal dendritic growth is not expected, in order to study the mossy and microstructural growth of Li.

Bhattacharyya et al. developed a method to quantify and distinguish between different types of microstructures that form during Li deposition based on the skin depth effect of conductors and the bulk magnetic susceptibility (BMS) of Li metal in a magnetic field.⁷⁴ As electromagnetic waves penetrate metals to a certain depth called the skin depth, NMR is sensitive to the total surface area of the Li electrode.^{74,135} The increase in signal intensity upon cycling can thus be attributed to the formation of high surface area structures.

We show that under constant current in LP30 + FEC the microstructures form a compact layer on the electrode surface with high current efficiency compared to a more open whisker-like growth for LP30. In addition, experiments were performed using pulse electrolysis, an electrochemical method that has been used to deposit a range of metals where the advantages

cited in the literature include improved control over the size of the metal deposits and less porous morphology.^{104–107,158} Previous studies on Li pulse plating have both demonstrated a smoother morphology and a less porous microstructural layer on the Li electrode.^{71,159–162} However, in order to study the effectiveness of Li pulse plating it is crucial to use a quantitative technique such as *in situ* NMR spectroscopy.

The work presented in this Chapter benefitted from the intellectual input of all the co-authors of the project, Sundeeep Vema, Svetlana Menkin, Lauren Marbella and Clare Grey. The current author performed all of the experimental work and data analysis. The main part of this chapter is published in the Journal of Materials Chemistry A, 2020, 8, 14975–14992.

4.2 Experimental Details

4.2.1 Materials

The electrolyte used was 1 M LiPF₆ in 1:1 v/v ethylene carbonate/dimethyl carbonate (EC/DMC; Sigma Aldrich, LP30). For experiments using an additive, fluoroethylene carbonate (FEC; Sigma Aldrich, 99%) was added to the electrolyte in 1:10 ratio by volume (LP30 + FEC). The water content of the LP30 electrolyte was measured with Karl Fischer titration and was < 40 ppm. For *in situ* NMR experiments, Li electrodes were prepared by cutting fresh Li from a Li rod (Sigma, 99.9% trace metal basis, 12.7 mm diameter) and rolled with an Al roller inside a plastic bag (polyester pouch, VWR) to an approximate thickness of 0.15 mm. This was done to try to minimise the native SEI on the Li metal before it is immersed in the electrolyte. In all coin cells, pre-cut lithium metal disks (LTS research, 99.95%) were used. The materials were stored and handled in an Ar atmosphere glovebox (O₂, H₂O < 1 ppm, MBraun).

4.2.2 Cell fabrication

All cell assembly and disassembly was performed in an Ar atmosphere glovebox (O₂, H₂O < 1 ppm, Mbraun). The design and assembly of the *in situ* capsule cell (made from polyether ether ketone, PEEK) has been described before.¹²³ The capsule cell provides a constant pressure across the cell and a similar pressure for all the experiments, which gives an increased reproducibility between *in situ* experiments compared to earlier work on plastic bag-cells.¹³⁵

The Li rod was rolled as described above and cut into a rectangular electrode with a razorblade, dimensions around 4 mm \times 13 mm. Two separators were used between the Li electrodes, both a glass microfiber separator (Whatman, thickness = 0.68 mm, dried under vacuum at 100°C) and a polypropylene-polyethylene separator (Celgard 3501). The glass separator is used to decrease BMS effects by increasing the distance between the electrodes³⁵ and the polymer separator makes it possible remove the electrodes gently from the separator to study the Li morphology *ex situ*. The electrolyte consisted of 75 μ l of either LP30 or LP30 + FEC. Stainless-steel 2032 type coin cells (Cambridge Energy Solutions) with a conical spring and two 0.5mm thick spacer disks were assembled with the pre-cut Li disks described above, glass microfiber separator (Whatman) and 75 μ l of either LP30 or LP30 + FEC.

4.2.3 Electrochemical measurements

Electrochemical measurements were performed using a Biologic VSP potentiostat with EC-Laboratory software. For symmetrical Li-Li *in situ* cells, galvanostatic constant current or pulsed current was applied in a single direction. For the *in situ* cell setup in this study, the calculated limiting current density is $j_{lim} \sim 7$ mA/cm² (equation (2.20)). This is calculated assuming $D_{Li^+} = 1.70 \times 10^{-10}$ m² s⁻¹, the diffusion coefficient measured for the free electrolyte by PFG-NMR. However, the separator will influence the effective diffusion coefficient and the limiting current density will be slightly lower in the current setup.¹⁶³ However, the cells studied here, with the applied current densities 0.5-2 mA/cm² are expected to operate in the ‘low current regime’.³³ For symmetrical Li-Li coin cells, the cells were pre-conditioned for 5 cycles using 0.02 mA/cm² for a total capacity of 0.04 mAh/cm² followed by 10 cycles using 0.5, 1 or 2 mA/cm² for 2 mAh/cm². This was done to give reproducible starting electrode surface.

4.2.4 *In situ* NMR spectroscopy

In situ NMR measurements were performed on a Bruker Avance 7.1 T spectrometer, operating at a Larmor frequency of 300.1 MHz for ¹H and 116.6 MHz for ⁷Li. The spectra were recorded on a Bruker HX double resonance static probe with a solenoidal coil. The *in situ* capsule cell (described above) was aligned in a Ag-coated Cu solenoid coil such that the Li electrodes were oriented perpendicular to B_0 and parallel with respect to the B_1 rf field. For each cell, a series

of single pulse experiments were recorded continuously during the entire length of the electrochemical measurement. For ^7Li metal measurements, the pulse duration was chosen to give maximum intensity of the bulk Li metal (corresponding to a flip angle of 133° and $10.2\ \mu\text{s}$), a recycle delay of 1 s (T_1 of ^7Li metal ~ 100 ms) and 256 transients recorded. This resulted in an experimental time of ~ 4.5 min. The ^7Li signals were referenced to 1 M aqueous solution of LiCl at 0 ppm. The spectra were processed in Bruker Topspin software, using the automatic phase and baseline correction.

The deconvolution of the *in situ* NMR spectra was carried out in R using a homebuilt code published in reference [133]. Pseudo-Voigt curves are used and least-squares fitting with 3-4 peaks; two metal peaks (Metal peak 1 and 2), referred to as “bulk metal” and two microstructural peaks (Microstructure 1 and 2). Adding a second peak to fit the bulk metal is consistent with earlier work, the asymmetry of the peak assigned to the edges of the metal electrodes and inhomogeneities on the metal surface such as pitting.^{75,141,164} Adding a second microstructures peak (Microstructure peak 2) was only needed when using $2\ \text{mA}/\text{cm}^2$ in LP30 electrolyte and is assigned to microstructures growing relatively further away from the electrode’s surface. The fitting parameters are the height, position, width (half width half maximum, HWHM) and a ratio of the Gaussian/Lorentzian line shape. Constraints were added to the shift of the peaks, Metal peak 1: 245-247.5 ppm, Metal peak 2: 247.5- 252.5 ppm, Microstructure 1: 257.5-262.5 ppm and Microstructure 2: 267.5 – 272.5 ppm.

Data analysis was done using both dplyr and ggplot packages.¹⁶⁵ The theory developed by Bhattacharyya et al. was used to quantify the NMR signal of the Li metal and is described in detail in Chapter 3, section 3.2.4.⁷⁴ The skin depth of Li metal in this study is $d = 12.1\ \mu\text{m}$ (see equation (3.11)). All *in situ* measurements were performed at room temperature (293 K).

4.2.5 Pulsed-field gradient NMR spectroscopy

Pulsed-field gradient (PFG) NMR was performed with a MicWB40 probe inside a Micro2.5 triple axis gradient system at 298 K. A stimulated echo (STE) pulse sequence was used with a gradient pulse length of 2.5 ms, a diffusion time of 200 ms, a recycle delay of 3 s, number of transients 32, and 16 gradient steps ($3.2\text{-}146\ \text{G cm}^{-1}$). The data was fit to the Stejskal-Tanner equation using Bruker Topspin Software.¹⁶⁶ The gradient strength was calibrated by measuring the Li^+ diffusion coefficient of 0.25 M LiCl in water at 298 K, with the diffusion coefficient

set to $0.96 \times 10^{-9} \text{ m}^2/\text{s}$.¹⁶⁷

4.2.6 Scanning electron microscopy

After electrochemically plating, the *in situ* cells were transferred into an Ar glovebox, disassembled and mounted onto the SEM stage of the transfer module (Kammrath & Weiss, type CT0) and dried under vacuum. The electrodes were not rinsed with a solvent. The samples were transferred into the SEM chamber using the air-sensitive transfer module under an inert atmosphere (Ar), without being exposed to air. SEM images were acquired with a Tescan MIRA3 FEG-SEM instrument at an acceleration voltage of 5.0 kV.

4.3 Results

4.3.1 Constant plating with and without an additive

In situ NMR was performed to study Li deposition in LP30 and LP30 + FEC. Figure 4.1a shows the ^7Li *in situ* NMR spectra continuously acquired during a constant current experiment. The resonance from Li metal depends on the orientation of the Li metal anode strip with respect to the static magnetic field, \mathbf{B}_0 , due to Li metal's temperature independent paramagnetism (TIP).^{74,135} Aligning the cell perpendicular to the \mathbf{B}_0 field results in a ^7Li resonance at around 245 ppm for the pristine Li metal⁷⁴ (Figure 4.1a) and all *in situ* cells presented in this chapter were aligned in this fashion.

When depositing Li in both LP30 and LP30 + FEC, a new peak around 260 ppm emerges that continues to grow as a current of $0.5 \text{ mA}/\text{cm}^2$ is passed (Figure 4.1a). This new resonance is indicative of mossy structures growing near to the Li metal surface.^{74,76} Whisker-like morphologies are observed in the SEM micrographs as the major morphology after plating for $3.5 \text{ mAh}/\text{cm}^2$ in LP30 electrolyte, whereas dense, thick buds (diameter of surface features $\sim 5\text{-}10 \text{ }\mu\text{m}$) are observed for LP30 + FEC (Figure 4.1c).

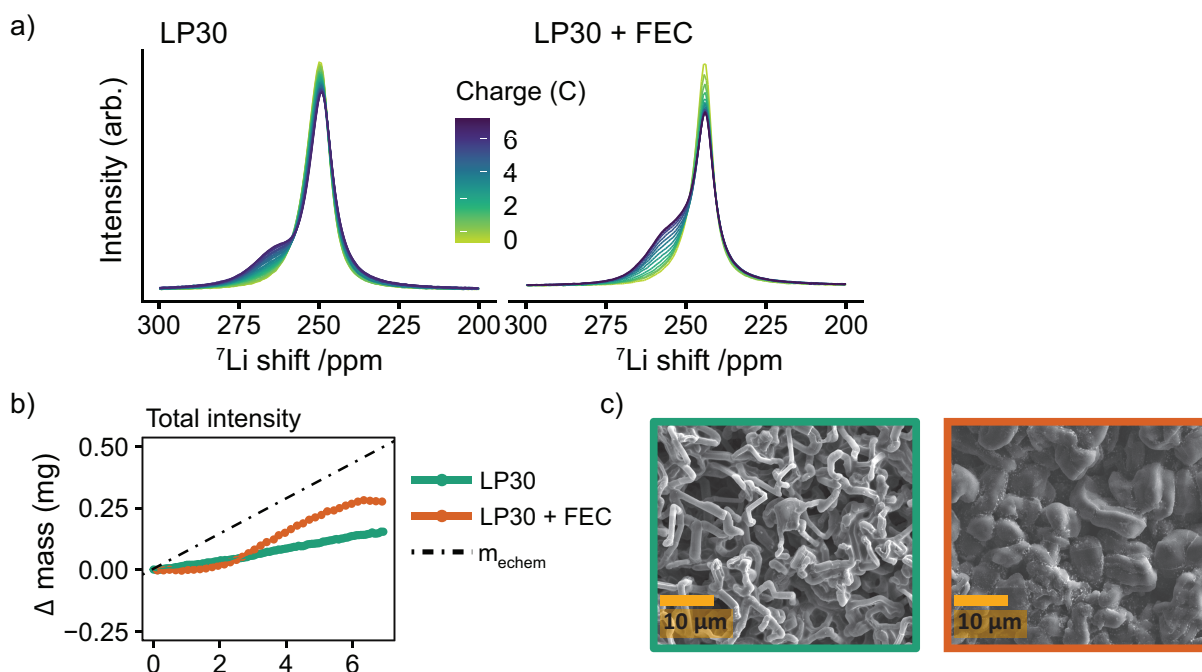


Figure 4.1 **a)** *In situ* NMR spectra obtained under a constant current of 0.5 mA/cm² in LP30 and LP30 + FEC. **b)** The total integrated intensity detected by NMR converted into mass change (mg) for a constant current of 0.5 mA/cm² in LP30 (green) and LP30 + FEC (orange). **c)** SEM images of the microstructures formed during 0.5 mA/cm² constant current in LP30 (left) and LP30 + FEC (right).

The overall increase in the ^7Li NMR signal intensity for Li metal can be attributed to the formation of high surface area deposits where the signal intensity is directly proportional to the volume of Li metal excited by the radio-frequency (rf) field (as described by (3.16)) due to the fact they are smaller in diameter than the skin depth of 12 μm .^{74,76} The change in the total integrated intensity between 220-280 ppm, termed “total intensity”, was converted into the mass change (i.e., the change in the Li mass detected by NMR spectroscopy.), Δ mass (Figure 4.1b).

The quantification of the NMR signal followed the theory developed by Bhattacharyya et al. and is described in detail in section 3.2.4.^{74,76} Δ mass is then plotted against charge passed (in C, coulombs) in order to compare it to the total amount of mass of Li deposited based on the electrochemistry, $m_{\text{echem}} = 0.072$ mg/C (Figure 4.1b). m_{echem} was calculated by Faraday’s law of electrolysis for the ideal case without considering the Coulombic losses associated with the formation of the SEI, the competing reaction to Li metal deposition:

$$m_{echem} = \frac{Q M}{F n} \quad (4.1)$$

where n is the number of electrons consumed in the reaction, M is the molar mass, F is the Faraday constant and Q is the charge passed in the cell. The charge (Figure 4.1) corresponds roughly to 3.5 mAh/cm² (the slight differences between cells arising from small variations in electrode area).

For both electrolyte systems, the mass increase calculated from the total intensity is lower than that expected from the applied electrochemistry (Figure 4.1b), i.e., $m_{\text{NMR}} < m_{\text{echem}}$. There are three possible scenarios that can account for this. In the first scenario, part of the Li is plated as a smooth deposit and does not result in an increased intensity of the Li signal, since it does not change the overall Li metal surface area. This is due to the skin depth effect of metals, where the rf field penetrates only the surface of the metal, $\sim 12 \mu\text{m}$ for Li, (note that the diamagnetic SEI does not impede rf penetration).⁷⁴ In the second scenario, the growth of dense Li metal microstructures may also lead to an attenuation of the rf signal and poor excitation of the underlying bulk film.^{75,80} Third, the competing reduction reaction, SEI formation, results in lower Li metal deposition than expected based on the current passed, i.e., lower current efficiency (Faradaic efficiency). To gain more insight into the morphological changes on the electrodes, as well as the causes of $m_{\text{NMR}} < m_{\text{echem}}$, spectral fittings were performed to determine how the relative fractions of the peaks assigned to Li microstructures vs. “bulk metal” change upon plating.

4.3.1.1 Deconvolution of the NMR spectra

The spectra were deconvoluted by using two peaks around 245-252.5 ppm (“bulk metal”) and one peak at around 257.5-262.5 ppm corresponding to the microstructural peak (Figure 4.2d).⁷⁵ For the LP30 + FEC electrolyte, the initial increase in microstructure intensity is compensated by a concurrent decrease in the metal intensity (Figure 4.2b and c, orange), both corresponding roughly to m_{echem} (i.e., the decrease of metal signal is -0.07 mg/C and increase in microstructural intensity $0.08 \text{ mg/C} \sim m_{\text{echem}}$) and thus the total signal intensity (total volume of Li detected by NMR) (Figure 4.2a, orange) stays almost constant. This is ascribed to an

attenuation of the rf field by the thick microstructures formed in LP30 + FEC (Figure 4.1c), so that the rf field penetration into the bulk metal is less than that for the initial Li film.

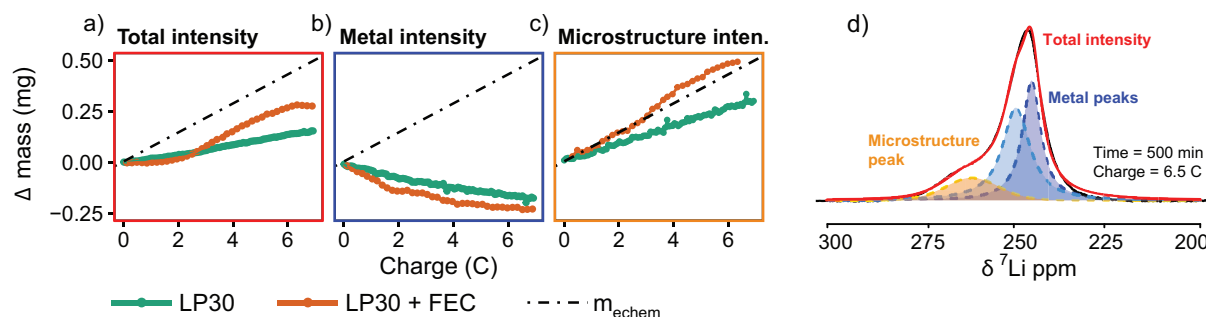


Figure 4.2 The integrated intensity detected by NMR converted into mass change (mg) for the **a)** the total intensity **b)** the metal intensity and **c)** the microstructural. The dashed line indicates m_{echem} , the mass deposited calculated based on the electrochemistry. **d)** An example of how the spectra for the LP30 electrolyte were deconvoluted into two overlapping metal peaks and one microstructural peak.

The intensity of the bulk metal peak in the LP30 electrolyte similarly decreases with charge (Figure 4.2b, green), but now the steady intensity increase of the microstructure peak is lower than that observed for LP30 + FEC, corresponding to only 0.053 mg/C, i.e., approximately 74% of what is expected by the electrochemistry. This is attributed to poorer current efficiency (Faradaic efficiency, the amount of charge used to deposit Li metal) as a result of the higher surface area Li whiskers formed in the LP30 electrolyte, as compared to the dense buds formed in LP30 + FEC, coupled with the larger extent of SEI formation on freshly exposed surface.

Of note is that previous work has shown both experimentally and with simulations that dendrites and structures growing away from the Li metal surface give rise to larger shift around 270 ppm compared to microstructures close to the surface.^{75,76} In the current study, the *in situ* PEEK capsule cell applies constant pressure within the cell and more compact structures form, leading to a narrower range of shifts.^{75,123} The ^7Li shifts of the microstructure peaks (Figure 4.3) are thus similar for both electrolytes although the microstructures have very distinct morphologies as seen in the SEM figures (Figure 4.1c).⁷⁹ Similar for both electrolytes is the shift to lower ppm values during the initial plating. This will be explored further in Chapter 6.

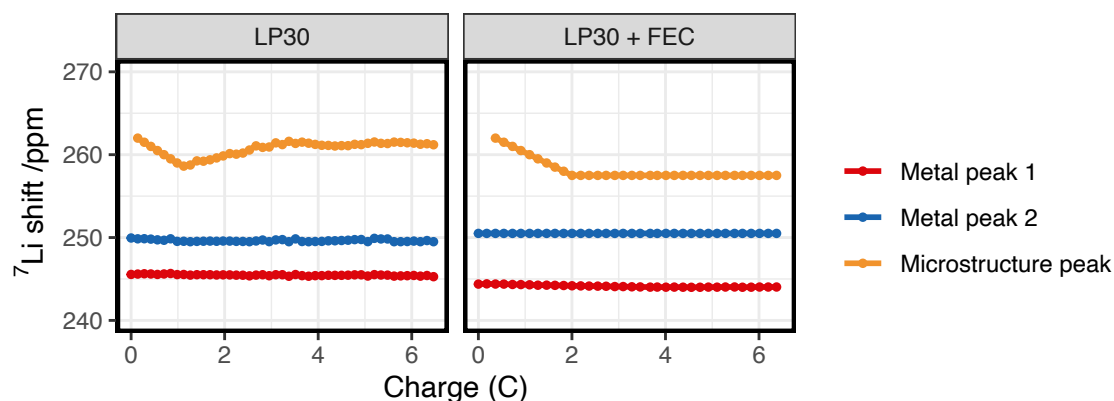


Figure 4.3 The ${}^7\text{Li}$ shift of the fitted peaks in the two electrolyte systems LP30 (left) and LP30 + FEC (right) during constant plating at 0.5 mA/cm^2 .

4.3.1.2 Higher current densities

To explore the effect of current density on both the plating efficiency and the resulting morphology *in situ* NMR measurements were performed at higher constant current densities of 1 and 2 mA/cm^2 . The quantified intensities of the deconvoluted peaks are shown in Figure 4.4. For a constant current of 1 mA/cm^2 , the bulk metal peak for LP30 + FEC electrolyte again decreases due to an attenuation of the signal (Figure 4.4b, orange), while the increase in the microstructural peak corresponds roughly to m_{echem} (Figure 4.4c, orange).

For the LP30 electrolyte, the bulk metal peak now stays close to constant indicating that more porous structures, growing away from the electrode's surface, are formed; these microstructures no longer shield the bulk metal leaving its the intensity detected by the NMR unchanged. Again, the total increase in intensity for LP30 electrolyte is less than m_{echem} , indicating that some of the charge is consumed to form the SEI.

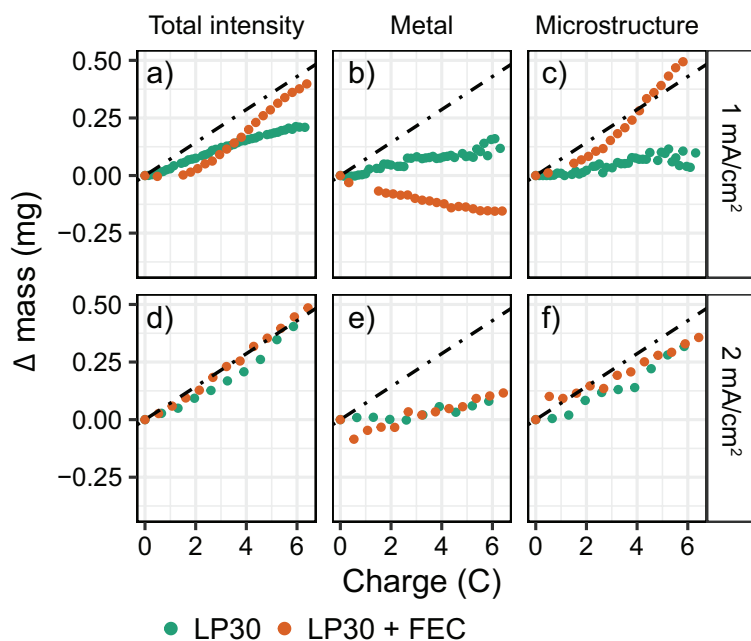


Figure 4.4 The quantified intensities of the fitted ${}^7\text{Li}$ metal peaks for the constant current experiments of **a-c**) 1 mA/cm² and **d-f**) 2 mA/cm² in the two electrolytes LP30 (green) and LP30 + FEC (orange). The dashed line indicates m_{chem} , the calculated mass deposited according to the current passed by the electrochemistry.

In contrast, for the higher constant current of 2 mA/cm², a close to constant intensity of the metal peak is observed for both electrolyte systems, with a slight increase occurring after passing 5 coulombs (3.25 mAh/cm², Figure 4.4e). Now m_{NMR} is only slightly lower than m_{chem} for both electrolytes, indicating a higher current efficiency for the LP30 electrolyte at 2 mA/cm². This is tentatively ascribed to the competing reactions of SEI formation and Li deposition where at higher overpotentials, electrodeposition of Li metal occurs more rapidly than the kinetically-limited degradation reaction involving the electrolyte species.⁶⁸ The morphology of the lithium deposits for the two electrodes is now very similar (Figure 4.5).

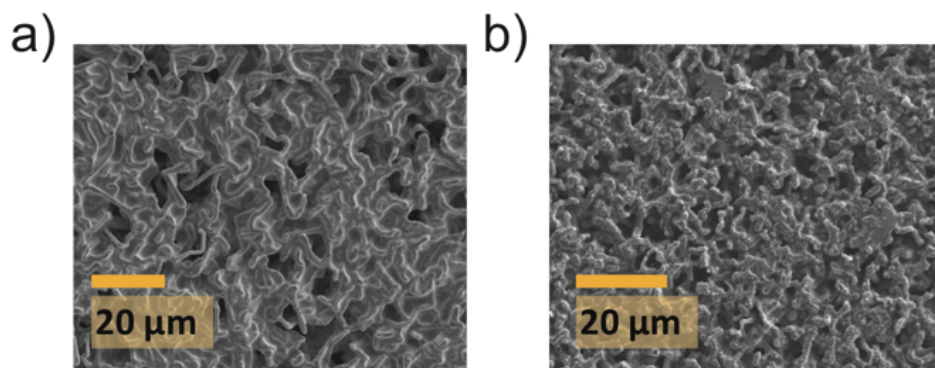


Figure 4.5 SEM images of the microstructures formed during 2 mA/cm^2 constant plating in a) LP30 and b) LP30 + FEC.

4.3.2 Voltage traces in coin cells as an indirect way to study surface kinetics

To study the distinctive SEI formed in the two electrolytes and the corresponding plating behaviour, symmetrical Li-Li coin cells were assembled and cycled using continuous plating and stripping cycles for current densities of 0.5, 1 and 2 mA/cm^2 applied for a total capacity of 2 mAh/cm^2 per cycle (Figure 4.6). A different protocol was used in the first cycle for the three current densities in order to compare the ‘peaking behaviour’ seen on stripping: while either 0.5, 1 or 2 mA/cm^2 was applied during plating, a current density of 1 mA/cm^2 was used on stripping for the second half of the first cycle (Figure 4.6b-d).

The study of the voltage traces follows the methodology introduced in previous studies,^{44,64} to observe the characteristic peaking behaviour that originates from surface pitting of the stripping electrode. Previous reports have assigned the typical voltage profile to specific deposition and pitting processes: initially, there is an overpotential associated with the nucleation of Li deposits on Li metal due to the kinetic hindrance depositing underneath the SEI, which then decreases rapidly towards a local minimum due to an increased surface area on the electrode.^{44,64} When switching polarity after the first deposition, the microstructures formed previously in the first half cycle are oxidised and removed from the stripping electrode. When all of the microstructures have been dissolved completely (or been detached from the electrode surface forming ‘dead Li’) the overpotential increases rapidly. A peak is seen as the overpotential drops again, labelled “pitting” (Figure 4.6a) as this behaviour has been assigned

to the onset of bulk metal dissolution or pitting of the Li metal surface and an increase in surface area.^{44,64} When comparing different electrolytes, a more pronounced peaking behaviour has been associated with substantial impedance differences and spatial variations in the SEI that lead to non-uniform stripping and the formation of dead Li.⁴⁴

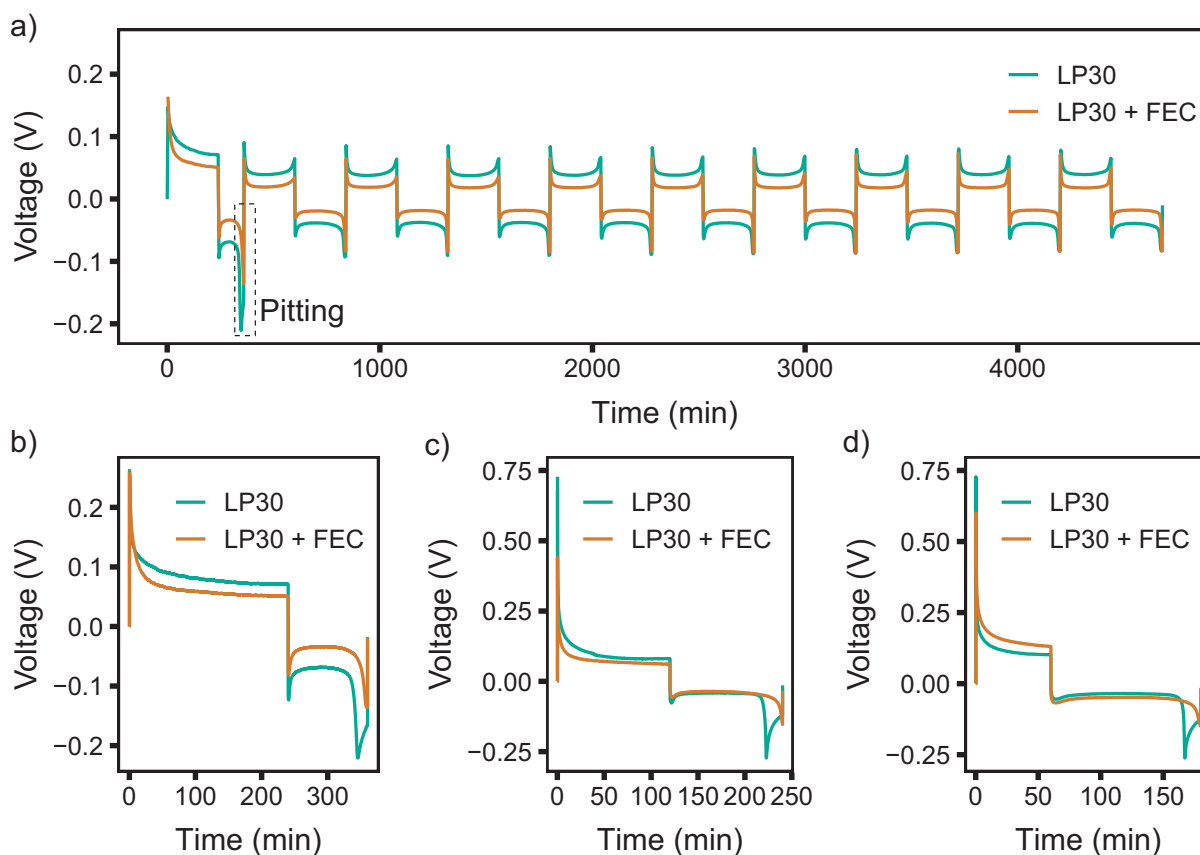


Figure 4.6 Galvanostatic cycling of symmetric Li-Li coin cells during **a)** the first 10 cycles at 0.5 mA/cm² for both stripping and plating. In the first cycle, shown in the enlargement in **b)** 0.5 mA/cm² was used for plating and 1.0 mA/cm² for stripping. First cycle using **c)** 1.0 and **d)** 2.0 mA/cm² plating and 1.0 mA/cm² for stripping in LP30 (green) and LP30 + FEC (orange).

For the first cycle in LP30 a more apparent “pitting” peak is observed that occurs at an earlier time compared to LP30 + FEC (occurring at ~78% and ~92% capacity, respectively for 0.5 mA/cm²). The inhomogeneous dissolution of the lithium whiskers can lead to dead Li formation under stripping and early peaking behaviour. However, the lower plating efficiency quantified with *in situ* NMR can also lead to the early peaking behaviour observed when lower amounts of microstructures are present. With 1 and 2 mA/cm², the peaking in the first cycle (where the stripping current is kept at 1 mA/cm²) occurs at 85% and 89% capacity respectively.

This correlates well with the *in situ* NMR, which indicated higher plating efficiencies for the higher current densities in LP30. For LP30 + FEC electrolyte the voltage traces are flatter compared to LP30, consistent with both the higher plating efficiency seen in the *in situ* NMR and of studies showing minuscule dead lithium formation in LP30 + FEC.^{56,157}

4.3.3 Pulse plating

To test the differences in Li deposition between the two electrolytes further, *in situ* NMR measurements using pulsed currents were carried out. When applying a pulsed current, short pulses for a period T_{ON} are applied, which is followed by a rest period T_{OFF} where no current is passed (as shown in the schematic, Figure 2.5).

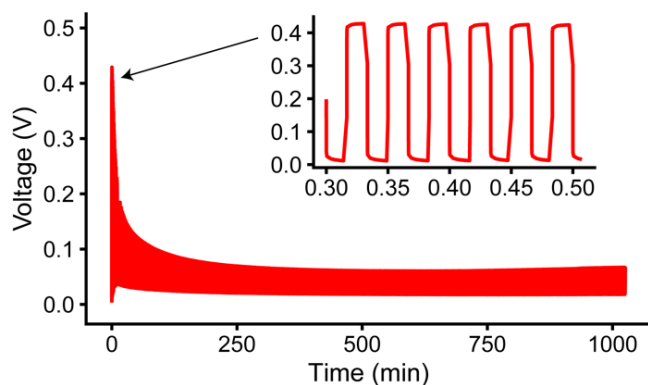


Figure 4.7 Representative pulsed current plot for symmetric Li *in situ* cell at 1 mA/cm^2 with $T_{ON}, T_{OFF} = 1 \text{ s}$ in the LP30 + FEC electrolyte.

During the rest period, T_{OFF} , two main processes occur: (i) Diffusion of Li ions in the electrolyte leading to relaxation of concentration gradients in the electrolyte and around protruding points on the electrode, and within the liquid components of the SEI; this should result in a more uniform lithium ion distribution near the electrode surface.¹⁰⁷

(ii) The chemical formation and growth of the SEI on fresh Li sites (the initial SEI formation has been suggested to be completed in less than 1 s ^{168,169} but as demonstrated in Chapter 5 the full passivation of Li metal can take longer time, up to hours/days). Cracked and newly formed SEI typically has a lower impedance than more mature SEI, which has been suggested to result in preferential deposition sites.^{37,44} The formation and maturation of the SEI during rest will increase its impedance and result in levelling effects. As a consequence, Li deposition is anticipated to be more homogeneous using pulse plating. The chemical formation of the SEI

during the rest period T_{OFF} has also been suggested to increase the current efficiency.¹⁶⁰ The electrochemistry for pulse plating, with $j_p = 1 \text{ mA/cm}^2$ and $T_{\text{ON}}, T_{\text{OFF}} = 1 \text{ s}$ in the LP30 + FEC electrolyte is shown Figure 4.7.

4.3.3.1 Pulse plating in LP30

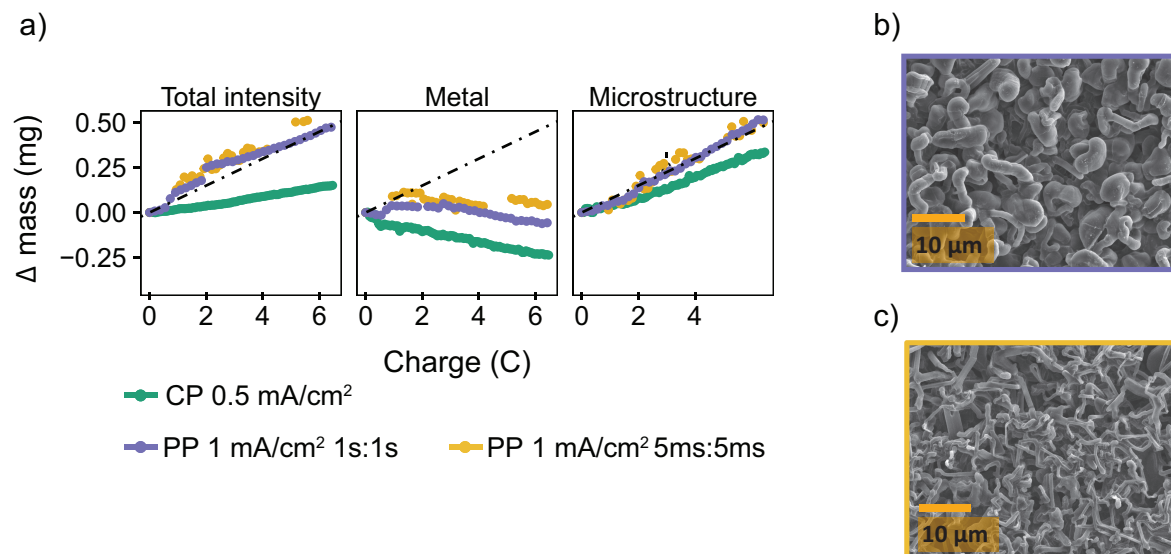


Figure 4.8 Pulse plating in LP30 **a)** The deconvoluted intensities of the *in situ* spectra for LP30 during constant plating (CP) at 0.5 mA/cm^2 (green, also shown in Figure 4.2) and pulse plating (PP) at 1 mA/cm^2 with $T_{\text{ON}}, T_{\text{OFF}} = 1 \text{ s}$ (purple) and $T_{\text{ON}}, T_{\text{OFF}} = 5 \text{ ms}$ (yellow). The dashed line indicates m_{echem} . SEM images of the Li metal morphology using 1 mA/cm^2 and $T_{\text{ON}}, T_{\text{OFF}}$ **b)** 1s **c)** 5 ms.

To compare different time scales, both relatively long and short pulse lengths were initially chosen, with $T_{\text{ON}}=T_{\text{OFF}}$ of either 1 s or 5 ms, which corresponds to a duty cycle of $\theta_{\text{duty}} = T_{\text{ON}}/(T_{\text{ON}} + T_{\text{OFF}}) = 0.5$ and an average current density of 0.5 mA/cm^2 . Thus, the data can be readily compared to the constant current experiments at 0.5 mA/cm^2 . Figure 4.8a shows a comparison of the microstructure masses determined by the NMR for both constant and pulse plating experiments in LP30. During pulse plating with $T_{\text{ON}}, T_{\text{OFF}} = 1 \text{ s}$ and $T_{\text{ON}}, T_{\text{OFF}} = 5 \text{ ms}$ (Figure 4.8a), the NMR-derived Li mass changes (Δmass) give a slope that corresponds closely to the microstructural mass predicted from the electrochemistry (m_{echem}), indicating high current efficiency of Li plating.

For both cases, the bulk metal intensity stays close to constant, indicating that the microstructure morphology is more porous as compared to that seen for constant plating at 0.5 mA/cm^2 , and thus does not attenuate the rf field. The resulting morphology (Figure 4.8b) for $T_{\text{ON}}, T_{\text{OFF}} = 1 \text{ s}$, comprises a mixture of both whisker- and dense-like buds, whereas short pulse

lengths, T_{ON} , $T_{OFF} = 5$ ms, result in the formation of narrow whiskers (Figure 4.8c). This demonstrates that applying short pulses in the LP30 electrolyte does not result in more uniform and dense morphologies. This may be due to the fact that significant capacitive effects were observed in symmetrical Li-Li cells, using the short $T_{ON} = 5$ ms pulse (Figure 2.6).

In addition, to study the effect of the pulse length, the pulse waveforms were systematically varied with T_{ON} , $T_{OFF} = 500$ ms, 100 ms or 50 ms and measured with *in situ* NMR spectroscopy. Surprisingly, denser microstructures are observed for T_{ON} , $T_{OFF} = 500$ ms and increasingly more open and whisker-like morphologies are seen as the time intervals decrease (Figure 4.10). Overall, the slope of the microstructural intensity for all the pulse waveforms is close to m_{chem} (Figure 4.9) indicating higher current efficiency compared to that observed for constant currents.

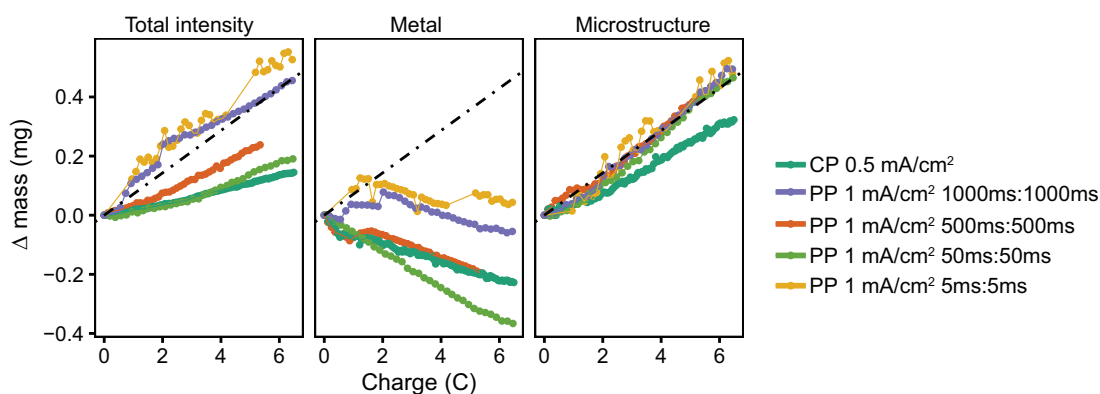
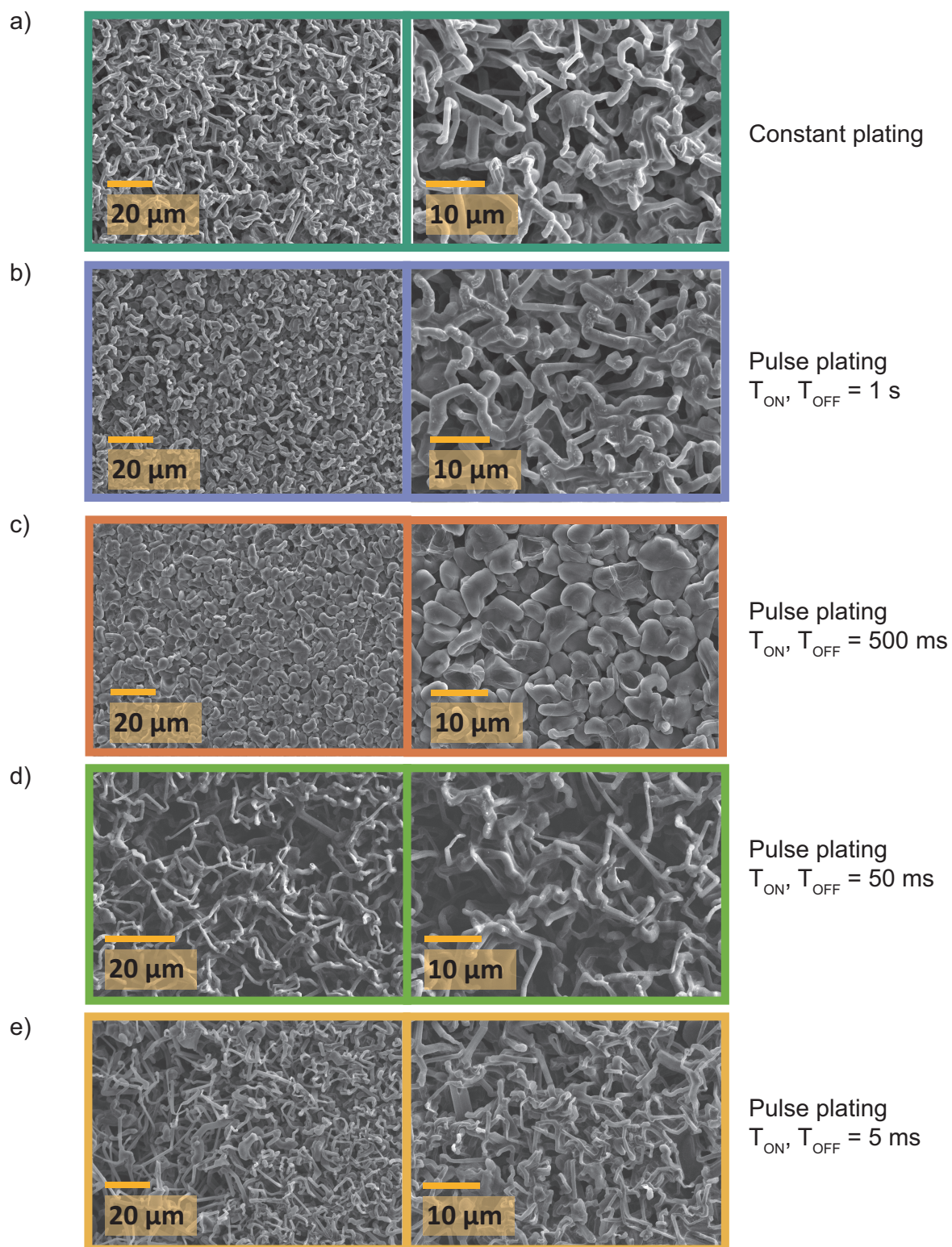


Figure 4.9 The deconvoluted intensities of the *in situ* NMR spectra during constant plating and pulse plating (PP) in the LP30 electrolyte with current density 1 mA/cm^2 and various pulse lengths of $T_{ON}:T_{OFF}$.



To further investigate the effect of the rest period on mitigating microstructural growth, longer rest periods of T_{OFF} were explored. Previous studies^{110,159,160} have suggested that in order for pulse plating to be beneficial, setting the timings such that $T_{ON} < T_{OFF}$ is crucial, the studies even proposing an optimal $T_{ON}:T_{OFF}$ ratio of close to 1:3.¹⁵⁹ Thus, $T_{ON} = 5$ ms with a longer rest period of $T_{OFF} = 15$ ms was considered with the applied current densities $j_{inst} = 1$ and 2 mA/cm². This gives average current densities of 0.25 and 0.5 mA/cm².

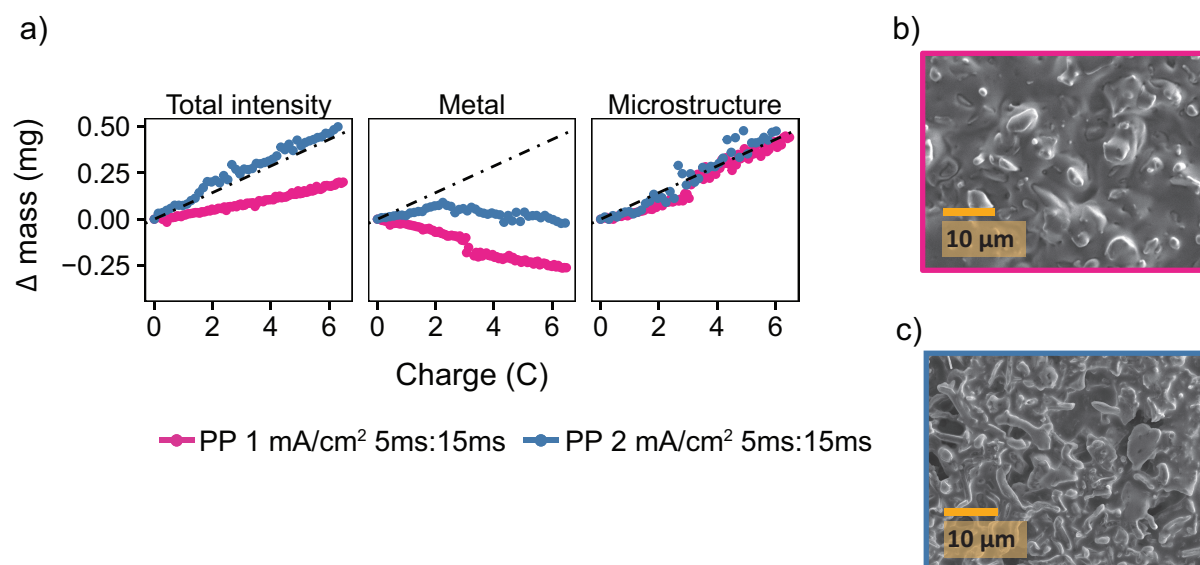


Figure 4.11 Pulse plating in LP30 **a)** The deconvoluted intensities of the *in situ* spectra during pulse plating with $T_{ON}:T_{OFF} = 5$ ms:15 ms using current density 1 mA/cm² (pink) and 2 mA/cm² (blue). SEM images of the Li metal morphology using $T_{ON}:T_{OFF} = 5$ ms:15 ms and **b)** 1 mA/cm² **c)** 2 mA/cm².

The deconvoluted intensities (Figure 4.11a) from the *in situ* NMR measurements show microstructural growth corresponding roughly to m_{chem} . Furthermore, the morphology for the lower $j_{inst} = 1$ mA/cm² remains relatively smooth which can be seen both in the SEM image (Figure 4.11b) and with the decreasing metal intensity (Figure 4.11a, pink). The attenuation of the bulk metal signal indicates (for reasons discussed in the previous section) that pulsed currents with $T_{ON} < T_{OFF}$ do indeed lead to more dense deposition near the electrode surface.

For the higher current density, $j_p = 2$ mA/cm², the morphology again becomes uneven (Figure 4.11c), which can also be seen in the intensity of the metal peak (Figure 4.11a, blue) that even grows slightly, suggesting roughening on the stripping electrode. Interestingly, of note is that the “bulk metal” peak consistently increases for relatively high, applied current densities of 2 mA/cm², both for constant and pulsed current (Figure 4.4 and Figure 4.11). An increase in the bulk metal peak can derive from roughening of the stripping electrode as a result of pitting.^{80,164}

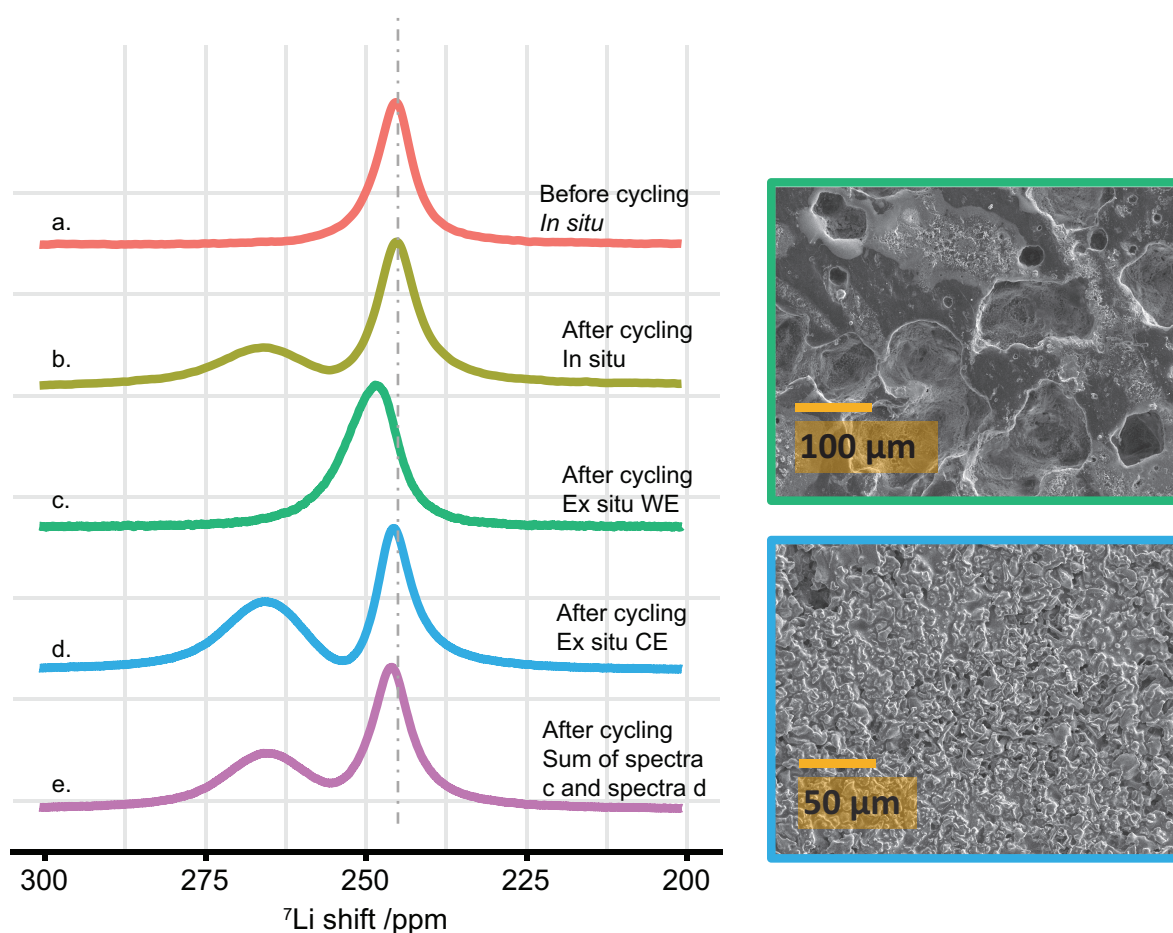


Figure 4.12 *Ex situ* ${}^7\text{Li}$ NMR spectra of pitting on the stripping electrode showing **a**) the *in situ* cell before and **b**) after cycling. **c**) The *ex situ* NMR of the disassembled cell on the plated electrode (working electrode, WE), **d**) and of the stripping electrode (counter electrode, CE) with the corresponding SEM images showing the pits. **e**) And the sum of spectra c and d, of the WE and CE. The metal peak of the stripping electrode after cycling, shown in green, has shifted to higher frequency (247.5 ppm compared to 245 ppm before cycling) and indicates roughening of the electrode surface.¹⁶⁴ Shown for LP30, 2 mA/cm² and $T_{\text{ON}} = 5$ ms, $T_{\text{OFF}} = 15$ ms.

The effect of pitting on the NMR spectra was explored by disassembling the *in situ* cell after plating and *ex situ* NMR measured of the separate electrodes (Figure 4.12). The stripping electrode gives a broader signal, shifted upfield about 2.5 ppm to a value of 247.5 ppm, indicating roughening of the electrode that is consistent with the pits shown in the SEM (Figure 4.12).¹⁶⁴ The experiment is not necessarily quantitative to the extent of pitting, as NMR signal intensities depend strongly on the amount of metal inside the NMR coil and considerable errors are introduced when taking the cells in and out of the coil. Thus, it is difficult to estimate the pitting on the Li electrode in the current study but is of considerable interest for future studies

where the two Li electrodes could be placed apart in the rf-coil (in a modified cell design) to perform NMR on them separately.

4.3.3.2 Pulse plating in LP30 + FEC

The pulse plating experiments were repeated in LP30 + FEC (Figure 4.13a) where both long (1s, purple) and short (5 ms, yellow) pulse lengths seem to delay the onset of the microstructural growth. For both experiments, the microstructural intensity stays constant for the first two coulombs of charge before increasing with a slope close to m_{echem} . Thus, we conclude that the $m_{\text{NMR}} < m_{\text{echem}}$ is a result of smooth deposition that is not detected by the NMR as a result of skin depth effects. The SEM images (Figure 4.13b and Figure 4.13c) show the resulting relatively smooth and dense morphology of the Li deposits.

For $T_{\text{ON}}:T_{\text{OFF}} = 5\text{ms}:15\text{ ms}$ and $j_p = 1\text{ mA/cm}^2$, the morphology is even more uniform (Figure 4.13e) and for $j_p = 2\text{ mA/cm}^2$, as seen for LP30, the morphology becomes rougher again (Figure 4.13d, f). Overall, pulse plating appears to be more beneficial for Li deposition in the LP30 + FEC electrolyte and suggest that local concentration gradients at the metal surface are levelled out more effectively. This is not expected to arise from the better transport in the electrolyte as similar Li^+ diffusion coefficients were measured by PFG-NMR, $D_{\text{LP30}} = 1.70 \times 10^{-10}\text{ m}^2\text{ s}^{-1}$ and $D_{\text{LP30 + FEC}} = 1.74 \times 10^{-10}\text{ m}^2\text{ s}^{-1}$. That is, little to no effect is seen on the transport properties on adding FEC, which is consistent with the results from molecular dynamics (MD) simulations of Hou et al.¹⁷⁰

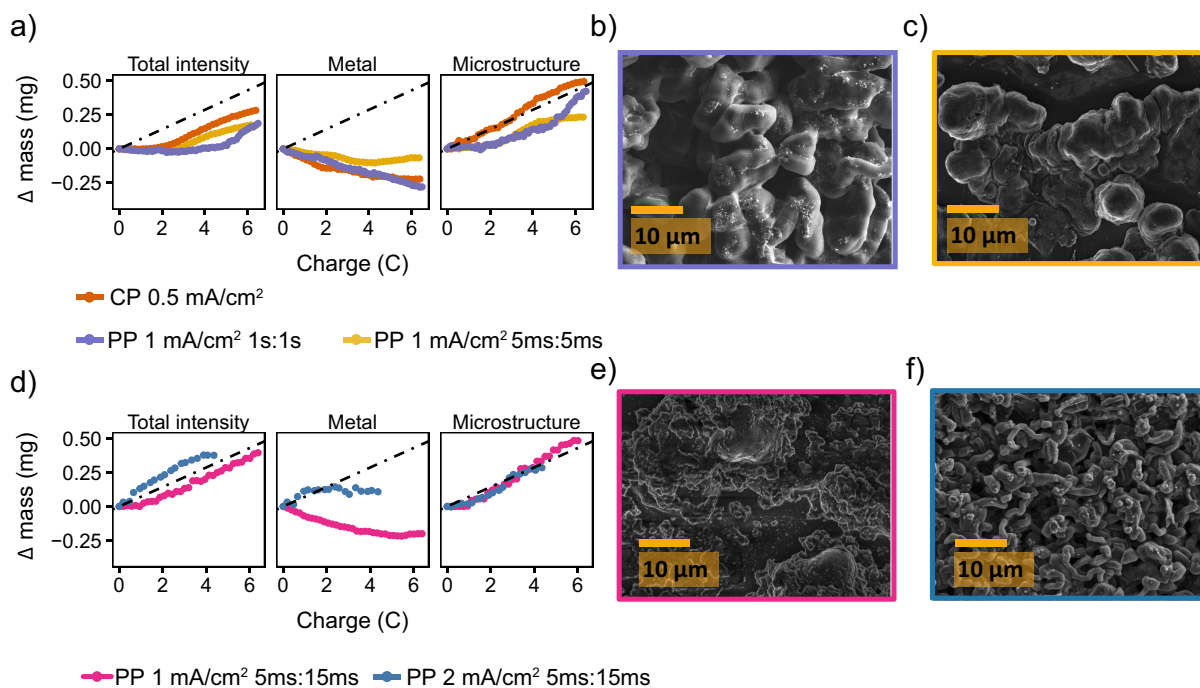


Figure 4.13 Pulse plating in LP30 + FEC **a)** The deconvoluted intensities of the *in situ* NMR in LP30 + FEC during constant plating (CP) at 0.5 mA/cm² (orange, also plotted in Figure 4.2) and pulse plating (PP) at 1 mA/cm² with T_{ON}, T_{OFF} = 1 s (purple) and T_{ON}, T_{OFF} = 5 ms (yellow). SEM images of the Li metal morphology using 1 mA/cm² and T_{ON}, T_{OFF} **b)** 1s and **c)** 5 ms. **d)** The deconvoluted intensities of the *in situ* NMR with T_{ON}:T_{OFF} = 5 ms:15 ms using current density 1 mA/cm² (pink) and 2 mA/cm² (blue) and the SEM images for **e)** 1 mA/cm² **f)** 2 mA/cm².

4.3.3.3 Ultra-high current densities

Finally, it was noted in Chapter 2 that high instantaneous current densities may be used for pulse plating due to the improved mass transport near the electrode (section 2.3.3.2).^{104,107} Higher overpotentials, associated with high current densities, will influence the nucleation rate significantly¹⁰⁸ and have been shown to result in smaller Li nuclei size and higher Li surface coverages.¹⁰⁹ This is a well-known effect and demonstrated for example when pulse plating silver, where high instantaneous current densities were used to achieve finer and more homogeneous deposits.¹⁰⁵

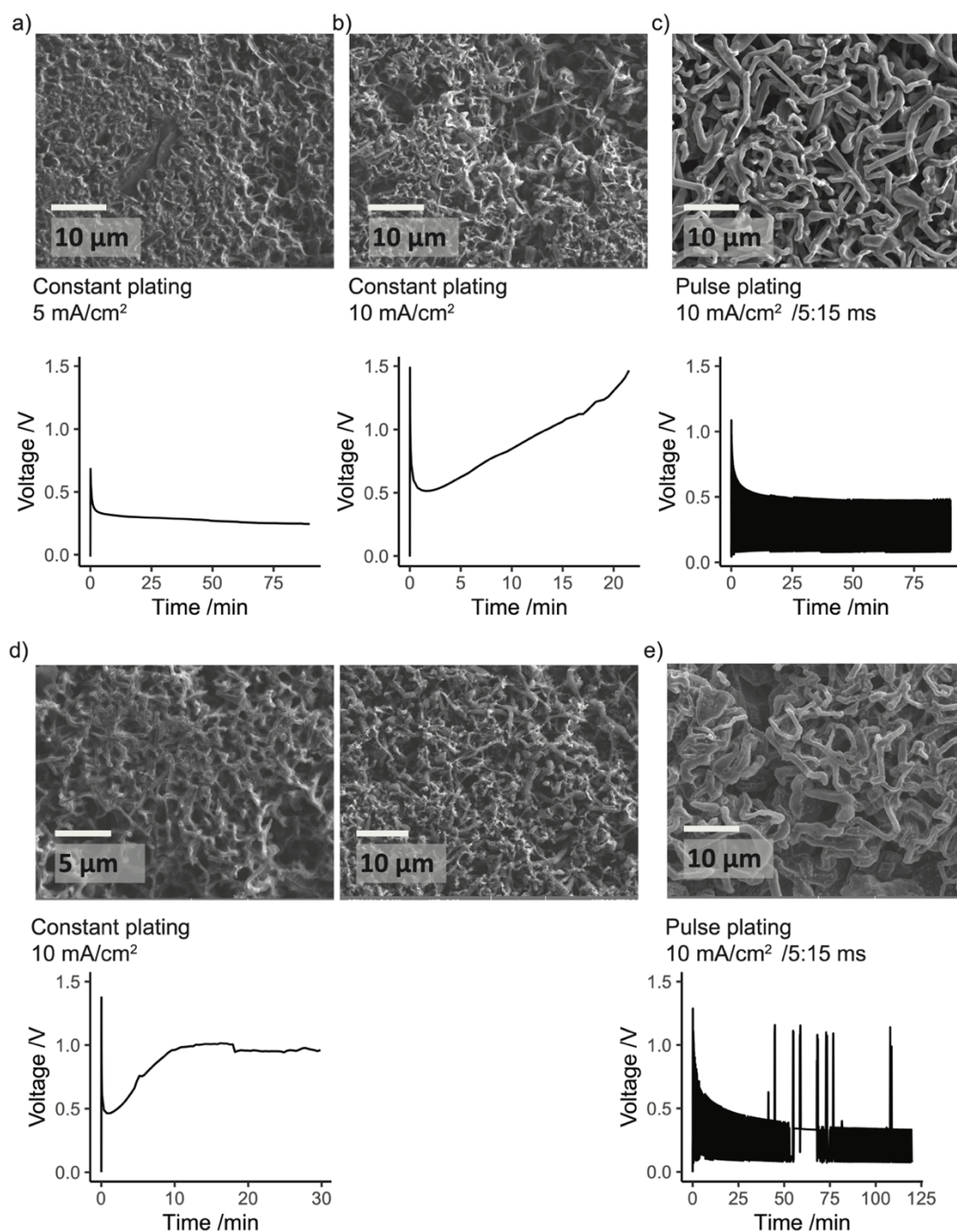


Figure 4.14 The SEM images and the corresponding voltage profile for **a)** constant plating at 5 mA/cm², **b)** constant plating at 10 mA/cm² and **c)** pulse plating using 10 mA/cm² with $T_{ON}:T_{OFF} = 5 \text{ ms}:15 \text{ ms}$ in LP30. **d)** Constant plating at 10 mA/cm² and **e)** pulse plating using 10 mA/cm² with $T_{ON}:T_{OFF} = 5 \text{ ms}:15 \text{ ms}$ in LP30 + FEC.

Here, both constant current and pulsed current with the relatively high current density of 10 mA/cm² was used in LP30 and LP30 + FEC (Figure 4.14). For the constant current

experiments, fine and needle like deposits were observed under the SEM. The overpotential is seen to increase quickly upon deposition, most likely due to the concentration overpotential associated with mass transport limitations. For the pulse plating experiments the overpotential is more stable (although erratic behavior is observed in LP30 + FEC in Figure 4.14e) and the whisker-like deposits are observed again. This demonstrates that high current densities may be used when pulse plating Li metal. However, in the case here it does not result in more homogeneous deposition.

4.4 Discussion

The results suggest that the lower CEs reported for the commercial carbonate electrolyte⁴⁵ are in part due to low current efficiency associated with the electrochemical SEI formation during plating as a result of the formation of higher surface area Li whiskers. This was demonstrated by using *in situ* NMR, where the mass of the Li deposits is compared to the mass expected to be deposited from the electrochemistry, m_{echem} (Figure 4.2). This is also consistent with the earlier “peaking” behaviour seen for the LP30 electrolyte during the 1st stripping (Figure 4.6) although dead Li formation will have the same effect.

For the pulse plating experiments, the morphology of the Li deposits in LP30 were seen to be highly dependent on both plating and rest time. For experiments in LP30 with the longer pulses of both $T_{\text{ON}}, T_{\text{OFF}} = 1$ s and 500 ms, denser morphology was achieved compared to constant plating whereas $T_{\text{ON}}, T_{\text{OFF}} = 5$ ms resulted in the formation of narrow whiskers. Therefore, recommending short pulses for Li deposition,¹¹⁰ nominally to ensure minimal concentration gradients at the electrode’s surface, may not always be appropriate. This may be due to the capacitive effects that become important for short current pulses (Figure 2.6). However, for the short pulses $T_{\text{ON}} = 5$ ms, applying a longer rest time of $T_{\text{OFF}} = 15$ ms improved the plating with smoother deposits forming (Figure 4.11). The results illustrate the important effect of the rest period in pulse plating Li metal, where both diffusion and healing of the SEI takes place.

Of note is that full passivation of the Li metal surface is not achieved on the timescale of the rest periods used here, as will be discussed in Chapter 5. Despite this, the *in situ* NMR of pulse plating demonstrated that less charge was wasted to form the SEI during plating and indicates

that even time intervals of 15 ms can be sufficient to, at least partially, heal hotspots formed during plating. Note that this process, discussed in Chapter 6 as Li corrosion, still consumes lithium and is another mechanism responsible for degradation in a metal cell: in experiments performed with a fixed and finite lithium concentration (e.g., when plating using a lithium-ion cathode as the lithium source), this will lead to more rapid cell termination.

Pulse plating in LP30 + FEC led consistently to more dense morphologies and was seen to delay the onset of microstructural formation (Figure 4.13a). As shown in section 4.3.1, the microstructures formed under constant plating in LP30 + FEC are generally more uniform compared to LP30. Hence, local concentration gradients that develop at the electrode during plating, which are amplified at rough sites and protrusions, are less pronounced for the smoother metal surface in LP30 + FEC. Thus, relaxation of local concentration gradients will not be as important as in the case for LP30.

In addition, isotope exchange simulations covered in Chapter 5 show that SEI formation and Li^+ transport in the SEI is faster in LP30 + FEC. That further explains why pulse plating is more effective in LP30 + FEC. Both faster SEI passivation, which reduces impedance differences over the electrode's surface, and more rapid Li^+ transport should result in more homogeneous plating. However, although the SEI in LP30 + FEC has better transport properties, at high current densities it is still not fast enough to allow for a sufficiently uniform transport at higher plating current densities, the morphology of the Li deposits were similar for the two electrolytes (Figure 4.5 and Figure 4.14), consistent with other studies.¹⁵⁷

4.5 Conclusions

This chapter has presented a careful comparison of the SEI formed in the standard carbonate electrolyte, with quantitative and non-invasive NMR measurements. The *in situ* NMR measurements have shown that both the plating efficiency and growth mode of lithium deposits are governed by the choice of the electrolyte as well as the applied current density.

As a result of the skin depth on Li metal, the \mathbf{B}_1 rf-field will only excite metal deposits of thickness 12 μm and the first 12 μm on the metal surface. This effect means that completely smooth Li plating should lead to no change in the NMR intensity and Li plating would not be detected with NMR. In all cases here the NMR intensity grows in intensity demonstrating the

technique is very sensitive to Li deposition. Even in the case of pulse plating in LP30 + FEC where the surface appears smooth by SEM (Figure 4.13), the deposits are detected by the NMR and resonate around 260 ppm. The quantitative nature of the technique can thus be used with confidence and allows the estimation of current efficiency; where the slope of the microstructural peak is compared to the mass of Li calculated according to the charge passed in the electrochemistry.

The effect of the FEC additive was systematically studied under different plating conditions and correlate different Li growth and current efficiency to the nature of the SEI. Pulse plating is shown to influence the morphology of Li deposits, which were seen to be highly dependent on both plating and rest time. This illustrates the important effect of the rest period in pulse plating Li metal, namely the healing of the SEI layer that can increase the current efficiency of Li deposition, and the relaxation of local concentration gradients that lead to a more uniform morphology.

Chapter 5 Lithium Isotope Exchange

5.1 Introduction

The SEI forms on Li metal due to the reduction of the electrolyte on the electrode surface and influences the stability and cyclability of lithium metal batteries (LMBs).¹⁴ Much work is being carried out to correlate the electrochemical behaviour of LMBs to the chemical, structural and mechanical properties of the SEI as well as Li-ion transport properties and the time-dependent evolution of the SEI.

Studies on the chemical composition of the SEI commonly involve *ex situ* measurements e.g. by XPS^{81,171} and Fourier transform infrared spectroscopy (FTIR).⁹⁷ Studies on the structural composition by cryo-EM have correlated an ordered and homogeneous distribution of SEI components to more uniform plating and stripping of Li.^{31,82,83} But the SEI is reactive and air-sensitive, and post-mortem studies might not accurately capture the nature of the thin SEI in a real battery. Therefore, techniques that study the SEI under operating conditions are constantly being developed, such as *in situ* atomic force microscopy (AFM)^{24,172} and ambient-pressure XPS.¹⁷³ NMR spectroscopy is a non-invasive, chemically specific and quantitative, which makes it an excellent technique to study the SEI in LIBs.^{84,174,175} However, NMR suffers from issues of low sensitivity and selectivity, which makes *in situ* NMR studies of the SEI difficult. In a recent study, we used dynamic nuclear polarization (DNP) to selectively enhance the signal of the SEI on Li metal that makes it a promising method for future *in situ* DNP-NMR studies on the SEI.⁸⁷

The flux of Li⁺ ions towards to surface will dictate the growth morphology of Li deposits and thus it is crucial to understand the transport properties of the SEI in different electrolytes. But the transport properties and the transport mechanism in the SEI remain inconclusive. Lu and Harris quantified the Li-ion diffusion in the SEI by ^{6,7}Li isotope labelling and time-of-flight secondary-ion mass spectrometry (TOF-SIMS).¹⁷⁶ The SEI was formed on Cu in a natural

abundance electrolyte and then soaked in an ^6Li enriched electrolyte for different time periods for an ion exchange to occur. The ratio of $^6\text{Li}/^7\text{Li}$ in the SEI measured by TOF-SIMS indicated that the Li^+ ions first diffuse through a porous organic SEI layer and then to a more densely packed layer that limits the transport.¹⁷⁶ Li^+ ion transport was further investigated in a $\text{Li}_7\text{La}_3\text{Zr}_2\text{O}_{12}$ (LLZO)–polymer composite electrolyte using $^6,^7\text{Li}$ isotope labelling and NMR spectroscopy.¹⁷⁷ The ion conduction mechanism was shown to be dependent on the ratio between the LLZO and the poly(ethylene oxide) (PEO), the conduction pathway changing between polymer matrix and the LLZO.¹⁷⁷ Previously, isotope labelling has been used to study the solid/liquid interface in heterogeneous systems including solids such as ion exchanger beads and ionic crystals.^{178–181} Ilott and Jerschow used NMR to study isotope exchange between an enriched ^6Li metal and a natural abundance ^7Li electrolyte, probing the kinetics at the Li metal–electrolyte interface.¹⁸²

In this chapter, isotope exchange measurements are further used to study the transport properties and the time-dependent evolution of the SEI in different electrolytes. Using NMR, we observe *in situ* the isotope exchange of $^6\text{Li}/^7\text{Li}$ ions between ^6Li -enriched Li metal (95% ^6Li and 5% ^7Li) and natural abundance electrolyte (i.e. 92.4% ^7Li and 7.6%, ^6Li).^{75,182} When ^6Li metal is soaked in the natural abundance ^7Li electrolyte, the exchange between the two isotopes can be described as:



and is comparable to Li metal anode at an open circuit voltage (OCV). The relevant processes that affect the isotope exchange is the exchange rate at the surface of the metal, the self-diffusion of Li atoms within the metal, diffusion of Li^+ in the SEI, and the chemical formation of the SEI and the desolvation of the Li^+ ions (see the schematic Figure 5.1).

A numerical model is developed to describe the exchange and discussed in the context of the standard model of electrochemical kinetics. Simulations of the NMR measurements allow us both to extract the exchange current at the OCV, which takes into account the growth of the SEI, and allows the extent of Li metal corrosion due to chemical SEI formation to be quantified. The results demonstrate that the isotope exchange rate depends significantly on the electrolyte and the corresponding SEI.

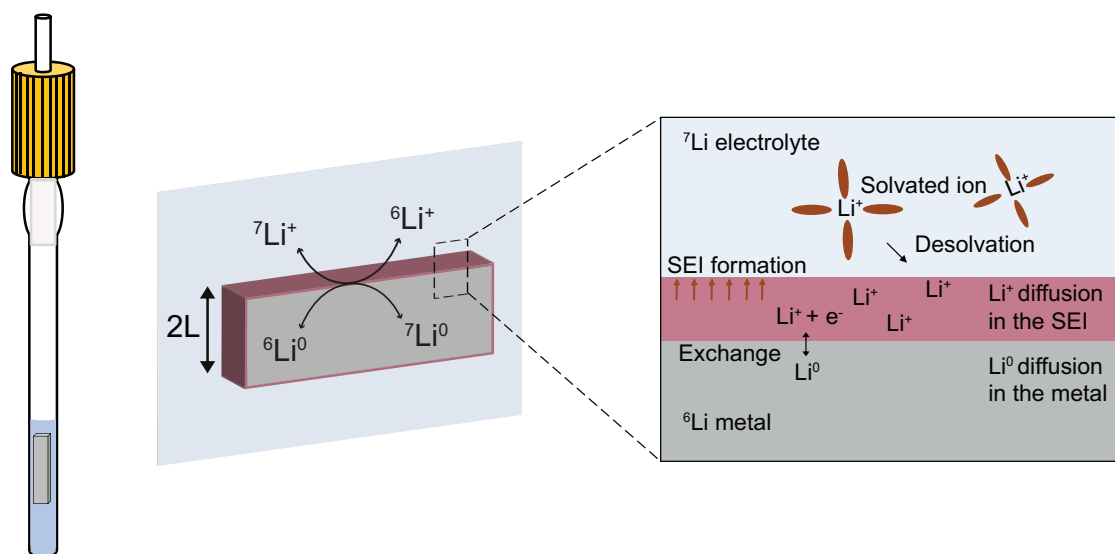


Figure 5.1 A schematic representing the 5mm J-Young NMR tube, the yellow cap seals the NMR tube making it airtight. The dominant processes occurring at the metal-electrolyte interface are shown, which will influence the exchange rate.

In Chapter 4, Li deposition was studied in the two electrolytes LP30 and LP30 + FEC. The Li morphology was shown to differ significantly between the two electrolytes. Furthermore, in all cases was pulse plating more effective in mitigating microstructural growth in LP30 + FEC. However, the effectiveness of pulse plating using the FEC additive is not expected to derive from the Li^+ transport in the electrolyte as the diffusion coefficients measured in both systems were shown to be similar and thus it must be an effect of the SEI. Here, by simulating the isotope exchange, we identify the key beneficial effects of the FEC additive: faster Li^+ transport in the SEI and faster SEI formation.

Finally, the methodology is further extended and isotope exchange is studied as a function of temperature. It is demonstrated by numerical simulations that initially, the isotope exchange is faster at higher temperatures, but then decreases to lower values. This is due to the continuous SEI formation that occurs more rapidly at elevated temperatures.⁵¹ The activation energy of the exchange between the electrolyte and metal is estimated by assuming the exchange to be an Arrhenius thermally activated process.

The work presented in this Chapter benefitted from the intellectual input of all the co-authors of the project, Sundeep Vema, Svetlana Menkin, Lauren Marbella and Clare Grey.

The numerical model was developed in collaboration with Sundeep Vema and Clare Grey and the MATLAB code written in collaboration with Sundeep Vema.

The MATLAB code for fitting the electrochemical impedance spectroscopy data was written by Sundeep Vema. The current author performed all of the experimental work.

The main part of this chapter is published in the Journal of Materials Chemistry A, 2020, 8, 14975–14992.

5.2 Experimental Details

5.2.1 Materials

The materials were stored and handled in an Argon atmosphere glovebox (O_2 , H_2O < 1 ppm, MBraun). The ^6Li metal (Cambridge Isotope Laboratories, 95% ^6Li), which is supplied in mineral oil, was rinsed with hexane (Sigma Aldrich) and rolled with an Al roller inside a plastic bag (polyester pouch, VWR) to an approximate thickness of 0.15 mm. In all coin cells, pre-cut lithium metal disks (LTS research, 99.95%) were used. The electrolyte was 1 M LiPF_6 in 1:1 v/v ethylene carbonate/dimethyl carbonate (EC/DMC; Sigma Aldrich, referred to as LP30). For experiments using an additive, fluoroethylene carbonate (FEC; Sigma Aldrich, 99%) was added to the electrolyte in 1:10 ratio by volume (LP30 + FEC). The water content of the LP30 electrolyte was measured with Karl Fischer titration and was < 40 ppm. The 4M LiFSI in DME was prepared by mixing lithium bis(fluorosulfonyl)imide (LiFSI, Fluorochem, battery grade) with 1,2-dimethoxyethane (DME, Sigma Aldrich, 99.5% and distilled). The ^6Li metal was cut into a rectangular electrode with a razorblade, of dimensions 3 mm \times 13 mm. The electrode was placed in an airtight 5mm J-Young NMR tube filled with 400 μL of electrolyte and transferred as quickly as possible to the NMR spectrometer for the measurements, which took approximately 10 minutes.

5.2.2 NMR spectroscopy

The ^7Li NMR isotope exchange measurements were performed on a Bruker Avance III 300 spectrometer, operating at a Larmor frequency of 300.1 MHz for ^1H and 116.6 MHz for ^7Li . The measurements were recorded with a MicWB40 probe inside a Micro2.5 triple axis gradient system at 298 K, using a water-cooling unit, and a 10 mm ^1H - ^{19}F / ^7Li coil. ^7Li shifts were referenced to a 1 M aqueous solution of LiCl at 0 ppm. The electrode was centred in the NMR

coil, with the Li metal placed parallel to the \mathbf{B}_0 field (resulting in a ${}^7\text{Li}$ shift of 275 ppm) and parallel to the \mathbf{B}_1 rf-field to get maximum excitation.¹⁴¹ Single pulse ${}^7\text{Li}$ NMR experiments were recorded on a series with a recycle delay of 15 s was used and 48 transients recorded, resulting in an experimental time of about 12 minutes. The recycle delays were chosen to ensure full relaxation of the electrolyte components, with the delay $> 5 \times T_1$. The isotope exchange at elevated temperatures was performed by raising the temperature of the NMR probe to 313 K and 323 K. For the 313 K experiment that was first soaked at room temperature for 25 hrs; the ${}^6\text{Li}$ -enriched metal was soaked in LP30 for 25 hours at 298 K and the electrolyte then switched for a fresh electrolyte. The soaking of the Li metal was then continued at 313 K.

5.2.3 Electrochemical impedance spectroscopy

For the impedance measurements, symmetrical Li-Li coin cells were pre-conditioned using 1 mA/cm² for 0.04 mAh/cm² for one cycle, followed by potentiostatic electrochemical impedance spectroscopy (EIS) measurements using 10 mV voltage perturbation at the open circuit voltage in a frequency range of 0.5 MHz to 1 Hz with 10 steps per decade. The impedance data was fitted to the equivalent circuit displayed in Figure 5.9, using a home-built MATLAB code with a non-linear least square solver, lsqcurvefit.

5.3 Numerical Modelling

The numerical model to simulate the isotope exchange is derived in this section. For a one-electron, one-step process at equilibrium, a continuous oxidation and reduction takes place at the electrode/electrolyte interface. In the system under study where Li metal is soaked in an electrolyte and no overpotential applied, the equilibrium process is:



where the forward and backwards reactions occur at the same rate resulting in a zero net overall current, termed the exchange current density j_0 .⁹⁰ The traditional exchange current density, j_0 , describes the electron transfer kinetics of the electrochemical system. When described in terms of the Butler-Volmer formulation (equation (2.11)) the exchange current density for Li^+/Li^0 is:⁹⁰

$$j_0 = F k_0 [Li^+]^\beta [Li^0]^{1-\beta} \quad (5.3)$$

where F is the Faraday constant, k_0 is the standard rate constant and β is the transfer coefficient. The transfer coefficient is a constant (between 0 and 1) that reflects how closely the activated state resembles the oxidised or reduced products.¹ Boyle et al. showed how Li metal deposition is more accurately described by a Marcus-based model where the transfer coefficient β is a function of the applied potential.¹¹³ However, at small overpotentials (or at the OCV) the Butler-Volmer and Marcus-based theories should be indistinguishable.¹¹³

Equation (5.3) can be rewritten in terms of the exchange flux at the interface J_0 [$\text{mol m}^{-2} \text{s}^{-1}$], where $j_0 = FJ_0$. This equilibrium process (strictly the OCV process) can be followed *via* the isotope exchange current when an enriched Li metal electrode is soaked in a non-enriched electrolyte (for example), because the ${}^6,{}^7\text{Li}$ concentrations are not in equilibrium (i.e. the concentrations of ${}^6,{}^7\text{Li}$ are different in the Li metal and electrolyte).

In contrast to the traditional definition of the exchange current density j_0 (described in equation (5.3) and in detail in section 2.3.1), the rate of exchange determined in the current measurement will depend not only on the electron transfer kinetics of Li^+/Li^0 but as well on the rate of the subsequent transport of the Li^+ through the SEI. To make a distinction between our model and the traditional one, and to generalise our model, we will hereafter refer to the isotope exchange flux occurring at OCV measured here as J_{ex} [$\text{mol m}^{-2} \text{s}^{-1}$]; furthermore, since the SEI continues to grow on Li metal, J_{ex} , is expected to be time dependent (as explored below *via* two different models).

To model the isotope exchange intensity curves obtained by NMR measurements, the concentration of ${}^7\text{Li}$ in the metal needs to be considered. The ${}^7\text{Li}$ concentration c_{m7} , at distance x from the SEI-metal interface and at time t , is described in the following equation:

$$c_{m7}(x, t) = [Li^0] f_{m7}(x, t) \quad (5.4)$$

where $f_{m7}(x, t)$ is the ${}^7\text{Li}$ mole fraction at position x from the metal surface. The metal is of thickness $2L$ (Figure 5.2) and is represented on a discretised one-dimensional grid, where $x = 0$ represents the surface of the Li metal and $x = L$ represents the centre of the metal. The concentration of Li in the metal electrode is $[Li^0] = \frac{\rho}{M} = \frac{0.534 \text{ g/cm}^3}{6.94 \text{ g/mol}} = 77 \text{ M}$ where ρ is the

density of Li metal and M the molar mass. The initial condition for the fraction of ${}^7\text{Li}$ in the metal is $f_{m7}(x, 0) = 0.05$, since we use a 95% enriched ${}^6\text{Li}$ metal. Note that at time $t = 0$ in the simulations, approximately 10 minutes have passed since immersing the enriched Li metal in the electrolyte and until the start of the NMR experiment. This will only result in a minimal error in the initial starting condition as the experiment is performed over multiple hours and the second data point in the experimental measurements (at $t \sim 25$ mins) shows minimal change from the first data point ($t = 0$ min) in mole fraction of ${}^7\text{Li}$ in both electrolyte and metal (Figure 5.4). To test for this, the initial conditions of the first few points of $f_{m7}(x, 0)$ were increased to 0.055, which qualitatively did not result in any significant changes between the fitted parameters between the two electrolytes.

The concentration of ${}^7\text{Li}$ electrolyte as a function of time is, $c_{e7}(t) = [\text{Li}^+]f_{e7}(t)$ with the initial condition for the fraction of ${}^7\text{Li}$ in the electrolyte, $f_{e7}(0) = 0.92$ (the natural abundance of ${}^7\text{Li}$). Since the diffusion coefficient in lithium metal, D_m , is five orders of magnitude smaller than the diffusion coefficient in the electrolyte (Table 5.1), the diffusion of Li^+ throughout the electrolyte is considered instantaneous.

The self-diffusion of Li atoms within the metal is described by Fick's law:

$$\frac{\partial c_{m7}(x, t)}{\partial t} = D_m \frac{\partial^2 c_{m7}(x, t)}{\partial x^2}, \quad 0 < x < L \quad (5.5)$$

And the symmetric boundary condition at $x = L$ is:

$$\frac{\partial c_{m7}(L, t)}{\partial x} = 0 \quad (5.6)$$

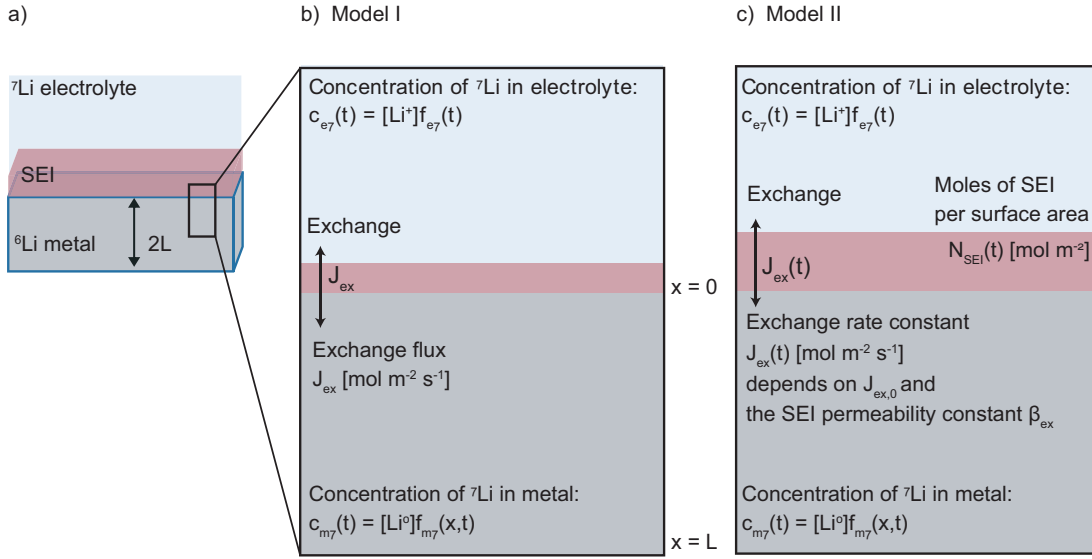


Figure 5.2 A schematic of the numerical model showing **a)** the geometry of the Li metal electrode. **b)** Model I, which describes the isotope exchange with one fitting parameter, the exchange flux, J_{ex} [$\text{mol m}^{-2} \text{s}^{-1}$] describing the rate of exchange and **c)** Model II, which describes both isotope exchange and SEI formation, with the time-dependent exchange flux $J_{ex}(t)$ [$\text{mol m}^{-2} \text{s}^{-1}$], which depends on the SEI permeability constant β_{ex} .

Due to the difference in isotope ratio between the electrolyte and metal, the flux at equilibrium J_{ex} , will lead to change in the isotope ratio of the metal, described by the partial differential equations of the concentration of ${}^7\text{Li}$ in the metal:

$$D_m \frac{\partial c_{m7}(x=0, t)}{\partial x} = J_{ex} (f_{e7}(t) - f_{m7}(0, t)) \quad (5.7)$$

And a change in the isotope ratio in the electrolyte, described by the ordinary differential equation of the concentration of ${}^7\text{Li}$ in the electrolyte:

$$\frac{dc_{e7}(t)}{dt} = -\frac{S_a}{V_e} J_{ex} (f_{e7}(t) - f_{m7}(0, t)) \quad (5.8)$$

where S_a is the surface area of the soaked electrode and V_e is the volume of the electrolyte.

For **Model I** it is assumed that the SEI of Li metal is of fixed thickness (that is it is not growing during the experiment). The experimental curves are thus fitted with one fitting parameter J_{ex} and equations (5.4)-(5.8), as shown schematically in Figure 5.2b.

Table 5.1. List of all the model input parameters and methods used to measure or estimate their values.

Symbol	Description	Value/Unit	Determination
S_a	Surface area of Li metal	$8.2 \times 10^{-5} \text{ m}^2$	Measured
L	Half thickness of the Li metal	$0.12 \times 10^{-3} \text{ m}$	Estimated from S_a and weight of Li metal
V_e	Volume of the electrolyte	400 μL	Measured
D_m	Self-diffusion coefficient in Li metal	$7.11 \times 10^{-15} \text{ m}^2 \text{ s}^{-1}$	Estimated by NMR relaxometry (in ref. ¹⁸³)
D_{LP30}	Diffusion coefficient in LP30	$1.70 \times 10^{-10} \text{ m}^2 \text{ s}^{-1}$	Measured by PFG-NMR
$D_{\text{LP30 + FEC}}$	Diffusion coefficient in LP30 + FEC	$1.74 \times 10^{-10} \text{ m}^2 \text{ s}^{-1}$	Measured by PFG-NMR
$[\text{Li}^+]_{\text{LP30}}$	Concentration of LP30 electrolyte	1000 mol m^{-3}	From supplier
$[\text{Li}^+]_{\text{LP30 + FEC}}$	Concentration of LP30 + FEC electrolyte	909 mol m^{-3}	Diluted with 1:10 volum ratio of FEC

Model II: It was necessary to extend the model to take into account the temporal evolution of the SEI. In the system under study, where the SEI forms without any applied current, simultaneous oxidation of the Li metal to Li^+ is required in order to maintain the charge balance (see equation (2.16)). SEI formation has previously been modelled as being proportional to the exchange current density at the metal/electrolyte interface.¹⁸⁴ A similar approach is used here where the SEI formation, dN_{SEI}/dt , is taken to be proportional to J_{ex} :

$$\frac{dN_{\text{SEI}}}{dt} = \alpha_{\text{SEI}}(t)J_{ex} \quad (5.9)$$

Where N_{SEI} [mol m^{-2}] is the total number of moles of Li in the SEI per surface area of Li metal and $\alpha_{\text{SEI}}(t)$ is the SEI formation constant, a proportionality constant that captures the rate of the SEI formation. The isotope ratio of SEI that forms at each time step is assumed to be equal to the electrolyte, $c_{e7}(t)$. The SEI formation is expected to slow down with time and the formation constant $\alpha_{\text{SEI}}(t)$ includes an exponential decaying term that varies with the amount of SEI formed:¹⁸⁵

$$\alpha_{\text{SEI}}(t) = \alpha_{\text{SEI},0} \exp(-\beta_{\text{SEI}} N_{\text{SEI}}(t)) \quad (5.10)$$

Where β_{SEI} [$\text{m}^2 \text{mol}^{-1}$] is the SEI growth constant. The growth of the SEI will also affect the overall permeability of the SEI and slow down the exchange flux over time, again captured here with a decaying exponential:¹⁸²

$$J_{ex}(t) = J_{ex,0} \exp(-\beta_{ex} N_{SEI}(t)) \quad (5.11)$$

Where β_{SEI} [$\text{m}^2 \text{mol}^{-1}$] is the SEI permeability constant. In addition, the SEI formation will affect the isotope ratio in the electrolyte. As described in equation (2.16), the chemical formation of the SEI involves the reduction of an electrolyte component resulting in depositing a (Li^+ electrolyte $^-$) salt (such as LiF, Li_2CO_3 or an organic, e.g., lithium diethylcarbonate) that is coupled with oxidation of Li metal. Overall the Li^+ ion concentration in the electrolyte should remain constant but differences in isotope ratio between the electrolyte and metal will result in changes to the isotope concentration in the electrolyte, c_{e7} as follows:

Since the consumption of $^7\text{Li}^+$ in the electrolyte to form the SEI is $\frac{dN_{SEI}}{dt} f_{e7}(t)$ and the rate of ^7Li metal oxidised to Li^+ is $\frac{dN_{SEI}}{dt} f_{m7}(0, t)$, the change in moles of the ^7Li isotope in the electrolyte as a result of this process is $\frac{dN_{SEI}}{dt} (f_{e7}(t) - f_{m7}(0, t)) S_a$, and equation (5.8) becomes instead:

$$\frac{dc_{e7}}{dt} = -\frac{S_a}{V_e} (J_{ex}(t) + \frac{dN_{SEI}}{dt} (f_{e7}(t) - f_{m7}(0, t))) \quad (5.12)$$

The final model, termed **Model II** and shown schematically in Figure 5.2c, solves Equations (5.4)-(5.7) and (5.9)-(5.12) with the four fitting parameters, $J_{ex,0}$, $\alpha_{SEI,0}$, β_{ex} and β_{SEI} .

To fit the experimental data, the equations for Model I and II were discretised using method of lines and solved using an ode-solver in MATLAB (ode45 function).¹⁸⁶ A nonlinear least-square solver (lsqcurvefit function) was used to fit the experimental data, the ^7Li intensity of the metal and the ^7Li diamagnetic intensity (including the electrolyte and SEI), to the numerical model. The nlparci function was used to generate a 95% confidence interval of the fitting parameters. The skin depth of the Li metal is taken into account when fitting the model to the NMR intensity of the metal peak, the NMR being only sensitive to the surface of the Li metal, the skin depth described in equation (3.11).

Note, the exact chemical composition of the SEI is unknown and thus the thickness of the SEI, $s(t)$, can only be compared by assuming a certain chemical composition with a molar mass, M , and a density ρ :¹⁸²

$$s(t) = \frac{M}{n\rho} N_{SEI}(t) \quad (5.13)$$

where n is the number of Li atoms per SEI component. For the sake of discussion only, the SEI is assumed to be comprised of pure Li_2CO_3 ($M = 29.88$ g/mol, $n = 2$ and $\rho = 2.01$ g/cm³); although the presence of organic, less dense components will result in an even thicker SEI than obtained using this composition, the current assumption allows for an order-of-magnitude estimation of the SEI thickness, which is helpful for comparison with experimental data.

5.4 Results

5.4.1 Isotope exchange measurements in different electrolytes

To understand the effect that the FEC additive has on the SEI formed on Li metal and the corresponding plating behaviour as observed in Chapter 4, isotope exchange measurements were performed in both LP30 and LP30 + FEC electrolytes. Static ^7Li NMR (Figure 5.3, in LP30 electrolyte) was used to follow the changes in signal intensities of Li metal and the electrolyte as a function of time.

When the ^6Li -metal is soaked in the ^7Li -electrolyte, the ^7Li NMR signal centred around 0 ppm decreases and the ^7Li metal signal, centred at approximately 275 ppm grows in (Figure 5.3).¹³⁵ This is due to the continuous oxidation and reduction between the metal and the electrolyte during equilibrium as described in equation (5.1). Because of the skin depth effect, the NMR is only sensitive to the surface layers of the metal whereas the signal intensity for the diamagnetic peak corresponds to the whole volume of the electrolyte and the SEI.

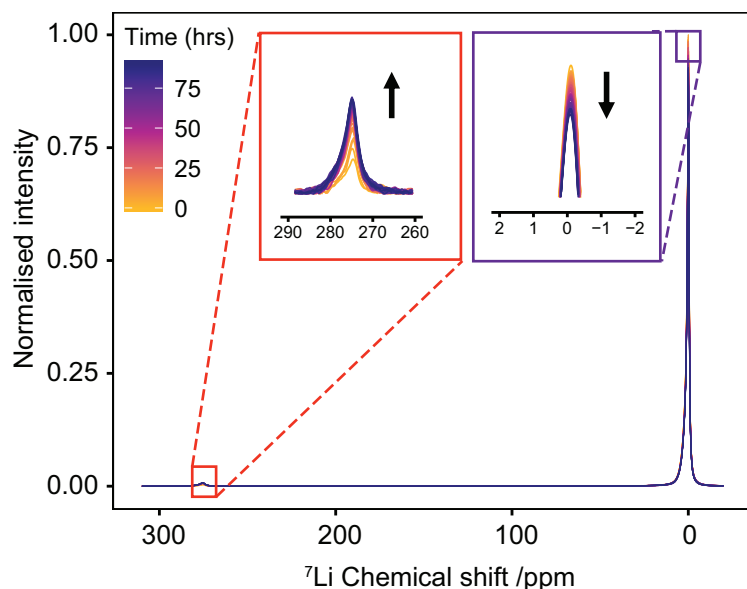


Figure 5.3 ^7Li NMR spectra of the electrolyte (around 0 ppm) and metal (around 275 ppm) during the ~ 75 -hour time period that the ^6Li -enriched strip of metal was soaked in natural abundance LP30 + FEC electrolyte.

Integration of the ^7Li NMR signal intensities as a function of time (Figure 5.4) shows significant differences between the two electrolytes; in LP30 + FEC (Figure 5.4a, orange) the ^7Li metal intensity increases faster and the ^7Li electrolyte peak intensity drops more quickly compared to LP30 (Figure 5.4, green), indicating more rapid exchange of lithium between the metal and electrolyte in the presence of FEC. The results were found to be reproducible shown with the shorter ‘Experiment 2’ in Figure 5.4 (in purple and light-green).

A control experiment, using a natural abundance Li metal electrode (“ ^7Li rich”, 92.4% ^7Li and 7.6% ^6Li) in LP30 + FEC electrolyte was performed to observe the trends when the effect of isotope exchange is eliminated. The changes in intensities are minimal (Figure 5.4, pink) indicating that the formation of the SEI should not change the overall Li^+ concentration in the electrolyte substantially. The NMR intensity of the electrolyte even increases very slightly (Figure 5.4b, pink), which is ascribed to the SEI and partial dissolution of the SEI into the electrolyte.¹⁶²

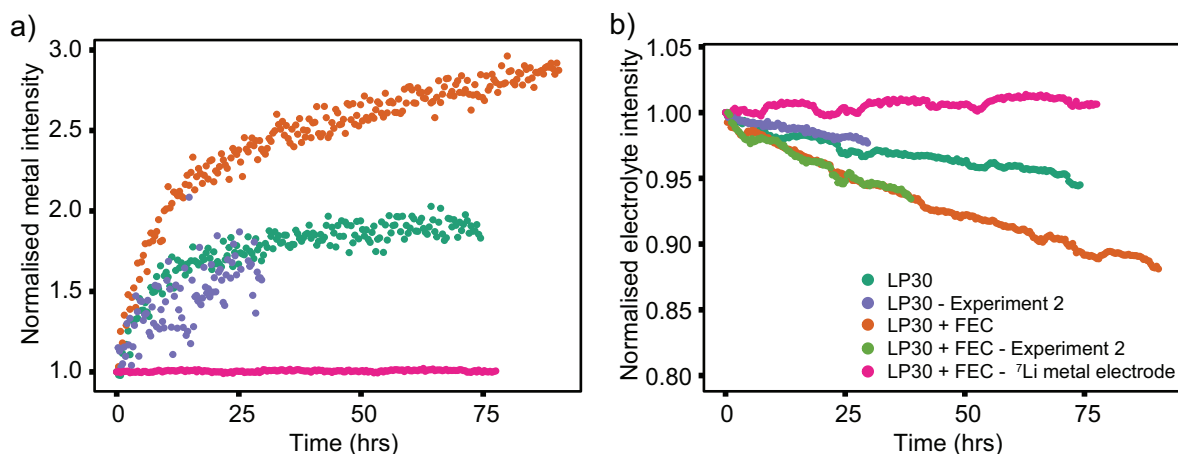


Figure 5.4 The intensity changes of the ^7Li NMR spectra recorded over 75 hours for **a)** the lithium metal signal and **b)** the diamagnetic lithium signal in the two electrolytes LP30 (green and purple) and LP30 + FEC (orange and light-green). The curve in pink shows the “control experiment” using a natural abundance Li metal strip where the effect of isotope exchange is removed.

5.4.1.1 Numerical fit to the isotope exchange curves

The mathematical model described in section 5.3 for the $^6\text{Li}/^7\text{Li}$ isotopic exchange was used to extract the associated kinetic data from the NMR experiments. Initially, a simplified model was formulated that only takes into account the isotope exchange between the metal and the electrolyte and neglects the formation of the SEI (Model I).

The fitting of the experimental curves using Model I and equations (5.4)-(5.8), involves only one fitting parameter, J_{ex} and implicitly assumes that the SEI remains constant with time. The values of J_{ex} obtained from a least-square fit are $0.77 \times 10^{-6} \text{ mol m}^{-2} \text{ s}^{-1}$ for LP30 and $1.5 \times 10^{-6} \text{ mol m}^{-2} \text{ s}^{-1}$ for LP30 + FEC (approximately twice as fast in LP30 + FEC). However, the experimental curves are not well described by Model I as seen in Figure 5.5 (dashed lines).

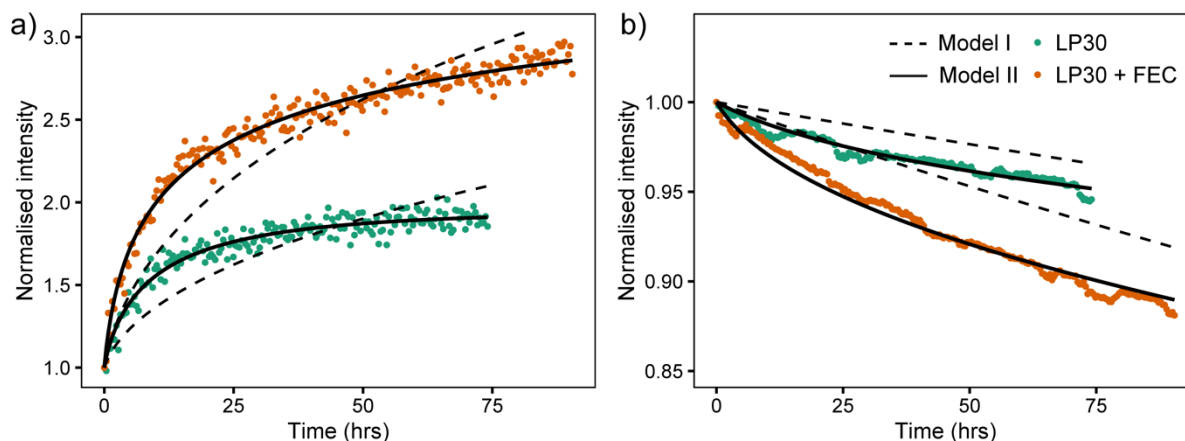


Figure 5.5 The intensity changes of the ^7Li NMR spectra (points) and the model fit results for Model I (dashed lines) and Model II (black lines) for **a)** the lithium metal and **b)** the lithium ions in the electrolyte, in the two electrolytes LP30 (green) and LP30 + FEC (orange).

The model was then further extended to take into account the long-term formation of the SEI (Model II).¹⁸² The fit to the experimental curves is shown in Figure 5.5 (Model II, black lines) and the corresponding parameters are presented in Table 5.2. At the beginning of the experiment, the exchange flux for LP30 + FEC, $J_{ex,0}$ is again roughly two times that for LP30 (Table 5.2). The exchange flux of Li includes the rate of charge-transfer, diffusion through the SEI and desolvation of Li^+ ions.

To describe the rate of SEI formation the model assumes the formation of the SEI to be proportional to the isotope exchange flux, J_{ex} and includes the dimensionless SEI formation constant, $\alpha_{SEI}(t)$, equation (5.9). Of note is that the SEI forms instantly when the Li metal is immersed in the electrolyte but grows gradually over time periods of hours to several days as indicated by the increasing impedance measured by EIS.^{116,169} The SEI formation constant α_{SEI} , is greater in LP30 + FEC indicating faster SEI formation (Table 5.2).

The rate of SEI formation slows down with time, as can be seen from the impedance analysis in section 5.4.2. This is described with the decreasing exponential in equation (5.10), which includes the fitting parameter β_{SEI} , the SEI growth constant. The formation rate in LP30 + FEC decreases faster as described by β_{SEI} , indicating better passivation.

In addition, the model includes the maturation of the SEI, which leads to reduced permeability of the SEI and the exchange flux becomes time-dependent, $J_{ex}(t)$, as described in equation

(5.11). The decrease in the permeability of the SEI due to the growing SEI, captured with β_{ex} , is greater in LP30, which leads to an increased difference in the exchange flux at 74 hrs. The ratio of $J_{\text{ex},74}$ between the two electrolytes grows from 2 to 2.5 and indicates increasingly reduced transport properties in the LP30-derived SEI.

Table 5.2 List of the fitted model parameters ($J_{\text{ex},0}$, β_{ex} , $\alpha_{\text{SEI},0}$ and β_{SEI}) obtained from the numerical simulation of the isotopic exchange in the electrolytes, LP30 and LP30 + FEC from Model II. The upper and lower values for the 95% confidence bounds are given in brackets. The ratio between the values for (LP30 + FEC)/(LP30) is displayed.

Symbol	Description/Unit	LP30	LP30 + FEC	Ratio
$J_{\text{ex},0}$	Isotope exchange flux at the time of the first NMR measurement [10^{-6} mol m^{-2} s^{-1}]	1.6 (1.5 – 1.7)	3.1 (2.9 – 3.3)	1.9
$J_{\text{ex},74}$	Isotope exchange flux at 74 hrs [10^{-6} mol m^{-2} s^{-1}]	0.49	1.2	2.5
β_{ex}	SEI permeability constant [m^2 mol^{-1}]	19 (6.8 – 31)	7.8 (5.3 – 10)	0.41
$\alpha_{\text{SEI},0}$	SEI formation proportionality constant Dimensionless	0.38 (0.13 – 0.63)	0.85 (0.53 – 1.2)	2.2
β_{SEI}	SEI growth constant [m^2 mol^{-1}]	8.7 (0 – 18)	17 (11 – 23)	2.0
N_{SEI}	Number of moles of SEI formed per surface area at time 74 hrs [mmol m^{-2}]	61	120	2.0

According to the simulation, the number of moles per surface area formed in the two electrolytes, N_{SEI} (Table 5.2) is greater for the LP30 + FEC electrolyte, indicating a thicker SEI being formed. We have estimated the growth rate of the SEI by using equation (5.13), assuming it to be pure Li_2CO_3 so as to provide a qualitative understanding of the extent of SEI formation. Averaging over the whole experiment (74 hours) the SEI formation rate is 6.1 nm/hr in LP30 and 12 nm/hr for LP30 + FEC. The values are relatively large and seem to overestimate the thickness of the SEI but are on a similar scale to what was estimated in an earlier isotope exchange study (14 nm/hr in LP30).¹⁸² One possible reason for this overestimation of thickness is the assumption that all of the reduced electrolyte species are deposited to form the SEI. However, it has been shown experimentally that a wide range of the reduced electrolyte species

are soluble and go into the electrolyte.^{168,187,188} We also note that the comparison of SEI thicknesses needs to be interpreted with caution as the chemical composition and density is expected to differ between the two electrolytes.

The confidence interval of the fitted parameters is displayed in brackets in Table 5.2. The most important observation is the large interval for β_{SEI} in LP30, which is 0-18 $\text{m}^2 \text{mol}^{-1}$ compared to 11-23 $\text{m}^2 \text{mol}^{-1}$ for LP30 + FEC. This may indicate that the exponential decay of the SEI growth rate with time (equation (5.10)) does not fully capture the SEI formation process. Alternatively, this could also demonstrate the instability of the SEI formed in LP30 which has been shown to form more soluble SEI products on silicon compared to LP30 + FEC.¹⁸⁹ This explanation is consistent with the impedance data analysed in section 5.4.2 where the resistance of the SEI for LP30, R_{SEI} , keeps growing with time.

Of note is that the ratio between $J_{ex,0}$ for LP30 + FEC and LP30 is roughly the same for both models, Model I and Model II (a factor of two), although the resulting values of the parameter are different. To examine the sensitivity of the fit to $J_{ex,0}$, a fit using Model II was performed with the value of $J_{ex,0}$ fixed to the results from Model I ($0.77 \times 10^{-6} \text{mol m}^{-2} \text{s}^{-1}$ for LP30 and $1.5 \times 10^{-6} \text{mol m}^{-2} \text{s}^{-1}$ for LP30 + FEC).

Figure 5.6 shows that we cannot fit the data with the $J_{ex,0}$ fixed to the values obtained from Model I.

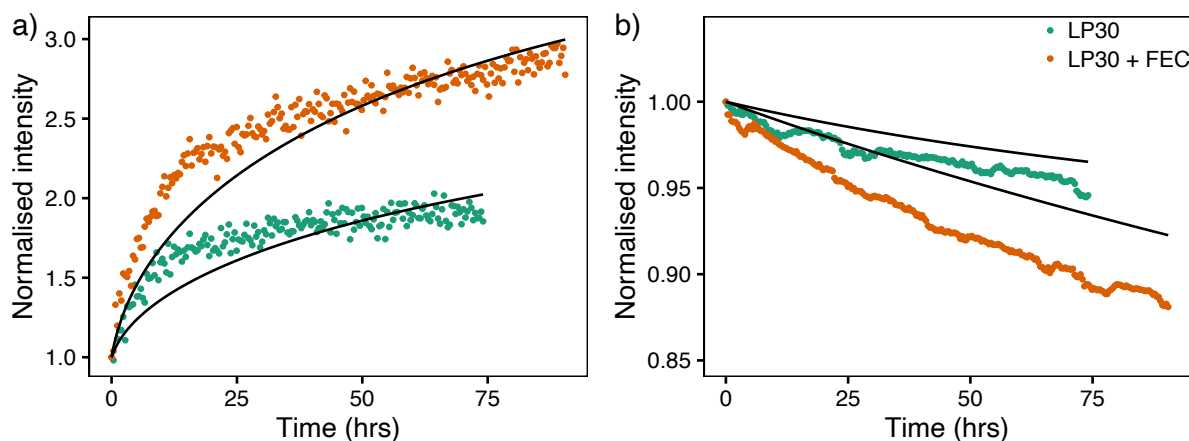


Figure 5.6 Sensitivity analysis using fixed values of $J_{ex,0}$ obtained from Model I.

5.4.1.2 The isotope exchange current density

Multiplying the exchange flux, $J_{ex}(t)$ by the Faraday constant gives the isotope exchange current density:

$$j_{ex}(t) = F \times J_{ex}(t) \quad (5.14)$$

which at the beginning of the simulation is $15 \mu\text{A}/\text{cm}^2$ for LP30 and $30 \mu\text{A}/\text{cm}^2$ for LP30 + FEC. The exchange current density decreases with time due to the reduced permeability of the SEI (Figure 5.7a).

To demonstrate how this methodology can be applied to different electrolytes, the results for isotope exchange in 4 M LiFSI in DME (referred to as 4M-LiFSI) are included in Figure 5.7. Qian et al. reported stable cycling of Li metal in this highly concentrated electrolytes, with CE above 99% at high rates.⁶² The excellent cycling in this electrolyte was attributed to the high Li^+ ion concentration, which result in a more uniform Li^+ flux to the electrode but also to a more stable and less soluble SEI.⁶² The initial j_{ex} in 4M-LiFSI is $34 \mu\text{A}/\text{cm}^2$ that has decreased to $13 \mu\text{A}/\text{cm}^2$ at 50 hrs. Of note is the fast stabilisation of the exchange current in 4M-LiFSI that indicates rapid passivation of the Li metal and that leads to more uniform exchange flux.

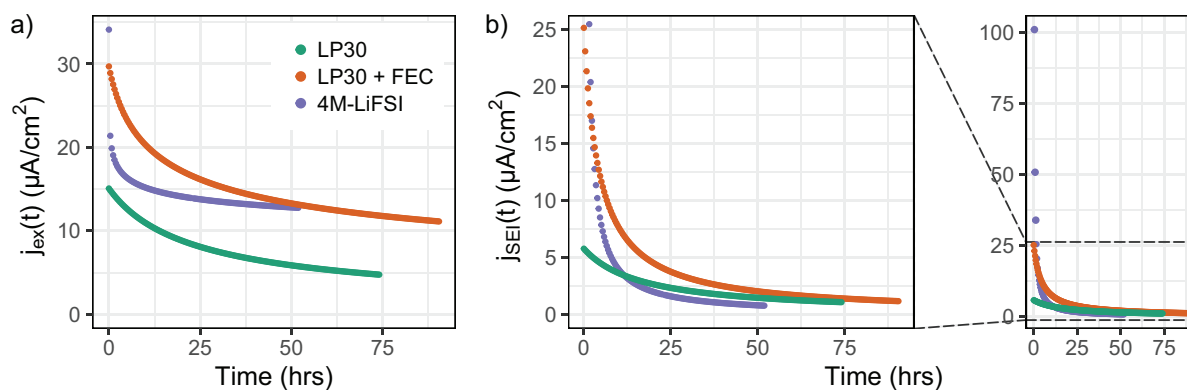


Figure 5.7 **a)** The exchange current density j_{ex} ($\mu\text{A cm}^{-2}$) and **b)** the SEI formation current density j_{SEI} ($\mu\text{A cm}^{-2}$) in LP30 (green), LP30 + FEC (orange) and 4M LiFSI in DME (purple). The plot for the SEI formation current density is shown by zooming in on a subset of the data, to aid for comparison. The whole range is shown to the left.

The SEI formation current at OCV is calculated similarly (using equation (5.9)):

$$j_{SEI}(t) = F \times \alpha_{SEI} \times J_{ex}(t) \quad (5.15)$$

and is around $6 \mu\text{A}/\text{cm}^2$ in LP30 and $26 \mu\text{A}/\text{cm}^2$ in LP30 + FEC. For 4M-LiFSI it starts at $100 \mu\text{A}/\text{cm}^2$ but drops rapidly to an equilibrium current density of $0.8 \mu\text{A}/\text{cm}^2$ at 50 hours, compared to $1.5 \mu\text{A}/\text{cm}^2$ and $2 \mu\text{A}/\text{cm}^2$ in LP30 and LP30 + FEC (Figure 5.7b).

Using the Butler-Volmer formulism to describe the isotope exchange current j_{ex} ; an estimate of the isotope exchange rate constant, k_{ex} [m s^{-1}], can be obtained according to:

$$j_{ex}(t) = Fk_{ex}(t)[Li^+]^\beta [Li^0]^{1-\beta} \quad (5.16)$$

The value of the transfer coefficient β , is assumed to be 0.5, which has been found to fit a range of experimental data adequately.^{113,190,191} Similarly, the SEI formation rate constant is defined as $k_{SEI} = \alpha_{SEI} k_{ex}$ (equation (5.9)). The calculated values of the rate constants are listed in Table 5.3.

Table 5.3 The rate constants calculated from the simulation of the isotopic exchange in the electrolytes, LP30, LP30 + FEC and 4M LiFSI in DME (4M-LiFSI).

Symbol	Description/Unit	LP30	LP30 + FEC	4M-LiFSI
$k_{ex,0}$	Exchange rate constant [$10^{-10} \text{ m s}^{-1}$]	1.8	3.7	4.03
$j_{ex,0}$	Exchange current [$\mu\text{A cm}^{-2}$]	15	30	34
$k_{ex,50hrs}$	Exchange rate constant at 50 hrs [$10^{-10} \text{ m s}^{-1}$]	0.70	1.6	1.5
$k_{SEI,0}$	The SEI formation rate constant [$10^{-10} \text{ m s}^{-1}$]	0.68	3.1	12
$k_{SEI,50hrs}$	The SEI rate constant at 50 hrs [$10^{-10} \text{ m s}^{-1}$]	0.17	0.25	0.09

5.4.2 Impedance spectroscopy

Impedance measurements of Li metal are extremely sensitive to how the Li is handled beforehand. An untreated Li foil will most likely have a native SEI (formed in the inert atmosphere in the glovebox from trace amounts of impurities such as O_2 , CO_2 and H_2O), which results in a high impedance. After plating Li, the semicircle in the Nyquist plot is generally seen to shrink significantly due to the increased surface area of the electrode. Impedance spectroscopy of Li metal can be hard to interpret and deconvolute because of the combined effect of the SEI and surface area. The exact impedance values obtained by EIS on Li metal should thus be compared with caution between systems. However, the temporal evolution of the Li metal impedance may be readily analysed to monitor the long-term temporal stability of the SEI. The Li metal, with the initially formed SEI layer, continues to react with the electrolyte where the reduction products precipitate, partly dissolve and redeposit throughout what has been referred to as “the aging process”.¹¹⁶

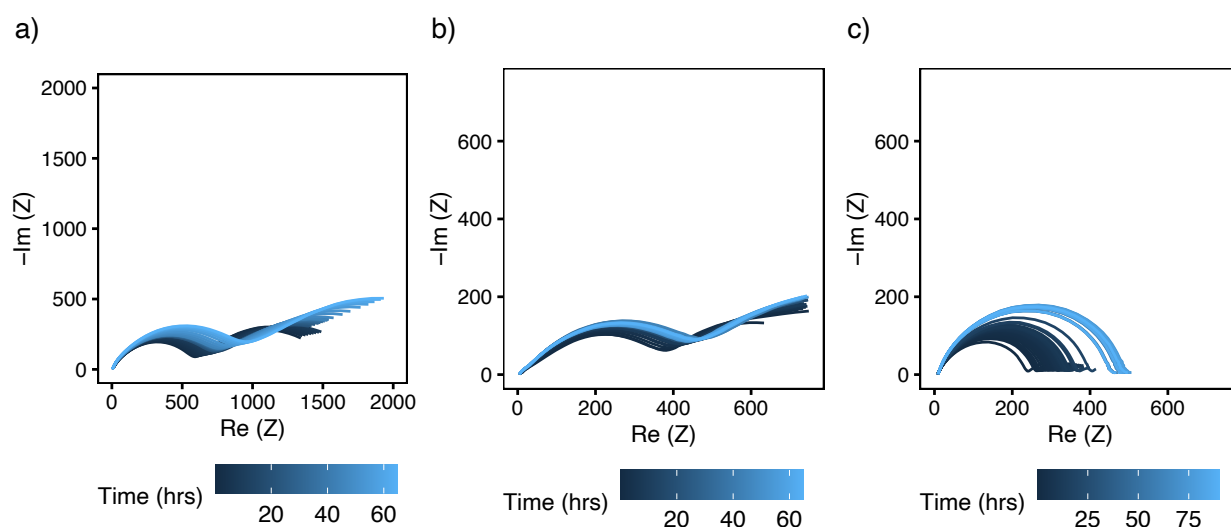


Figure 5.8 The Nyquist plot for symmetric Li-Li coin cells at OCV in **a)** LP30 electrolyte, **b)** LP30 + FEC and **c)** 4M-LiFSI.

EIS was performed in symmetrical Li-Li coin cells at the OCV. Before the measurement the Li metal was pre-conditioned using 1 mA/cm^2 for 0.04 mAh/cm^2 for one plating and stripping cycle. This was done to ensure fresh Li deposits on the surface that then react with the

electrolyte to form the SEI. The Nyquist plots for both carbonate electrolytes show two depressed semicircles (Figure 5.8) that are typical for processes with a distribution of time constants, e.g. the physical properties of different parts of the SEI (often referred to as the porous and dense part or the inorganic and organic part).¹¹⁸

The equivalent circuit used to fit the spectra included three ‘R-C circuit’ elements, but instead of a pure capacitor the constant phase element (CPE) was used, which reflects the distribution in time constants due to the Li^+ migration in the compact and porous layers of the SEI.^{116,118} The resistances of the compact SEI layer (R_1), the porous SEI layer (R_2) and the charge transfer resistance (R_3) were combined into $R_{\text{SEI}} = (R_1 + R_2 + R_3)/2$, and divided by two to account for the two Li metal electrodes. R_{SEI} is shown as a function of time in Figure 5.10.

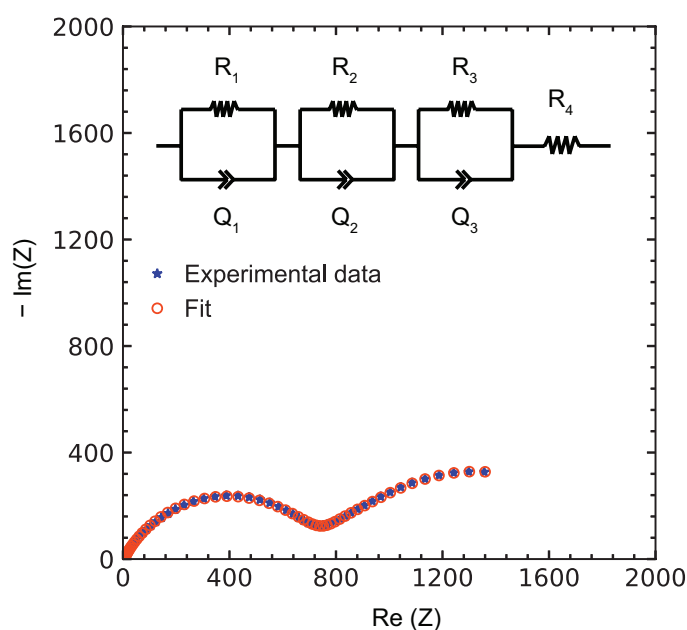


Figure 5.9 The fit to the EIS data in LP30, at time = 12 hours and the equivalent circuit used to fit the spectra, where R_1 and Q_1 (C_1 , capacitance and a_1 , parameter which describes how close it is to an ideal capacitor) are the resistance and the constant phase element (CPE) for the SEI compact layer respectively, R_2 and Q_2 (C_2 and a_2) for the porous part of the SEI layer respectively, R_3 and Q_3 (C_3 and a_3) for the charge transfer between SEI film and electrolyte, and R_4 is the bulk electrolyte resistance. Fitting of impedance spectra to the equivalent circuit was carried out in MATLAB using a code written by Sundeep Vema.

Comparing the carbonate electrolytes, the resistance of the LP30 + FEC is both lower and reaches an equilibrium value whereas for LP30 it continues to increase with time. The 4M-LiFSI electrolyte is seen to have both lower and more stable impedance. This is consistent with

the isotope exchange results of the SEI formation current density, which stabilised and plateaued faster compared to the carbonate electrolytes (Figure 5.7). The apparent exchange current density may be calculated from the resistance value of the SEI, according to:¹¹³

$$j_{ex,EIS} = \frac{RT}{FR_{SEI}} \quad (5.17)$$

where R is the gas constant and T the temperature. This results in an initial exchange current of $32 \mu\text{A}/\text{cm}^2$ for LP30, $57 \mu\text{A}/\text{cm}^2$ for LP30 + FEC and $176 \mu\text{A}/\text{cm}^2$ for 4M-LiFSI. In all cases, the exchange current estimated from EIS is higher than by isotope exchange simulations (Table 5.3).

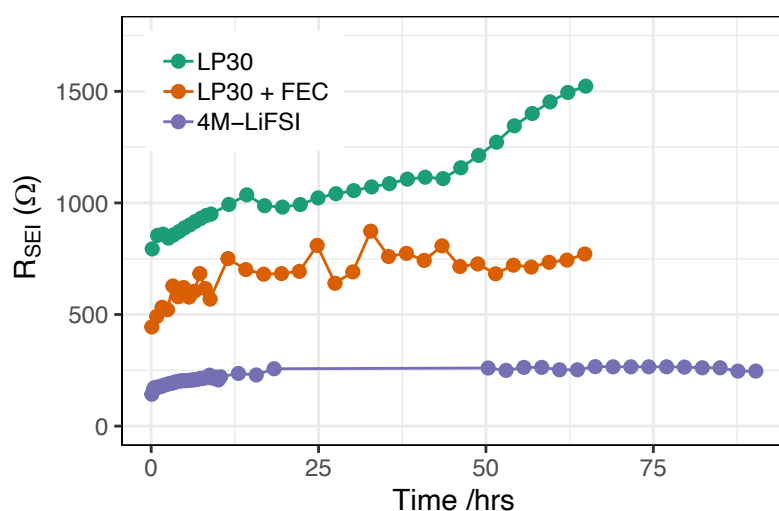


Figure 5.10 The resistance of the SEI on Li metal, $R_{SEI} = (R_1 + R_2 + R_3)/2$, determined from the fitting of the impedance spectra in LP30 (green), LP30 + FEC (orange) and 4M-LiFSI (purple).

5.4.3 Temperature dependence on isotope exchange

Finally, isotope exchange was studied with temperature, the exchange expected to speed up at elevated temperatures. The exchange rate constant is expected to show Arrhenius dependence on temperature, as described in Chapter 2 in equation (2.4):⁸⁸

$$k_{ex} = A \exp\left(-\frac{\Delta G_{ex}^\ddagger}{RT}\right) \quad (5.18)$$

where ΔG_{ex}^\ddagger is the transition state for the electrode-electrolyte exchange.⁹⁰ Included in the activation energy is the Li^+ ion desolvation, transport through the SEI and charge transfer at the electrode surface.⁴⁴ In addition, degradation of electrolytes is accelerated at elevated temperatures (>313 K) that leads to an increased SEI thickness.⁵¹ The ^6Li -enriched metal electrodes were soaked in LP30 electrolyte at two temperatures, 313 K and 323 K. The integrated NMR intensities of the ^7Li metal and electrolyte peaks are shown in Figure 5.11. The ^7Li electrolyte peak intensity decreases faster at elevated temperatures (Figure 5.11b).

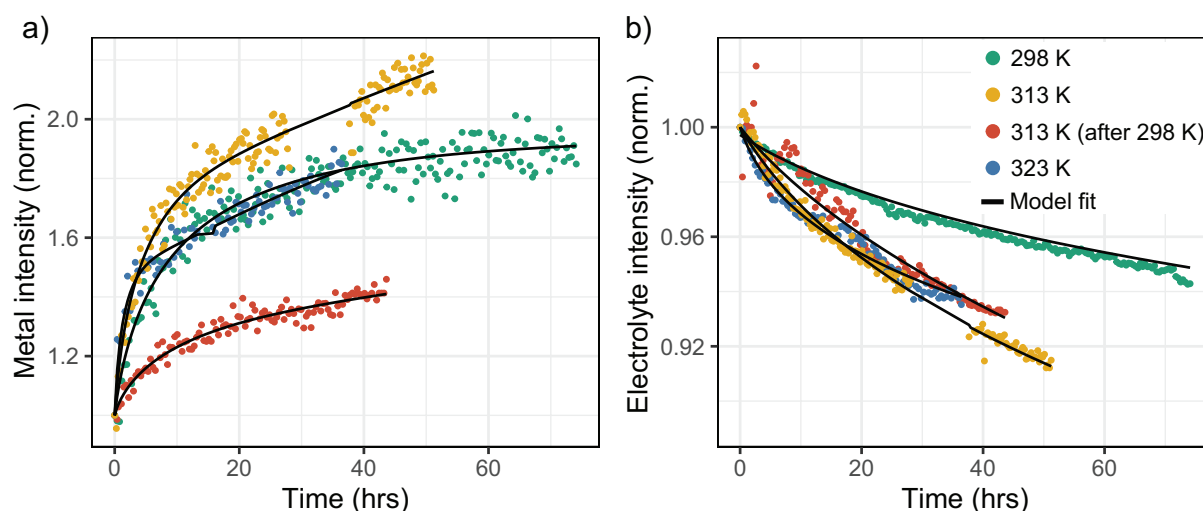


Figure 5.11 The intensity changes of the ^7Li NMR spectra (points) for **a)** the Li metal and **b)** the diamagnetic Li^+ in the LP30 electrolyte and at three temperatures; 298 K (green, also displayed and analysed in section 5.4.1), 313 K (yellow) and 323 K (blue). In red is the measurement at 313 K, which has been soaked initially at 298 K for 25 hrs. The electrolyte was replaced at 25 hours with a fresh LP30 electrolyte and the temperature raised to 313 K. The corresponding fit to the curves, using Model II explained in 5.3, is shown in black.

The change in the metal peak intensity is more convoluted; at the same time an increased exchange rate is expected an increased SEI thickness will likely lead to a decreased exchange rate (as observed in section 5.4.1.1 for growing SEI). In addition, the self-diffusion in the Li metal increases at higher temperatures. The diffusion coefficient of the Li metal is estimated

using the empirical equation obtained in the NMR relaxometry study by Messer and Noack, which gives $D_{m,313K} = 2.06 \times 10^{-14} \text{ m}^2 \text{ s}^{-1}$ and $D_{m,323K} = 3.99 \times 10^{-14} \text{ m}^2 \text{ s}^{-1}$.¹⁸³

To lessen the effect of the SEI formation, an enriched ^6Li metal was also soaked in the electrolyte at 298 K for 25 hours before increasing the temperature to 313 K (Figure 5.11b, red). During the first 25 hours, both isotope exchange and formation of the SEI will occur as described in section 5.4.1.1. The electrolyte was replaced at 25 hours with fresh LP30 electrolyte, the temperature raised to 313 K and the NMR measurements performed. For fitting of this data set, the initial input for the ^7Li concentration in the metal, $f_{m7}(x, 0)$, will be the output for $f_{m7}(x, t = 25 \text{ hrs})$ in section 5.4.1.1. The initial value for the electrolyte is $f_{e7}(x, 0) = 0.92$, as before.

Fitting of the experimental curves was performed using **Model II** presented in section 5.3. The fitted curves are shown in black (Figure 5.11 a, b) and the resulting values of the fitted parameters are displayed in Table 5.4. The value of the isotope exchange flux $J_{ex,0}$ increases at higher temperatures (Table 5.4), as expected from equation (5.18). However, the rate of SEI formation (captured with $\alpha_{SEI,0} \times J_{ex,0}$) does not follow any obvious trend. This is examined on more detail by calculating the exchange and SEI current density as a function of time, j_{ex} and j_{SEI} , according to equations (5.14) and (5.15) and shown in Figure 5.12.

Table 5.4 The model parameters ($J_{ex,0}$, β_{ex} , $\alpha_{SEI,0}$ and β_{SEI}) obtained from the fits of the isotope exchange curves in LP30 electrolyte and at three different temperatures, shown in Figure 5.11. The 95% confidence intervals are given. The initial rate of the SEI formation is calculated as: $\alpha_{SEI,0} \times J_{ex}$.

Symbol	298 K	313 K	323 K	313 K (after 298 K)
$J_{ex,0}$	1.6 ± 0.09	3.7 ± 0.2	6.5 ± 0.8	3.6 ± 0.2
β_{ex}	20 ± 10	60 ± 90	150 ± 300	10 ± 7
$\alpha_{SEI,0}$	0.4 ± 0.3	0.09 ± 0.1	0.09 ± 0.2	0.2 ± 0.1
β_{SEI}	9 ± 9	40 ± 60	70 ± 150	20 ± 17
$\alpha_{SEI,0} \times J_{ex}$	0.64	0.33	0.59	0.72

The exchange current density is higher at the elevated temperatures, 313 K and 323 K as expected, and seen to drop more rapidly due to the SEI formation. This is especially evident for j_{ex} at 323 K (Figure 5.11a, blue) where j_{ex} decreases and is of similar magnitude to j_{ex} at 298 K after 20 hours. Interestingly, j_{ex} is comparable for the two measurements at 313 K (Figure 5.11c, red and yellow), which gives confidence in the approach. In principle, the exchange rate constant should be identical for the two measurements at 313 K unless the SEI formed initially at room temperature differs drastically in composition and transport properties.

The calculated SEI current density is seen to be lower at elevated temperatures (Figure 5.12b, yellow and blue), contrary to what is expected. However, these measurements might not capture the continuously evolving SEI accurately. That is, because the initial SEI is expected to form within seconds after immersing the Li metal into the electrolyte¹⁶⁹ and transferring the sample to the NMR spectrometer takes about 15 minutes. This means the initial SEI forms during the preparation time, *at room temperature*. In addition, heating the NMR probe takes about 30 minutes, so overall about 45 minutes have passed before the NMR measurements are performed. The initial data points of the isotope exchange are thus missing.

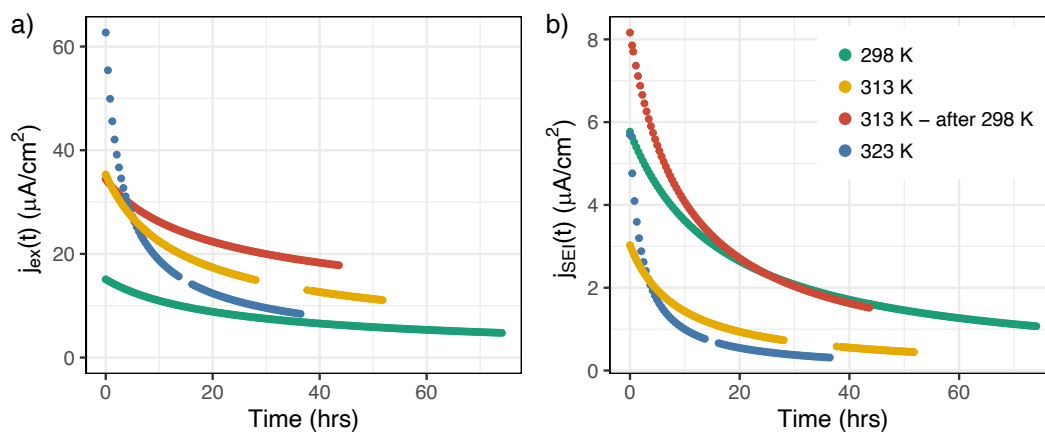


Figure 5.12 **a)** The exchange current density and **b)** the SEI formation current density calculated from the fit in LP30 electrolyte at 298 K (green), 313 K (yellow) and 323 K (blue). In red is the measurement at 313 K, that has prior been soaked at 298 K for 25 hrs.

The error is evident in the confidence intervals of the fitted parameters (Table 5.4) that increases for the measurements at elevated temperatures. Of note is especially the large confidence interval for the fitting parameters associated with the SEI formation, which is problematic and indicates that the numerical model does not describe the SEI formation process

in LP30 fully. This was discussed briefly in section 5.4.1.1 and attributed to the instability of the SEI formed in LP30. However, it is clear that the experimental procedure and/or the numerical model needs refining to fully capture the SEI formation and the values reported here should be interpreted with caution.

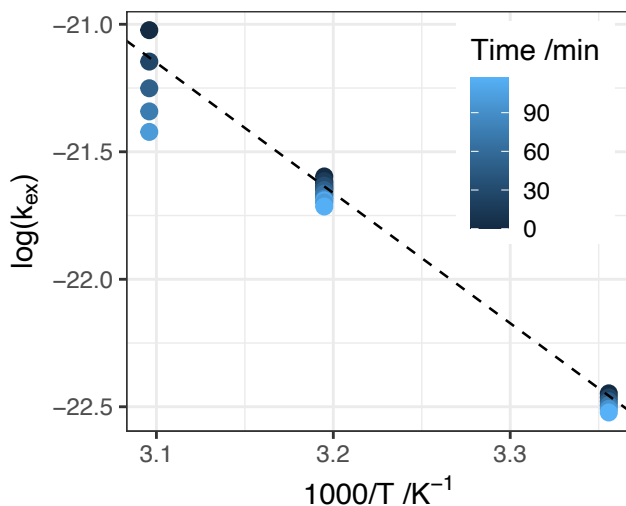


Figure 5.13 The temperature dependence of the exchange rate constant extracted from the simulation over the initial two hours of measurements. The rate constant is seen to decrease in magnitude, most noticeable at 323 K. The activation energy is calculated from the slope of the Arrhenius plot, only taking into account the first hour of measurements.

The exchange rate constant, $k_{ex}(t)$, is calculated directly from the exchange flux extracted from the fit, according to equation (5.16). $k_{ex}(t)$ decreases with temperatures as seen with the drop in j_{ex} (Figure 5.12a). Figure 5.13a shows the value of the exchange rate constant over the initial two hours of the simulations (that drops significantly at 323 K). The activation energy was calculated from the slope, assuming an Arrhenius relationship and only taking into account the first hour of measurement. The activation energy obtained is 0.44 eV.

5.5 Discussion

The exchange current density of a system reflects the kinetic properties of the electrode-electrolyte interface at equilibrium, when there is no net current flowing at the electrode. Thus,

it cannot be measured directly by electrochemical methods where a net current is generated and the system moves away from equilibrium.⁸⁹ The exchange current density is generally calculated from the so-called Tafel slope on a current–overpotential plot.⁹⁰ It is especially difficult to measure it on Li metal due to the concurrent SEI that forms when passing charge and a single Tafel slope cannot be obtained.¹⁸ This is evident in the simulations where J_{ex} was found to be time-dependent because of the growing SEI, the isotope exchange current decreasing over the whole time period (Figure 5.7).

Boyle et al. overcame the issue and minimised the influence of the SEI by measuring the exchange current density for Li metal deposition using an ultramicroelectrode and fast scan rates of >1000 mV/s.¹¹³ This should ensure the exchange current is only affected by the charge transfer kinetics and not diffusion in the SEI.¹¹³ Our results from the isotope exchange simulations should be contrasted with those of Boyle et al. who found similar to us that j_0 was higher in a carbonate electrolyte with FEC, approximately 1.5 times.¹¹³ They attributed the faster electron transfer kinetics to the slightly lower Li^+ concentration when the FEC is added to the electrolyte and thus weaker interactions between ions.¹¹³ Here, the exchange current differs initially by a factor of 2 which grows to a factor of 2.5 at longer time periods, and depends on both the electrode kinetics and the mass transport through the SEI.

It is noted that the exchange current density estimated by isotope exchange is three orders of magnitude lower than that obtained by Boyle et al. by Li plating on a tungsten-ultramicroelectrode (with little to no SEI) and an order of magnitude lower than that estimated on Li metal by impedance spectroscopy (with SEI).¹¹³ Here, the exchange current estimated from impedance measurements (section 5.4.2) is on the same order of magnitude as from the isotope exchange, although in all cases a higher value is calculated from the impedance. This may indicate, that the SEI resistance measured with impedance spectroscopy is not fully comparable with the exchange current measured here. Impedance spectroscopy resolves components at different frequencies, and thus captures local phenomena, while the isotope exchange directly probes the entire interphase between the electrolyte and metal, in addition to the charge transfer. Furthermore, the impedance spectroscopy shows correlates with the SEI formation current extracted from the isotope exchange model, with faster stabilisation observed for LP30 + FEC and 4M-LiFSI.

The electrolytes studied in this work show clear differences: the ${}^6\text{Li}/{}^7\text{Li}$ exchange is twice as fast in LP30 + FEC compared to LP30 (Table 5.2, due to faster Li^+ transport in the SEI), and the SEI formation rate is more than four times faster, as compared to LP30. For LP30, the slower Li^+ transport can lead to non-uniform current distribution during plating, localised deposition resulting in stress-build up in the SEI and whisker-growth.^{37,39,57} The more whisker-like morphology that forms in LP30 as shown in Chapter 4 can be explained, at least in part, by the slower Li^+ transport in the SEI. The high surface area of the whiskers leads to low current efficiency due to constant SEI formation, the slow SEI formation rate also impeding the full repair of the SEI.

However, low exchange current density has been associated with levelling effects and smoother deposition of metals.^{192,193} This might not be entirely accurate for Li metal deposition, where the effective exchange current density is constantly changing due to the SEI formation. Instead, the spatial distribution of rate constants on the Li metal surface should be minimized to obtain a homogeneous current distribution on the electrode surface.^{44,194} That is, an SEI that results in an even deposition over the Li metal surface is more significant here and fast SEI kinetics are preferable, which have been suggested as an important parameter in choosing electrolytes for LMBs.³²

This is because in the event that the SEI breaks, fresh Li deposits will have faster effective exchange current density. Fast SEI repair on the freshly exposed lithium will reduce impedance differences on different sites on the electrode's surface leading to more homogeneous deposition.⁴⁴ This points to rapid passivation on Li metal being key parameter of a good SEI layer. The simulations of the isotope exchange indicate that the SEI growth rate is more than four times faster in LP30 + FEC, clearly demonstrating the faster kinetics associated with FEC degradation. This is consistent with the higher reduction potential of FEC¹⁷⁰ that has been shown to occur at ~ 1.3 V compared to ~ 0.8 V (vs Li/Li^+) for the EC solvent molecule.¹⁹⁵ The initial SEI formation is even faster in 4M-LiFSI (Figure 5.7b), which than passivates rapidly indicating a stable and robust SEI.⁶²

Of note is that there may be differences between the chemically formed SEI studied here and that formed on cycling in terms of composition and morphology (section 2.2.2). The SEI formed during the rest period in pulse plating is directly related to the isotope exchange

measurements, as it forms under OCV. The values obtained are particularly relevant to Li corrosion,^{196,197} which will be discussed in Chapter 6.

We show that the metal-electrolyte exchange occurs faster at elevated temperatures. While the temperature measurements are preliminary, it demonstrates that the activation energy of charge transfer and the ion transport through the SEI may be obtained using isotope exchange. The activation energy (~ 0.4 eV, albeit only from three data points) is comparable to values reported from temperature-dependent EIS measurements. Due to the difficulties in measuring accurate values on Li metal, studies have turned to model system of the SEI; Guo and Gallant measured the activation energy for ionic conduction in LiF and Li₂O pellets on Li metal of 0.47 eV and 0.58 eV.¹⁹⁸ Schranzhofer et al. measured the activation energy for the SEI formed on Ni electrode to be 0.66 eV.¹⁹⁹ Wang et al. prepared pellets of lithium ethylene mono-carbonate (LEMC), believed to be a key component in the SEI, and calculated an activation energy of 0.76 eV.²⁰⁰ The range in reported activation energies reflects the inherent challenges of these measurements but also the heterogeneity of the SEI that forms on Li metal. Further work is needed here, with a wider temperature range and electrolytes, to establish the relationship of the coupled effect of exchange and SEI formation with temperature. Measuring the isotope exchange at lower temperatures, where there is less SEI growth might improve this methodology.

5.6 Conclusions and Outlook

Using ⁶Li/⁷Li isotope exchange NMR measurements, the exchange between Li metal and the electrolyte was studied (at the OCV), the exchange occurring simultaneously with SEI growth. The measured exchange flux at the open circuit was related to the traditional Butler-Volmer model of electrochemical kinetics and demonstrates a novel method to measure electrode kinetics. Measuring the ⁶Li/⁷Li isotope exchange is shown to be an easy and effective approach to monitor the exchange current (affected by transport through the SEI) and the growth of SEI on Li metal anodes. The exchange current is shown to decrease with time, corresponding to a decreased permeability of the SEI.

Via this NMR study two SEI parameters are identified and quantified – namely the Li⁺ ion transport and the rate of healing – that are important in controlling Li metal deposition. It is important to identify what makes an optimal SEI on Li metal that achieves uniform plating and stripping at commercially relevant current densities ($> 0.5 \text{ mA/cm}^2$) with high CEs. A screening study with a wide range of additives and electrolytes is the subject for future studies. Measurements of isotope exchange as a function of temperature have been carried out and are planned as a subject of future studies.

Chapter 6 *In situ* NMR Studies of Full-Cell Lithium Metal Batteries

6.1 Introduction

The greatest obstacles to the commercialisation of LMBs are safety issues associated with dendrite growth of electrodeposited Li as well as the low capacity retention and short cycle life.¹⁷ The low capacity retention of LMBs tends to be overlooked because an excess amount of Li metal is typically used in research-scale cells that leads to an artificially enhanced cycling efficiency.^{2,48,49} Realistic LMB designs thus either limit the amount of excess Li, e.g., by using thin Li foils² or they operate in an ‘anode-free’ battery design that replaces the Li metal anode with a bare Cu current collector.^{48,50} Both these battery designs tend to have a fast capacity fade, which is directly associated with the irreversible loss of active Li in the cell. This has been ascribed to the SEI that forms both chemically on the Li metal and electrochemically during plating, and the formation of inactive Li metal typically known as ‘dead Li’.^{40,41} Dead Li corresponds to Li that no longer has electronic contact with the current collector.^{19,41–43}

Improvements in the capacity retention of LMBs have been attributed to both decreasing the extent of SEI formation and to the formation of more dense Li deposits that decreases the dead Li and SEI formation.^{25,48,62,201} Dead Li formation has been attributed to inhomogeneous stripping of Li, which leads to detachment of Li microstructures from the bulk electrode.^{37,44} Electrolytes that result in fast SEI formation kinetics and ensure full and homogeneous passivation on the Li metal should stabilise these capacity losses, leading to more uniform plating and stripping.^{31,32,56}

Methods to observe dead Li include scanning electron microscopy (SEM)^{2,42} and *in situ* optical microscopy.^{41,43,202} Quantitative methods have been recently developed; using quantitative titration gas chromatography, Fang et al. determined for a range of electrolytes and additives that, contrary to common belief, capacity losses in LMBs are mainly due to the dead Li formation and not SEI formation.⁵⁶ A recent study performed *in situ* NMR on Li metal

deposition on Cu and quantified the dead Li formation in a Cu-Li cell *ex situ* after disassembling the cell.²⁰³ A non-destructive *in situ* methodology that allows the dead Li formation to be quantified during the operation of the battery is preferable. Our previous work on *in situ* NMR in Li metal cells allowed the microstructures that form during plating to be directly quantified.⁷⁴ The methodology uses the intensity of the pristine ⁷Li metal peak before passing any current (with a known surface area) to calibrate the NMR intensity and allows the NMR intensity to be converted into mass of deposited Li.⁷⁴ Here, we develop and apply a quantitative *in situ* NMR metrology to determine the origin of lithium losses in the Cu-LFP full cell during operation.

In an anode-free battery, the Li deposits and Cu metal are in intimate contact with each other and the electrolyte, potentially creating the conditions of a short-circuited galvanic cell. Two recent studies have drawn attention to this phenomenon,^{196,197} the first attributing the enhanced rates of corrosion to electrolyte reduction to form the SEI on Cu, reduction on copper being promoted by the poorer (less protective/passivating) SEI formed on the Cu surface.¹⁹⁶ A galvanic current can also result from the reduction of copper oxides. The various reduction reactions on Cu have been widely studied.^{96,204–207} Li metal deposition on Cu is analogous to the formation of a sacrificial coating, where the Li metal serves to inhibit Cu corrosion: while desirable for the Cu, this phenomenon potentially results in enhanced rates of corrosion for the Li.⁹⁶

Li corrosion is here defined as both the chemical formation of the SEI on Li metal, which is accompanied by Li oxidation, and the galvanic corrosion of Li by the coupled Li-oxidation and reduction of the electrolyte on the Cu. It is crucial to understand how to mitigate the dissolution of Li metal by forming a protective SEI on the Li deposits, but it is equally important to passivate the Cu surface,^{196,197} both limiting the corrosion current. The morphology of the Li deposits will have an influence on the galvanostatic corrosion mechanism, with smoother morphology and greater surface coverages of Li (minimising areas where Cu is in contact with the electrolyte) both expected to result in lower corrosion current.

One strategy is to replace the natural SEI with an artificial SEI, to ensure chemical passivation of the electrodes and to mitigate side reactions with the electrolyte.²⁰⁸ Polymer-coatings are an attractive option as they are easily scalable and have been shown to enhance the cycle life of LMBs by promoting homogeneous plating and stripping.^{14,209,210} Here we chose to study three

common polymers (PEO, PMMA and PVDF) with different chemical and mechanical properties,²¹¹ as a case study for screening different artificial SEIs. PEO is a common solid polymer electrolyte and PVDF and PMMA are used as part of gel polymer electrolytes.^{211–215} Furthermore, PVDF is commercially used as a binder in composite battery electrodes.²¹⁶

The main aim of the chapter is to develop an *in situ* NMR metrology to study the dead Li formation and corrosion behaviour of Li metal in an anode-free cell. LiFePO₄ (LFP) was chosen as a stable cathode material with a flat voltage profile at 3.5 V vs. Li/Li⁺, but in principle, any lithiated cathode material can be used.²¹⁷ The quantification of metal deposits has been explained in section 3.2.4, where the integrated intensity of the metal peak was calibrated to the total surface area of the pristine Li metal electrode before passing any current. Using this method, the NMR intensity of the metal peak was directly converted into mass of Li metal deposited.⁷⁴ In this chapter, initially there is no Li metal present in the cell and a calibration of the NMR peak intensity to mass cannot be obtained. However, based on quantitative NMR and the CE calculated from the electrochemical measurements, the amount of dead Li and SEI formation is quantified and compared in carbonate and ether-electrolytes. In addition, we use the BMS effects of Li metal and LFP, performing a careful analysis of the ⁷Li NMR shift, to provide insight into the surface coverage and the morphology of the Li deposits.^{75,76}

Finally, the Li metal dissolution that occurs during rest periods was monitored by *in situ* NMR, the results revealing that the total corrosion of Li (both the chemical SEI formation and galvanic corrosion) remains a major concern for rechargeable LMBs and is expected to be especially important for batteries with a limited amount of Li present in the cell. The effect of Cu surface treatments, electrolytes, and polymer-coatings on the Cu current collector (PEO, PVDF and PMMA) is then studied as an approach to mitigate Li corrosion.

The chapter benefitted from the intellectual input of all co-authors of this project, Dr. Chibueze V. Amanchukwu, Dr. Svetlana Menkin and Prof. Clare P. Grey.

*The handling and preparation of the polymer-coated Cu was performed by Dr. Chibueze V. Amanchukwu and the *in situ* NMR experiments using polymer-coated Cu were performed in collaboration with Dr. Chibueze V. Amanchukwu.*

The preparation of the LiFePO₄ cathode films was performed by Dr. Yumi Kim.

The Python code for the simulations of bulk magnetic susceptibility effects was written by Dr. Andrew Illott.

6.2 Experimental Details

6.2.1 Materials and cell fabrication

LiFePO₄ (LFP) positive electrode contained 90% active material, 5% wt SuperP-Li (Timcal) and 5% wt PVDF (Arkema, HSV 900) was casted with N-methyl-2-pyrrolidone (NMP, Sigma Aldrich, 99.5%, anhydrous) on an aluminum foil, initially dried at 80 °C and calendared. Hydrochloric acid (Honeywell Fluka) was diluted to 1.1 M HCl in deionised water. The Cu foil was soaked in 1.1 M HCl (*aq.*) for 10 minutes for a surface oxide removal, followed by a rinse with ethanol. The Cu foil was then quickly transferred into a glovebox antechamber, where it was dried under vacuum before transferring into an Argon glovebox for storage. For the experiment using AcH-treated Cu, the Cu foil was soaked in concentrated acetic acid (Fischer Chemical, lab reagent grade) for 10 minutes and dried with N₂ gas before being transferred into a vacuum oven at 100°C where it was dried for 24 hours. This procedure ensures a homogeneous passivation layer on the Cu surface.^{218,219} Poly (ethylene oxide) (PEO, M_w = 600.000, Sigma Aldrich), poly (vinylidene fluoride) (PVDF, Kynar HSV 900) and poly (methyl methacrylate) (PMMA, M_w = 75.000, Polysciences) were used as received. The PEO and PMMA were dissolved in 0.02 g/ml acetonitrile (Sigma Aldrich) and the PVDF dissolved in 0.02 g/ml NMP. All polymers were spin-coated on Cu foil (15 mm diameter) at 4000 rpm for 30 seconds. The copper foil was not treated beforehand. After the spin-coating, the polymer-coated Cu foil was allowed to dry at room temperature overnight. Then, the PEO-coated foil was dried at 50°C overnight, while the PVDF and PMMA coatings were vacuum dried at 100°C overnight.

Cell assembly and handling of air sensitive materials was done in an Argon glovebox (MBraun, O₂, H₂O < 1 ppm). The electrolytes used were the following; 1 M LiPF₆ in ethylene carbonate and dimethyl carbonate (EC:DMC 1:1 volume ratio, Sigma Aldrich, battery grade), termed LP30 in this study. LP30+FEC was prepared by mixing LP30 with fluoroethylene carbonate additive in 10:1 volume ratio (FEC, Sigma Aldrich, 99%). The electrolyte referred to as DOL/DME was prepared using 1 M lithium bis-(trifluoromethanesulphonyl)imide (LiTFSI,

Acros Organic, 99%) in 1,3-dioxolane (Sigma Aldrich, anhydrous, 99.8%) and 1,2-dimethoxyethane (Sigma Aldrich, anhydrous, 99.5%) (DOL/DME in 1:1 volume ratio) with 2 wt % lithium nitrate (LiNO_3 , Alfa Aesar, anhydrous, 99%). The LiTFSI and LiNO_3 salts were dried for 20 hours at 100°C under vacuum before use. A capsule cell (NMR Service) made out of PEEK (polyether ether ketone) was used for all *in situ* NMR experiments, and has been described before.¹²³ Working electrodes consisted of either a bare Cu current collector or polymer-coated Cu foil. The amount of electrolyte added to each cell was 75 μL for the carbonate electrolyte and 80-100 μL for the DOL/DME electrolyte. Glass fiber (Whatman GF/A) separators were used after being dried in vacuum at 100°C . Cells with polymer-coated Cu were rested for 2 hours after assembly before any current was applied.

6.2.2 Electrochemistry

Galvanostatic cycling was performed using current density of 0.5 mA/cm^2 for an areal capacity of 1 mAh/cm^2 on the Cu current collector, unless otherwise stated. At the end of each charge/discharge step the cell was rested for 10 minutes to make sure there were around 3-5 NMR experiments measured in order to get an accurate value of the integrated Li metal intensity. A cut-off capacity of 1 mAh/cm^2 was used for plating and stripping and a cut-off voltage of 2.8 V during stripping. Note that the LFP cathode is not fully delithiated, the areal capacity of the LFP cathode is roughly 2.3 mAh/cm^2 . For the experiments with longer SEI formation periods on Cu, a current density of 0.02 mA/cm^2 was used before the Li deposition at 0.5 mA/cm^2 . The first plating cycle in PVDF was performed using 0.1 mA/cm^2 current density.

6.2.3 *In situ* NMR spectroscopy

The *in situ* NMR experiments were conducted on a Bruker Avance 300 MHz spectrometer (the respective Larmor frequency for ^7Li being 116.6 MHz) using a solenoidal Ag-coated Cu coil. The spectra were recorded using an *in situ* automatic-tuning-and-matching probe (ATM VT X *in situ* WB NMR probe, NMR Service) that allows for an automatic recalibration of the NMR rf-circuit during an *in situ* electrochemistry experiment. The re-tuning of the rf-circuit becomes essential in order to quantify the NMR signals when the sample conditions are changing during the electrochemistry.¹⁵¹ The probe has highly shielded wire connections to the electrochemistry

with low-pass filters (5 MHz) attached to the probe, minimizing the interferences between the NMR- and the electrochemistry-circuit, as described in a previous publication.¹⁵¹ Overall, the *in situ* setup allows for highly reproducible NMR measurements. Single-pulse experiments were used to collect the NMR data, with a recycle delay of 1 s ($> 5 \times T_1$) and 256 transients recorded. This resulted in an experimental time of about 4.5 minutes. The ^7Li shift was referenced to 1 M LiCl in water at 0 ppm. The spectra were processed in the Bruker Topspin software, using the automatic phase and baseline correction. Further data processing was done in R. The total intensity of the Li metal peak was integrated over the shift range 310-220 ppm and normalised to the intensity measured at the end of plating in the first cycle.

6.2.4 Susceptibility calculations

Susceptibility calculations were used to understand the shift of Li metal deposits on the electrode surface of both Li and Cu. The calculations were performed using a simulation code written and provided by Dr. Andrew Illott (Bristol-Myers Squibb, previously at New York University) and first published in (<https://doi.org/10.1016/j.jmr.2014.06.013>).¹⁴¹ The code was then modified to fit the experimental setup presented here, simulating Li deposits on a Cu electrode.

The method takes a 3D grid as an input that represents the macroscopic structure that needs simulating, where the grid contains the susceptibility values representing each material in the model. A 3D Fourier transform (using the fast Fourier transform (FFT) method^{139,140}) is taken of the susceptibility distribution to calculate any modifications to the magnetic field at each position.^{75,141} The susceptibility-corrected field-map is then used to calculate the shift at each point in the cell and an NMR spectrum created by representing the ^7Li shift distribution in a histogram as described in previous work.¹⁴¹

The Knight shift of metals must be accounted for when calculating the shift of Li metal. The Knight shift results in a constant offset that scales directly with the resonance frequency (section 3.2.1), with $\Delta B = -KB_0$ and $K = 0.0261\%$ for ^7Li metal.^{128,130} Thus, an additional shift of 261 ppm is added to the local susceptibility-corrected magnetic field of Li metal.¹⁴¹

An array of 256^3 points was used for the input grid, representing a cubic cell with 12.75 mm sides and each point in the array corresponding to a $50 \mu\text{m}^3$ voxel. A pristine Li or Cu electrode was represented by a rectangular electrode in the middle of the cubic array, with sides $4.0 \times$

10.0 × 0.4 mm in x, y and z directions. The applied magnetic field, \mathbf{B}_0 is aligned along z direction matching the geometry of the NMR experiment. The voxels inside the rectangular electrode were either assigned volume susceptibility $\chi_{Cu,vol}$ or $\chi_{Li,vol}$. The susceptibility values used are in SI units and are: $\chi_{Cu,vol} = -9.63 \times 10^{-6}$,²²⁰ $\chi_{Li,vol} = 24.5 \times 10^{-6}$ and the rest of the cell is modelled as a vacuum with $\chi_{vol} = 0$.¹⁴¹ The formation of the microstructures was modelled by assigning single voxels at random points next to the rectangular electrode surface with a susceptibility value of $\chi_{Li,vol}$ following the approach of Ilott et al. The surface coverage of the voxels was varied from 2.5-95%.⁷⁵

6.3 Results

6.3.1 Detection of dead Li by *in situ* NMR

In situ NMR was performed to study Li deposition and stripping in a Cu-LFP cell. Figure 6.1a shows the ^7Li *in situ* NMR spectra of the Cu-LFP full cell before cycling. The resonances in the ^7Li diamagnetic region at around 0 ppm correspond to the electrolyte (and the SEI after its formation).¹³⁵ The LFP cathode resonance is broad, spreading over thousands of ppm, with a range of hyperfine and bulk magnetic susceptibility (BMS) shifts that depend on the LFP particles' aspect ratio, packing density of the film and orientation in the magnetic field.^{137,142} The resonance consequently overlaps with the diamagnetic (and Li metal) peaks, and in the current study, with an NMR spectral window range of 800 ppm, and the carrier frequency centred at around 257 ppm, it will simply be seen as a contribution to the broad baseline. This is adjusted automatically in our data-processing via a baseline correction.¹⁵¹

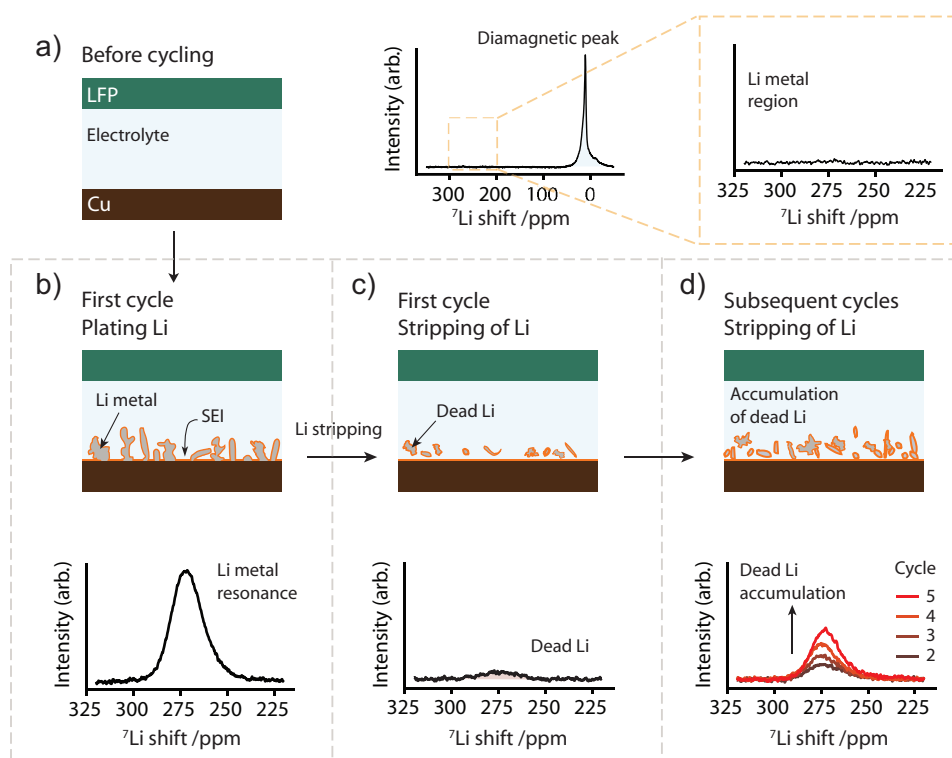


Figure 6.1. Schematic of the ${}^7\text{Li}$ *in situ* NMR technique used to study dead Li formation and the resulting ${}^7\text{Li}$ NMR spectra. **a**) The Cu-LiFePO₄ (LFP) cell before cycling and the corresponding ${}^7\text{Li}$ NMR spectrum showing the resonance of the diamagnetic Li (the SEI and Li⁺ ions) and the absence of the lithium metal peak. **b**) Charging the cell results in lithium metal electrodeposition, as shown in the ${}^7\text{Li}$ NMR spectrum of the Li metal region. **c**) At the end of discharge the Li metal signal can still be observed, which is attributed to dead Li. **d**) Further cycling of the Cu-LFP cell results in an accumulation of dead Li over the next cycles (cycle 2-5), the intensity of the Li metal signal increasing at the end of stripping in each cycle.

Upon charging the Cu-LFP cell, Li deposition takes place on the Cu electrode and the Li metal resonance appears in the spectrum (Figure 6.1b). The Li metal resonates on average at around 260 ppm, the shift arising from the Knight shift, a measure of the density of states at the Fermi level (as probed by the Li 2s orbital).¹³⁰ Thus, the Li metal resonance is easily distinguishable from the diamagnetic electrolyte-SEI peak.^{128,130,135} The Li metal peak still remains at the end of discharge (stripping, Figure 6.1c), indicative of the formation of electrically isolated Li deposits, termed ‘dead Li_{NMR}’ to denote the dead Li measured by NMR. Upon further cycling, the intensity of the Li metal peak seen at the end of stripping grows, indicating further accumulation of the dead Li in the cell (Figure 6.1d). The *in situ* technique presented here can be used to observe and quantify the formation of dead Li during the galvanostatic cycling.

6.3.1.1 Nutation of the Li metal peak to probe skin depth effects

Skin depth effects must be considered when NMR is performed on metallic samples.^{74,141} The rf-field used to excite the nuclear spins penetrates the metal only up to a certain depth on the order of the skin depth, d , which at the frequency $\nu = 116.7$ MHz (the ${}^7\text{Li}$ Larmor frequency used here) is $12.1 \mu\text{m}$ for Li metal (equation (3.11)). The skin effects can be observed in a so-called nutation experiment, described in detail in section 3.2.3, which is used here to measure the radio frequency (rf) field felt by the Li metal spins.

The application of the excitation rf-pulse in NMR spectroscopy, generates a \mathbf{B}_1 -field perpendicular to the static \mathbf{B}_0 -field. This causes a rotation of the net nuclear magnetization about the \mathbf{B}_1 axis where the flip angle of the spins depends on the duration and the amplitude of the rf pulse. For non-metallic samples that do not experience skin effects, the nutation of the nuclear magnetization results in a sinusoidal curve for the signal intensity with the highest signal intensity observed for a flip angle of 90° (as shown for the ${}^7\text{Li}$ NMR signal of the Li^+ electrolyte in Figure 3.7).

For metallic samples however, due to skin depth effects the rf field varies as a function of distance in the sample (equation (3.10)), and the corresponding flip angle varies at different depths from the metal surface.^{74,76,141} This leads to a more complex nutation behaviour (as described in equation (3.13) and shown in Figure 6.2) with the maximum signal intensity obtained at a flip angle of about 133° .

A nutation experiment was performed at the end of plating Li metal on Cu (plating capacity of 1 mAh/cm^2) to inspect whether skin depth effects were observed for the Li deposits. A sinusoidal nutation curve is observed for the Li deposits (Figure 6.2a), typically observed for samples that do not experience skin effects. The corresponding 90° pulse for a pulse duration of $5.5 \mu\text{s}$ in contrast to the highest intensity for the Li metal foil is at $\sim 8.1 \mu\text{s}$. This confirms that the Li deposits are fully excited and are thus less than $12 \mu\text{m}$ in thickness.²²¹ Furthermore, the linear increase in intensity observed on plating below (Figure 6.3b) is consistent with a quantitative excitation. For the remainder of the chapter we assume that the whole volume of the Li metal deposits is being excited.

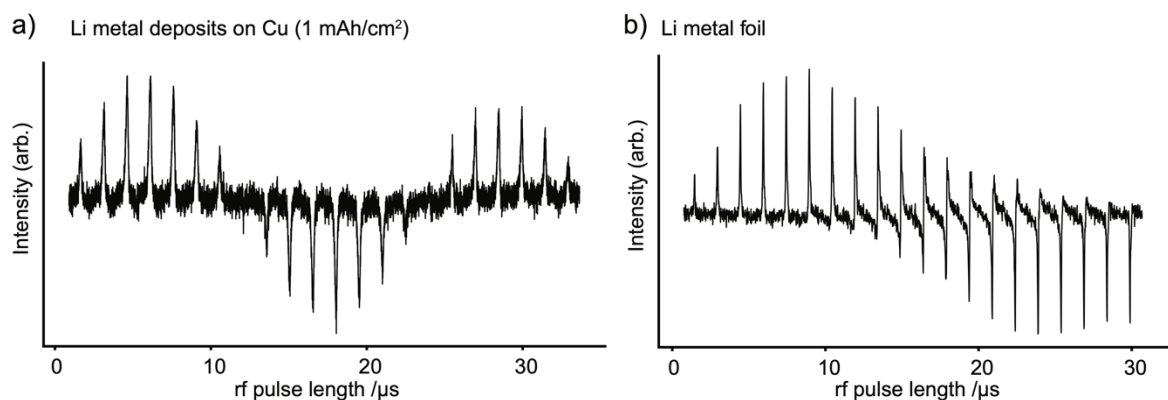


Figure 6.2 Experimental nutation curves of **a)** the Li deposits on Cu (1 mAh/cm^2) nutate sinusoidally as expected for samples that do not experience skin depth issues. **b)** The pristine Li metal foil nutates according to equation (3.13) due to skin depth effects.

6.3.2 Capacity losses during plating and stripping

6.3.2.1 The effect of the electrolyte on Li metal cycling

In situ NMR was performed to study the capacity losses in Cu-LFP cells, in three different electrolytes; 1 M LiPF_6 in EC/DMC (LP30), LP30 + FEC and 1 M LiTFSI in DOL/DME + 2% wt LiNO_3 (DOL/DME). The FEC additive has been shown to be beneficial for plating and stripping Li, resulting in higher CE in Li-Cu cells and better capacity retention in Li-NMC cells.^{45,82} The DOL/DME electrolyte is widely used in Li-S battery research²²² and the Li deposits have been shown to have a characteristic round-shape morphology.^{109,223,224}

Figure 6.3 shows one *in situ* NMR data set for measurements in LP30 during galvanostatic plating and stripping at a current density of 0.5 mA/cm^2 and a capacity of 1 mAh/cm^2 on charge (Li plating). The integrated intensity of the Li metal peak grows linearly with charge (Figure 6.3b). Upon discharge (Li stripping), the metal peak decreases in intensity until the cell hits the cut-off voltage (Figure 6.3c) and the active Li metal has been stripped of the Cu electrode. As can be seen in Figure 6.3b, the normalised intensity at the end of discharge is not equal to zero due to the formation of dead Li_{NMR} .

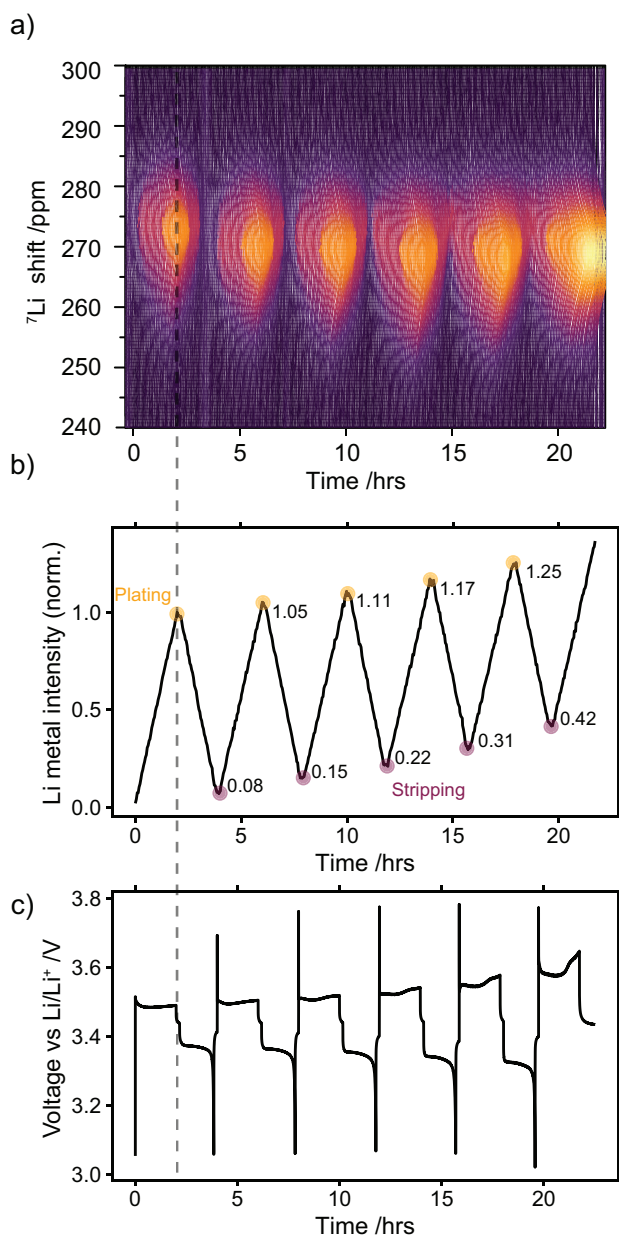


Figure 6.3. *In situ* ^7Li NMR measurement of a Cu-LFP cell cycled in LP30 electrolyte with $0.5 \text{ mA}/\text{cm}^2$ current density and $1 \text{ mAh}/\text{cm}^2$ capacity for each plating step. **a)** The ^7Li NMR spectra acquired during the plating and stripping of Li metal. The resonance of Li metal appears at around 270 ppm. **b)** The corresponding integrated intensity of the Li metal peak normalised to the intensity at the end of plating in the first charge and **c)** voltage profile for the galvanostatic cycling.

In the next cycles, a capacity of 1 mAh/cm² can still be passed in each plating-step as the LFP cathode has not been fully delithiated (it holds ~2.3 mAh/cm² areal capacity). The dead Li_{NMR} accumulates over the first five cycles reaching approximately 40% of the Li metal deposited in the first cycle. Similarly, the intensity of Li metal at the end of plating, termed ‘total Li_{NMR}’ hereafter, increases in each cycle (Figure 6.3b). The increase in total Li_{NMR} and dead Li_{NMR} does not fully correlate, as seen in Figure 6.3b where the dead Li_{NMR} is roughly 8% of the metal deposited in the first cycle but the increase at the end of plating in the second cycle is only 5%. This can be explained in terms of changes in the charge wasted in parasitic reactions and the SEI formation (termed SEI capacity), which affects the amount of total Li_{NMR} measured in each cycle.

The methodology and cycling protocol were implemented in the electrolytes LP30, LP30 + FEC and DOL/DME, with three sets of *in situ* cells measured for each electrolyte. In Figure 6.4, averaging over three data sets, the same trends are observed for the LP30 electrolyte as in Figure 6.3, with a roughly 20% increase in the average total Li_{NMR} over the first five cycles (Figure 6.4a, green) and the accumulation of dead Li_{NMR} accounting to roughly 40% of the initial Li (Figure 6.4b, green). The CE is 82-85% over the first five cycles. For LP30 + FEC almost no dead Li is detected (Figure 3c, orange), consistent with the study by Fang et al.⁵⁶ The CE was noticeably lower for DOL/DME in the first cycle compared to the other electrolytes, around 75%, and correlates with greater amount of dead Li being formed. High CE in DOL/DME is typically reported in Cu-Li cells.^{56,224} Low CE in the DOL/DME electrolyte was however observed in Cu-LFP cells.²²⁴

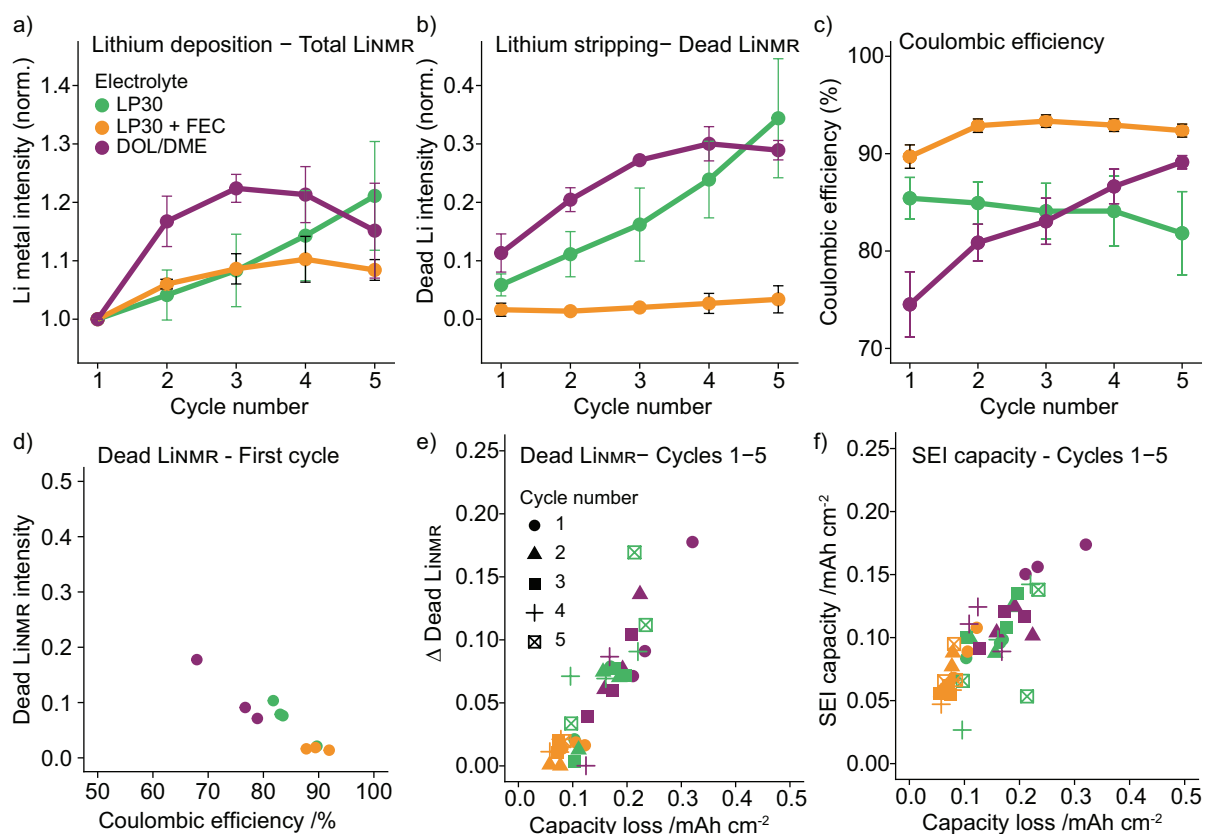


Figure 6.4 The average value of the a) normalised total Li_{NMR} intensity at the end of plating, b) normalised dead Li_{NMR} intensity at the end of stripping and c) electrochemically obtained CE for the first five cycles in the three electrolytes, LP30 (green), LP30 + FEC (orange) and DOL/DME (purple). The error bars represent the standard deviation of the average values obtained in three different experiments. d) The dead Li_{NMR} measured in the first cycle plotted against the CE. e) The difference in dead Li_{NMR} between subsequent cycles plotted against the capacity loss (mAh/cm²) calculated from the CE. f) The SEI capacity (mAh/cm²) calculated in each cycle against the corresponding capacity loss (mAh/cm²).

The capacity loss due to the electrochemical SEI formation (defined here as the capacity lost due to all irreversible side reactions when current is being passed) can be estimated from the dead Li_{NMR} measured by NMR and the capacity loss from the electrochemistry. The Coulombic efficiency (CE) measured electrochemically is defined as:

$$CE = \frac{\text{Discharge capacity}}{\text{Charge capacity}} \quad (6.1)$$

And the capacity loss (CL) is defined as:

$$CL = C_{\text{plating}} - C_{\text{stripping}} \quad (6.2)$$

i.e. the difference between the full plating capacity and the stripping capacity. Here $C_{\text{plating}}=1$ mAh/cm² is the full plating capacity, not accounting for side reactions. The CL results from a combination of the capacity lost due to dead Li formation, $C_{\text{dead Li}}$ and the SEI capacity, C_{SEI} described as:

$$CL_n = C_{\text{dead Li},n} + C_{\text{SEI},n} \quad (6.3)$$

where the subscript n denotes the cycle number n . The dead Li_{NMR} value measured by the NMR denoted here as $\chi_{\text{dead Li}_{\text{NMR}}}$, is the fractional amount of dead Li measured by NMR normalised to the Li metal intensity at the end of the charge in the first cycle (which depends on both the charge passed and the charge consumed in forming the SEI). Thus, $C_{\text{dead Li},n}$ is not directly proportional to $\chi_{\text{dead Li}_{\text{NMR}}}$ and a correction is needed to account for the capacity used to form the SEI electrochemically in the first cycle. The dead Li capacity, $C_{\text{dead Li},n}$ is instead given:

$$C_{\text{dead Li},n} = (C_{\text{plating}} - C_{\text{SEI},n=1}) \times \chi_{\text{dead Li}_{\text{NMR}},n} \quad (6.4)$$

$C_{\text{plating}} - C_{\text{SEI},n=1}$ corresponding to the actual capacity used to deposit the Li metal on the first cycle, and effectively used to normalise the subsequent NMR measurements. Equation (6.3) can now be rewritten as:

$$CL_n = (C_{\text{plating}} - C_{\text{SEI},n=1}) \times \chi_{\text{dead Li}_{\text{NMR}},n} + C_{\text{SEI},n} \quad (6.5)$$

By solving for $C_{\text{SEI},1}$ in the first cycle, $C_{\text{SEI},n}$ and $C_{\text{dead Li},n}$ can now be determined.

As an example of this method, the SEI capacity is now calculated for the set of data presented for LP30 in Figure 6.3. The $CL_{n=1}$ on first cycle is 0.17 mAh/cm² and $\chi_{\text{dead Li}_{\text{NMR}}}$ is 0.08 after one cycle (Figure 6.3b). This results in an SEI capacity of approximately 0.1 mAh/cm² and dead Li value of 0.07 mAh/cm². This indicates that in the case of LP30, the CL is influenced significantly by both the dead Li formation and the SEI formation capacity. The CE in the first cycle as well as the SEI capacity and dead Li are displayed in Table 6.1.

Table 6.1 The CE, SEI formation capacity and dead Li capacity in the first cycle calculated using the dead Li_{NMR} intensity determined by *in situ* NMR and the CE determined from electrochemistry. The standard deviation is that derived from the three separate *in situ* NMR experiments.

Electrolyte/ Polymer coating	Coulombic efficiency	SEI formation capacity (mAh/cm ²)	Dead Li capacity (mAh/cm ²)
LP30	85 ± 2%	0.09 ± 0.005	0.06 ± 0.02
LP30 + FEC	90 ± 1%	0.09 ± 0.01	0.01 ± 0.001
DOL/DME	75 ± 3%	0.16 ± 0.01	0.11 ± 0.03

A slightly higher value for the SEI capacity is observed for each electrolyte compared to the amount of dead Li. It should be noted that this calculation neglects Li corrosion, that is the dissolution of Li due to chemical SEI formation and galvanic corrosion that do not result in a net current in the cell. The effect of the Li corrosion current as quantified below, was estimated and seen to be negligible in quantifying the SEI formation capacity.

The difference in the dead Li value between cycles, “Δ dead Li”, which corresponds to the dead Li formation per cycle, and the SEI capacity per cycle are shown against the corresponding capacity loss (Figure 6.4e, f). Both the dead Li and SEI capacity displayed a linear relationship with the capacity loss per cycle, demonstrating that both processes determine the cycling stability of LMBs. The same values (per cycle) are shown as a function of cycle number to visualize whether any stabilization occurs with cycling (Figure 6.5). For the carbonate electrolytes there is continuous SEI formation in each cycle, the SEI capacity remaining steady at around 0.05-0.1 mAh/cm². For the DOL/DME however, the SEI capacity drops significantly after the first cycle before stabilising at around 0.1 mAh/cm² (Figure 6.5). Similarly, the dead Li formation in DOL/DME drops with cycling in contrast to in LP30 where it increases slightly (Figure 6.5).

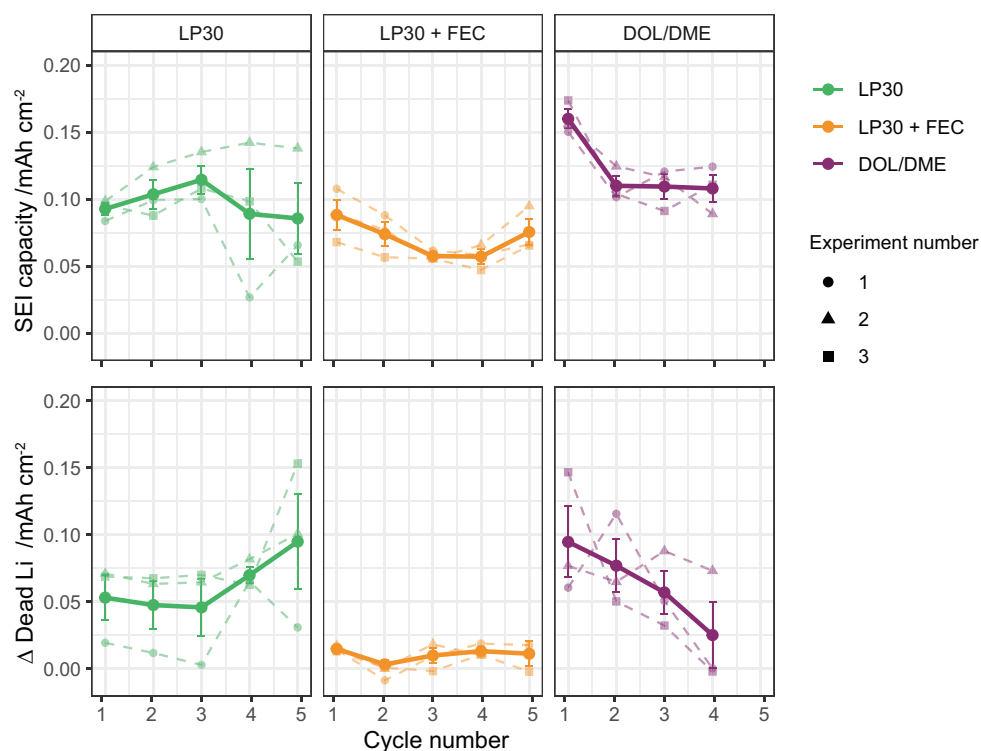


Figure 6.5 The average SEI formation capacity (top) and dead Li (bottom) per cycle, in LP30, LP30 + FEC and DOL/DME. The dashed lines show the values used to calculate the mean and the standard deviation, for the three different sets of *in situ* NMR experiments.

6.3.2.2 Polymer-coated Cu electrodes

To extend the *in situ* NMR method further, three common polymers (PEO, PMMA and PVDF) that have been heavily studied in batteries were investigated. The polymers were cast onto Cu current collectors, the cell was assembled and then left to rest for two hours before any current was passed.

The *in situ* NMR data of the polymer-coated Cu electrodes cycled in LP30 and the CE calculated from the electrochemistry are presented in Figure 6.6. The PEO- and PVDF-coatings show considerably lower first cycle CE of about 65% (Figure 5c) compared to 85% on bare Cu and 83% with PMMA-coated Cu. Interestingly, lower dead Li formation was detected (Figure 6.6b), which indicates increased capacity losses due to SEI formation when using these coatings. The cycling efficiency for both the PEO- and PVDF-coated Cu increases, however, after the first cycle indicating that surface reactions have occurred to form a more

stable SEI/coating on the Cu. The PMMA presents a similar CE to that of a bare Cu in LP30 but less dead Li formation is seen.

The SEI capacity and dead Li values are summarised for the first cycle in Figure 6.7. In all cases, less dead Li formation but higher SEI capacity is measured on the polymer-coated compared to bare Cu, indicating more side reactions in the polymer systems (Figure 6.7). Although we have not explored the effect of polymer swelling and/or interaction with the electrolyte, and we did not optimize polymer coating thickness,^{209,211} the results demonstrate the power of the quantitative NMR technique to deconvolute the contributions to the capacity losses, which cannot be determined from the electrochemistry alone.

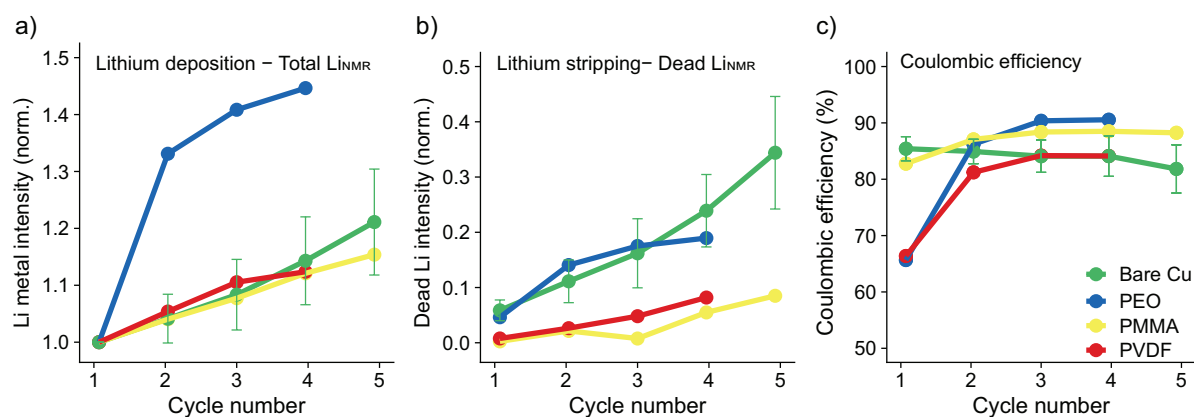


Figure 6.6 The Li metal intensity for the ^7Li *in situ* NMR measurements when cycling Cu-LFP cells in LP30 with polymer-coated Cu. **a)** The normalised total L_{NMR} intensity at the end of plating, **b)** the normalised dead L_{NMR} intensity at the end of stripping and **c)** the CE for PEO- (blue), PMMA- (yellow) and PVDF-coated (red) Cu electrodes. The measurements for bare Cu (in green) are shown here to aid comparison.

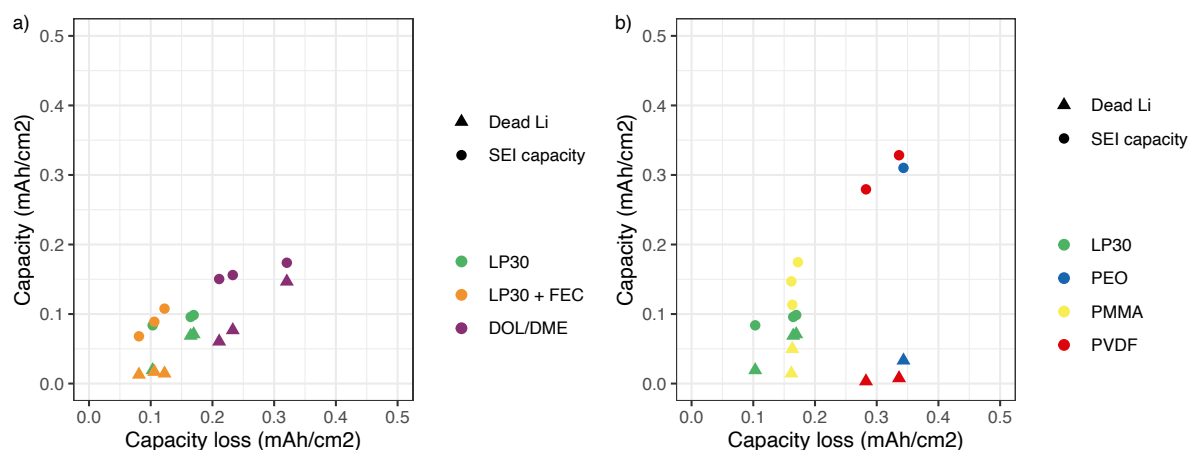


Figure 6.7 Capacity losses in the first cycle, the SEI capacity C_{SEI} (circles) and the dead Li capacity $C_{dead Li}$ (triangles) plotted against the corresponding capacity loss, CL . a) In the three electrolytes, LP30, LP30 + FEC and DOL/DME on bare Cu current collector. The different data points corresponds to different sets of *in situ* experiments. b) In LP30 on bare Cu (green) and on polymer-coated Cu (PEO, PMMA and PVDF). More significant SEI formation is observed for the polymer-coated Cu cell.

6.3.3 Bulk magnetic susceptibility effects of Li metal

This section explores the shift of the ^7Li metal peak, which is sensitive to orientation and morphology of the Li deposits. Chandrashekar et al. showed with ^7Li MRI how the shift of Li metal can be used to distinguish between electrodeposits growing close to the Li metal (at around 260 ppm) and dendritic structure extending further away from the surface (at around 270 ppm).⁷⁶ This was later confirmed in a detailed study by Chang et al., where different resonances in the *in situ* NMR spectra were correlated with SEM images of Li microstructure morphology formed under different stack pressures and using different separators.⁷⁵ Overall, the study by Chang et al. demonstrated how *in situ* NMR can track the Li metal morphology in real time.⁷⁵ However, in section 4.3.1 the ^7Li metal shift was shown to be on average 260 ppm for the different morphologies (whisker-like and nodular) formed in LP30 and LP30 + FEC. This is attributed to improvements in the *in situ* cell design, where the *in situ* PEEK cell (Figure 3.8) provides a homogeneous and consistent pressure between different cells that leads to microstructures growing close to the electrode's surface (resulting in similar shifts of 260 ppm, Figure 4.3). The NMR spectrum in Li-Li cells is convoluted with the bulk Li metal, where pitting of the stripping electrode may influence the spectrum as shown in Figure 4.12. In this

section, the shift of the ^7Li metal peak in Cu-LFP cells will be examined in detail. Owing to the fact that the ^7Li metal resonance in these cells is not convoluted with the bulk Li metal the shift is more sensitive to the Li morphology.

6.3.3.1 ^7Li shift of the pristine Li metal

To understand the shifts observed in the *in situ* Cu-LFP cells, the effect of the paramagnetic LFP cathode on the ^7Li metal shift is first studied in a pristine Li-LFP cell. The Li metal peak of a pristine Li-Li cell (when the electrodes are oriented perpendicular to the static, applied magnetic field) appears at 245 ppm (Figure 6.8, black) but when paired with the LFP cathode, the Li metal peak shifts to 260 ppm (Figure 6.8, purple).

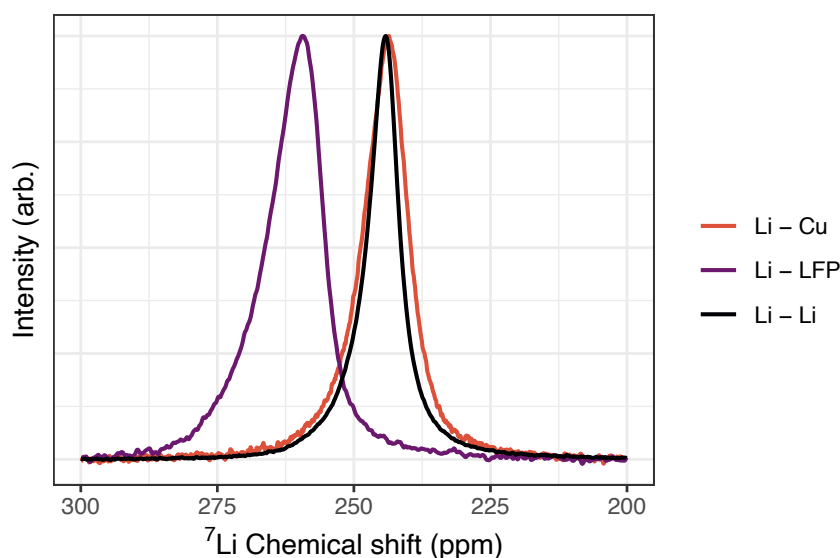


Figure 6.8 BMS effects on the pristine Li metal resonance: ^7Li NMR spectra of pristine Li metal oriented perpendicular to the magnetic field in three different configurations; Li-Cu cell, Li-LFP cell and Li-Li cell. The ^7Li shift of Li metal when assembled against the paramagnetic LFP cathode shifts from 245 ppm to 260 ppm due to BMS effects. The main plane of the rectangular electrode is facing perpendicular with respect to the applied magnetic field B_0 , that is at 90° .

A paramagnetic material can cause both a shift and significant broadening of NMR resonances due to BMS effects.¹³⁷ Previously, the resonance of Li metal has been shown to shift significantly when assembled with the paramagnetic spinel cathode, $\text{Li}_{1.08}\text{Mn}_{1.92}\text{O}_4$, from 245 ppm to 368 ppm (and with additional asymmetric broadening of the metal peak).¹³⁷ In a Li-Cu

cell, there is no significant shift in the ^7Li metal peak (Figure 6.8, red), since Cu metal shows only a small diamagnetic contribution ($\chi_{\text{Cu},\text{volume}} = -9.63 \times 10^{-6}$).²²⁰ Thus, the ^7Li metal peak in Cu-LFP cells is expected to be shifted by approximately 15 ppm to higher frequencies from the signal typically observed in Li-Li cells (Figure 6.8) due to the LFP cathode.

6.3.3.2 ^7Li shift of Li metal deposits in Cu-LFP cells

Analysing now the ^7Li shift of the Li deposits, the Li metal peak emerges at around 275 ppm in the Cu-LFP cells at the start of plating (Figure 6.9a, in LP30 electrolyte) and shifts to lower ppm values both during plating and on further cycling (as seen for the NMR spectra on fourth cycle, Figure 6.9b). The shift of the peak maximum was extracted (Figure 6.9c) and interestingly is shown to cycle with the electrochemistry, moving to lower shifts during Li plating and to higher shifts during Li stripping. During plating, the LFP cathode is delithiated (charged) and the oxidation state of iron changes from Fe^{2+} in LiFePO_4 to Fe^{3+} in FePO_4 , which increases the susceptibility of the cathode.²²⁵ Thus, the change in shift observed for the Li metal can either be due to changes in the susceptibility of the LFP cathode that will influence the susceptibility of the whole cell,²²⁵ or due to the dependence of the shift on the Li morphology as reported in previous studies.⁷⁵

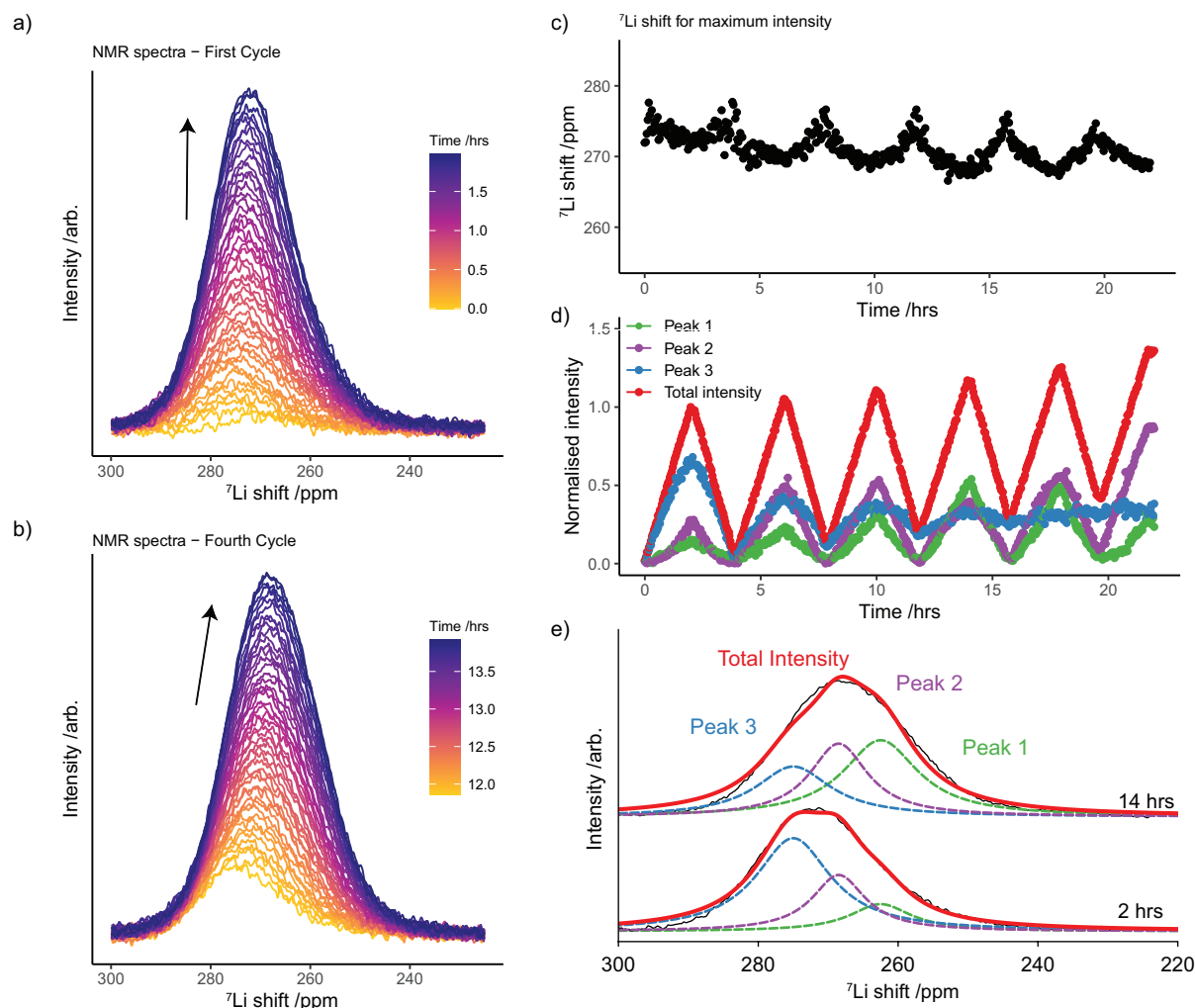


Figure 6.9 BMS effects for the Li metal peak in the LP30 electrolyte. **a)** Stack plot of the Li metal spectra during charge (plating) in the first cycle (where the same metal spectra are shown vs. time in Figure 6.3a). **b)** The Li metal spectra during charge (plating) in the fourth cycle. **c)** The frequency of the Li metal shift, measured at the maximum intensity of the Li metal resonance, during cycling. **d)** The deconvoluted intensities of the Li metal spectra during cycling. **e)** An example of the fitted spectra at the end of charge in first and fourth cycle.

To gain more insight into this phenomenon the spectra were fitted using the least-squares method with three overlapping peaks (using pseudo-Voigt curves, Figure 6.9e); peaks at 260.5 ppm (Peak 1), 268.5 ppm (Peak 2) and 272.5 ppm (Peak 3) were used and their position was allowed to vary ± 2.5 ppm from the set values. In order to explore the sensitivity of the deconvolution method, a fit with two components (two peaks) was attempted but found that in later cycles, three peaks were essential.

The normalised intensity of the deconvoluted peaks shows how the Li metal resonance is mainly captured with Peak 3 in the first cycle (at the highest Li metal shift, Figure 6.9d, in blue). Upon further cycling, Peak 2 becomes more dominant, indicating that the main resonance is moving towards lower shifts. Peak 1, at the lowest shift, appears in the fit in later cycles albeit with low intensities. Of note, the dead Li_{NMR} at the end of stripping and the initial Li deposits resonate at shifts of around 272-275 ppm at the same position as with Peak 3 (Figure 6.9d). Taking into account the additional shift observed for a pristine Li metal strip assembled with an LFP electrode (15 ppm higher than in Cu-Li cell), the shift at 275 ppm can be corrected for the LFP BMS effect and resulting in a shift of 260 ppm, which is consistent for the Knight shift of Li metal.²²⁶

The ^7Li shift in LP30 + FEC and DOL/DME shows a different behaviour to the LP30 with the Li metal signal appearing at lower values after plating (Figure 6.10 and Figure 6.11). For both electrolytes, Peak 1 at the lowest shift, is more pronounced in the deconvolution during cycling of the cell. This difference between electrolytes indicates that the Li metal shift is not dictated wholly by the state of charge of the LFP cathode (which is similar for all the cells) but that the nature of the Li deposits – morphology and surface coverage - must influence the shift. Susceptibility calculations were thus performed to explore how the deposition may affect the shift.

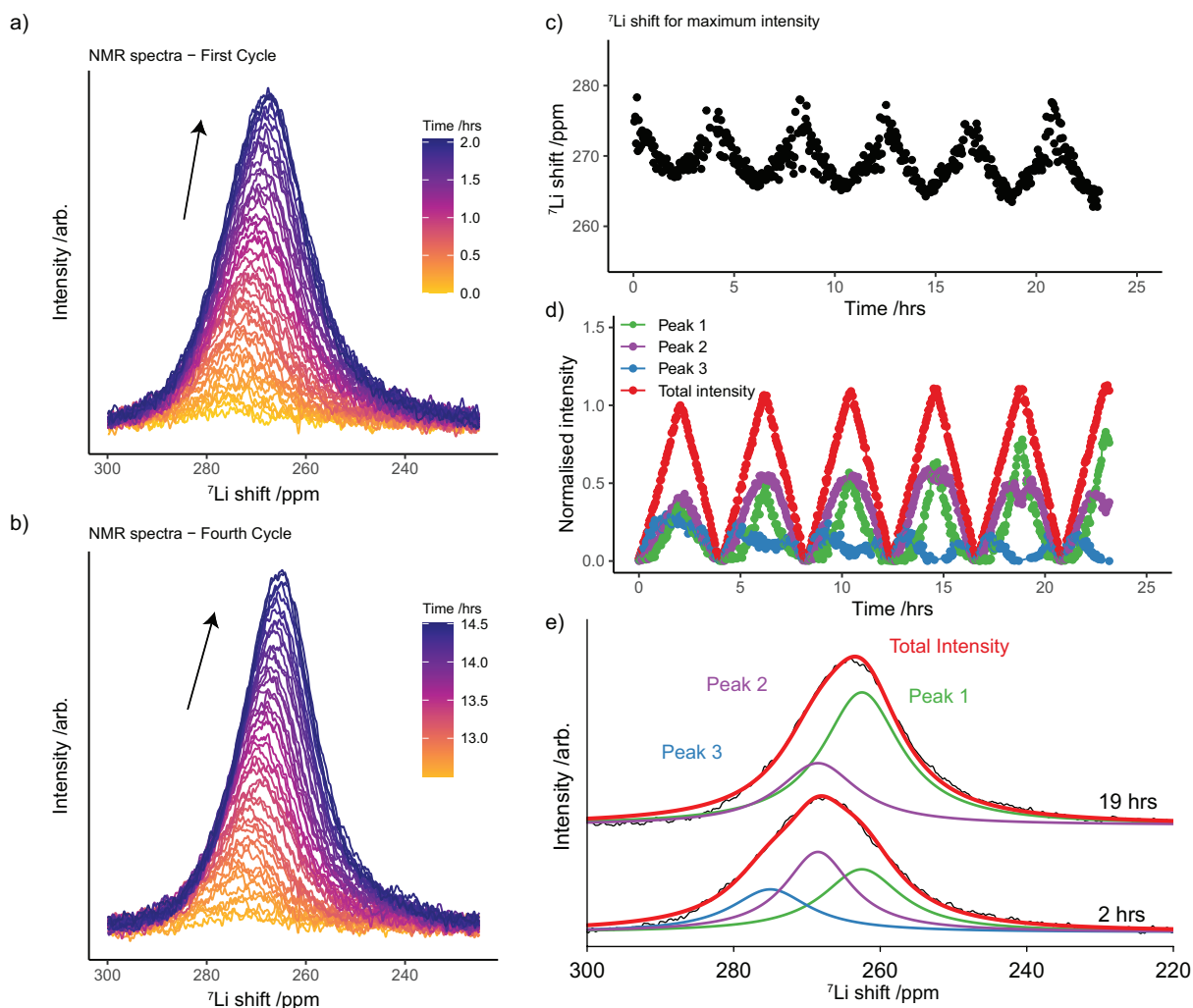


Figure 6.10 BMS effects for the Li metal peak in the LP30 + FEC electrolyte. **a)** Stack plot of the Li metal spectra during charge (plating) in the first cycle. **b)** The Li metal spectra during charge (plating) in the fourth cycle. **c)** The frequency of the Li metal shift, measured at the maximum intensity of the Li metal resonance, during cycling. **d)** The deconvoluted intensities of the Li metal spectra during cycling. **e)** An example of the fitted spectra at the end of charge in first and fifth cycle.

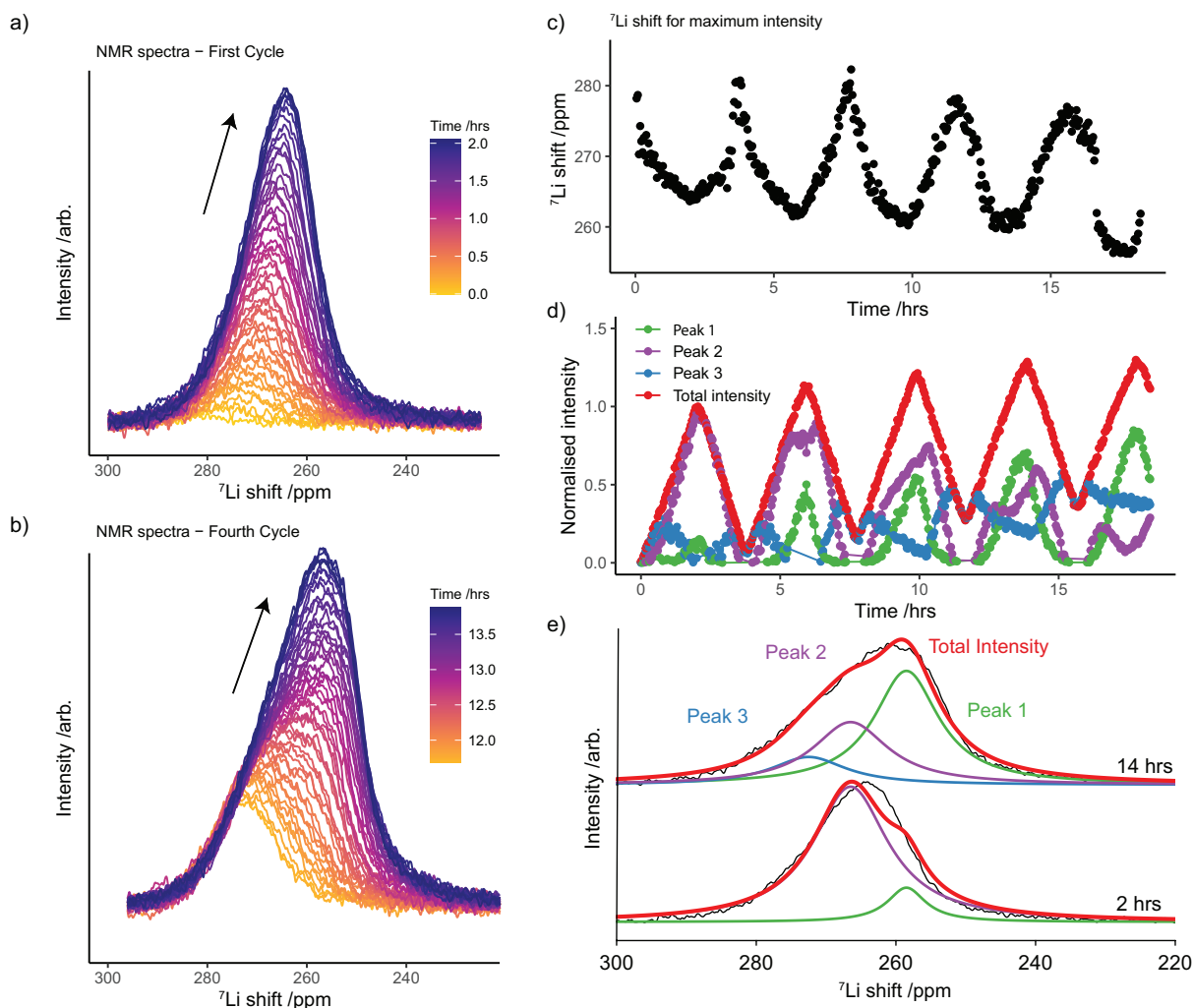


Figure 6.11 BMS effects for the Li metal peak in the DOL/DME electrolyte. **a)** Stack plot of the Li metal spectra during charge (plating) in the first cycle. **b)** The Li metal spectra during charge (plating) in the fourth cycle. **c)** The frequency of the Li metal shift, measured at the maximum intensity of the Li metal resonance, during cycling. **d)** The deconvoluted intensities of the Li metal spectra during cycling. **e)** An example of the fitted spectra at the end of charge in first and fourth cycle.

6.3.3.3 Susceptibility calculations of ^7Li metal shifts

Susceptibility calculations were performed to simulate the ^7Li NMR spectrum and estimate the shift of Li metal deposits on Cu and Li metal electrodes. The code was written and provided by Dr. Andrew Ilott (Bristol-Myers Squibb, previously at New York University).¹⁴¹ First the results from reference ⁷⁵ were reproduced (Figure 6.12, also shown in Figure 3.6) for Li deposits on a Li electrode and the code was then modified to fit the experimental setup presented here, simulating Li deposits on a Cu electrode.

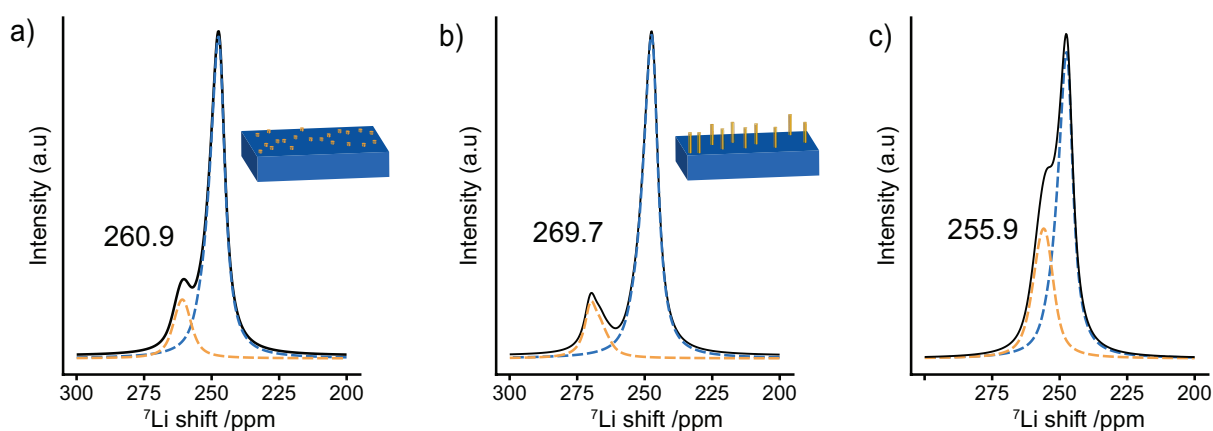


Figure 6.12 Simulated NMR spectrum of electrodeposits on Li metal from the susceptibility calculations of a pristine Li metal (in blue) and Li electrodeposits (in orange), the sum of the two shown in black. **a)** The simulated NMR spectrum with 20% coverage of Li microstructures and **b)** of Li dendrites with 2.5% coverage, reproducing the results found in reference [75] with the shift of mossy microstructures at around 260 ppm and around 270 ppm for dendrites. **c)** The simulated NMR spectrum with a microstructure coverage of 50%. The shift is at 256 ppm for the microstructure peak (in orange).

As described in section 3.2.2, Li microstructures on a Li metal electrode result in a shift of 261 ppm (Figure 6.12a, also shown in Figure 3.6) and Li dendrites result in a shift at 270 ppm (Figure 6.12b).⁷⁵ The shift of the dendrites is due to BMS effects and agrees well with the experimental observations by Chandrashekar et al.^{33,75,76} To extend this study further, here the surface coverage of the microstructures was increased to 50% (Figure 6.12c). The microstructure peak now shifts to 256 ppm, indicating that due to BMS effects, higher surface coverages of Li deposits move to lower shifts, starting to resemble more the bulk Li metal at 245 ppm.

The microstructure surface coverage (randomly placed voxels on the electrode surface) was varied between 2.5-95% on both Li metal and Cu foil (Figure 6.13). The overall trend is that a higher surface coverage leads to a lower shift due to BMS effects (Figure 6.13b). A shift to lower resonances correlates with what is seen experimentally in Li-Li cells (Figure 4.3) and Cu-LFP cells (Figure 6.9 to Figure 6.11), where a gradual shift in the Li metal peak occurs during plating, indicating a higher coverage of deposits. Due to the susceptibility of Li metal being slightly paramagnetic ($\chi_{Cu,vol} = -9.63 \times 10^{-6}$,²²⁰ $\chi_{Li,vol} = 24.5 \times 10^{-6}$ in SI units), the calculated values are at a slightly lower shift compared to when simulated on Cu. In practice, the shift is influenced by all the components of the cell.

The shift on Cu for the lowest surface coverage is around 260 ppm. An additional shift of about 15 ppm is expected in Cu-LFP cells due to the paramagnetic LFP cathode and is consistent with the shifts observed experimentally, the initial peak emerging at 273 ppm (Figure 6.11).

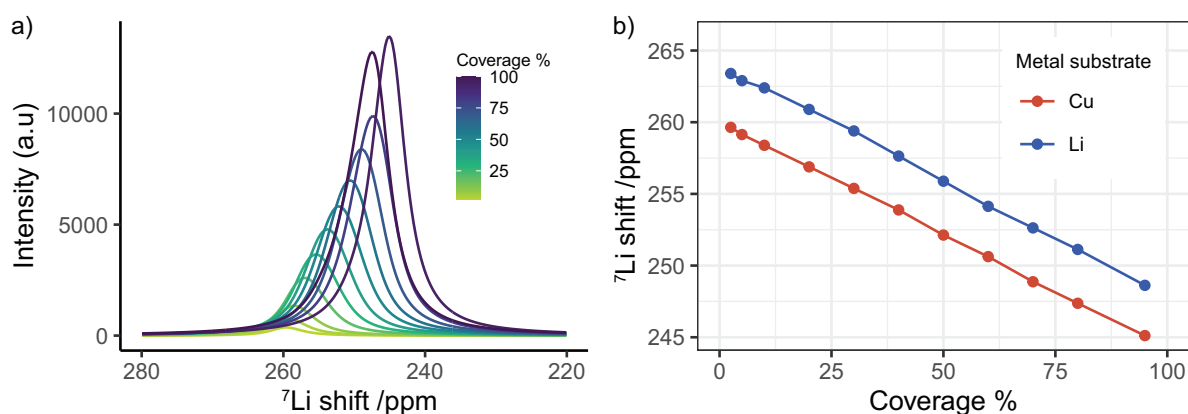


Figure 6.13 The Li metal shift as a function of surface coverage of Li microstructures. **a)** The simulated NMR spectra of the microstructure deposits on Cu, varying the surface coverage from 2.5-95%. **b)** The ${}^7\text{Li}$ metal shift at the peak maxima of the Li microstructure peak on a Cu (red) or Li metal (blue) electrode. The calculated shift at 2.5% surface coverage is 260 ppm on Cu and 263 ppm on Li.

Going back to the Cu-LFP results in section 6.3.3.2, the peak at lowest shift becomes more apparent in all electrolytes with cycling, suggesting the Li coverage on Cu is becoming greater. The trend in metal shift observed for the different electrolytes is summarised in Figure 6.14, showing the intensity of the fitted peaks at the end of plating and the end of stripping. The intensity of Peak 1 is greatest in the DOL/DME electrolyte (Figure 6.14a, green), which is consistent with ether-based electrolytes having more complete surface coverages compared to the LiPF_6 – carbonate electrolytes.⁴⁴ Of note, the dead Li peak with the highest shift is only affected by the LFP BMS effect and not the BMS effects due to Li metal. This is consistent with the removal of smoothly deposited Li and the formation of randomly oriented and disconnected Li deposits in a diamagnetic (SEI) matrix. The NMR spectra of the Li metal on polymer-coated Cu was deconvoluted into three peaks using the same method as described above and shows a higher contribution of Peak 3 for PMMA and PEO-coated Cu, indicating less homogeneous deposition on the polymer-coated Cu (Figure 6.15).

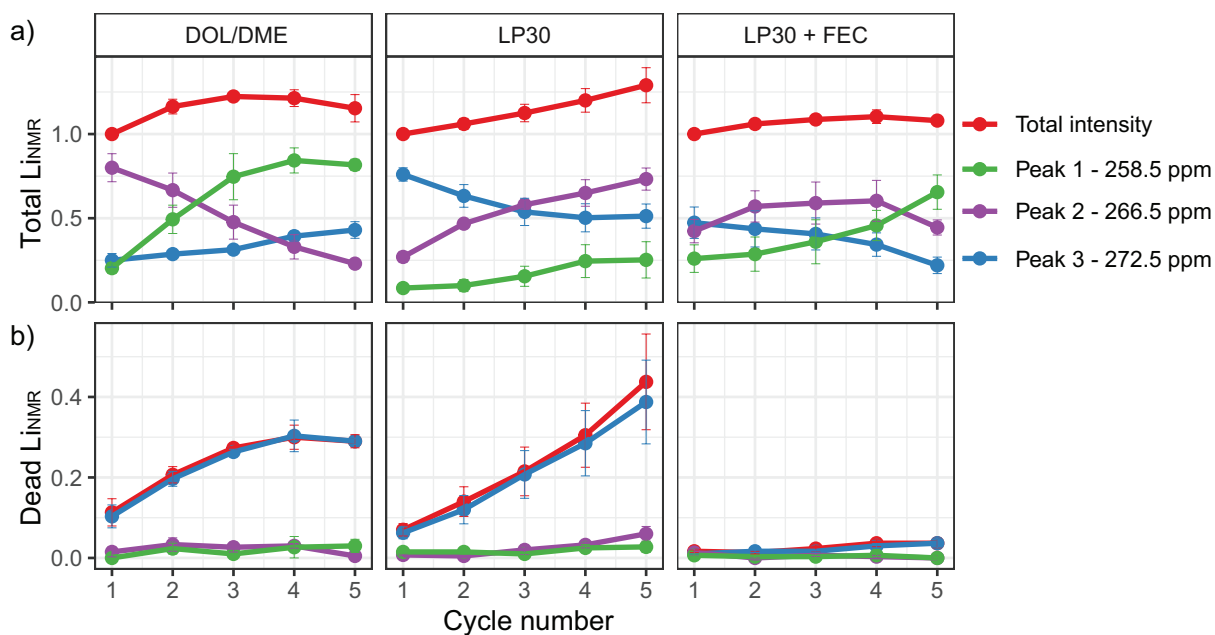


Figure 6.14 The normalised intensity of the deconvoluted peaks at **a)** the end of charge (plating, after depositing 1 mAh/cm² of Li metal) and **b)** at the end of discharge (stripping) in the three electrolytes. Peak 1, at the lowest ⁷Li metal shift, increases in intensity between cycles for all electrolytes during plating and is most apparent in the DOL/DME electrolyte. The dead Li peak measured in DOL/DME and LP30 is fully captured by Peak 3, at the highest ⁷Li metal shift.

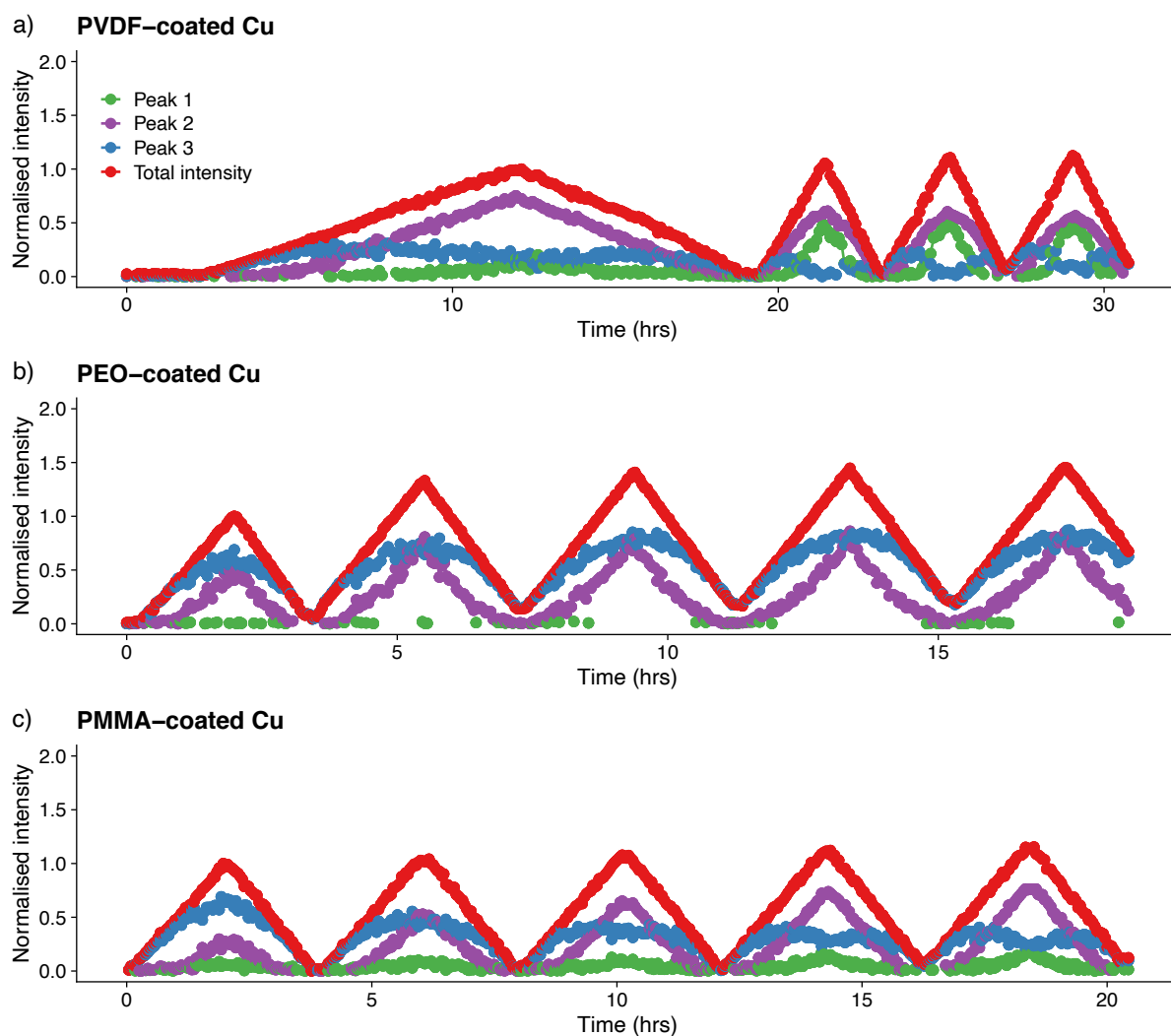


Figure 6.15 The normalised intensity of the deconvoluted peaks of Li metal spectra during cycling on a) PVDF-coated, b) PEO-coated and c) PMMA-coated Cu current collector.

6.3.4 Dissolution of Li metal

In practice, batteries are not constantly in use and it is important to understand the processes that occur during the periods when no current is passed. To investigate what occurs during the rest period in LMBs, Li metal was again deposited using 0.5 mA/cm^2 current density and 1 mAh/cm^2 plating capacity and the evolution of the Li metal signal recorded during the open circuit voltage (OCV) using *in situ* NMR.

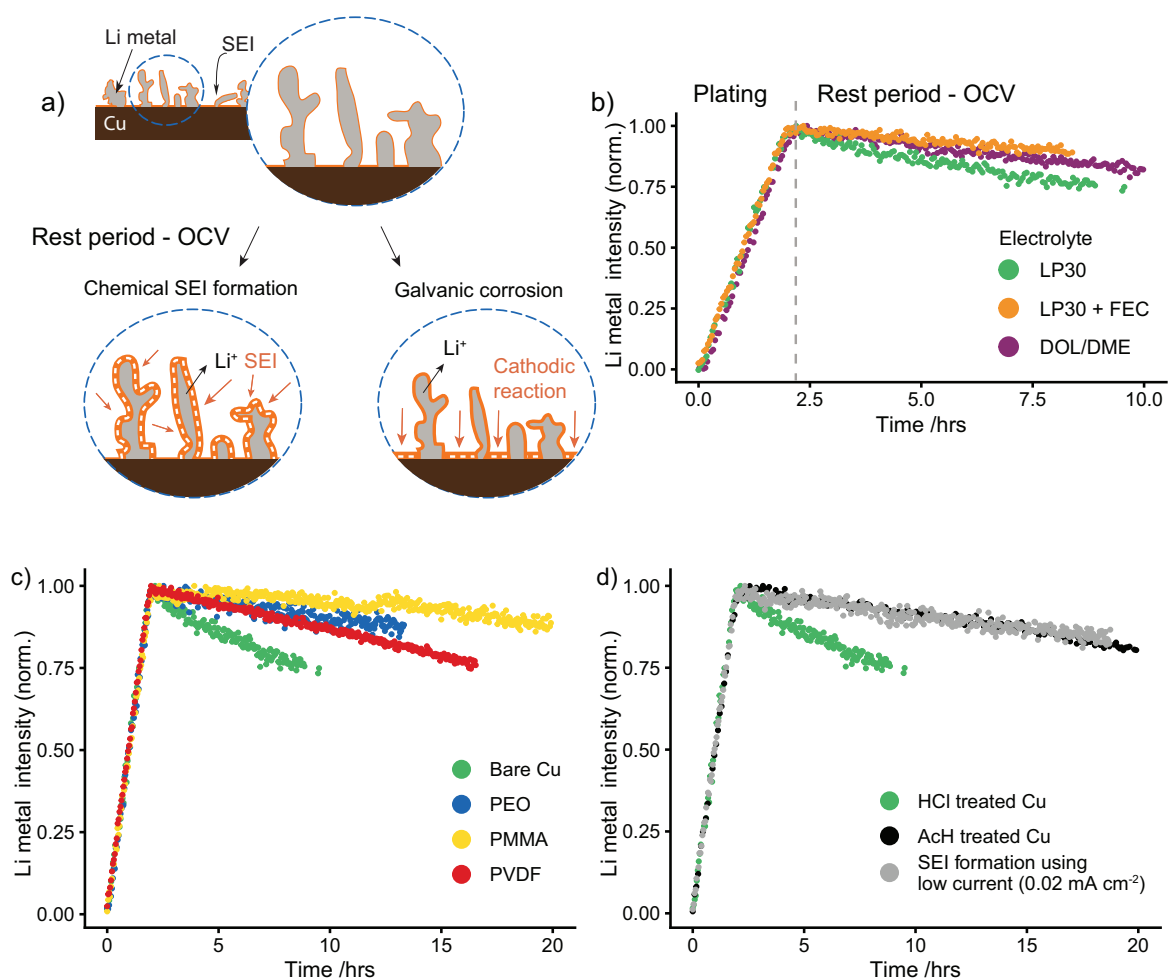


Figure 6.16. *In situ* NMR experiments of Li metal dissolution during the OCV period. **a)** A schematic representation of the processes that lead to Li metal corrosion: the chemical formation of the SEI on Li results in the spontaneous reduction of the electrolyte and oxidation of the Li metal. Galvanic corrosion results in the dissolution of Li metal (Li oxidation) and a cathodic reaction on the Cu electrode. **b)** Integrated intensity of the Li metal signal during the NMR experiment. The intensity increases during deposition (corresponding to 1 mAh/cm²) of charge and decreases constantly during the rest period at OCV for the three electrolytes, LP30, LP30 + FEC and DOL/DME. Plating and resting experiments for **c)** different polymer coatings: PEO-, PMMA- and PVDF-coated Cu current collector and **d)** different Cu treatments in LP30 electrolyte: Cu treated with HCl acid (green), Cu treated with glacial acetic acid (AcH, black). The grey curve shows the effect of a slow SEI formation step before deposition on HCl-treated Cu at 0.02 mA/cm² followed by a 12 hours voltage hold at 3.2 V before deposition at 0.5 mA/cm² (grey). The green curve in b, c and d) is for the same experiment, performed on bare Cu treated in HCl-acid and in LP30 electrolyte. Each experiment was performed twice, and the rate of dissolution was found to be highly reproducible.

Note that this experiment tracks capacity losses in a charged battery, which is particularly critical in anode-free batteries. The intensity of the Li metal grows for the first two hours during the plating (Figure 6.16b), a decrease in intensity is seen during the OCV period, indicating loss of Li metal. The dissolution (or corrosion) of Li metal can be due to both the chemical SEI formation on Li and the galvanic corrosion between Li and Cu that are in direct contact with the electrolyte (see the schematic, Figure 6a).

Figure 6.16b shows that different electrolytes have a significant impact on the rate of Li dissolution. The electrolyte effect on corrosion observed here is influenced by the Li morphology and bare Cu areas, and a ‘protective coating effect’ due to formation of a stable SEI. Amongst the three electrolytes studied here the fastest dissolution of Li metal is in the LP30 electrolyte and the greatest stability is in LP30 + FEC (Figure 6.16a). The stabilisation due to FEC is likely due to the interplay of greater surface coverages (as indicated by the lower ^7Li metal shift seen after plating in LP30 + FEC, Figure 6.10) as well as the difference in the SEI formed with FEC both on Li and Cu.^{157,206}

The same set of experiments were performed on the polymer-coated Cu current collectors in LP30 electrolyte (Figure 6.16c), demonstrating that all the coatings have a stabilising effect on the Li dissolution. This is likely due to the passivating effect of the coating, passivating both the Li deposits and the Cu current collector. Interestingly, the PMMA-coating has the greatest stabilising effect and correlates with the higher CE observed in Figure 6.6.

To investigate the effect of the Cu surface on corrosion, the same experiments were performed on a Cu current collector pre-treated in concentrated acetic acid (denoted AcH, the Cu used in all other experiments was pre-treated in HCl acid). The surface treatments on Cu current collectors and the corresponding SEI have been studied in detail in our previous work²¹⁸ where by XPS it was shown that the surface of the AcH-treated Cu (prior to assembly in a battery cell) was better passivated with high concentrations of $\text{Cu}(\text{OH})_2/\text{CuO}$ on the surface whereas the HCl-treated showed the Auger Cu metal peaks, indicating either a thinner or a more heterogeneous surface oxide layer on the Cu electrode with no $\text{Cu}(\text{OH})_2$ observed.²¹⁸

Figure 6.16d (black) shows that the corrosion of Li metal is slowed down using AcH-treated Cu, demonstrating the importance of surface passivation on Cu. In addition and following the approach of Lin et al.,¹⁹⁶ the corrosion was monitored on a (HCl-pretreated) Cu electrode, following an initial low-current step of 0.02 mA/cm^2 prior to Li deposition, the electrolyte

reduction products precipitating on the Cu surface resulting in an SEI that grows in thickness during polarization.^{206,218} This was followed by Li deposition at 0.5 mA/cm² (Figure 6d, grey). As shown previously by electrochemical measurements, the long SEI formation step on Cu slows down the Li metal dissolution under OCV consistent with passivation of the Cu electrode surface.¹⁹⁶ This stabilization is likely a combined effect of the reduction of the copper oxides/hydroxides on the Cu surface, minimising possible galvanostatic reduction reactions involving Cu²⁺ and Cu⁺, and formation of a more stable SEI layer, reducing the SEI reduction rate.

A linear fit was used to extract the slope of the dissolution curve during the OCV period, as shown in Figure 6.17. The slope of the linear fit was extracted for the entire measurements, χ_{slope} in s⁻¹, (data in Figure 6.16) and is displayed in the bar chart Figure 6.18. A steeper slope was obtained when for the initial two hours of the rest period indicating that some stabilisation occurs on the Li metal and Cu during the measurement.

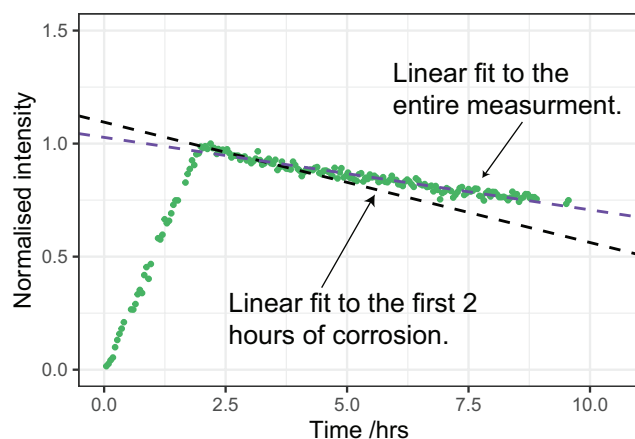


Figure 6.17. The linear fit to the corrosion curve of Li metal on bare Cu in LP30. The dashed lines show the linear fit obtained when accounting for only the first two hours compared to for the entire measurement. The corrosion current, i_{corr} for the first two hours is 49 $\mu\text{A cm}^{-2}$. Averaging over the whole measurement results in 28 $\mu\text{A cm}^{-2}$.

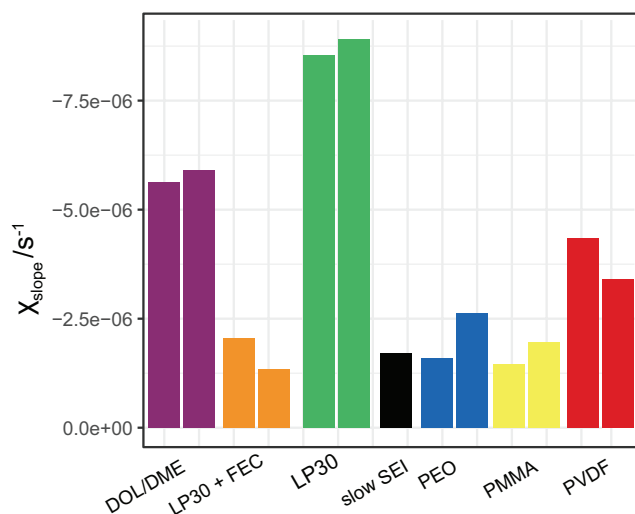


Figure 6.18 A bar chart showing the slope of the dissolution curve from a linear fit to the different sets of *in situ* NMR measurements in different electrolytes and with different polymer coatings.

The corrosion current can be estimated from the slope by using the SEI capacity determined above. The full plating capacity is $C_{\text{plating}} = 1 \text{ mAh/cm}^2 = 3.6 \text{ C/cm}^2$. The corrosion current density, i_{corr} , becomes:

$$i_{\text{corr}} = (C_{\text{plating}} - C_{\text{SEI},1}) \times \chi_{\text{slope}} \quad (6.6)$$

The corrosion current for each electrolyte was calculated using the mean of two separate experiments, with the values listed in Table 6.2. The highest corrosion current is for LP30 on bare Cu, around $30 \mu\text{A/cm}^2$.

Table 6.2. The mean of the slope (for two sets of experiments) obtained from a linear fit to the decreasing intensity of the ⁷Li NMR metal signal during the OCV period (Figure 6.16) and the calculated corrosion current i_{corr} . For experiments using the polymer-coated Cu, LP30 electrolyte was used in all cases.

Electrolyte/ Polymer coating	$\chi_{\text{slope}} / \text{s}^{-1}$	$i_{\text{corr}} / \mu\text{A cm}^{-2}$
LP30	-8.7	29
LP30 – 6th cycle	-9.6	31
LP30 – slow SEI formation step	-1.7	5.6
LP30 + FEC	-1.7	5.5
DOL/DME	-5.8	18
PEO-coating	-2.1	5.3
PMMA-coating	-1.7	5.2

6.3.4.1 Long term Li metal dissolution

The long-term corrosion behaviour of the Li electrodeposits was probed in LP30 and LP30 + FEC by acquiring few *ex situ* NMR measurements over a 50-80 hour period while storing the cells in an inert Argon glovebox in between measurements (Figure 6.19). Both electrolytes show a continuous Li corrosion throughout the measurement that does not seem to slow down notably with time. The Li metal deposits in LP30 have disappeared after 50 hours, whereas there is still Li metal left in LP30 + FEC after ~ 80 hours, albeit a small amount. The dissolution of the Li metal was also probed after the 6th deposition cycle in LP30 (Figure 6.19, black). Interestingly, the corrosion rate does not decrease after further cycling, as indicated by the similar slope of the two dissolution curves

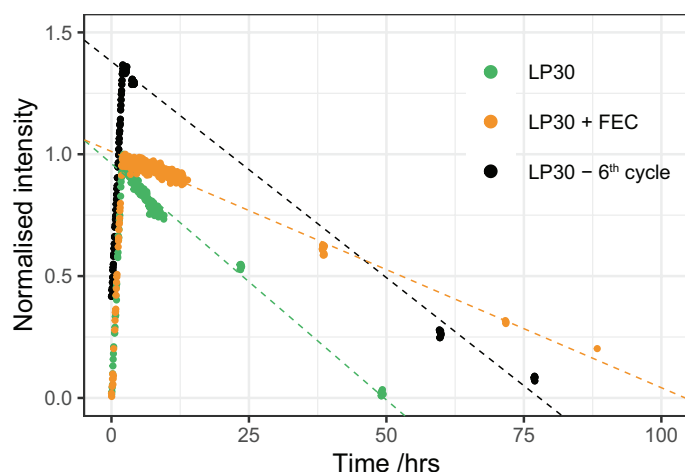


Figure 6.19 The long-term corrosion behaviour was probed by *ex situ* NMR measurements. In black is the corrosion of Li metal at the top of charge for the 6th deposition, normalised to the first cycle intensity, for the cell shown in Figure 6.3b. The dashed line represents the linear fit through the data points to guide the eye.

6.3.4.2 Li corrosion followed by stripping

Figure 6.20 shows the corrosion experiment for DOL/DME (the dissolution curve also shown in Figure 6.16b) and LP30 (using 0.02 mA/cm² SEI formation current) where after about 18 hours of rest at the OCV, the Li was completely stripped off using 0.5 mA/cm². Interestingly, for DOL/DME the amount of dead Li after stripping (Figure 6.20) is less for the corrosion experiment compared to stripping without the rest period; that is a dead Li of around 5% of the

plating capacity compared to on average of 11% without the rest period (Table 6.1). For LP30, the dead Li_{NMR} after stripping is on average 6% (Table 6.1), which is the same as measured after stripping with the rest period (Figure 6.20).

This indicates that the corrosion of Li metal, as measured here by NMR, does not result in a significant formation of dead Li prior to stripping by loss of contact to the Cu electrode. Furthermore, the small amount of dead Li_{NMR} left in the cell after stripping does not dissolve further (stable intensity seen after stripping at ~21-24 hours) further indicating the corrosion of Li is mainly due to the galvanic corrosion between the Cu and Li.

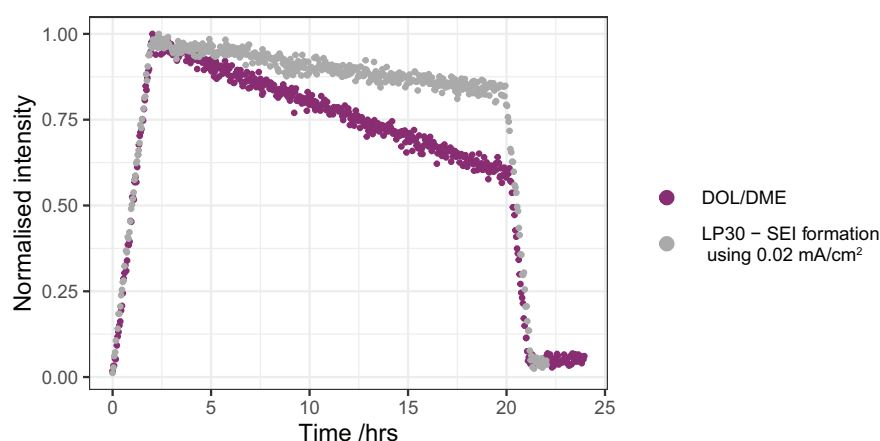


Figure 6.20 *In situ* NMR measurements of the corrosion followed by stripping. The normalised integrated intensity of the Li metal intensity during the first 2 hours of deposition using 0.5 mA/cm^2 (corresponding to 1 mAh/cm^2) and the corresponding decrease during the OCV period of roughly 18 hours followed by stripping at 0.5 mA/cm^2 in DOL/DME (purple) and LP30 with the initial SEI formation on Cu using 0.02 mA/cm^2 (compared to 0.5 mA/cm^2 used in all experiments where it is not stated specifically, grey). The formation period on Cu using 0.02 mA/cm^2 before plating is not shown as there is no Li metal signal to integrate. Thus, time = 0 equals to the time at the start of Li plating.

6.3.5 ^7Li shift of the diamagnetic peak

Finally, the ^7Li shift of the diamagnetic region was analysed. The diamagnetic region of the ^7Li *in situ* NMR spectrum typically shows a single peak around 0 ppm that captures both the Li^+ ions in the electrolyte and the lithium-containing species in the SEI. For the Cu-LFP cell however, the diamagnetic resonance becomes relatively broad and multiple resonances are observed (Figure 6.21a). When the LFP electrode is oriented perpendicular to the magnetic

field there are on average two peaks observed, one around 0 to -15 ppm (Peak A) and one peak around +30 to +10 ppm (Peak B, Figure 6.21a). A similar split in the shift of the diamagnetic resonances was previously observed in an *in situ* $\text{Li}_{1.08}\text{Mn}_{1.92}\text{O}_4$ cell (albeit with larger shifts of +100 and -67 ppm).¹³⁷ The shifts were assigned to the electrolyte in different regions in the cell induced by the different dipolar fields from the $\text{Li}_{1.08}\text{Mn}_{1.92}\text{O}_4$ film; within the glass fibre separator, at the edges of the cell, between current collectors or close to the cathode electrode.¹³⁷

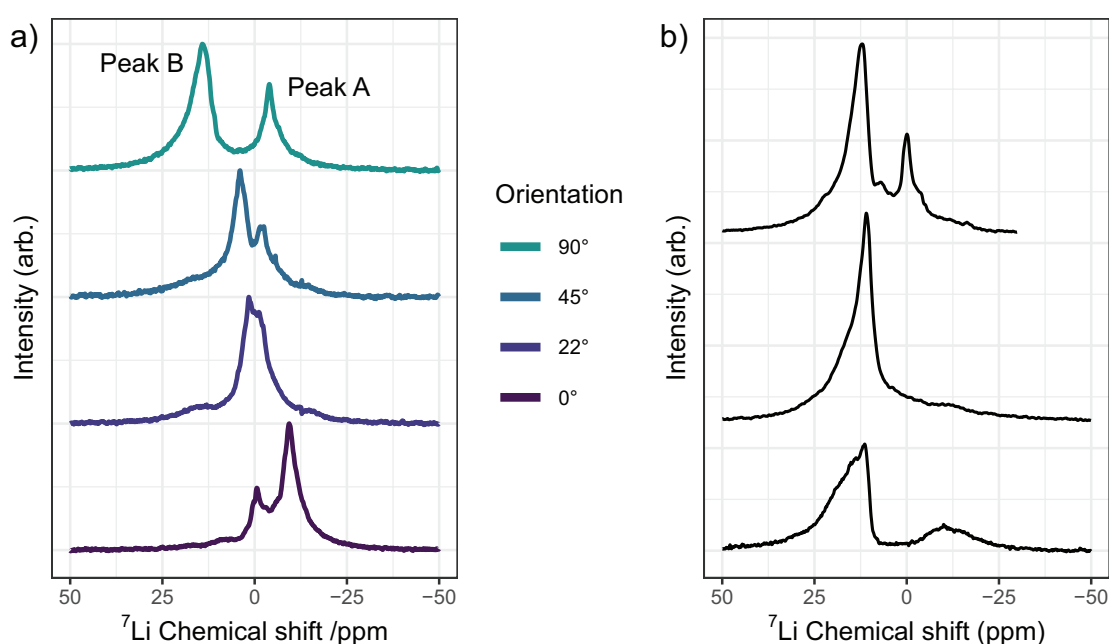


Figure 6.21 The ^7Li NMR spectra of the diamagnetic peak in Cu-LFP *in situ* cells before any current has been passed. **a)** A Cu-LFP cell that was rotated in the NMR rf-coil so that the electrodes were oriented at approximately 0°(parallel), 22°, 45° and 90° (perpendicular, same as all the *in situ* experiments unless otherwise stated) with respect to the magnetic field. **b)** Three different Cu-LFP cells (oriented perpendicular with respect to the magnetic field) using LP30 electrolyte, demonstrating how sensitive it is to cell assembly.

Shifts caused by BMS effects are influenced by the shape of the sample container and all of the cell components; that is the Cu current collector, the electrolyte and electrolyte separator, the Li metal (after plating), but the dominant contribution is expected to come from the paramagnetic LFP cathode.¹³⁷ The peaks shift when the orientation of the electrode with respect to the applied magnetic field, \mathbf{B}_0 , was changed by rotating the Cu-LFP cell in the NMR coil (Figure 6.21a). This can be explained by the non-spherical shape of the paramagnetic LFP cathode film.¹³⁵ Following previous assignments, Peak B is tentatively assigned to Li^+ ions

close to the LFP cathode and Peak A to the electrolyte in the glass fibre separator further away from the cathode. Figure 6.21b shows the ^7Li NMR spectra of the diamagnetic region for three pristine *in situ* Cu-LFP cells, that is before any current was applied. Of note is how the peaks differ between cells that were assembled with identical procedures, which demonstrates how sensitive the electrolyte peak is to the cell assembly.

During cycling of the Cu-LFP cell, the shift cycles with the electrochemistry, that is Peak B shifts to lower frequencies during plating (delithiation of the LFP) whereas Peak A stays constant (Figure 6.22a). The change in shift may be attributed to the changes in the magnetic susceptibility of the LFP, which increases during delithiation at a higher state of charge of the cathode.^{225,227}

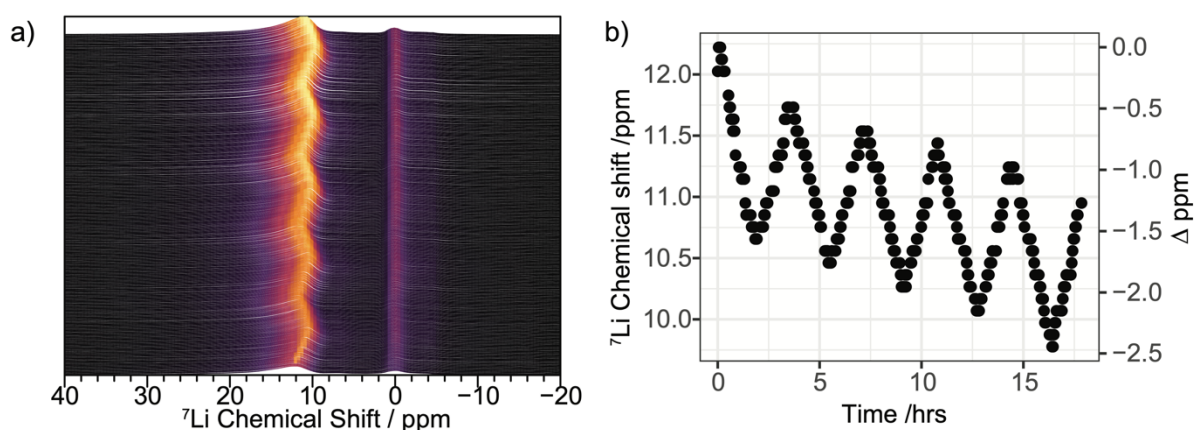


Figure 6.22 The ^7Li NMR spectra of the diamagnetic region in a Cu-LFP cell during plating and stripping at 0.5 mA/cm² current density and with 1 mAh/cm² capacity. **a)** A heatmap of the NMR spectra, showing how Peak A stays constant during cycling whereas Peak B cycles with the electrochemistry. **b)** The shift (ppm) and ‘shift change’ (Δ ppm) for Peak B. The shift is going towards lower shifts in each cycle due to capacity losses in the cell pushing the LFP to a higher state of charge in each cycle (and the plating capacity kept constant at 1 mAh/cm²).

A similar trend was recently demonstrated by Ilott et al. where the changes in magnetic susceptibility within a lithium-ion battery cell was measured using an indirect ^1H magnetic resonance imaging (MRI).²²⁷ The authors showed that the average oxidation state of an NMC cathode could be tracked by measuring the susceptibility-induced shift change of the resonance of water (that surrounded the battery cell) with negative shift changes observed with increasing susceptibility of the NMC.²²⁷ The trend in Figure 6.22b is consistent with their study, with a negative shift in Peak B during delithiation when the susceptibility of the LFP is increasing.²²⁵ We observe the change in shift to be linear with the state of charge.

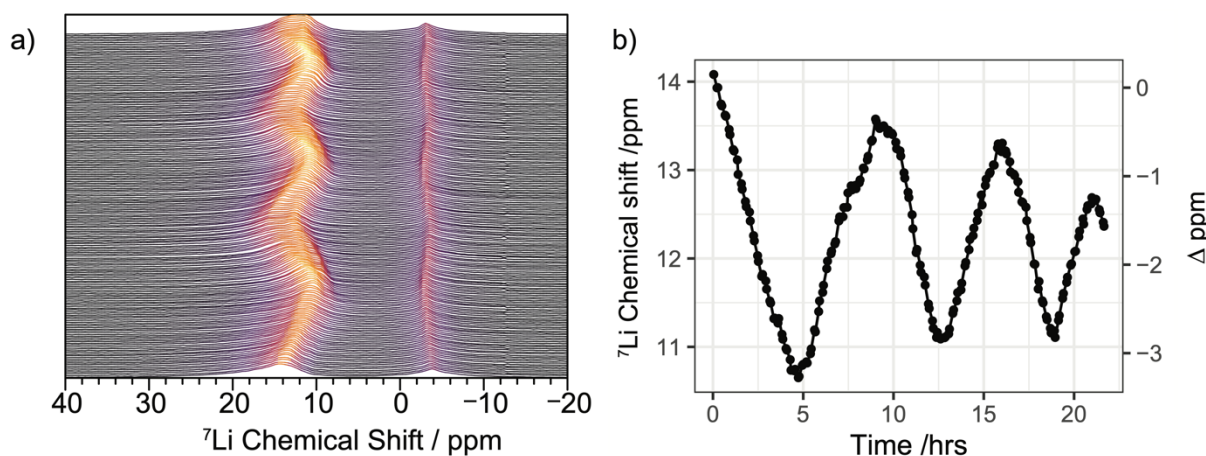


Figure 6.23 **a)** The ${}^7\text{Li}$ NMR diamagnetic region for a Cu-LFP cell, which was fully charged (delithiated) at 0.5 mA/cm^2 current density, reaching 2.3 mAh/cm^2 capacity. **b)** The ${}^7\text{Li}$ shift (ppm) and shift change (Δ ppm) for Peak B.

In order to observe the change in shift in more detail, the LFP cathode was fully charged (corresponding to an areal capacity of 2.3 mAh/cm^2), which results in a change in shift of -3.3 ppm of Peak B (Figure 6.23). Testing whether the change in shift, Δ ppm, can be used as a method to directly predict the state of charge of the LFP cathode, the change in Figure 6.23b corresponds to $-1.4 \text{ ppm per mAh/cm}^2$ of capacity for the LFP cathode. Comparing this value to the Δ ppm in Figure 6.22 the change is equivalent to $-1.7 \text{ ppm per mAh/cm}^2$ of LFP capacity. In analysing more cells, we discover that Δ ppm normalised to the LFP areal capacity is not consistent between cells. This is likely due to the trend observed in Figure 6.21, where a significantly different spectrum are observed for different *in situ* cells, but a more accurate method would be to account for the gravimetric capacity of the cathode and is a subject of future studies.

6.4 Discussion

The *in situ* NMR technique allows the capacity losses due to SEI formation and dead Li to be quantified during cycling. Importantly, it demonstrates that both the SEI formation and dead Li formation contribute significantly to the cycling stability of LMBs. In all cases,

electrochemical SEI formation was shown to contribute more to the capacity losses in the anode-free battery compared to dead Li formation. This is in contrast to the results reported by Fang et al., where the authors concluded that the dead Li is the main reason behind capacity losses in LMBs in the first cycle as well as in subsequent cycles.⁵⁶ The studies are not entirely comparable as Fang et al. performed the measurements in Cu-Li coin cells.⁵⁶ Having Li foil in the cell has been shown to boost the cycling performance and the CE compared to anode-free cells.⁴⁹ The Li foil not only supplies the battery with enough reservoir of Li⁺ ions but critically may also act as a scavenger for any impurities or electrolyte degradation products in the electrolyte, which likely influences the amount of SEI that forms on the Li deposits on Cu.

In LP30 + FEC small amount of dead Li was observed on the first cycle (0.01 mAh/cm²) and on cycle five the total dead Li capacity amounted to 0.04 mAh/cm², although the CE remained 90-93% over the first five cycles demonstrating that the SEI needs reforming and continues to grow every cycle. This is consistent for all three electrolytes as shown in Figure 6.5 where the SEI formation capacity for the carbonate electrolytes remains around 0.05-0.1 mAh/cm². This is also consistent with the corrosion rate seen on the 6th cycle in LP30 (Figure 6.19) where a stabilization after five cycles of plating and stripping was not observed. This is probably due to the volume changes associated with the complete stripping of Li metal in an anode-free battery, damaging the SEI in each cycle. But it also indicates that the film formed on Cu is still poorly passivating, even after 6 cycles. By contrast, the corrosion current drops by a factor of five (Table 6.2) when a passivating film is formed electrochemically on Cu prior to deposition. In this case, a larger contribution to the corrosion current is presumably coming from Li corrosion due to chemical SEI formation (Figure 6.16a). Further studies are needed to explore this phenomenon, additives such as FEC clearly affecting both the galvanic and chemical SEI formation. This may also indicate that the full stripping of the Li is too extreme in LMBs and a gentler approach where a reservoir of Li is left on the anode after fully discharging the cell may help stabilise the SEI in later cycles.²²⁸

In contrast to the carbonate electrolytes, the CE of the DOL/DME increased in the first five cycles with a concurrent drop in dead Li formation and SEI formation (Figure 6.5). In addition, the Li deposits in DOL/DME appear at a lower shift (Figure 6.11) indicating formation of a more homogeneous coverage of Li on the Cu electrode. The CE on the PEO- and PVDF-coated Cu was low on the first cycle compared to that on bare Cu (Figure 6.6) without an

increase in the observed dead Li concentration, indicating an increase in side reactions during plating. This may partly be due to less homogeneous deposition (as indicated with the higher Li metal shift in Figure 6.15), that causes enhanced SEI formation. Assegie et al. demonstrated the importance of optimizing the PEO-film on a Cu current collector, where high CE was only achieved with a uniform and defect-free PEO coating.²¹⁰

The quantitative *in situ* NMR allows the corrosion current of Li metal on Cu to be estimated. The corrosion current density (with respect to the Cu electrode area) of Li electrodeposits on Cu was measured as 29 $\mu\text{A}/\text{cm}^2$ in LP30 and 5.5 $\mu\text{A}/\text{cm}^2$ in LP30 + FEC. The lower corrosion current measured for LP30 + FEC is likely due to both a denser Li morphology and differences in the SEI that forms. The isotope exchange experiments in Chapter 5 showed a noticeably faster SEI formation in LP30 + FEC at the OCV, that led to faster stabilisation of the SEI on Li metal. This will lead to more effective passivation of Li metal and slower Li corrosion at later times. In addition, the chemical composition and the nanostructure of the SEI on both Li metal and Cu has been shown to be different in LP30 + FEC.^{45,82,157,206}

The rate of galvanic corrosion measured here should be contrasted with the values measured by zero resistance ammetry (ZRA).¹⁹⁷ Kolesnikov et al. found the corrosion rate to be highly dynamic with the initial corrosion current $> 160 \mu\text{A}/\text{cm}^2$ that decreased rapidly to $< 1 \mu\text{A}/\text{cm}^2$ after 10 hours of measurements, reaching a steady-state value of $0.2 \mu\text{A}/\text{cm}^2$ after 100 hrs in LiPF_6 – carbonate electrolyte. They again attribute this decrease in the corrosion current to the formation of a passive film on the Cu, which decreases the reduction reactions at the Cu surface.¹⁹⁷ The passivation of the Cu is consistent with the reduced corrosion rate when using a slow SEI formation step on Cu prior to Li deposition, which indicates that if the Cu electrode is properly stabilised the Li corrosion can be mitigated (Figure 6.16c). The results are also consistent with the data for LP30, where an enlargement of measurements of Li corrosion immediately after the current is switched off show an enhanced rate of corrosion (initially around $50 \mu\text{A}/\text{cm}^2$, Figure 6.17) that settles to a steadier value after two hours. However, no complete stabilisation was observed here over longer time-periods (Figure 6.19) in the carbonate electrolytes.

Finally, Kolesnikov et al. describe the corrosion effect in terms of the differences in the standard electrode potentials of two metals – here Li and Cu. Strictly this is only true if the Li corrosion is coupled with either Cu^+ or Cu^{2+} reduction to Cu metal. Instead it is more

appropriate to view galvanic corrosion as arising from a difference in the rates of SEI formation on Li and Cu, which will arise from both a difference in the passivating nature of the SEI on the Cu as discussed in reference¹⁹⁶, and also simply due to differences in surface area.

6.5 Conclusions and Outlook

In this chapter the application of *in situ* ⁷Li NMR was demonstrated to study the plating and stripping, and the corrosion of Li metal on Cu current collector. The *in situ* NMR method is shown to be a valuable technique for deconvoluting the multiple capacity losses that occur in LMBs, which will enable further studies on different electrolytes as well as on the compatibility of protective coatings and artificial SEIs for Li deposition.

Almost no dead Li is observed in LP30 + FEC although the CE is < 100% (~92%) indicating that capacity losses are mainly due to the SEI formation. Similarly, for LP30 and DOL/DME electrolytes the dead Li accumulates continuously for the first five cycles but cannot account for the entire capacity loss and again the SEI formation is a significant part of the coulombic losses. Importantly, we show that the SEI does not stabilise with the cycling of the battery and indicates that full stripping of lithium metal in anode-free batteries might aggravate battery degradation, thus a reservoir of lithium metal may be needed on the anode side

The bulk magnetic susceptibility shifts caused by Li metal results in lower ⁷Li shift of the deposits formed in DOL/DME and LP30 + FEC, indicating higher surface coverage of Li as suggested by the susceptibility calculations. In contrast, the ⁷Li metal shift in LP30 on both bare Cu and polymer-coated Cu is at a higher metal shift indicating less dense coverage of the deposits. Of note, the dead Li deposits show essentially no BMS effect due to the Li metal, consistent with their random orientations within the electrode; their shift is dominated by the BMS effect arising from the LFP electrode (and the Li Knight shift).

The evolution of Li metal was monitored under OCV conditions by *in situ* ⁷Li NMR and revealed that the Li metal corrosion rate is highly sensitive to the type of electrolyte and the surface of the Cu current collector. The rate of corrosion is high and remains a critical issue for LMBs to be a viable option for energy storage technologies. Strategies to protect the Li metal deposits need to be studied systematically and with quantitative techniques such as presented here. Polymer coatings were shown to protect the Li metal deposits from dissolution and may

be studied further with respect to reactivity, conductivity and coating homogeneity and thickness.²⁰⁹ Furthermore, it is crucial to perform more controlled study of the Cu films, to correlate Cu surface chemistries and the passivating films that are formed with the rates of galvanic corrosion. We note, however, that simple pre-treatments of the Cu metal to remove surface oxides, and to reduce $\text{Cu}^{2+}/\text{Cu}^+$ species electrochemically and form an SEI on Cu before Li deposition were shown to noticeably reduce the corrosion rate.

The *in situ* NMR technique can be further used to study corrosion in lithium-sulfur batteries that remains a critical issue due to the dissolution of polysulfides.²²⁹ Other strategies to mitigate Li corrosion that will be interesting to study include artificial SEI layers such as Al_2O_3 ,²²⁹ metal coatings^{230–233} and inactive additives such as hydrocarbons that have been shown to decrease the corrosion rate and lead to more homogeneous Li plating and lower Li^+ solvation energies.^{234,235} Furthermore, this technique could be used to study corrosion in Na metal batteries using ^{23}Na *in situ* NMR.

The ^7Li shift of the diamagnetic peak was shown to be highly susceptible to the electrochemistry of the battery, with a shift to lower frequencies when the LFP cathode is at higher state of charge. The change in shift did not correlate with the state of charge of the LFP when normalised to the charge/discharge areal capacity of the cathode. A more detailed study, where the gravimetric capacity is fully accounted for, will clarify whether a specific change in the ^7Li shift may be extracted to predict the state of charge of the cathode with NMR.

Chapter 7 Conclusions and Future Work

The major objective of this thesis was to gain a better understanding of how the SEI that forms spontaneously on Li metal affects the cyclability of LMBs. Throughout this work two electrolytes, the commercial carbonate electrolyte LP30 and LP30 with the widely known additive FEC, are studied together with various electrochemical and *in situ* NMR measurements. NMR spectroscopy is both a non-invasive and a quantitative technique, and can be used to study lithium losses during operation of the battery. The resonance of Li metal is easily resolved from other lithium-containing components in the cell due to the metallic Knight shift, which makes NMR an ideal technique to study LMBs.

In Chapter 4, *in situ* NMR was used to study the microstructural growth of Li and the effect of FEC systematically studied under different plating conditions. Having FEC additive in the cell led to denser Li deposits and higher current efficiency. This can be explained by the results presented in Chapter 5 where $^{6,7}\text{Li}$ isotope exchange measurements are used to probe the SEI. The isotope exchange between Li metal and the electrolyte was reported in an earlier study,¹⁸² but has never been used as a direct tool to study the dynamic differences between SEIs. The charge transfer and the SEI formation kinetics are an important aspect of Li plating and expected to influence the electrodeposition and Li morphology. The isotope exchange measurements reveal the distinct kinetics on Li metal and the corresponding SEI with FEC. By numerical modelling, we show how exchange occurs twice as fast when using FEC additive and the SEI formation occurs five times faster. Together with the results on pulse plating this illustrates the important effect of the SEI when using FEC, the faster Li^+ transport and healing of the SEI leads to increased levelling effects.

There is currently an intense research effort underway to study the capacity losses in LMBs and *ex situ* methods for quantitative Li measurement have recently been developed. A non-destructive *in situ* technique is important for characterising such losses because, as shown in Chapter 6, the capacity losses during rest periods due to lithium corrosion are significant in LMBs and will affect any type of an *ex situ* measurement. A new *in situ* NMR metrology was developed to study the capacity losses in a full cell LMB and the different processes that lead

to capacity fading are quantified, namely the dead lithium formation (that corresponds to lithium metal that no longer has electronic contact with the current collector), the formation of the SEI and Li corrosion, which all lead to a loss of active material in the battery cell. Importantly, we show that the SEI does not stabilise with cycling of the battery and indicates that full stripping of Li metal in anode-free batteries might aggravate battery degradation, thus a reservoir of Li metal may be needed on the anode side. The technique will be extended to other high-voltage cathodes, where degradation mechanisms such as electrolyte oxidation may occur at high state-of-charge and contribute to the capacity losses. More detailed measurements and analysis of the diamagnetic ^7Li NMR peak should be performed on different cathodes, the results here on the LFP cathode indicate that changes in ^7Li shift may be used to infer about the state-of-charge of the cathode during battery operation.

By *in situ* NMR, we quantify processes that occur during the OCV when the battery is not in use, which is hard to measure with other quantitative techniques. The corrosion current is here calculated directly from the decrease in intensity of the Li metal NMR peak. The measurements reveal that Li corrosion is significant and stabilisation of the Li metal is crucial for these types of batteries. Strategies to mitigate the corrosion are explored and show that electrolyte additives, polymer-coatings and copper surface treatments lead to a reduction in the corrosion current up to a factor of five. There is an extensive scope to apply both the isotope exchange methodology and the *in situ* NMR presented in Chapter 6: exploring different electrolyte systems and other surface chemistries being investigated for LMBs. Ideally, a fast screening method should be developed for the isotope exchange measurements allowing them to be performed in an NMR solution-state facility found in many university chemistry departments. As most facilities do not allow direct access to the NMR magnets and probes, the orientation and thus the excitation profile of the metal electrode cannot be controlled. A cylindrical Li metal piece should remove this orientation issue and preliminary work has been carried out by soaking an extruded Li metal wire in an electrolyte using a typical NMR tube.

Isotope labelling should be used to greater extent when studying Li metal with NMR; emerging and promising techniques such as DNP-NMR, used to study the SEI on Li metal,⁸⁷ will benefit from the wider chemical shift range of ^6Li compared to ^7Li . The transport mechanism in a ceramic-polymer composite electrolyte was investigated in an elegant study by Zheng and Hu using isotope labelling by cycling the electrolyte using ^6Li metal.¹⁷⁷ The dissolution of Li metal

into PEO has also recently been shown to occur at elevated temperatures by NMR.²³⁶ Thus, there is great potential to study the reactivity of Li metal and Li⁺ transport in different polymer electrolytes, composite electrolytes and solid electrolytes using NMR. Isotope labelling and isotope exchange measurements could be used to study Li metal solid-state batteries (under pressure) where improved fundamental understanding of the buried ceramic/Li metal interface is needed. The pitting of Li, or void formation, is also recognised as one of the main problems for Li metal solid-state batteries, which leads to a loss of contact to the solid electrolyte.²³⁷ In Chapter 4, the pitting of the Li metal electrode was shown to affect the NMR spectrum by broadening of the ⁷Li metal peak. Due to skin depth effects, the NMR is sensitive to the total surface area on bulk Li metal and there is a potential here to develop an NMR method to quantify the extent of pitting on a stripping electrode, an underexplored area when it comes to Li metal studies.

References

- (1) Atkins, P. W.; de Paula, J.; Keeler, J. *Atkins' Physical Chemistry*, 11th ed.; Oxford University Press: Oxford, 2017.
- (2) Liu, J.; Bao, Z.; Cui, Y.; Dufek, E. J.; Goodenough, J. B.; Khalifah, P.; Li, Q.; Liaw, B. Y.; Liu, P.; Manthiram, A.; Meng, Y. S.; Subramanian, V. R.; Toney, M. F.; Viswanathan, V. V.; Whittingham, M. S.; Xiao, J.; Xu, W.; Yang, J.; Yang, X. Q.; Zhang, J. G. Pathways for Practical High-Energy Long-Cycling Lithium Metal Batteries. *Nat. Energy* **2019**, *4* (3), 180–186.
- (3) Dunn, B.; Kamath, H.; Tarascon, J. M. Electrical Energy Storage for the Grid: A Battery of Choices. *Science* **2011**, *334* (6058), 928–935.
- (4) Dominko, R.; Fichtner, M.; Otuszewski, T.; Punckt, C.; Tarascon, J.; Vegge, T.; Dominko, R.; Edström, K.; Fichtner, M.; Punckt, C. *BATTERY 2030+ Roadmap 1*; 2020.
- (5) Choi, J. W.; Aurbach, D. Promise and Reality of Post-Lithium-Ion Batteries with High Energy Densities. *Nat. Rev. Mater.* **2016**, *1* (4), 16013.
- (6) Manthiram, A. A Reflection on Lithium-Ion Battery Cathode Chemistry. *Nat. Commun.* **2020**, *11* (1), 1–9.
- (7) Nitta, N.; Wu, F.; Lee, J. T.; Yushin, G. Li-Ion Battery Materials: Present and Future. *Mater. Today* **2015**, *18* (5), 252–264.
- (8) Whittingham, M. S. Electrical Energy Storage and Intercalation Chemistry. *Science* **1976**, *192* (4244), 1126–1127.
- (9) Mizushima, K.; Jones, P. C.; Wiseman, P. J.; Goodenough, J. B. Li_xCoO_2 ($0 < x < 1$): A New Cathode Material for Batteries of High Energy Density. *Mater. Res. Bull.* **1980**, *15* (6), 783–789.
- (10) Yoshino, A. The Birth of the Lithium-Ion Battery. *Angew. Chemie Int. Ed.* **2012**, *51* (24), 5798–5800.
- (11) Schmuck, R.; Wagner, R.; Hörpel, G.; Placke, T.; Winter, M. Performance and Cost of Materials for Lithium-Based Rechargeable Automotive Batteries. *Nat. Energy* **2018**, *3* (4), 267–278.
- (12) Albertus, P.; Babinec, S.; Litzelman, S.; Newman, A. Status and Challenges in Enabling the Lithium Metal Electrode for High-Energy and Low-Cost Rechargeable Batteries. *Nat. Energy* **2018**, *3* (1), 16–21.
- (13) Winter, M.; Barnett, B.; Xu, K. Before Li Ion Batteries. *Chem. Rev.* **2018**, *118* (23), 11433–11456.
- (14) Zheng, J.; Kim, M. S.; Tu, Z.; Choudhury, S.; Tang, T.; Archer, L. A. Regulating Electrodeposition Morphology of Lithium: Towards Commercially Relevant Secondary

- Li Metal Batteries. *Chem. Soc. Rev.* **2020**, *49* (9), 2701–2750.
- (15) Bruce, P. G.; Hardwick, L. J.; Abraham, K. M. Lithium-Air and Lithium-Sulfur Batteries. *MRS Bull.* **2011**, *36* (7), 506–512.
- (16) Liu, T.; Vivek, J. P.; Zhao, E. W.; Lei, J.; Garcia-Araez, N.; Grey, C. P. Current Challenges and Routes Forward for Nonaqueous Lithium–Air Batteries. *Chem. Rev.* **2020**, *120* (14), 6558–6625.
- (17) Fang, C.; Wang, X.; Meng, Y. S. Key Issues Hindering a Practical Lithium-Metal Anode. *Trends Chem.* **2019**, *1* (2), 152–158.
- (18) Peled, E. The Electrochemical Behavior of Alkali and Alkaline Earth Metals in Nonaqueous Battery Systems—The Solid Electrolyte Interphase Model. *J. Electrochem. Soc.* **1979**, *126* (12), 2047.
- (19) Chen, K.-H.; Wood, K. N.; Kazyak, E.; LePage, W. S.; Davis, A. L.; Sanchez, A. J.; Dasgupta, N. P. Dead Lithium: Mass Transport Effects on Voltage, Capacity, and Failure of Lithium Metal Anodes. *J. Mater. Chem. A* **2017**, *5* (23), 11671–11681.
- (20) Wood, K. N.; Noked, M.; Dasgupta, N. P. Lithium Metal Anodes: Toward an Improved Understanding of Coupled Morphological, Electrochemical, and Mechanical Behavior. *ACS Energy Lett.* **2017**, *2* (3), 664–672.
- (21) Liu, B.; Zhang, J.-G. G.; Xu, W. Advancing Lithium Metal Batteries. *Joule* **2018**, *2* (5), 833–845.
- (22) Paunovic, M.; Schlesinger, M. *Fundamentals of Electrochemical Deposition*; John Wiley & Sons, Inc.: Hoboken, NJ, USA, 2006.
- (23) Peled, E.; Golodnitsky, D.; Penciner, J. The Anode/Electrolyte Interface. In *Handbook of Battery Materials*; Besenhard, J. O., Ed.; Wiley-VCH: Weinheim, 1999.
- (24) Cohen, Y. S.; Cohen, Y.; Aurbach, D. Micromorphological Studies of Lithium Electrodes in Alkyl Carbonate Solutions Using in Situ Atomic Force Microscopy. *J. Phys. Chem. B* **2000**, *104* (51), 12282–12291.
- (25) Jurng, S.; Brown, Z. L.; Kim, J.; Lucht, B. L. Effect of Electrolyte on the Nanostructure of the Solid Electrolyte Interphase (SEI) and Performance of Lithium Metal Anodes. *Energy Environ. Sci.* **2018**, *11* (9), 2600–2608.
- (26) Zhang, X.-Q.; Chen, X.; Cheng, X.-B.; Li, B.-Q.; Shen, X.; Yan, C.; Huang, J.-Q.; Zhang, Q. Highly Stable Lithium Metal Batteries Enabled by Regulating the Solvation of Lithium Ions in Nonaqueous Electrolytes. *Angew. Chemie Int. Ed.* **2018**, *57* (19), 5301–5305.
- (27) Qian, J.; Xu, W.; Bhattacharya, P.; Engelhard, M.; Henderson, W. A.; Zhang, Y.; Zhang, J. G. Dendrite-Free Li Deposition Using Trace-Amounts of Water as an Electrolyte Additive. *Nano Energy* **2015**, *15*, 135–144.
- (28) Zheng, J.; Engelhard, M. H.; Mei, D.; Jiao, S.; Polzin, B. J.; Zhang, J. G.; Xu, W. Electrolyte Additive Enabled Fast Charging and Stable Cycling Lithium Metal Batteries. *Nat. Energy* **2017**, *2* (3), 1–15.
- (29) Markevich, E.; Salitra, G.; Chesneau, F.; Schmidt, M.; Aurbach, D. Very Stable Lithium Metal Stripping-Plating at a High Rate and High Areal Capacity in Fluoroethylene

- Carbonate-Based Organic Electrolyte Solution. *ACS Energy Lett.* **2017**, *2* (6), 1321–1326.
- (30) Peled, E.; Menkin, S. Review—SEI: Past, Present and Future. *J. Electrochem. Soc.* **2017**, *164* (7), A1703–A1719.
- (31) Wang, X.; Zhang, M.; Alvarado, J.; Wang, S.; Sina, M.; Lu, B.; Bouwer, J.; Xu, W.; Xiao, J.; Zhang, J. G.; Liu, J.; Meng, Y. S. New Insights on the Structure of Electrochemically Deposited Lithium Metal and Its Solid Electrolyte Interphases via Cryogenic TEM. *Nano Lett.* **2017**, *17* (12), 7606–7612.
- (32) He, M.; Guo, R.; Hobold, G. M.; Gao, H.; Gallant, B. M. The Intrinsic Behavior of Lithium Fluoride in Solid Electrolyte Interphases on Lithium. *Proc. Natl. Acad. Sci. U. S. A.* **2020**, *117* (1), 73–79.
- (33) Chang, H. J.; Ilott, A. J.; Trease, N. M.; Mohammadi, M.; Jerschow, A.; Grey, C. P. Correlating Microstructural Lithium Metal Growth with Electrolyte Salt Depletion in Lithium Batteries Using ⁷Li MRI. *J. Am. Chem. Soc.* **2015**, *137* (48), 15209–15216.
- (34) Nishikawa, K.; Mori, T.; Nishida, T.; Fukunaka, Y.; Rosso, M. Li Dendrite Growth and Li⁺ionic Mass Transfer Phenomenon. *J. Electroanal. Chem.* **2011**, *661* (1), 84–89.
- (35) Yoon, G.; Moon, S.; Ceder, G.; Kang, K. Deposition and Stripping Behavior of Lithium Metal in Electrochemical System: Continuum Mechanics Study. *Chem. Mater.* **2018**, *30* (19), 6769–6776.
- (36) Nishikawa, K.; Mori, T.; Nishida, T.; Fukunaka, Y.; Rosso, M.; Homma, T. In Situ Observation of Dendrite Growth of Electrodeposited Li Metal. *J. Electrochem. Soc.* **2010**, *157* (11), A1212.
- (37) Kushima, A.; So, K. P.; Su, C.; Bai, P.; Kuriyama, N.; Maebashi, T.; Fujiwara, Y.; Bazant, M. Z.; Li, J. Liquid Cell Transmission Electron Microscopy Observation of Lithium Metal Growth and Dissolution: Root Growth, Dead Lithium and Lithium Flotsams. *Nano Energy* **2017**, *32* (11), 271–279.
- (38) Crowther, O.; West, A. C. Effect of Electrolyte Composition on Lithium Dendrite Growth. *J. Electrochem. Soc.* **2008**, *155* (11), A806.
- (39) Yamaki, J.; Tobishima, S.; Hayashi, K.; Keiichi Saito; Nemoto, Y.; Arakawa, M. A Consideration of the Morphology of Electrochemically Deposited Lithium in an Organic Electrolyte. *J. Power Sources* **1998**, *74* (2), 219–227.
- (40) Yoshimatsu, I. Lithium Electrode Morphology during Cycling in Lithium Cells. *J. Electrochem. Soc.* **1988**, *135* (10), 2422.
- (41) Steiger, J.; Kramer, D.; Mönig, R. Microscopic Observations of the Formation, Growth and Shrinkage of Lithium Moss during Electrodeposition and Dissolution. *Electrochim. Acta* **2014**, *136*, 529–536.
- (42) Lu, D.; Shao, Y.; Lozano, T.; Bennett, W. D.; Graff, G. L.; Polzin, B.; Zhang, J.; Engelhard, M. H.; Saenz, N. T.; Henderson, W. A.; Bhattacharya, P.; Liu, J.; Xiao, J. Failure Mechanism for Fast-Charged Lithium Metal Batteries with Liquid Electrolytes. *Adv. Energy Mater.* **2015**, *5* (3), 1400993.
- (43) Sanchez, A. J.; Kazyak, E.; Chen, Y.; Chen, K. H.; Pattison, E. R.; Dasgupta, N. P. Plan-View Operando Video Microscopy of Li Metal Anodes: Identifying the Coupled

- Relationships among Nucleation, Morphology, and Reversibility. *ACS Energy Lett.* **2020**, *5* (3), 994–1004.
- (44) Wood, K. N.; Kazyak, E.; Chadwick, A. F.; Chen, K. H.; Zhang, J. G.; Thornton, K.; Dasgupta, N. P. Dendrites and Pits: Untangling the Complex Behavior of Lithium Metal Anodes through Operando Video Microscopy. *ACS Cent. Sci.* **2016**, *2* (11), 790–801.
- (45) Zhang, X. Q.; Cheng, X. B.; Chen, X.; Yan, C.; Zhang, Q. Fluoroethylene Carbonate Additives to Render Uniform Li Deposits in Lithium Metal Batteries. *Adv. Funct. Mater.* **2017**, *27* (10), 1–8.
- (46) Fan, X.; Chen, L.; Ji, X.; Deng, T.; Hou, S.; Chen, J.; Zheng, J.; Wang, F.; Jiang, J.; Xu, K.; Wang, C. Highly Fluorinated Interphases Enable High-Voltage Li-Metal Batteries. *Chem* **2018**, *4* (1), 174–185.
- (47) Wang, J.; Yamada, Y.; Sodeyama, K.; Chiang, C. H.; Tateyama, Y.; Yamada, A. Superconcentrated Electrolytes for a High-Voltage Lithium-Ion Battery. *Nat. Commun.* **2016**, *7* (May), 1–9.
- (48) Weber, R.; Genovese, M.; Louli, A. J.; Hames, S.; Martin, C.; Hill, I. G.; Dahn, J. R. Long Cycle Life and Dendrite-Free Lithium Morphology in Anode-Free Lithium Pouch Cells Enabled by a Dual-Salt Liquid Electrolyte. *Nat. Energy* **2019**, *4* (8), 683–689.
- (49) Xiao, J.; Li, Q.; Bi, Y.; Cai, M.; Dunn, B.; Glossmann, T.; Liu, J.; Osaka, T.; Sugiura, R.; Wu, B.; Yang, J.; Zhang, J.-G.; Whittingham, M. S. Understanding and Applying Coulombic Efficiency in Lithium Metal Batteries. *Nat. Energy* **2020**, *5* (8), 561–568.
- (50) Qian, J.; Adams, B. D.; Zheng, J.; Xu, W.; Henderson, W. A.; Wang, J.; Bowden, M. E.; Xu, S.; Hu, J.; Zhang, J. G. Anode-Free Rechargeable Lithium Metal Batteries. *Adv. Funct. Mater.* **2016**, *26* (39), 7094–7102.
- (51) Xu, K. Electrolytes and Interphases in Li-Ion Batteries and Beyond. *Chem. Rev.* **2014**, *114* (23), 11503–11618.
- (52) Zhang, H.; Eshetu, G. G.; Judez, X.; Li, C.; Rodriguez-Martínez, L. M.; Armand, M. Electrolyte Additives for Lithium Metal Anodes and Rechargeable Lithium Metal Batteries: Progress and Perspectives. *Angew. Chemie Int. Ed.* **2018**, *57* (46), 15002–15027.
- (53) Tripathi, A. M.; Su, W. N.; Hwang, B. J. In Situ Analytical Techniques for Battery Interface Analysis. *Chem. Soc. Rev.* **2018**, *47* (3), 736–751.
- (54) Peled, E.; Golodnitsky, D.; Ardel, G. Advanced Model for Solid Electrolyte Interphase Electrodes in Liquid and Polymer Electrolytes. *J. Electrochem. Soc.* **1997**, *144* (8), L208.
- (55) Xu, K. Nonaqueous Liquid Electrolytes for Lithium-Based Rechargeable Batteries. *Chem. Rev.* **2004**, *104* (10), 4303–4417.
- (56) Fang, C.; Li, J.; Zhang, M.; Zhang, Y.; Yang, F.; Lee, J. Z.; Lee, M.-H.; Alvarado, J.; Schroeder, M. A.; Yang, Y.; Lu, B.; Williams, N.; Ceja, M.; Yang, L.; Cai, M.; Gu, J.; Xu, K.; Wang, X.; Meng, Y. S. Quantifying Inactive Lithium in Lithium Metal Batteries. *Nature* **2019**, *572* (7770), 511–515.
- (57) He, Y.; Ren, X.; Xu, Y.; Engelhard, M. H.; Li, X.; Xiao, J.; Liu, J.; Zhang, J. G.; Xu, W.; Wang, C. Origin of Lithium Whisker Formation and Growth under Stress. *Nat.*

- Nanotechnol.* **2019**, *14* (11), 1042–1047.
- (58) Stark, J. K.; Ding, Y.; Kohl, P. A. Nucleation of Electrodeposited Lithium Metal: Dendritic Growth and the Effect of Co-Deposited Sodium. *J. Electrochem. Soc.* **2013**, *160* (9), D337–D342.
- (59) Ota, H.; Shima, K.; Ue, M.; Yamaki, J. ichi. Effect of Vinylene Carbonate as Additive to Electrolyte for Lithium Metal Anode. *Electrochim. Acta* **2004**, *49* (4), 565–572.
- (60) Lin, D.; Liu, Y.; Cui, Y. Reviving the Lithium Metal Anode for High-Energy Batteries. *Nat. Nanotechnol.* **2017**, *12* (3), 194–206.
- (61) Yamada, Y.; Wang, J.; Ko, S.; Watanabe, E.; Yamada, A. Advances and Issues in Developing Salt-Concentrated Battery Electrolytes. *Nat. Energy* **2019**, *4* (4), 269–280.
- (62) Qian, J.; Henderson, W. a.; Xu, W.; Bhattacharya, P.; Engelhard, M.; Borodin, O.; Zhang, J.-G. High Rate and Stable Cycling of Lithium Metal Anode. *Nat. Commun.* **2015**, *6* (1), 6362.
- (63) Jiao, S.; Ren, X.; Cao, R.; Engelhard, M. H.; Liu, Y.; Hu, D.; Mei, D.; Zheng, J.; Zhao, W.; Li, Q.; Liu, N.; Adams, B. D.; Ma, C.; Liu, J.; Zhang, J. G.; Xu, W. Stable Cycling of High-Voltage Lithium Metal Batteries in Ether Electrolytes. *Nat. Energy* **2018**, *3* (9), 739–746.
- (64) Bieker, G.; Winter, M.; Bieker, P. Electrochemical in Situ Investigations of SEI and Dendrite Formation on the Lithium Metal Anode. *Phys. Chem. Chem. Phys.* **2015**, *17* (14), 8670–8679.
- (65) Aurbach, D.; Zaban, A. Impedance Spectroscopy of Lithium Electrodes. *J. Electroanal. Chem.* **1993**, *348* (1–2), 155–179.
- (66) Basile, A.; Bhatt, A. I.; O’Mullane, A. P. Stabilizing Lithium Metal Using Ionic Liquids for Long-Lived Batteries. *Nat. Commun.* **2016**, *7*, ncomms11794.
- (67) Beyene, T. T.; Jote, B. A.; Wondimkun, Z. T.; Olbassa, B. W.; Huang, C. J.; Thirumalraj, B.; Wang, C. H.; Su, W. N.; Dai, H.; Hwang, B. J. Effects of Concentrated Salt and Resting Protocol on Solid Electrolyte Interface Formation for Improved Cycle Stability of Anode-Free Lithium Metal Batteries. *ACS Appl. Mater. Interfaces* **2019**, *11* (35), 31962–31971.
- (68) Aurbach, D.; Moshkovich, M. A Study of Lithium Deposition-Dissolution Processes in a Few Selected Electrolyte Solutions by Electrochemical Quartz Crystal Microbalance. *J. Electrochem. Soc.* **1998**, *145* (8), 2629.
- (69) Periyapperuma, K.; Arca, E.; Harvey, S.; Pathirana, T.; Ban, C.; Burrell, A.; Pozo-Gonzalo, C.; Howlett, P. C. High Current Cycling in a Superconcentrated Ionic Liquid Electrolyte to Promote Uniform Li Morphology and a Uniform LiF-Rich Solid Electrolyte Interphase. *ACS Appl. Mater. Interfaces* **2020**, *12* (37), 42236–42247.
- (70) Wang, E.; Dey, S.; Liu, T.; Menkin, S.; Grey, C. P. Effects of Atmospheric Gases on Li Metal Cyclability and Solid-Electrolyte Interphase Formation. *ACS Energy Lett.* **2020**, 1088–1094.
- (71) Yang, H.; Fey, E. O.; Trimm, B. D.; Dimitrov, N.; Whittingham, M. S. Effects of Pulse Plating on Lithium Electrodeposition, Morphology and Cycling Efficiency. *J. Power Sources* **2014**, *272*, 900–908.

-
- (72) Brissot, C.; Rosso, M.; Chazalviel, J. N.; Lascaud, S. Dendritic Growth Mechanisms in Lithium/Polymer Cells. *J. Power Sources* **1999**, *81*, 925–929.
- (73) Wandt, J.; Marino, C.; Gasteiger, H. A.; Jakes, P.; Eichel, R. A.; Granwehr, J. Operando Electron Paramagnetic Resonance Spectroscopy-Formation of Mossy Lithium on Lithium Anodes during Charge-Discharge Cycling. *Energy Environ. Sci.* **2015**, *8* (4), 1358–1367.
- (74) Bhattacharyya, R.; Key, B.; Chen, H.; Best, A. S.; Hollenkamp, A. F.; Grey, C. P. In Situ NMR Observation of the Formation of Metallic Lithium Microstructures in Lithium Batteries. *Nat. Mater.* **2010**, *9* (6), 504–510.
- (75) Chang, H. J.; Trease, N. M.; Ilott, A. J.; Zeng, D.; Du, L. S.; Jerschow, A.; Grey, C. P. Investigating Li Microstructure Formation on Li Anodes for Lithium Batteries by in Situ $^6\text{Li}/^7\text{Li}$ NMR and SEM. *J. Phys. Chem. C* **2015**, *119* (29), 16443–16451.
- (76) Chandrashekar, S.; Trease, N. M.; Chang, H. J.; Du, L.-S. S.; Grey, C. P.; Jerschow, A. ^7Li MRI of Li Batteries Reveals Location of Microstructural Lithium. *Nat. Mater.* **2012**, *11* (4), 311–315.
- (77) Ilott, A. J.; Mohammadi, M.; Chang, H. J.; Grey, C. P.; Jerschow, A. Real-Time 3D Imaging of Microstructure Growth in Battery Cells Using Indirect MRI. *Proc. Natl. Acad. Sci.* **2016**, *113* (39), 10779–10784.
- (78) Bayley, P. M.; Trease, N. M.; Grey, C. P. Insights into Electrochemical Sodium Metal Deposition as Probed with in Situ ^{23}Na NMR. *J. Am. Chem. Soc.* **2016**, *138* (6), 1955–1961.
- (79) Küpers, V.; Kolek, M.; Bieker, P.; Winter, M.; Brunklau, G. In Situ ^7Li -NMR Analysis of Lithium Metal Surface Deposits with Varying Electrolyte Compositions and Concentrations. *Phys. Chem. Chem. Phys.* **2019**, *21* (47), 26084–26094.
- (80) Wang, H.; Sa, N.; He, M.; Liang, X.; Nazar, L. F.; Balasubramanian, M.; Gallagher, K. G.; Key, B. In Situ NMR Observation of the Temporal Speciation of Lithium Sulfur Batteries during Electrochemical Cycling. *J. Phys. Chem. C* **2017**, *121* (11), 6011–6017.
- (81) Aurbach, D.; Weissman, I.; Schechter, A.; Cohen, H. X-Ray Photoelectron Spectroscopy Studies of Lithium Surfaces Prepared in Several Important Electrolyte Solutions. A Comparison with Previous Studies by Fourier Transform Infrared Spectroscopy. *Langmuir* **1996**, *12* (16), 3991–4007.
- (82) Brown, Z. L.; Jurng, S.; Nguyen, C. C.; Lucht, B. L. Effect of Fluoroethylene Carbonate Electrolytes on the Nanostructure of the Solid Electrolyte Interphase and Performance of Lithium Metal Anodes. *ACS Appl. Energy Mater.* **2018**, *1* (7), 3057–3062.
- (83) Li, Y.; Li, Y.; Pei, A.; Yan, K.; Sun, Y.; Wu, C. L.; Joubert, L. M.; Chin, R.; Koh, A. L.; Yu, Y.; Perrino, J.; Butz, B.; Chu, S.; Cui, Y. Atomic Structure of Sensitive Battery Materials and Interfaces Revealed by Cryo-Electron Microscopy. *Science* (80-.). **2017**, *358* (6362), 506–510.
- (84) Michan, A. L.; Divitini, G.; Pell, A. J.; Leskes, M.; Ducati, C.; Grey, C. P. Solid Electrolyte Interphase Growth and Capacity Loss in Silicon Electrodes. *J. Am. Chem. Soc.* **2016**, *138* (25), 7918–7931.
- (85) Jin, Y.; Kneusels, N. J. H.; Marbella, L. E.; Castillo-Martínez, E.; Magusin, P. C. M.

- M.; Weatherup, R. S.; Jónsson, E.; Liu, T.; Paul, S.; Grey, C. P. Understanding Fluoroethylene Carbonate and Vinylene Carbonate Based Electrolytes for Si Anodes in Lithium Ion Batteries with NMR Spectroscopy. *J. Am. Chem. Soc.* **2018**, *140* (31), 9854–9867.
- (86) Haber, S.; Leskes, M. What Can We Learn from Solid State NMR on the Electrode-Electrolyte Interface? *Adv. Mater.* **2018**, *30* (41), 1706496.
- (87) Hope, M. A.; Rinkel, B. L. D.; Gunnarsdóttir, A. B.; Märker, K.; Menkin, S.; Paul, S.; Sergeev, I. V.; Grey, C. P. Selective NMR Observation of the SEI–Metal Interface by Dynamic Nuclear Polarisation from Lithium Metal. *Nat. Commun.* **2020**, *11* (1), 2224.
- (88) Newman, J. S.; Thomas-Alyea, K. E. *Electrochemical Systems*, 3rd ed.; John Wiley & Sons, Inc.: Hoboken, NJ, USA, 2004.
- (89) Bockris, J. O.; Reddy, A. K. N. *Modern Electrochemistry: An Introduction to an Interdisciplinary Area. Volume 2*; Plenum Press: New York, 1970.
- (90) Bard, A. J.; Faulkner, L. R. *Electrochemical Methods Fundamentals of Electrochemistry*; 2001.
- (91) Elgrishi, N.; Rountree, K. J.; McCarthy, B. D.; Rountree, E. S.; Eisenhart, T. T.; Dempsey, J. L. A Practical Beginner's Guide to Cyclic Voltammetry. *J. Chem. Educ.* **2018**, *95* (2), 197–206.
- (92) Chadwick, A. F.; Vardar, G.; DeWitt, S.; Sleightholme, A. E. S.; Monroe, C. W.; Siegel, D. J.; Thornton, K. Computational Model of Magnesium Deposition and Dissolution for Property Determination via Cyclic Voltammetry. *J. Electrochem. Soc.* **2016**, *163* (9), A1813–A1821.
- (93) Heusler, K. E.; Landolt, D.; Trasatti, S. Electrochemical Corrosion Nomenclature (Recommendations 1988). *Pure Appl. Chem.* **1989**, *61* (1), 19–22.
- (94) Wood, M.; Clarke, S. Neutron Reflectometry for Studying Corrosion and Corrosion Inhibition. *Metals (Basel)*. **2017**, *7* (8), 304.
- (95) Gileadi, E. *Electrode Kinetics for Chemists, Engineers, and Materials Scientists*; Wiley-VCH: New York, 1993.
- (96) Gileadi, E. *Physical Electrochemistry: Fundamentals, Techniques and Applications*; Wiley-VCH; Weinheim, 2011.
- (97) Aurbach, D. Review of Selected Electrode – Solution Interactions Which Determine the Performance of Li and Li Ion Batteries. *J. Power Sources* **2000**, *89*, 206–218.
- (98) Bai, P.; Guo, J.; Wang, M.; Kushima, A.; Su, L.; Li, J.; Brushett, F. R.; Bazant, M. Z. Interactions between Lithium Growths and Nanoporous Ceramic Separators. *Joule* **2018**, *2* (11), 2434–2449.
- (99) Barton, J. L.; Bockris, J. O. The Electrolytic Growth of Dendrites from Ionic Solutions. *Proc. R. Soc. A Math. Phys. Eng. Sci.* **1962**, *268* (1335), 485–505.
- (100) Chazalviel, J. N. Electrochemical Aspects of the Generation of Ramified Metallic Electrodeposits. *Phys. Rev. A* **1990**, *42* (12), 7355–7367.
- (101) Sand, H. J. S. III. On the Concentration at the Electrodes in a Solution, with Special Reference to the Liberation of Hydrogen by Electrolysis of a Mixture of Copper

- Sulphate and Sulphuric Acid. *London, Edinburgh, Dublin Philos. Mag. J. Sci.* **1901**, *1* (1), 45–79.
- (102) Bai, P.; Li, J.; Brushett, F. R.; Bazant, M. Z. Transition of Lithium Growth Mechanisms in Liquid Electrolytes. *Energy Environ. Sci.* **2016**, *9* (10), 3221–3229.
- (103) Rosso, M.; Gobron, T.; Brissot, C.; Chazalviel, J.-N.; Lascaud, S. Onset of Dendritic Growth in Lithium/Polymer Cells. *J. Power Sources* **2001**, *97–98*, 804–806.
- (104) Cheh, H. Y. Electrodeposition of Gold by Pulsed Current. *J. Electrochem. Soc.* **1971**, *118* (4), 551–557.
- (105) Fukunaka, Y. Electrodeposition of Silver under Direct and Pulsed Current. *J. Electrochem. Soc.* **1989**, *136* (11), 3278.
- (106) Ul-Hamid, A.; Dafalla, H.; Quddus, A.; Saricimen, H.; Al-Hadhrami, L. M. Microstructure and Surface Mechanical Properties of Pulse Electrodeposited Nickel. *Appl. Surf. Sci.* **2011**, *257* (22), 9251–9259.
- (107) Ibl, N. Some Theoretical Aspects of Pulse Electrolysis. *Surf. Technol.* **1980**, *10* (2), 81–104.
- (108) Scharifker, B.; Hills, G. Theoretical and Experimental Studies of Multiple Nucleation. *Electrochim. Acta* **1983**, *28* (7), 879–889.
- (109) Pei, A.; Zheng, G.; Shi, F.; Li, Y.; Cui, Y. Nanoscale Nucleation and Growth of Electrodeposited Lithium Metal. *Nano Lett.* **2017**, *17* (2), 1132–1139.
- (110) Aryanfar, A.; Brooks, D.; Merinov, B. V.; Goddard, W. A.; Colussi, A. J.; Hoffmann, M. R. Dynamics of Lithium Dendrite Growth and Inhibition: Pulse Charging Experiments and Monte Carlo Calculations. *J. Phys. Chem. Lett.* **2014**, *5* (10), 1721–1726.
- (111) Puipe, J. C. Influence of Charge and Discharge of Electrical Double Layer in Pulse Plating. *Theory Pr. Pulse Plat.* **1986**, *10*, 41–54.
- (112) Irvine, J. T. S.; Sinclair, D. C.; West, A. R. Electroceramics: Characterization by Impedance Spectroscopy. *Adv. Mater.* **1990**, *2* (3), 132–138.
- (113) Boyle, D. T.; Kong, X.; Pei, A.; Rudnicki, P. E.; Shi, F.; Huang, W.; Bao, Z.; Qin, J.; Cui, Y. Transient Voltammetry with Ultramicroelectrodes Reveals the Electron Transfer Kinetics of Lithium Metal Anodes. *ACS Energy Lett.* **2020**, *5* (3), 701–709.
- (114) Lacey, M. *ImpedanceR: Functions for Simulating Impedance Spectra. R Package Version 0.0.1.*; 2020.
- (115) Aurbach, D.; Zaban, A. Impedance Spectroscopy of Nonactive Metal Electrodes at Low Potentials in Propylene Carbonate Solutions: A Comparison to Studies of Li Electrodes. *J. Electrochem. Soc.* **1994**, *141* (7), 1808–1819.
- (116) Zaban, A.; Zinigrad, E.; Aurbach, D. Impedance Spectroscopy of Li Electrodes. 4. A General Simple Model of the Li-Solution Interphase in Polar Aprotic Systems. *J. Phys. Chem.* **1996**, *100* (8), 3089–3101.
- (117) Barsoukov, E.; Macdonald, J. R. *Impedance Spectroscopy: Theory, Experiment, and Applications*; John Wiley & Sons, Incorporated: Hoboken, UNITED STATES, 2005.

-
- (118) Aurbach, D.; Zaban, A. Impedance Spectroscopy of Lithium Electrodes. Part 3. The Importance of Li Electrode Surface Preparation. *J. Electroanal. Chem.* **1994**, *365* (1–2), 41–45.
- (119) Apperley, D. C.; Harris, R. K.; Hodgkinson, P. *Solid-State NMR: Basic Principles and Practice*; Momentum Press: New York, 2012.
- (120) Halat, D. M. *¹⁷O Solid-State NMR Spectroscopy of Functional Oxides for Energy Conversion* (Doctoral Thesis), University of Cambridge, Cambridge, 2018.
- (121) Illott, A. J.; Jerschow, A. Aspects of NMR Reciprocity and Applications in Highly Conductive Media. *Concepts Magn. Reson. Part A Bridg. Educ. Res.* **2018**, *47A* (2), 1–8.
- (122) Keeler, J. *Understanding NMR Spectroscopy*, 2nd ed.; John Wiley: Chichester, 2010.
- (123) Pecher, O.; Carretero-Gonzalez, J.; Griffith, K. J. J.; Grey, C. P. P. Materials' Methods: NMR in Battery Research. *Chem. Mater.* **2017**, *29* (1), 213–242.
- (124) Grey, C. P.; Dupré, N. NMR Studies of Cathode Materials for Lithium-Ion Rechargeable Batteries. *Chem. Rev.* **2004**, *104* (10), 4493–4512.
- (125) Pell, A. J.; Pintacuda, G.; Grey, C. P. Paramagnetic NMR in Solution and the Solid State. *Prog. Nucl. Magn. Reson. Spectrosc.* **2019**, *111*, 1–271.
- (126) Knight, W. D. Nuclear Magnetic Resonance Shift in Metals. *Phys. Rev.* **1949**, *76* (8), 1259–1260.
- (127) Levitt, M. H. *Spin Dynamics: Basics of Nuclear Magnetic Resonance*; John Wiley & Sons Ltd.: Chichester, 2000.
- (128) Kittel, C. *Introduction to Solid State Physics, 8th Edition*; John Wiley & Sons, Inc.: Hoboken, NJ, USA, 2005.
- (129) MacKenzie, K. J. D.; Smith, M. E. *Multinuclear Solid-State Nuclear Magnetic Resonance of Inorganic Materials, Pergamon Materials Series Vol. 6*; 2002.
- (130) Rowland, T. J. Nuclear Magnetic Resonance in Metals. *Prog. Mater. Sci.* **1961**, *9* (1), 3–91.
- (131) Bennett, L. H.; Watson, R. E.; Carter, G. C. Relevance of Knight Shift Measurements to the Electronic Density of States. *J. Res. Natl. Bur. Stand. Sect. A Phys. Chem.* **1970**, *74A* (4), 569.
- (132) Letellier, M.; Chevallier, F.; Clinard, C. C.; Frackowiak, E.; Rouzaud, J. N.; Béguin, F.; Morcrette, M.; Tarascon, J. M. The First in Situ ⁷Li Nuclear Magnetic Resonance Study of Lithium Insertion in Hard-Carbon Anode Materials for Li-Ion Batteries. *J. Chem. Phys.* **2003**, *118* (13), 6038–6045.
- (133) Stratford, J. M.; Allan, P. K.; Pecher, O.; Chater, P. A.; Grey, C. P. Mechanistic Insights into Sodium Storage in Hard Carbon Anodes. *Chem. Commun.* **2016**, *52* (84), 12430–12433.
- (134) Au, H.; Alptekin, H.; Jensen, A. C. S.; Olsson, E.; O'Keefe, C. A.; Smith, T.; Crespo-Ribadeneyra, M.; Headen, T. F.; Grey, C. P.; Cai, Q.; Drew, A. J.; Titirici, M.-M. A Revised Mechanistic Model for Sodium Insertion in Hard Carbons. *Energy Environ. Sci.* **2020**.

-
- (135) Trease, N. M.; Zhou, L.; Chang, H. J.; Zhu, B. Y.; Grey, C. P. In Situ NMR of Lithium Ion Batteries: Bulk Susceptibility Effects and Practical Considerations. *Solid State Nucl. Magn. Reson.* **2012**, *42*, 62–70.
- (136) Cheng, D. K. *Field and Wave Electromagnetics*; Addison-Wesley: Reading, Mass., 1989.
- (137) Zhou, L.; Leskes, M.; Ilott, A. J.; Trease, N. M.; Grey, C. P. Paramagnetic Electrodes and Bulk Magnetic Susceptibility Effects in the in Situ NMR Studies of Batteries: Application to $\text{Li}_{1.08}\text{Mn}_{1.92}\text{O}_4$ spinels. *J. Magn. Reson.* **2013**, *234*, 44–57.
- (138) Kubo, A.; Spaniol, T. P.; Terao, T. The Effect of Bulk Magnetic Susceptibility on Solid State NMR Spectra of Paramagnetic Compounds. *J. Magn. Reson.* **1998**, *133* (2), 330–340.
- (139) Marques, J. P.; Bowtell, R. Application of a Fourier-Based Method for Rapid Calculation of Field Inhomogeneity Due to Spatial Variation of Magnetic Susceptibility. *Concepts Magn. Reson. Part B Magn. Reson. Eng.* **2005**, *25* (1), 65–78.
- (140) Salomir, R.; De Senneville, B. D.; Moonen, C. T. W. A Fast Calculation Method for Magnetic Field Inhomogeneity Due to an Arbitrary Distribution of Bulk Susceptibility. *Concepts Magn. Reson. Part B Magn. Reson. Eng.* **2003**, *19* (1), 26–34.
- (141) Ilott, A. J.; Chandrashekar, S.; Klöckner, A.; Chang, H. J.; Trease, N. M.; Grey, C. P.; Greengard, L.; Jerschow, A. Visualizing Skin Effects in Conductors with MRI: ^7Li MRI Experiments and Calculations. *J. Magn. Reson.* **2014**, *245*, 143–149.
- (142) Pigliapochi, R.; O’Brien, L.; Pell, A. J.; Gaultois, M. W.; Janssen, Y.; Khalifah, P. G.; Grey, C. P. When Do Anisotropic Magnetic Susceptibilities Lead to Large NMR Shifts? Exploring Particle Shape Effects in the Battery Electrode Material LiFePO_4 . *J. Am. Chem. Soc.* **2019**, *141* (33), 13089–13100.
- (143) Hoult, D. I. The Principle of Reciprocity in Signal Strength Calculations - A Mathematical Guide. *Concepts Magn. Reson.* **2000**, *12* (4), 173–187.
- (144) Lide, D. R. *CRC Handbook of Chemistry and Physics, 84th Edition*; CRC: Boca Raton; London, 2003.
- (145) Edmonds, R. N.; Harrison, M. R.; Edwards, P. P. Chapter 9. Conduction Electron Spin Resonance in Metallic Systems. *Annu. Reports Sect. "C" (Physical Chem.* **1985**, *82* (0), 265.
- (146) Mehring, M.; Kotzur, D.; Kanert, O. Influence of the Skin Effect on the Bloch Decay in Metals. *Phys. status solidi* **1972**, *53* (1), K25–K28.
- (147) Ilott, A. J.; Jerschow, A. Super-Resolution Surface Microscopy of Conductors Using Magnetic Resonance. *Sci. Rep.* **2017**, *7* (1), 1–7.
- (148) See, K. A.; Leskes, M.; Griffin, J. M.; Britto, S.; Matthews, P. D.; Emly, A.; Ven, A. Van Der; Wright, D. S.; Morris, A. J.; Grey, C. P.; Seshadri, R.; Van der Ven, A.; Wright, D. S.; Morris, A. J.; Grey, C. P.; Seshadri, R.; Ven, A. Van Der; Wright, D. S.; Morris, A. J.; Grey, C. P.; Seshadri, R. Ab Initio Structure Search and in Situ ^7Li NMR Studies of Discharge Products in the Li-S Battery System. *J. Am. Chem. Soc.* **2014**, *136* (46), 16368–16377.
- (149) Britton, M. M. Magnetic Resonance Imaging of Electrochemical Cells Containing Bulk

- Metal. *ChemPhysChem* **2014**, *15* (9), 1731–1736.
- (150) Britton, M. M.; Bayley, P. M.; Howlett, P. C.; Davenport, A. J.; Forsyth, M. In Situ, Real-Time Visualization of Electrochemistry Using Magnetic Resonance Imaging. *J. Phys. Chem. Lett.* **2013**, *4* (17), 3019–3023.
- (151) Pecher, O.; Bayley, P. M.; Liu, H.; Liu, Z.; Trease, N. M.; Grey, C. P. Automatic Tuning Matching Cyclor (ATMC) in Situ NMR Spectroscopy as a Novel Approach for Real-Time Investigations of Li-and Na-Ion Batteries. *J. Magn. Reson.* **2016**, *265* (2015), 200–209.
- (152) Bruce, P. G.; Freunberger, S. A.; Hardwick, L. J.; Tarascon, J.-M. Li–O₂ and Li–S Batteries with High Energy Storage. *Nat. Mater.* **2012**, *11* (02), 172–172.
- (153) Xu, W.; Wang, J.; Ding, F.; Chen, X.; Nasybulin, E.; Zhang, Y.; Zhang, J.-G. G. Lithium Metal Anodes for Rechargeable Batteries. *Energy Environ. Sci.* **2014**, *7* (2), 513–537.
- (154) Mogi, R.; Inaba, M.; Iriyama, Y.; Abe, T.; Ogumi, Z. In Situ Atomic Force Microscopy Study on Lithium Deposition on Nickel Substrates at Elevated Temperatures. *J. Electrochem. Soc.* **2002**, *149* (4), A385.
- (155) Heine, J.; Hilbig, P.; Qi, X.; Niehoff, P.; Winter, M.; Bieker, P. Fluoroethylene Carbonate as Electrolyte Additive in Tetraethylene Glycol Dimethyl Ether Based Electrolytes for Application in Lithium Ion and Lithium Metal Batteries. *J. Electrochem. Soc.* **2015**, *162* (6), A1094–A1101.
- (156) Ding, F.; Xu, W.; Chen, X.; Zhang, J.; Engelhard, M. H.; Zhang, Y.; Johnson, B. R.; Crum, J. V.; Blake, T. A.; Liu, X.; Zhang, J.-G. Effects of Carbonate Solvents and Lithium Salts on Morphology and Coulombic Efficiency of Lithium Electrode. *J. Electrochem. Soc.* **2013**, *160* (10), A1894–A1901.
- (157) Li, Y.; Huang, W.; Li, Y.; Pei, A.; Boyle, D. T.; Cui, Y. Correlating Structure and Function of Battery Interphases at Atomic Resolution Using Cryoelectron Microscopy. *Joule* **2018**, *2* (10), 2167–2177.
- (158) Popov, K. I.; Maksimović, M. D.; Oćokoljić, B. M.; Lazarević, B. J. Fundamental Aspects of Pulsating Current Metal Electrodeposition - I: The Effect of the Pulsating Current on the Surface Roughness and the Porosity of Metal Deposits. *Surf. Technol.* **1980**, *11*, 99–109.
- (159) Li, Q.; Tan, S.; Li, L.; Lu, Y.; He, Y. Understanding the Molecular Mechanism of Pulse Current Charging for Stable Lithium-Metal Batteries. *Sci. Adv.* **2017**, *3* (7), 1–10.
- (160) Maraschky, A.; Akolkar, R. Mechanism Explaining the Onset Time of Dendritic Lithium Electrodeposition via Considerations of the Li + Transport within the Solid Electrolyte Interphase. *J. Electrochem. Soc.* **2018**, *165* (14), D696–D703.
- (161) García, G.; Dieckhöfer, S.; Schuhmann, W.; Ventosa, E. Exceeding 6500 Cycles for LiFePO₄/Li Metal Batteries through Understanding Pulsed Charging Protocols. *J. Mater. Chem. A* **2018**, *6* (11), 4746–4751.
- (162) Rehnlund, D.; Ihrfors, C.; Maibach, J.; Nyholm, L. Dendrite-Free Lithium Electrode Cycling via Controlled Nucleation in Low LiPF₆ Concentration Electrolytes. *Mater. Today* **2018**, *21* (10), 1010–1018.
- (163) Saito, Y.; Morimura, W.; Kuratani, R.; Nishikawa, S. Ion Transport in Separator

- Membranes of Lithium Secondary Batteries. *J. Phys. Chem. C* **2015**, *119* (9), 4702–4708.
- (164) Marbella, L. E.; Zekoll, S.; Kasemchainan, J.; Emge, S. P.; Bruce, P. G.; Grey, C. P. 7Li NMR Chemical Shift Imaging To Detect Microstructural Growth of Lithium in All-Solid-State Batteries. *Chem. Mater.* **2019**, *31* (8), 2762–2769.
- (165) Wickham, H.; Francois, R.; Henry, L.; Müller, K. A Grammar of Data Manipulation. *Cran*. 2017.
- (166) Stejskal, E. O.; Tanner, J. E. Spin Diffusion Measurements: Spin Echoes in the Presence of a Time-Dependent Field Gradient. *J. Chem. Phys.* **1965**, *42* (1), 288–292.
- (167) Klaus Zick. Diffusion NMR User Manual. *Bruker Corp.* **2016**, No. 004.
- (168) Aurbach, D.; Zaban, A. Impedance Spectroscopy of Lithium Electrodes. *J. Electroanal. Chem.* **1994**, *367* (1–2), 15–25.
- (169) Odziemkowski, M. An Electrochemical Study of the Reactivity at the Lithium Electrolyte/Bare Lithium Metal Interface. *J. Electrochem. Soc.* **1993**, *140* (6), 1546.
- (170) Hou, T.; Yang, G.; Rajput, N. N.; Self, J.; Park, S.-W.; Nanda, J.; Persson, K. The Influence of FEC on the Solvation Structure and Reduction Reaction of LiPF₆/EC Electrolytes and Its Implication for Solid Electrolyte Interphase Formation. *Nano Energy* **2019**, *64* (July), 103881.
- (171) Philippe, B.; Hahlin, M.; Edström, K.; Gustafsson, T.; Siegbahn, H.; Rensmo, H. Photoelectron Spectroscopy for Lithium Battery Interface Studies. *J. Electrochem. Soc.* **2016**, *163* (2), A178–A191.
- (172) Lin, C. F.; Kozen, A. C.; Noked, M.; Liu, C.; Rubloff, G. W. ALD Protection of Li-Metal Anode Surfaces – Quantifying and Preventing Chemical and Electrochemical Corrosion in Organic Solvent. *Adv. Mater. Interfaces* **2016**, *3* (21), 1–7.
- (173) Maibach, J.; Källquist, I.; Andersson, M.; Urpelainen, S.; Edström, K.; Rensmo, H.; Siegbahn, H.; Hahlin, M. Probing a Battery Electrolyte Drop with Ambient Pressure Photoelectron Spectroscopy. *Nat. Commun.* **2019**, *10* (1), 1–7.
- (174) Meyer, B. M.; Leifer, N.; Sakamoto, S.; Greenbaum, S. G.; Grey, C. P. High Field Multinuclear NMR Investigation of the SEI Layer in Lithium Rechargeable Batteries. *Electrochem. Solid-State Lett.* **2005**, *8* (3), A145.
- (175) Michan, A. L.; Leskes, M.; Grey, C. P. Voltage Dependent Solid Electrolyte Interphase Formation in Silicon Electrodes: Monitoring the Formation of Organic Decomposition Products. *Chem. Mater.* **2016**, *28* (1), 385–398.
- (176) Lu, P.; Harris, S. J. Lithium Transport within the Solid Electrolyte Interphase. *Electrochem. Commun.* **2011**, *13* (10), 1035–1037.
- (177) Zheng, J.; Hu, Y. Y. New Insights into the Compositional Dependence of Li-Ion Transport in Polymer-Ceramic Composite Electrolytes. *ACS Appl. Mater. Interfaces* **2018**, *10* (4), 4113–4120.
- (178) Boyd, G. E.; Adamson, A. W.; Myers, L. S. The Exchange Adsorption of Ions from Aqueous Solutions by Organic Zeolites. II. Kinetics. *J. Am. Chem. Soc.* **1947**, *69* (11), 2836–2848.

-
- (179) Helfferich, F. G. Ion Exchange Kinetics--Evolution of a Theory. In *Mass Transfer and Kinetics of Ion Exchange*; 1983.
- (180) Kosmulski, M.; Jaroniec, M.; Szczypa, J. Liquid/Solid Interfaces: Studies of Kinetics of Isotope Exchange. *Adsorpt. Sci. Technol.* **1985**, *2* (2), 97–119.
- (181) Huang, T.-C.; Tsai, F.-N. Determination of Kinetic Parameters of Heterogeneous Isotopic Exchange Reaction. *J. Chem. Eng. Japan* **1977**, *10* (2), 131–136.
- (182) Ilott, A. J.; Jerschow, A. Probing Solid-Electrolyte Interphase (SEI) Growth and Ion Permeability at Undriven Electrolyte-Metal Interfaces Using ⁷Li NMR. *J. Phys. Chem. C* **2018**, *122* (24), 12598–12604.
- (183) Messer, R.; Noack, F. Nuclear Magnetic Relaxation by Self-Diffusion in Solid Lithium: T1-Frequency Dependence. *Appl. Phys.* **1975**, *6* (1), 79–88.
- (184) Christensen, J.; Newman, J. A Mathematical Model for the Lithium-Ion Negative Electrode Solid Electrolyte Interphase. *J. Electrochem. Soc.* **2004**, *151* (11), A1977.
- (185) Tang, M.; Newman, J. Why Is the Solid-Electrolyte-Interphase Selective? Through-Film Ferrocenium Reduction on Highly Oriented Pyrolytic Graphite. *J. Electrochem. Soc.* **2012**, *159* (12), A1922–A1927.
- (186) Shampine, L. F.; Reichelt, M. W. Matlab Ode Suite. *{SIAM} J. Sci. Comput.* **1995**, *18* (1), 1–22.
- (187) Tasaki, K.; Goldberg, A.; Lian, J.-J.; Walker, M.; Timmons, A.; Harris, S. J. Solubility of Lithium Salts Formed on the Lithium-Ion Battery Negative Electrode Surface in Organic Solvents. *J. Electrochem. Soc.* **2009**, *156* (12), A1019.
- (188) Tang, M.; Lu, S.; Newman, J. Experimental and Theoretical Investigation of Solid-Electrolyte-Interphase Formation Mechanisms on Glassy Carbon. *J. Electrochem. Soc.* **2012**, *159* (11), A1775–A1785.
- (189) Jin, Y.; Kneusels, N. J. H.; Magusin, P. C. M. M.; Kim, G.; Castillo-Martínez, E.; Marbella, L. E.; Kerber, R. N.; Howe, D. J.; Paul, S.; Liu, T.; Grey, C. P. Identifying the Structural Basis for the Increased Stability of the Solid Electrolyte Interphase Formed on Silicon with the Additive Fluoroethylene Carbonate. *J. Am. Chem. Soc.* **2017**, *139* (42), 14992–15004.
- (190) Verbrugge, M. W.; Koch, B. J. Microelectrode Study of the Lithium/Propylene Carbonate Interface: Temperature and Concentration Dependence of Physicochemical Parameters. *J. Electrochem. Soc.* **1994**, *141* (11), 3053.
- (191) Lee, S. I.; Jung, U. H.; Kim, Y. S.; Kim, M. H.; Ahn, D. J.; Chun, H. S. A Study of Electrochemical Kinetics of Lithium Ion in Organic Electrolytes. *Korean J. Chem. Eng.* **2002**, *19* (4), 638–644.
- (192) Cogswell, D. A. Quantitative Phase-Field Modeling of Dendritic Electrodeposition. *Phys. Rev. E* **2015**, *92* (1), 011301.
- (193) Enrique, R. A.; DeWitt, S.; Thornton, K. Morphological Stability during Electrodeposition. *MRS Commun.* **2017**, *7* (3), 658–663.
- (194) Hao, F.; Verma, A.; Mukherjee, P. P. Mesoscale Complexations in Lithium Electrodeposition. *ACS Appl. Mater. Interfaces* **2018**, *10* (31), 26320–26327.

-
- (195) Xu, C.; Lindgren, F.; Philippe, B.; Gorgoi, M.; Björefors, F.; Edström, K.; Gustafsson, T. Improved Performance of the Silicon Anode for Li-Ion Batteries: Understanding the Surface Modification Mechanism of Fluoroethylene Carbonate as an Effective Electrolyte Additive. *Chem. Mater.* **2015**, *27* (7), 2591–2599.
- (196) Lin, D.; Liu, Y.; Li, Y. Y.; Li, Y. Y.; Pei, A.; Xie, J.; Huang, W.; Cui, Y. Fast Galvanic Lithium Corrosion Involving a Kirkendall-Type Mechanism. *Nat. Chem.* **2019**, *11* (4), 382–389.
- (197) Kolesnikov, A.; Kolek, M.; Dohmann, J. F.; Horsthemke, F.; Börner, M.; Bieker, P.; Winter, M.; Stan, M. C. Galvanic Corrosion of Lithium-Powder-Based Electrodes. *Adv. Energy Mater.* **2020**, *2000017*, 1–9.
- (198) Guo, R.; Gallant, B. M. Li₂O Solid Electrolyte Interphase: Probing Transport Properties at the Chemical Potential of Lithium. *Chem. Mater.* **2020**, *32* (13), 5525–5533.
- (199) Schranzhofer, H.; Bugajski, J.; Santner, H. J.; Korepp, C.; Möller, K. C.; Besenhard, J. O.; Winter, M.; Sitte, W. Electrochemical Impedance Spectroscopy Study of the SEI Formation on Graphite and Metal Electrodes. *J. Power Sources* **2006**, *153* (2), 391–395.
- (200) Wang, L.; Menakath, A.; Han, F.; Wang, Y.; Zavalij, P. Y.; Gaskell, K. J.; Borodin, O.; Iuga, D.; Brown, S. P.; Wang, C.; Xu, K.; Eichhorn, B. W. Identifying the Components of the Solid–Electrolyte Interphase in Li-Ion Batteries. *Nat. Chem.* **2019**, *11* (September).
- (201) Cho, S. J.; Yu, D. E.; Pollard, T. P.; Moon, H.; Jang, M.; Borodin, O.; Lee, S. Y. Nonflammable Lithium Metal Full Cells with Ultra-High Energy Density Based on Coordinated Carbonate Electrolytes. *iScience* **2020**, *23* (2), 100844.
- (202) Pang, Q.; Liang, X.; Shyamsunder, A.; Nazar, L. F. An In Vivo Formed Solid Electrolyte Surface Layer Enables Stable Plating of Li Metal. *Joule* **2017**, *1* (4), 871–886.
- (203) Hsieh, Y.-C.; Leißing, M.; Nowak, S.; Hwang, B.-J.; Winter, M.; Brunklaus, G. Quantification of Dead Lithium via In Situ Nuclear Magnetic Resonance Spectroscopy. *Cell Reports Phys. Sci.* **2020**, 100139.
- (204) Novák, P. CuO Cathode in Lithium Cells-II. Reduction Mechanism of CuO. *Electrochim. Acta* **1985**, *30* (12), 1687–1692.
- (205) Klein, F.; Pinedo, R.; Hering, P.; Polity, A.; Janek, J.; Adelhelm, P. Reaction Mechanism and Surface Film Formation of Conversion Materials for Lithium- and Sodium-Ion Batteries: An XPS Case Study on Sputtered Copper Oxide (CuO) Thin Film Model Electrodes. *J. Phys. Chem. C* **2016**, *120* (3), 1400–1414.
- (206) Huang, W.; Boyle, D. T.; Li, Y. Y.; Li, Y. Y.; Pei, A.; Chen, H.; Cui, Y. Nanostructural and Electrochemical Evolution of the Solid-Electrolyte Interphase on CuO Nanowires Revealed by Cryogenic-Electron Microscopy and Impedance Spectroscopy. *ACS Nano* **2019**, *13* (1), 737–744.
- (207) Shu, J.; Shui, M.; Huang, F.; Xu, D.; Ren, Y.; Hou, L.; Cui, J.; Xu, J. Comparative Study on Surface Behaviors of Copper Current Collector in Electrolyte for Lithium-Ion Batteries. *Electrochim. Acta* **2011**, *56* (8), 3006–3014.
- (208) Yu, Z.; Cui, Y.; Bao, Z. Design Principles of Artificial Solid Electrolyte Interphases for

- Lithium-Metal Anodes. *Cell Reports Phys. Sci.* **2020**, *1* (7), 100119.
- (209) Lopez, J.; Pei, A.; Oh, J. Y.; Wang, G.-J. J. N.; Cui, Y.; Bao, Z. Effects of Polymer Coatings on Electrodeposited Lithium Metal. *J. Am. Chem. Soc.* **2018**, *140* (37), 11735–11744.
- (210) Assegie, A. A.; Cheng, J.-H.; Kuo, L.-M.; Su, W.-N.; Hwang, B.-J. Polyethylene Oxide Film Coating Enhances Lithium Cycling Efficiency of an Anode-Free Lithium-Metal Battery. *Nanoscale* **2018**, *10* (13), 6125–6138.
- (211) Manuel Stephan, A. Review on Gel Polymer Electrolytes for Lithium Batteries. *Eur. Polym. J.* **2006**, *42* (1), 21–42.
- (212) Fauteux, D.; Prud'Homme, J.; Harvey, P. E. Electrochemical Stability and Ionic Conductivity of Some Polymer-Lix Based Electrolytes. *Solid State Ionics* **1988**, *28–30*, 923–928.
- (213) Chiappone, A.; Jeremias, S.; Bongiovanni, R.; Schönhoff, M. NMR Study of Photo-Crosslinked Solid Polymer Electrolytes: The Influence of Monofunctional Oligoethers. *J. Polym. Sci. Part B Polym. Phys.* **2013**, *51* (21), 1571–1580.
- (214) Bohnke, O.; Rousselot, C.; Gillet, P. A.; Truche, C. Gel Electrolyte for Solid-State Electrochromic Cell. *J. Electrochem. Soc.* **1992**, *139* (7), 1862.
- (215) Appetecchi, G. B.; Croce, F.; Scrosati, B. Kinetics and Stability of the Lithium Electrode in Poly(Methylmethacrylate)-Based Gel Electrolytes. *Electrochim. Acta* **1995**, *40* (8), 991–997.
- (216) Obrovac, M. N.; Chevrier, V. L. Alloy Negative Electrodes for Li-Ion Batteries. *Chem. Rev.* **2014**, *114* (23), 11444–11502.
- (217) Padhi, A. K. Effect of Structure on the Fe³⁺/Fe²⁺ Redox Couple in Iron Phosphates. *J. Electrochem. Soc.* **1997**, *144* (5), 1609.
- (218) Menkin, S.; O'Keefe, C. A.; Gunnarsdottir, A. B.; Dey, S.; Pesci, F.; Shen, Z.; Aguadero, A.; Grey, C. P. Preprint: Towards an Understanding of the SEI Formation and Lithium Preferential Plating on Copper. *ChemRxiv* **2020**.
- (219) Chavez, K. L.; Hess, D. W. A Novel Method of Etching Copper Oxide Using Acetic Acid. *J. Electrochem. Soc.* **2001**, *148* (11), G640.
- (220) Schenck, J. F. The Role of Magnetic Susceptibility in Magnetic Resonance Imaging: MRI Magnetic Compatibility of the First and Second Kinds. *Med. Phys.* **1996**, *23* (6), 815–850.
- (221) Mohammadi, M.; Jerschow, A. In Situ and Operando Magnetic Resonance Imaging of Electrochemical Cells: A Perspective. *J. Magn. Reson.* **2019**, *308*, 106600.
- (222) Hagen, M.; Hanselmann, D.; Ahlbrecht, K.; Maça, R.; Gerber, D.; Tübke, J. Lithium-Sulfur Cells: The Gap between the State-of-the-Art and the Requirements for High Energy Battery Cells. *Adv. Energy Mater.* **2015**, *5* (16), 1401986.
- (223) Shi, F.; Pei, A.; Vailionis, A.; Xie, J.; Liu, B.; Zhao, J.; Gong, Y.; Cui, Y. Strong Texturing of Lithium Metal in Batteries. *Proc. Natl. Acad. Sci.* **2017**, *114* (46), 12138–12143.
- (224) Nilsson, V.; Kotronia, A.; Lacey, M.; Edström, K.; Johansson, P. Highly Concentrated

- LiTFSI-EC Electrolytes for Lithium Metal Batteries. *ACS Appl. Energy Mater.* **2019**, 4–11.
- (225) Kadyk, T.; Eikerling, M. Magnetic Susceptibility as a Direct Measure of Oxidation State in LiFePO₄ Batteries and Cyclic Water Gas Shift Reactors. *Phys. Chem. Chem. Phys.* **2015**, 17 (30), 19834–19843.
- (226) Gutowsky, H. S.; McGarvey, B. R. Nuclear Magnetic Resonance in Metals. I. Broadening of Absorption Lines by Spin-Lattice Interactions. *J. Chem. Phys.* **1952**, 20 (9), 1472–1477.
- (227) Ilott, A. J.; Mohammadi, M.; Schauerman, C. M.; Ganter, M. J.; Jerschow, A. Rechargeable Lithium-Ion Cell State of Charge and Defect Detection by in-Situ inside-out Magnetic Resonance Imaging. *Nat. Commun.* **2018**, 9 (1), 1776.
- (228) Lin, D.; Liu, Y.; Liang, Z.; Lee, H. W.; Sun, J.; Wang, H.; Yan, K.; Xie, J.; Cui, Y. Layered Reduced Graphene Oxide with Nanoscale Interlayer Gaps as a Stable Host for Lithium Metal Anodes. *Nat. Nanotechnol.* **2016**, 11 (7), 626–632.
- (229) Kozen, A. C.; Lin, C. F.; Pearse, A. J.; Schroeder, M. A.; Han, X.; Hu, L.; Lee, S. B.; Rubloff, G. W.; Noked, M. Next-Generation Lithium Metal Anode Engineering via Atomic Layer Deposition. *ACS Nano* **2015**, 9 (6), 5884–5892.
- (230) Ma, L.; Kim, M. S.; Archer, L. A. Stable Artificial Solid Electrolyte Interphases for Lithium Batteries. *Chem. Mater.* **2017**, 29 (10), 4181–4189.
- (231) Liang, X.; Pang, Q.; Kochetkov, I. R.; Sempere, M. S.; Huang, H.; Sun, X.; Nazar, L. F.; Se, B. A Facile Surface Chemistry Route to a Stabilized Lithium Metal Anode. *Nat. Energy* **2017**, 6 (July), 17119.
- (232) Choudhury, S.; Tu, Z.; Stalin, S.; Vu, D.; Fawole, K.; Gunceler, D.; Sundararaman, R.; Archer, L. A. Electroless Formation of Hybrid Lithium Anodes for Fast Interfacial Ion Transport. *Angew. Chemie - Int. Ed.* **2017**, 56 (42), 13070–13077.
- (233) Tu, Z.; Choudhury, S.; Zachman, M. J.; Wei, S.; Zhang, K.; Kourkoutis, L. F.; Archer, L. A. Fast Ion Transport at Solid-Solid Interfaces in Hybrid Battery Anodes. *Nat. Energy* **2018**, 3 (4), 310–316.
- (234) Besenhard, J. O.; Görtler, J.; Komenda, P.; Paxinos, A. Corrosion Protection of Secondary Lithium Electrodes in Organic Electrolytes. *J. Power Sources* **1987**, 20 (3–4), 253–258.
- (235) Amanchukwu, C. V.; Kong, X.; Qin, J.; Cui, Y.; Bao, Z. Nonpolar Alkanes Modify Lithium-Ion Solvation for Improved Lithium Deposition and Stripping. *Adv. Energy Mater.* **2019**, 9 (41), 1–11.
- (236) Galluzzo, M. D.; Halat, D. M.; Loo, W. S.; Mullin, S. A.; Reimer, J. A.; Balsara, N. P. Dissolution of Lithium Metal in Poly(Ethylene Oxide). *ACS Energy Lett.* **2019**, 4 (4), 903–907.
- (237) Pasta, M.; Armstrong, D.; Brown, Z. L.; Bu, J.; Castell, M. R.; Chen, P.; Cocks, A.; Corr, S. A.; Cussen, E. J.; Darnbrough, E.; Deshpande, V.; Doerr, C.; Dyer, M. S.; El-Shinawi, H.; Fleck, N.; Grant, P.; Gregory, G. L.; Grovenor, C.; Hardwick, L. J.; Irvine, J. T. S.; Lee, H. J.; Li, G.; Liberti, E.; McClelland, I.; Monroe, C.; Nellist, P. D.; Shearing, P. R.; Shoko, E.; Song, W.; Jolly, D. S.; Thomas, C. I.; Turrell, S. J.; Vestli,

M.; Williams, C. K.; Zhou, Y.; Bruce, P. G. 2020 Roadmap on Solid-State Batteries. *J. Phys. Energy* **2020**, 2 (3), 032008.